

Corso di laurea magistrale in Ingegneria Meccanica



**Politecnico
di Torino**

Tesi di Laurea Magistrale

**Study and modelling of a fuel cell air supply
system with turbocharger for a regional
hybrid electric aircraft**

Relatori accademici

Prof. Massimo Sorli
Ing. Antonio Carlo Bertolino
Ing. Andrea De Martin
Ing. Roberto Guida

Candidato

Onofrio Fattoruso 277636

Ottobre 2023

Abstract

The evolution and accumulation of operational experience in the field of fuel cells are opening new perspectives for the use of these technologies in continuous power generation in aviation. In this prospect, the pursuit for high power density and system efficiency becomes essential.

This thesis contributes to the initial stage of investigating and modelling auxiliary elements within a fuel cell power system (FCPS), which is intended to become an integral part of the powertrain of a regional hybrid more electric aircraft.

Starting from a previous thesis work conducted at the Polytechnic of Turin, where a model of air supply system for the aircraft was developed using a simple layout with the compressor powered by an electric motor, it emerged that the compressor system is the most significantly energy-impacting component among the auxiliary subsystems of the FCPS, powered directly by the fuel cell itself.

The air supply system is a crucial element in the fuel cell's interaction with its and has a significant impact on the performance, stability, and control of the fuel cell power system. Particularly in aviation, where high compression ratios are required, the design of this component is one of the main challenges in ensuring the overall effectiveness of the FCPS. Therefore, in some applications, harnessing the energy contained in the air exiting the fuel cell stack via an expander can become essential.

The primary aim of this thesis was to conduct a feasibility study, perform a preliminary design, and model an air supply system with a layout that provides for the recovery of the enthalpy energy of the gases leaving the stack.

After an accurate analysis of the state of the art regarding air supply system issues, energy recovery system integration and all the possible architectures used in the literature, two architectures widely adopted in the automotive sector were evaluated: the electric turbocharger type architecture and the serial booster type architecture.

Both architectures involve the use of a turbocharger with a radial turbine and compressor, similar to those used in internal combustion engines, making them robust choices suitable for aviation requirements.

Subsequently, a preliminary analysis of the system's performance was conducted in order to determine the optimal operating pressure for the fuel cell stack.

Next, the static sizing of the main components of the air supply system was performed, in particular the turbocharger, the process of which was described in detail. Through the dimensioning, it was possible to make a preliminary assessment of the masses, moments of inertia and power density of the architectures, as well as their impact on the overall efficiency of the system. Based on these results, the best architecture was selected for the case under consideration.

For the chosen architecture, a dynamic model was implemented using the Simulink platform. The turbomachines were modelled using the performance maps previously developed in static sizing. Using the dynamic model, it was possible to simulate the entire flight mission and evaluate the system's response to current disturbances at the fuel cell stacks.

A control system was devised to regulate the stack inlet air flow and operating pressure in order to optimise the overall system performance and ensure that the compressor operates safely with promising results.

Contents

1	Introduction	1
1.1	Background and motivation	1
1.2	Overview on Fuel cell	2
1.2.1	Architecture of fuel cell power system	8
1.2.2	Air supply system	11
1.3	Objectives	13
1.4	Methodology	13
1.5	Use case	14
2	State of the art: air supply system with turbocharger type layout	16
2.1	Overview	16
2.2	Main Architectures in Automotive Applications	16
2.3	Influence of operational parameters on Energy Recovery and alternative solutions	20
2.4	Theses research decisions and next steps	27
3	Performance Analysis	28
3.1	Performance analysis model	28
3.1.1	Efficiencies of the fuel cell power system	31
3.1.2	FC stacks performance model	32
3.1.3	Air supply system	34
3.1.4	intercooler model	36
3.2	Calculation of optimal FC operating pressure	37
3.2.1	<i>Performance Analysis Results</i>	45
4	Sizing	50
4.1	Scaling method	50
4.1.1	<i>Dimensional analysis</i>	50
4.1.2	Fluid Dynamics Similarity	51
4.1.3	Scaling laws	51
4.2	Turbocharger sizing procedure	55
4.2.1	Project requirements and plant configuration	56
4.2.2	Turbomatching procedure for electric turbocharger (e-turbo) architecture	58
4.2.3	Turbomatching procedure for serial booster architecture	60

4.2.4	Compressor sizing	64
4.2.5	Turbine sizing	66
4.2.6	Sizing output, masses, and moments of inertia	67
4.3	Off-design validation	68
4.3.1	Adjustment for off design	68
4.4	Fitting method	72
4.4.1	Curve fitting of turbine mass flow.	73
4.4.2	Curve fitting of turbine efficiency.	74
4.4.3	Fitting results	75
4.5	Sizing results.....	82
4.5.1	Sizing results for electric turbocharger architecture	83
4.5.2	Sizing results for serial booster architecture	90
4.5.3	Architecture comparison	97
5	Dynamic model	102
5.1	Cathode model	105
5.1.1	Back pressure valve.....	107
5.2	Air supply system	107
5.2.1	Turbine	108
5.2.2	Mechanical equilibrium at the shaft.....	113
5.2.3	Turbine inlet manifold	114
5.2.4	By-pass valve.....	115
6	Control and simulation.....	116
6.1	Control design	117
6.2	Simulation	120
6.2.1	Flight mission	120
6.2.2	Current disturbances	128
6.2.3	Comparison of results with and without the energy recovery system	150
6.2.4	comparison of the same system with and without turbine	155
6.2.5	comparison of the system with and without pressure control via the bypass valve 157	
7	Conclusions	163

List of figures

<i>Figure 1.1: Classification of fuel cell types</i> [4].....	3
<i>Figure 1.2: main advantages of various types of fuel cells in different applications</i> [6].	3
<i>Figure 1.3: Schematic representation of the reaction in a fuel cell</i> [3].....	5
<i>Figure 1.4: typical stack structure of a PEMFC with its main components: bipolar plates, gaskets, gas diffusion layers, and the MEA</i> [8].....	6
<i>Figure 1.5: Typical fuel cell polarization curve</i> [3].....	6
<i>Figure 1.6: polarization curves with varying stack operating pressure</i> [9].....	7
<i>Figure 1.7: Polarization curves as a function of the relative humidity of the membrane</i> [10].	8
<i>Figure 1.8: scheme of a fuel cell power system</i> [3]	9
<i>Figure 1.9: fuel cell powertrain configuration</i> [11]	10
<i>Figure 1.10: different types of air compressor</i> [12].....	12
<i>Figure 1.11: ATR72-600 in flight</i> [14].....	14
<i>Figure 1.12: streamlined flight mission profile</i> [11].	15
<i>Figure 2.1: Single level compressor (electric compressor)</i> [12]	16
<i>Figure 2.2: Electric turbocharger (volumetric/expander compressor or centrifugal turbine/compressor)</i> [12].....	17
<i>Figure 2.3: Serial booster (volumetric/centrifugal compressor and turbomachine)</i> [12]	17
<i>Figure 2.4: Different types of air supply system (a) single-level screw compressor, (b) serial booster and (c) expander.</i> [17]	19
<i>Figure 2.5: Overall efficiency for the three different configurations at varying net power output</i> [17]	19
<i>Figure 2.6: Different layout of air supply system (a) Schematic layout of the base case (b) Schematic layout of the case with turbocharger (c) Schematic layout of the case with combustor and turbocharger</i> [9].....	22
<i>Figure 2.7: Comparison of the energy balances obtained for cases b) and c) with those of a conventional APU</i> [9].....	24
<i>Figure 2.8: Efficiency of the recovery system at varying operating pressure and current density</i> [18]	25
<i>Figure 2.9: Efficiency of the recovery system at varying operating pressure and output power</i> [18]	26
<i>Figure 2.10: Power absorbed by compressor and power generated by the turbine</i> [18]	26
<i>Figure 2.11: Comparison of the overall efficiency of the PEMFC system in the presence or absence of the energy recovery turbine</i> [18]	27
<i>Figure 3.1: Schematic representation of the FCPS architecture.</i>	30
<i>Figure 3.2: Structure of the FCPS performance model.</i>	31
<i>Figure 3.3: Effect of stack pressure on the stacks electric efficiency and the plant efficiency for architecture without turbocharger system</i>	38
<i>Figure 3.4: Effect of stack pressure on polarization curve.</i>	39

Figure 3.5 : Effect of stack pressure on the overall efficiency for architecture without turbocharger system.	39
Figure 3.6: Effect of stack pressure on the stacks electric efficiency and the plant efficiency for architecture with turbocharger system.	40
Figure 3.7: Effect of stack pressure on the overall efficiency for architecture with turbocharger system.	41
Figure 3.8: Effect of stack pressure on the different power term for architecture without turbocharger system.	42
Figure 3.9: Effect of stack pressure on the different power term for architecture with turbocharger system.	42
Figure 3.10 : Effect of stack pressure on the reactants consumption for architecture without turbocharger system.	43
Figure 3.11: Effect of stack pressure on the reactants consumption for architecture with turbocharger system.	44
Figure 3.12: Trend of compressor inlet and outlet pressure and compressor inlet temperature during the mission.	46
Figure 3.13: Trend of compressor working line during the mission.	46
Figure 3.14: Trend of compressor outlet temperature during the mission for architecture with turbocharger system.	47
Figure 3.15: Trend of compressor outlet temperature during the mission for architecture without turbocharger system.	47
Figure 3.16: Trend of turbine inlet and outlet pressure and turbine inlet temperature during the mission.	48
Figure 3.17: FC stacks stable operating point.	48
Figure 3.18: Trend of the power terms along the mission.	49
Figure 3.19: Trend of the system efficiencies along the mission.	49
Figure 4.1: Parallel architecture for FCPS.	58
Figure 4.2: The matching procedure for the electric turbocharger architecture	60
Figure 4.3 design requirements for serial booster turbocharger.	62
Figure 4.4: The matching procedure for serial booster architecture	64
Figure 4.5 Representation of the compressor selection process[13], [38]	65
Figure 4.6: Different air supply system architectures with respective valve control modes [16]	69
Figure 4.7: Different valve control modes for electric turbocharger architecture [40]	70
Figure 4.8: Different adjustment modes on the turbine map [36].	71
Figure 4.9: Example of a BorgWarner turbine flow curve map [44], [45]	75
Figure 4.10: Sa-charging solution turbine flow curves map [46]	76
Figure 4.11: Sa-charging solution turbine efficiency map [46]	76
Figure 4.12: 3D fitting results against experimental data for BorgWarner turbine flow curves.	77
Figure 4.13: 3D fitting results against experimental data for Sa-charging solutions turbine flow curves.	77
Figure 4.14: 2D fitting results against experimental data for BorgWarner turbine flow curves.	78

Figure 4.15: 2D fitting results against experimental data for Sa-charging solutions turbine flow curves.....	78
Figure 4.16: Efficiency curves for BorgWarner turbine obtained using Andersson's formula.	79
Figure 4.17: Efficiency curves for Sa-charging solution turbine obtained using Andersson's formula.	79
Figure 4.18: 3D fitting results against experimental data for BorgWarner turbine efficiency curves using Jensen et al. method.....	80
Figure 4.19: 3D fitting results against experimental data for Sa-charging solutions turbine efficiency curves using Jensen et al. method.	80
Figure 4.20: 2D fitting results against experimental data for BorgWarner turbine efficiency curves using Jensen et al. method.....	81
Figure 4.21: 2D fitting results against experimental data for Sa-charging solutions turbine efficiency curves using Jensen et al. method.	81
Figure 4.22: Garrett G55-2100 compressor performance map [48]	84
Figure: 4.23 Fitted compressor map (Garrett G55-2100).	85
Figure 4.24: Trends in inlet and outlet pressure, inlet temperature and compressor rotation speed during the flight mission	86
Figure 4.25: Scaled compressor performance map	86
Figure 4.26: Performance map fitting of turbine efficiency curves.....	87
Figure 4.27: Performance map fitting of turbine flow curves.....	87
Figure 4.28: trends in inlet and outlet pressure, inlet temperature and turbine rotation speed during the flight mission	88
Figure 4.29: scaled turbine flow performance map.....	89
Figure 4.30: scaled turbine efficiency performance map	89
Figure 4.31: Garrett G25-550 performance map [38].....	91
Figure 4.32: Trends in inlet and outlet pressure, inlet temperature and compressor rotation speed during the flight mission	92
Figure 4.33: Fitted compressor performance map (Garrett G25-550)	93
Figure 4.34: Scaled compressor performance map	93
Figure 4.35: Trends in inlet and outlet pressure, inlet temperature and compressor rotation speed during the flight mission	94
Figure 4.36: Scaled turbine efficiency performance map	95
Figure 4.37: Scaled turbine flow performance map	95
Figure 4.38: Scaled compressor performance map	97
Figure 4.39: Comparison of stacks efficiency trends for the three architectures during the flight mission.....	98
Figure 4.40: Comparison of plant efficiency trends for the three architectures during the flight mission.....	99
Figure 4.41: Comparison of overall FCPS efficiency trends for the three architectures during the flight mission.....	99
Figure 4.42: comparison of the overall air supply system mass of the three architectures.....	101

Figure 4.43: comparison of the sum of the mass of the air supply system and the mass of the FC stacks of the three architectures	101
Figure 4.44: comparison of power density between the three architectures, calculated over the entire flight mission.....	102
Figure 5.1: Simulink FCPS model	104
Figure 5.2: Diagram of the FCPS structure.....	105
Figure 5.3: Simulink model of air supply system	108
Figure 5.4: Simulink model of turbine	112
Figure 5.5: Simulink model of turbine maps.....	113
Figure: 5.6: Free body diagram of electric turbocharger shaft	114
Figure 5.7: Simulink model of mechanical equilibrium at the shaft.....	114
Figure 5.8: Simulink model of turbine inlet manifold	115
Figure: 5.9: Simulink model of bypass valve	115
Figure 6.1: Closed loop flow control.....	118
Figure 6.2: Open loop pressure control	119
Figure 6.3: Closed loop pressure control	120
Figure 6.4: trend of controlled variables	122
Figure 6.5: Compressor performance map.....	123
Figure 6.6: Motor map	123
Figure 6.7: Performance map for turbine flow curves.....	124
Figure 6.8: Performance map for turbine efficiency	124
Figure 6.9: Reference voltage signals for the motor and the back pressure valve	125
Figure 6.10: Trend of the performance parameters	126
Figure 6.11: Control parameters for the bypass valve and turbine efficiency.....	127
Figure 6.12: Trend of motor, compressor and turbine torques.....	128
Figure 6.13: Effects of positive current step on pressure control	130
Figure 6.14: Effects of positive current step on mass flow control	131
Figure 6.15: Effects of positive current step on compressor performance map	132
Figure 6.16: Effects of positive current step on motor map	132
Figure 6.17: Effects of positive current step on turbine performance map (flow map)	133
Figure 6.18: Effects of positive current step on turbine performance map (efficiency map).....	133
Figure 6.19: Effects of positive current step on performance parameters of the system	134
Figure 6.20: Effects of positive current step on bypass pressure control and turbine efficiency ...	135
Figure 6.21: Effects of positive current step on motor, compressor and turbine torques.....	136
Figure 6.22: Effects of train of steps on pressure control	136
Figure 6.23: Effects of train of steps on mass flow control	137
Figure 6.24: Effects of train of steps on compressor performance map	138
Figure 6.25: Zoom on effects of train of steps on compressor performance map.....	138
Figure 6.26: Effects of train of steps on system performance parameters.....	139
Figure 6.27: Effects of train of steps on bypass pressure control and turbine efficiency	140
Figure 6.28: Effects of train of steps on motor map	141
Figure 6.29: Effects of train of steps on turbine map (flow map)	141

Figure 6.30: Effects of train of steps on turbine performance map (efficiency map).....	142
Figure 6.31: Effects of positive current step on motor, compressor and turbine torques.....	142
Figure 6.32: Effects of Gaussian noise current on pressure control.....	143
Figure 6.33: Effects of Gaussian noise on flow control	144
Figure 6.34: Effects of Gaussian noise on compressor performance map	145
Figure 6.35: Zoom on Effects of Gaussian noise on compressor performance map	145
Figure 6.36: Effects of Gaussian noise on motor map	146
Figure 6.37: Effects of Gaussian noise on turbine performance map (flow map)	146
Figure 6.38: Effects of Gaussian noise on turbine performance map (efficiency map).....	147
Figure 6.39: Effects of Gaussian noise on system performance parameters.....	148
Figure 6.40: Effects of Gaussian noise on bypass pressure control and turbine efficiency	149
Figure 6.41: Effects of Gaussian noise on motor, compressor and turbine torques.....	150
Figure 6.42: comparison of flight mission simulation results for the system with and without energy recovery	152
Figure 6.43: comparison of flight mission simulation results for the system with and without energy recovery	153
Figure 6.44: Comparison of simulation results of the application of a pulse train for the system with and without energy recovery	154
Figure 6.45: comparison of flight mission simulation results for the system with and without turbine	156
Figure 6.46: comparison of flight mission simulation results for the system with and without turbine	157
Figure 6.47: pressure trend during the flight mission for the system without bypass valve.....	158
Figure 6.48: compressor operating line during the flight mission for the system without bypass valve.....	159
Figure 6.49: efficiencies trend during the flight mission for the system without bypass valve.....	160
Figure 6.50: effect of a positive step disturbance on cathode pressure for the system without bypass valve	160
Figure 6.51: effect of a positive step disturbance on compressor operating line for the system without bypass valve.....	161
Figure 6.52: Effect of a positive step disturbance on efficiencies for the system without bypass valve.....	162
Figure 6.53: Effect of a Gaussian disturbance on cathode pressure for the system without bypass valve.....	162
Figure 6.54: effect of a Gaussian disturbance on cathode pressure for the system without bypass valve.....	163

List of tables

Table 1.1: main data of flight mission for the considered case study[13]	15
Table 3.1: parameters used in the performance analysis model in Federico Fasiello's thesis [13]..	37
Table 4.1: Compressor requirements	83
Table 4.2: turbine requirements.....	84
Table 4.3: Technical data of a turbocharger Garrett G55-2100 [48]	85
Table 4.4: Technical data of scaled compressor	86
Table 4.5 Technical data of turbine Garrett G25-550 [38]	88
Table 4.6: Technical data of scaled turbine.....	90
Table 4.7: Motor parameters.....	90
Table 4.8: First compressor requirements	90
Table 4.9: Turbine requirements	90
Table 4.10: Technical data of a compressor of turbocharger Garrett G25-550 [38].....	91
Table 4.11: Technical data of scaled compressor	94
Table 4.12: Technical data for turbine GBC14-200 [40]	94
Table 4.13: Technical data for scaled turbine	96
Table 4.14: Requirements for second compressor	96
Table 4.15: Technical data for scaled compressor	97
Table 4.16: Electric motor parameters	97
Table 5.1: Fitting parameters of flow curves performance maps.....	110
Table 5.2: Fitting parameters of efficiency performance maps.....	111
Table 6.1: Reference values for control	116

1 Introduction

1.1 Background and motivation

This thesis is placed within the context of research and development of advanced technologies for the production of clean and sustainable energy, at a time when sustainability and energy efficiency are issues of primary importance.

Today, more than 900 million tonnes of carbon dioxide CO_2 are emitted by the aviation sector every year and it is estimated that, considering the industry's continued growth, emissions could more than double by 2050.

With a view to this, the Air Transport Action Group (ATAG) has pledged to reduce carbon CO_2 emissions by 50 per cent compared to 2005, while the European Union (EU), through its Green Deal, has set the goal of achieving climate neutrality by 2050.

When assessing the impact of aviation on the environment, it must also be taken into account that in addition to CO_2 emissions, aircraft affect the climate system through the release of nitrogen oxides NO_x , particulate matter (soot) and water vapour [1]

To meet the decarbonisation challenge, the industry must adopt new low-carbon propulsion technologies and new fuels.

Among the most advanced alternatives for sustainable aviation fuels are biofuels such as HEFA derived from biomass or waste, followed by advanced biofuels made from solid materials. Another sustainable option is power-to-liquid fuels, also known as synthetic fuels (synfuels). These fuels are produced synthetically using hydrogen and carbon dioxide from industrial sources, biomass, or direct capture from the atmosphere.

While new propulsion technologies with low CO_2 emissions include battery-electric and turbo-electric technologies and the use of hydrogen as a fuel in turbines and fuel cells powering electric engines [1]

Between these technologies, hydrogen propulsion could play a crucial role in reducing carbon emissions in aviation. This system offers the opportunity for significant reductions in CO_2 emissions in flight and, more importantly, enables the production of hydrogen without any carbon emissions if it is produced through green hydrogen processes [1]

Green hydrogen production is a technology based on generating hydrogen through electrolysis, a chemical process that separates hydrogen from oxygen in water using electricity. When this electricity comes from renewable sources, green hydrogen becomes a carbon-free energy source. These processes require high costs but may be more sustainable in the future as the renewable energy economy grows [2].

It is estimated that the use of synthetic carbons could lead to a reduction in in-flight environmental impact of 30 to 60 %, hydrogen combustion propulsion would lead to a reduction of 50 to 70 %, and fuel cell propulsion 75 to 90 % [1].

These considerations make fuel cell technologies one of the most promising solutions in aeronautics for mitigating environmental impact. However, to make fuel cell-based propulsion systems

effectively usable in aviation, significant technological advances are required. These advances include increasing overall efficiency, making lighter tanks to store hydrogen, managing the distribution of liquid hydrogen (LH_2) within the aircraft, and enhancing the power density and specific power of fuel cell systems, with optimum values that could reach 2 kW/kg[1].

Considering these technological advances, the use of hydrogen as a means of propulsion is particularly suitable for aircraft intended for commuter, regional, short- and medium-haul flights. In these aircraft categories, fuel cell propulsion emerges as the most energy-efficient, environmentally friendly, and economical choice[1].

1.2 Overview on Fuel cell

A fuel cell (FC) is an electrochemical device that directly converts the chemical energy of a fuel into electrical energy through an oxidation-reduction reaction.

The core of a fuel cell consists of an electrolyte located between two electrodes, one anodic and one cathodic; the electrolyte is composed of a special material that allows positive hydrogen ions, known as protons, to pass through, while blocking electrons [3].

There are different types of fuel cells; they differ mainly based on the electrolyte used. This influences the type of catalysis required, the operating temperature and the cell's internal reactions. A second classification is made on the basis of the operating temperature of the stack, they can be high or low temperature[4]

Figures 1.1 and 1.2 show the various existing fuel cell types with their main advantages/disadvantages, operating conditions, and possible applications.

As shown in image 1.1, the various types of fuel cell use different types of fuel, in this work, fuel cells using hydrogen as fuel are considered.

High-temperature fuel cells do not require expensive catalysts such as platinum and allow steam reforming, i.e., the internal conversion of light fuels into hydrogen. However, these cells are not suitable for fast starts, which makes them impractical in the transport sector. On the other hand, low-temperature fuel cells allow rapid start-up but do not allow steam reforming, thus limiting the range of fuels that can be used.

Proton exchange membrane fuel cells (PEMFCs) are characterised by high power density at low temperatures, a lower environmental impact than PAFCs, and their insensitivity to carbon dioxide in the air [4]

This type of fuel cell operates in a temperature range of 50 to 100 °C, allowing reliable operation without requiring additional thermal insulation [3]

Therefore, PEMFCs are the optimal solution for use in the field of transport, including personal vehicles and public transport[4] and are an ideal choice for use in the automotive industry [3].

Both PEM-FC and SOFC have advantages for use in aviation. PEM-FC is a more established technology that has been in use for longer; in addition, it is more resistant to shocks and temperature fluctuations, which are important factors for in-flight application [5]

PEMFCs with hydrogen fuel are the ones considered in this thesis work.

High operating temperature fuel cell	Name of fuel cell	Solid oxide fuel cell (SOFC)		Molten carbonate fuel cell (MCFC)	
	Electrolyte	Hard, non-porous ceramic		Molten carbonate salt mixture	
	Operating Temperature	600 – 1100 °C		650°C	
	Fuel	Pure hydrogen, biogas or light fossil fuel		Hydrocarbon fuels	
	Benefits	<ul style="list-style-type: none"> Non-precious metal for catalysis Able to reform methanol and ethanol 		<ul style="list-style-type: none"> Non-precious metal for catalysis Efficiency : from 50% to 85% with cogeneration No carbon monoxide or dioxide poisoning 	
	Drawbacks	<ul style="list-style-type: none"> High operating temperature Complexity of heat management 		<ul style="list-style-type: none"> High operating temperature Poisoning by sulphur Use hydrocarbon fuel = greenhouse gas emissions 	
Low operating temperature fuel cell	Name of fuel cell	Proton exchange membrane fuel cell (PEMFC)	Alkaline fuel cells (AFCs)	Phosphoric acid fuel cell (PAFCs)	
	Electrolyte	Solid polymer (acid membrane)	Polymer (alkaline membrane)	Liquid phosphoric acid	
	Operating Temperature	80 – 100 °C	100 – 250°C	250 – 300 °C	
	Fuel	Pure hydrogen or methanol/ethanol (direct or indirect)	Pure hydrogen, borohydride or zinc	Hydrocarbon fuel	
	Benefits	<ul style="list-style-type: none"> Low operating temperature Quick start Environmentally friendly High power density 	<ul style="list-style-type: none"> High efficiency (60%) Non precious metal for catalysis 	<ul style="list-style-type: none"> High power (over 75 MW) High overall efficiency (80%) when combined with cogeneration 	
	Drawbacks	<ul style="list-style-type: none"> Use platinum for the catalysis Sensitive to carbon monoxide Water management 	<ul style="list-style-type: none"> Sensitive to carbon dioxide (the percentage in the air is enough to destroy the cell) 	<ul style="list-style-type: none"> Greenhouse gas emissions Low efficiency without cogeneration (less than 40%) 	

Figure 1.1: Classification of fuel cell types [4]

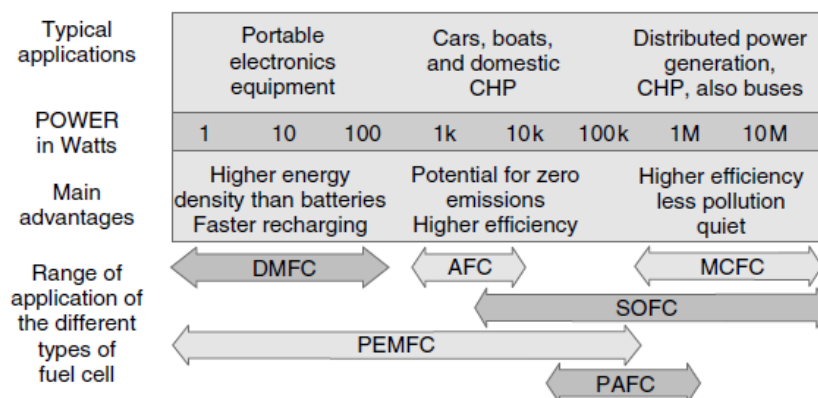


Figure 1.2: main advantages of various types of fuel cells in different applications [6].

To understand how the reaction between hydrogen and oxygen generates an electric current, it is possible to divide the reactions occurring at each electrode into two distinct reactions.

For a cell based on an acid electrolyte, such as the PEMFC, the following considerations apply.

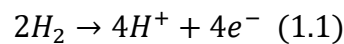
The electrode structure is designed to be porous to allow penetration of both the electrolyte on one side and the gas on the other, to maximise contact between the electrode, electrolyte, and gas[6]

The polymer electrolyte membrane acts as an insulator for electrons but is characterised by its high conductivity to hydrogen ions. Typically, this membrane consists of a fluorocarbon core to which sulphonic acid groups ($SO_3^-H^+$) are bonded.

When the membrane comes into contact with moisture, the hydrogen ions (H^+) present in the sulphonic groups become mobile, facilitating the ionic conduction process [3]

Hydrogen in its gaseous state passes through the anode and, with the assistance of a catalyst, its molecules separate into electrons and protons.

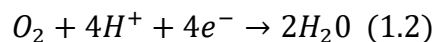
This is the hydrogen oxidation reaction shown in the following equation:



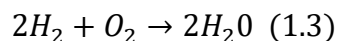
The protons flow towards the cathode, through the electrolyte, whereas the electrons traverse an external circuit, generating electric current.

Hydrogen protons and electrons unite in the presence of oxygen passing through the cathode, resulting in water formation [3].

This process involves the reduction of oxygen and is illustrated by the following equation:



The global reaction that occurs within the fuel cell is shown in the following reaction:



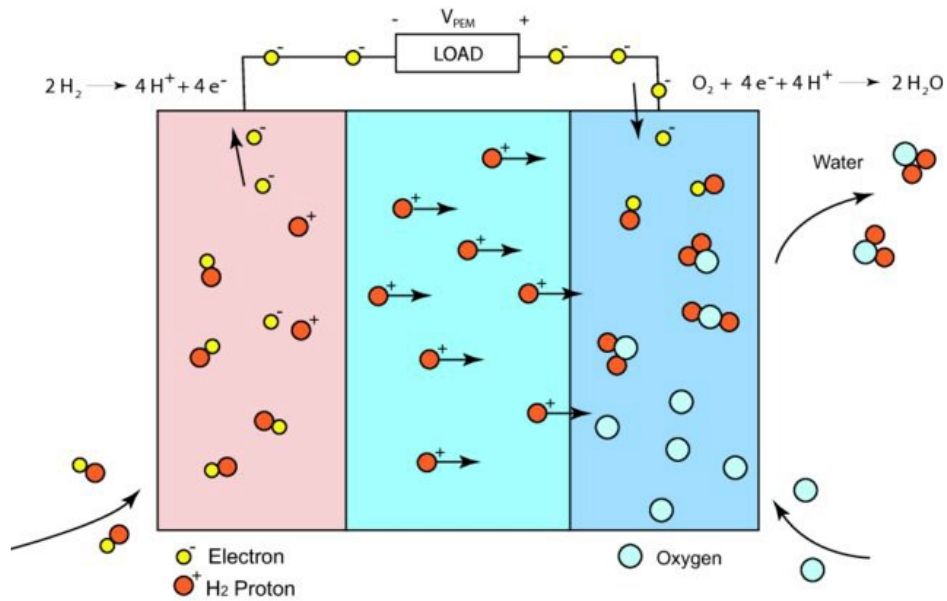


Figure 1.3: Schematic representation of the reaction in a fuel cell [3]

The potential difference produced by a single cell can vary between 0 and 1 volt depending on the operating conditions and the applied load. Typically, the average voltage of a fuel cell is around 0.7 volt[6]. To obtain higher voltages, several cells can be connected in series. The overall stack voltage is obtained by multiplying the number of cells by the average voltage of each cell [3]

Within fuel cells, there are electrical resistances that cause energy losses in the form of heat. In other words, part of the energy is dissipated as heat during fuel cell operation [3]

Unlike internal combustion engines, which convert the chemical energy of the fuel first into thermal energy and then into mechanical energy, fuel cells directly convert the chemical energy of the fuel into electrical energy. This means that they are not limited by the restrictions of the Carnot cycle (about 52% for a steam turbine [6]), which potentially allows for higher energy conversion efficiency. Fuel cells also offer advantages over batteries in that their reactants are stored externally. For example, oxygen is usually taken from the atmospheric air while hydrogen is stored in external tanks. This makes filling the fuel tanks much faster than recharging the batteries when the reactants are depleted [3]

In a PEMFC, the three essential components, namely the anode, electrolyte, and cathode, are assembled to form a single unit known as the membrane electrolyte assembly (MEA).

MEA is inserted between two support layers known as gas diffusion layers (GDL), whose task is to facilitate the diffusion of reactant gases to the catalyst site within the MEA.

The GDLs are in contact with two bipolar plates (BPs) that are responsible for distributing the reactants to the GDLs through a network of flow channels. These BPs are usually made of a lightweight, durable, gas-tight, and electrically conductive material, typically graphite. To prevent any leakage, gaskets are also present.

GDLs, MEA, BPs and gaskets constitute the repetitive hardware of the fuel cell, while non-repetitive hardware, such as end plates and bolts, is located at the end of the stack and has the main function of applying adequate mechanical pressure on the units [7]

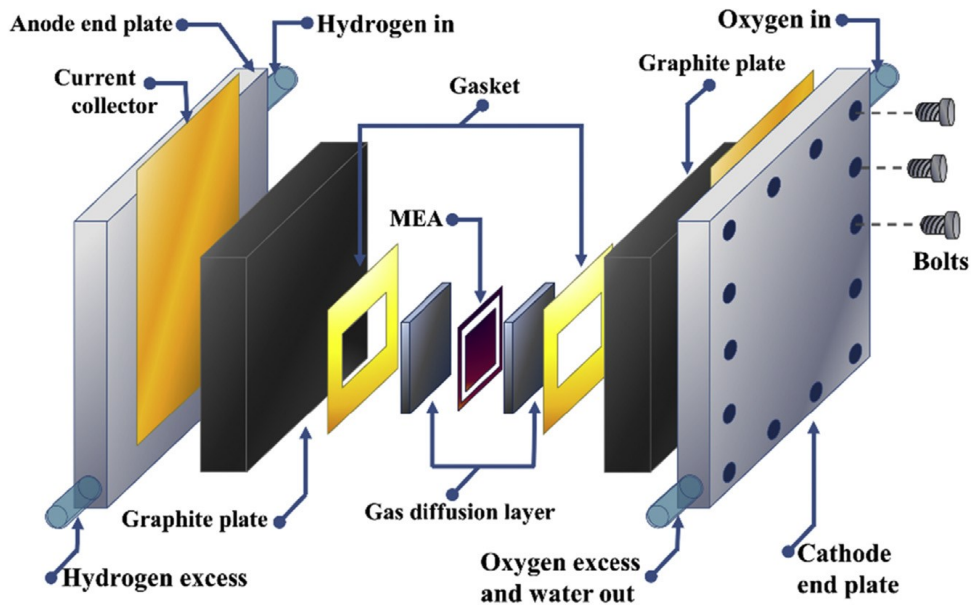


Figure 1.4: typical stack structure of a PEMFC with its main components: bipolar plates, gaskets, gas diffusion layers, and the MEA [8]

The common characteristics of fuel cells are often illustrated by a performance graph, which describes the relationship between the voltage generated by the cell and its current density (current for unit active area of the cell), this is called the polarisation curve, and an example is shown in figure 1.5.

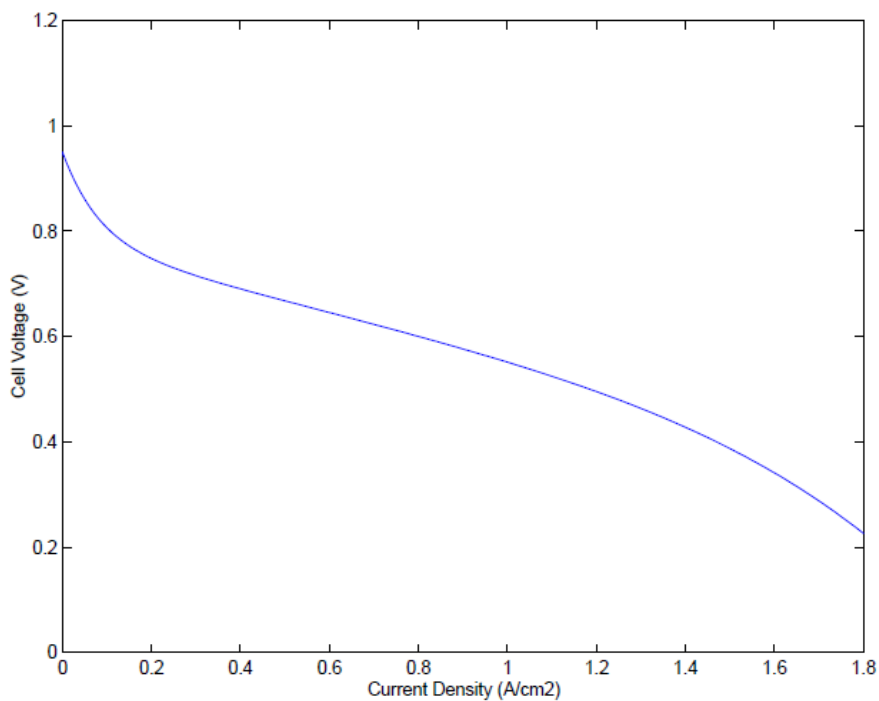


Figure 1.5: Typical fuel cell polarization curve[3]

From the trend of the polarisation curve, we can see that as the current drawn by the fuel cell increases, the voltage decreases due to various factors, including the cell's internal electrical resistance, inefficient transport of reactant gases, and limited reaction speed. Since a lower voltage indicates a lower efficiency of the fuel cell, it is generally desirable to operate the fuel cell with a reduced load that is with lower current levels. However, this choice leads to an increase in the size and overall weight of the fuel cell [3]; it is therefore essential to balance these two effects.

Furthermore, it should be considered that the polarization curve is specific to certain operating conditions and will vary depending on variables such as pressure, temperature, reagent partial pressure and membrane moisture level.

In particular, there is an increase in performance as the operating pressure of the stack and the relative humidity of the membrane increase; while for the operating pressure it is necessary to make a careful choice since an excessive increase in pressure has negative effects that will be discussed later, it is important that the membrane is always well hydrated while maintaining a relative humidity of 1.

Figures 1.6 and 1.7 show the effects of the polarisation curves as the operating pressure of the stack and the relative humidity of the membrane change.

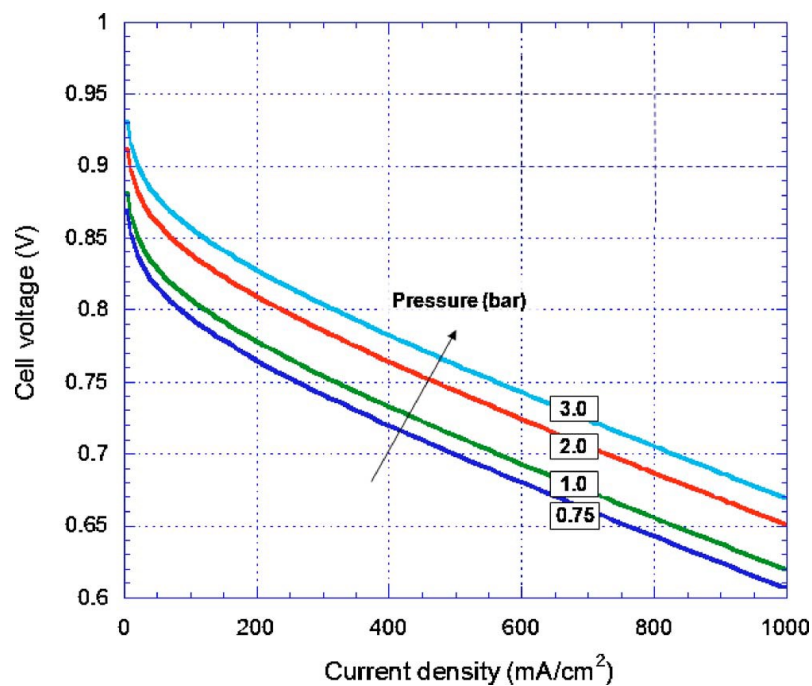


Figure 1.6: polarization curves with varying stack operating pressure [9]

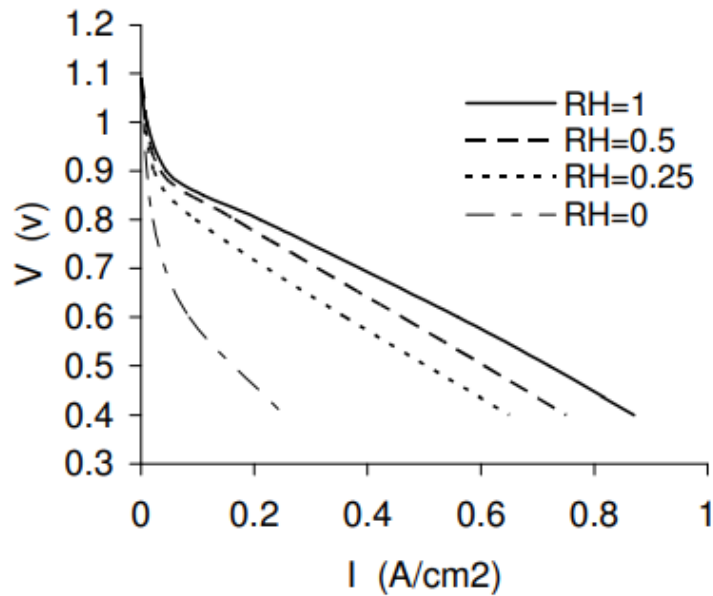


Figure 1.7: Polarization curves as a function of the relative humidity of the membrane [10].

1.2.1 Architecture of fuel cell power system

A fuel cell stack requires the integration of various auxiliary elements to constitute a complete fuel cell power system, these subsystems represent the balance of plant (BOP) [7] of the FCPS and include:

- air supply system.
- hydrogen supply system.
- thermal management system.
- water management system.
- power conditioning system [3]

A typical architecture of an FCPS in the automotive sector is presented in figure 1.8.

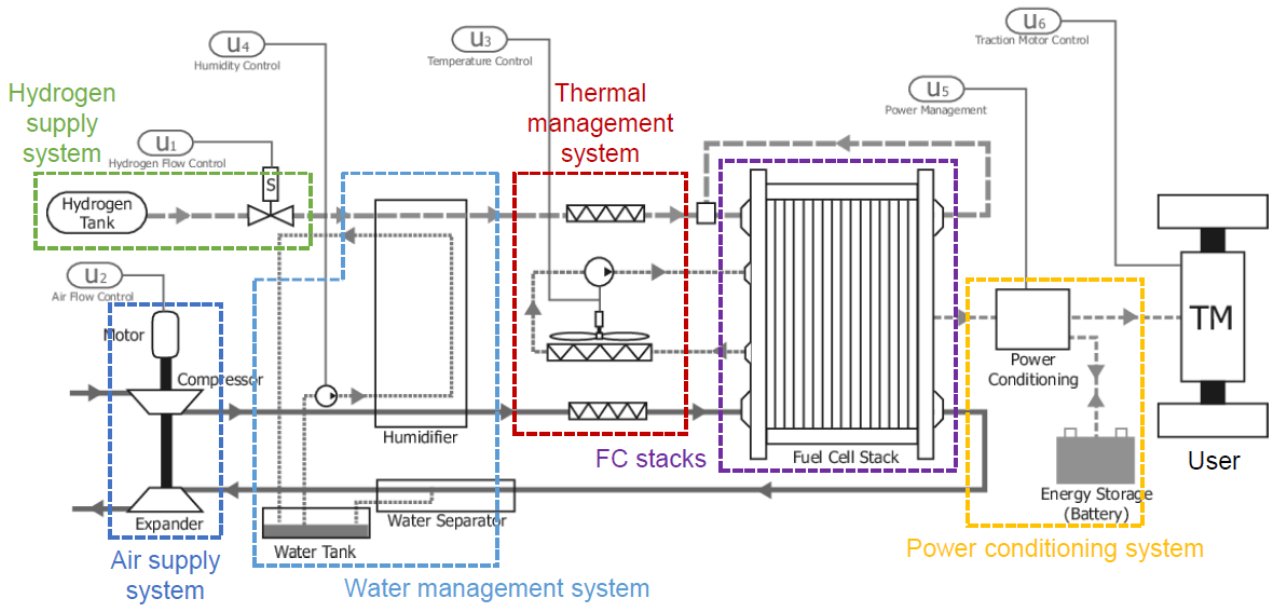


Figure 1.8: scheme of a fuel cell power system[3]

A proton exchange membrane fuel cell (PEMFC), as mentioned above, uses oxygen and hydrogen as reactants, which are consumed during the reaction, generating electricity, water, and heat.

Oxygen is taken directly from the external environment during the entire flight mission, the air supply system subsystem then deals with the aspiration of air and bringing it to the optimal pressure required by the fuel cell stack, this is done through a compressor that is commonly powered by an electric motor; it is also possible to insert a turbine or expander in the system that allows the recovery of the enthalpic energy of the gases coming out of the fuel cell.

Since the objective of this thesis is a preliminary design and modelling of all the components that form part of this subsystem, and in particular the use of a layout that includes a system for recovering the energy of the gases exiting the fuel cell stack through a turbine, all the aspects to be taken into account in the design of an air supply system are described in detail in the following section.

The hydrogen is stored inside a pressurised tank and is delivered to the anode of the stack through a valve to regulate the desired flow.

The flow of compressed air from the compressor is at a higher temperature than that required by the stack, i.e. 80 °C, so a heat exchanger is required to cool the air by reducing its temperature before it enters the stack; on the other hand, the flow of hydrogen is at a very low temperature and requires a heat exchanger to reach the stack's reaction temperature; these slides are part of the thermal management system.

The water management system takes care of maintaining the right degree of humidification of the polymer membranes, as mentioned it is important that the membrane is well hydrated while maintaining a relative humidity of 1 to avoid voltage losses and increase the efficiency of the stack. There is a humidifier in the system that is essential for humidifying both the hydrogen and the air coming from the compressor. The air leaving the fuel cell stack contains the steam generated by the reaction, which is why a water separator is used, through which the water produced can be recovered and used directly for humidifying the reactants.

In order to distribute the energy produced by the FCPS between the different equipment connected to the system, a power conditioning system incorporating a wide range of electronic devices such as inverters, DC/DC converters, voltage regulators, etc., is essential. The use of a storage battery is often necessary to manage the start-up phases and fluctuations in power demand.

An example of a fuel cell powertrain configuration for a hybrid-electric aircraft is shown in figure 1.9.

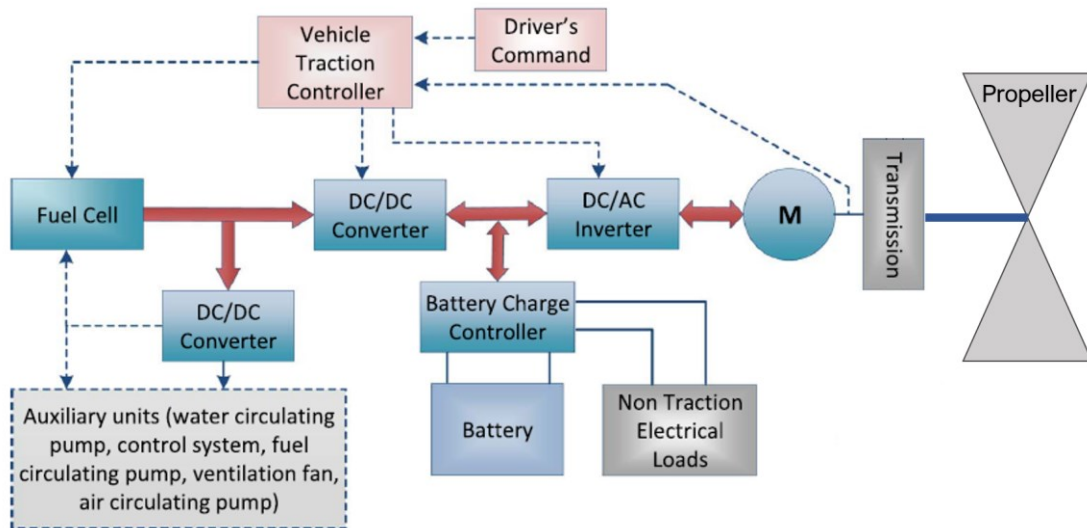


Figure 1.9: fuel cell powertrain configuration[11]

To ensure system stability, rapid response to transient variations in power demand, as well as reliable operation and maintenance of high overall efficiency, it is essential to carefully adjust a number of key parameters. These include managing reagent flows, controlling total and partial reagent pressures, and monitoring temperatures and moisture levels in the membranes. To this end, the FCPS is equipped with a system of piping and manifolds connecting the different components, as well as a series of valves, sensors, and transmitters, all aimed at optimal control and regulation of the system.

Among the options for placing fuel cell system components on an aircraft, there are several alternatives. These include placement on the fuselage, along the wings or outside the fuselage. One configuration of particular interest may be to integrate all the components of the fuel cell system together with the electric motor and propeller.

This arrangement can be realised on the wing of the aircraft, either above or below it, or potentially on the fuselage. This choice has several advantages, such as increased duplication of resources and simplified maintenance operations but could affect the aerodynamics of the wing and the overall structural design[7].

1.2.2 Air supply system

The air supply system for a Fuel Cell Power System (FCPS) plays two main roles:

- It supplies the necessary amount of oxygen to the cathode of the fuel cell stack needed to make the redox reaction take place and prevent reagent deficiency [3]; this oxygen is taken directly from the ambient air.
- It compresses the air from the external environment to the pressure required by the fuel cell stack.

Regarding the second aspect, the air supply system is of great importance in defining the optimum system pressure. As shown in the figure 1.6 above, which shows the different polarisation curves as the operating pressure changes, promoting the redox reaction in the fuel cell stack at a higher pressure improves the performance of the fuel cell stack by allowing a greater potential difference at the same current density, resulting in an improvement of the overall efficiency of the stack.

However, the increase in operating pressure also requires a higher compression ratio to be provided by the compressor, leading to an increase in the power absorbed by the latter. This in turn can negatively affect the overall performance of the entire fuel cell power system and is particularly critical in aeronautical applications where it is necessary to operate at high altitudes where atmospheric pressure is low.

It is therefore of paramount importance to find an optimum pressure point that balances these two effects in order to maximise overall system efficiency and reduce overall power density.

Other important factors to consider when designing an air supply system include:

- Maximising the efficiency of the compressor system to minimise the energy absorbed by this component in order to improve overall system efficiency and increase system power density.
- Implement an efficient control system capable of responding quickly to changes in current load in the CF stack, maintaining pressure fluctuations within a range of 200 mbar to avoid damage to the diaphragm and generate voltage pulsations.
- Use an oil-free compressor, as the presence of lubricant in the airflow to the stack can cause severe damage to the MEA.
- Minimise the noise level generated by the system.
- Reduce the size of the system, both in terms of weight and volume, in order to decrease power density.
- Exploring cost-effective solutions without compromising reliability[12].

The basic layout of an air supply system comprises a compressor driven by an electric motor. When choosing the compressor to be used in an air supply system with this basic layout, several options present themselves, each with their own advantages and disadvantages. The objective is to select the most suitable solution for the case study considering the requirements discussed above.

The main compressors to consider include:

- Centrifugal compressors: they offer several advantages, mainly their compactness and light weight. They are known for their high energy efficiency, although in a limited mass flow range, they are also less noisy than other applications and usually have lower costs than positive displacement compressors with internal compression. They do, however, have some disadvantages, such as the need to reach high rotational speeds, even higher than 100,000

rpm, in order to promote power density and to be able to reduce their size, which requires the use of magnetic or oil-free gas bearings.

Furthermore, their ability to work at a given mass flow rate is linked to the chosen compression ratio, making control more complex than in other applications.

- Positive displacement compressors without internal compression, known as blowers, can be of several types, including lobe, known as roots compressors, claw, radial and side channels, where compression is isochoric. These compressors are more efficient at lower pressures and are suitable for fuel cell applications operating at low operating pressures, generally below 1.5 bar. Although they are compact and lightweight, they are less so than centrifugal compressors. However, they offer a significant cost advantage, being cheaper, but tend to be noisier than other applications.
- Positive displacement compressors with internal compression, such as screw, rotary vane or scroll compressors, are known for their superior efficiency compared to blowers. They usually have a slightly lower internal compression ratio than external compression and require careful design to ensure that the output pressure approaches the optimal working pressure of the fuel cell. A key aspect of these compressors is their ability to integrate the humidification process directly into the compression system, eliminating the need for a separate humidification device and improving overall system efficiency due to the compression tending to be isothermal. Unlike centrifugal compressors, they allow the system to operate stably at constant pressure and with high efficiency over a wide range of mass flows. However, they are usually heavier and less compact, resulting in higher costs than other applications [4], [12].

In figure 1.10 there is a diagram of the various compressors described.

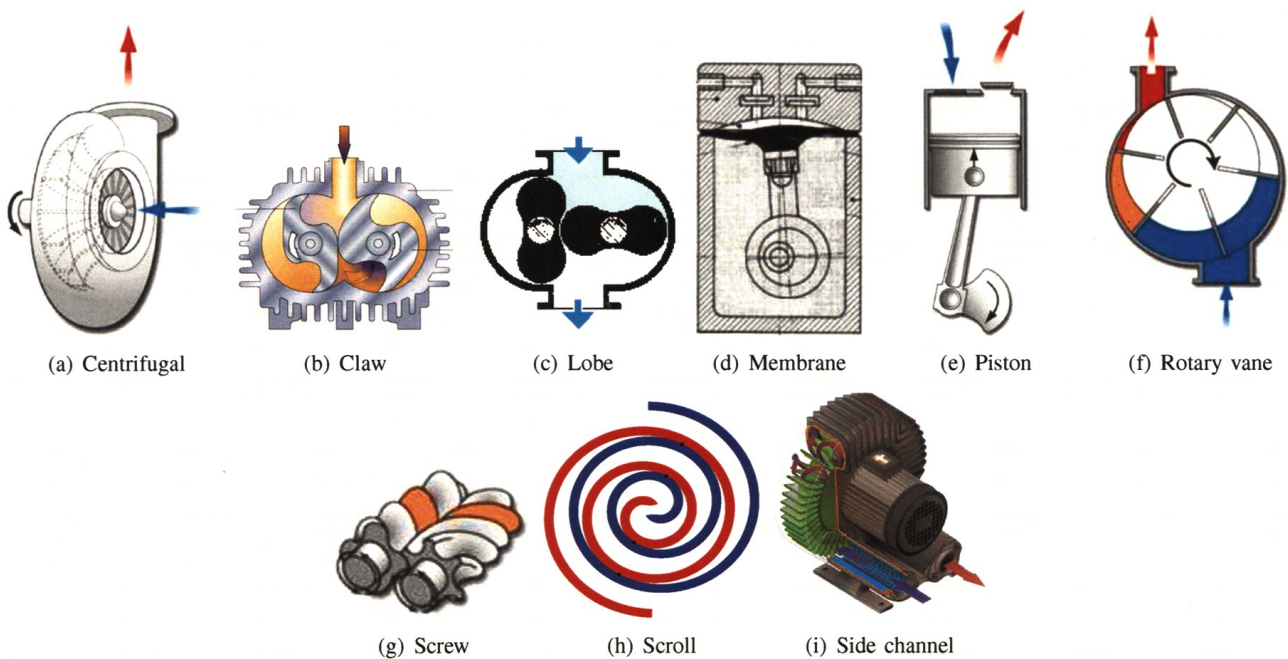


Figure 1.10: different types of air compressor[12]

1.3 Objectives

The layout with a compressor powered by an electric motor was implemented in Federico Fasiello's thesis [13], which is the starting point for this research. During this study, the use of a centrifugal compressor was identified as the optimal option.

In this thesis, a preliminary design and modelling of an air supply system layout including an energy recovery system that utilises the enthalpic energy of the gases exiting the fuel cell through a turbine system or an expander partially powering the compressor will be addressed.

By adding an energy recovery turbine, it is possible to decrease the power required from the electric motor, which is directly fed by the fuel cell, thus increasing the efficiency of the system while decreasing the size of the stack, since the latter is expected to produce less gross power; in this way, it should also be possible to improve the power density of the system.

The advantages of including the turbine are at the expense of greater system complexity and thus lower reliability and more complex control [12]

The results of the sizing and simulations will be compared with those resulting from the electric compressor case, and a feasibility study of the layout with the inclusion of the turbine will be carried out for this case.

1.4 Methodology

In the conducted thesis work, various solutions, and architectures in the state of the art for the integration of a turbine or expander for energy recovery from exhaust gases were first analysed, and optimal solutions suitable for the case study were identified.

Subsequently, the optimal operating pressure of the fuel cell stack was evaluated in order to optimize the performance of the FCPS. This assessment was carried out through the performance analysis model implemented in Federico Fasiello's Thesis[13], which was appropriately modified to include the modelling of the turbine system and all related flows.

Following this, a static sizing of the components of the air supply system was performed, particularly for the turbocharger. To achieve this, an automated and parametric model was implemented, allowing for matching and sizing of the turbine and compressor components of the turbocharger.

Based on previous thesis work and numerous preliminary turbomachinery design studies, it was decided to perform a sizing based on the scaling of existing turbomachinery, utilizing scaling laws derived from fluid dynamic similarity principles. All technical data of the basic turbomachinery used were compiled into a dedicated database.

This sizing methodology does not replace the ground-up design of turbomachinery but serves as an excellent tool for the purpose of preliminary design and modelling.

Subsequently, it became possible to implement the dynamic model of the turbocharger using the dimensioned performance maps and all components related to the air supply system with the energy recovery system. These were integrated into the dynamic model of the entire FCPS used in Federico Fasiello's thesis.

Furthermore, a control system for the air supply system was developed to regulate the airflow into the stack and the operating pressure to optimize the overall system performance and ensure safe compressor operation.

1.5 Use case

The described design is applied to the case study considered in Federico Fasiello's thesis [13], which is an ATR 72-600 aircraft [14].

This is a regional aircraft with twin-engine turboprop propulsion designed for short-haul flights, developed by ATR[15].



Figure 1.11: ATR72-600 in flight[14]

In the context of this project, the option of retrofitting the aircraft with a fuel cell-based propulsion system is considered, within a hybrid configuration oriented towards electrification.

The fuel cell propulsion system (FCPS) must ensure a certain net power, denoted as $P_{net,cruise}$, during the cruise phase. In a first approximation, the value of the gross power, denoted as P_{gross} , generated by the stack required to achieve the indicated net power is calculated and held constant throughout the entire flight mission to enable the compressor to operate with a constant mass flow rate [13].

As indicated in Federico Fasiello's thesis[13], the flight mission has been taken from Comincini's thesis [11] and consists of three phases: the climb phase, cruise phase, and descent phase, all at corresponding constant True Air Speed (TAS), where TAS represents the aircraft's speed relative to air mass flow.

The key data for the flight mission are provided in Table 1.1; the mission has a duration of one and a half hours.

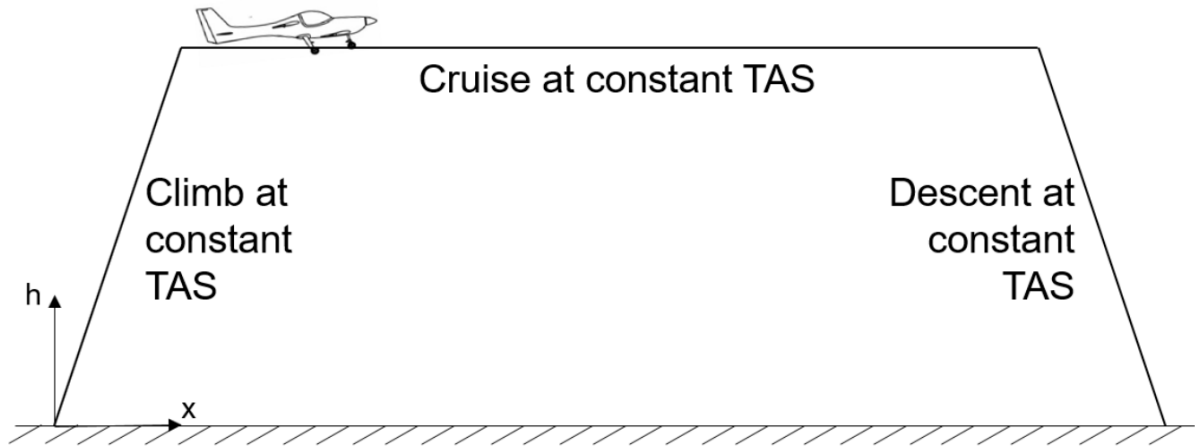


Figure 1.12: streamlined flight mission profile [11].

Mission profile	
Origin altitude	0 m
Cruise altitude	7000 m
Destination altitude	0 m
Total ground distance	700 km
Climb TAS	82.3 m/s
Rate of climb	4.9 m/s
Cruise TAS	137 m/s
Descent TAS	82.3 m/s
<i>Rate of descent</i>	<i>4.3 m/s</i>

Table 1.1: main data of flight mission for the considered case study[13]

2 State of the art: air supply system with turbocharger type layout

2.1 Overview

In this chapter, an overview is given of the issues and aspects to be considered when designing an air supply system with a turbocharger-type architecture, and the main solutions are illustrated.

Various solutions and architectures exist in the literature for incorporating a turbine in order to make the most of the energy from the gases leaving the fuel cell.

In this part of the analysis, solutions used in the automotive sector, where research is more advanced and has more practical applications, will be examined.

These solutions can be adapted for use in aircraft, but it is essential to take into account the different operating conditions of aircraft. For example, at higher altitudes, aircraft require a higher compression ratio because the external atmospheric pressure is lower as altitude increases. In addition, aircraft have significantly higher power requirements than automobiles, which results in a significantly higher air flow to be supplied by the compressor.

Therefore, in the process of designing an air supply system for an aircraft, it is of paramount importance to optimise the parameters of the system to suit the specific operating conditions of the aircraft. Furthermore, it is essential to explore innovative methods to maximise the energy derived from the gases from the fuel cell, which will be used in a turbine.

2.2 Main Architectures in Automotive Applications

In the article by Blunier et al. [12], three basic architectures for air supply systems employed in the automotive sector are presented, the diagrams of which are shown in figures (2.1), (2.2) and (2.3).

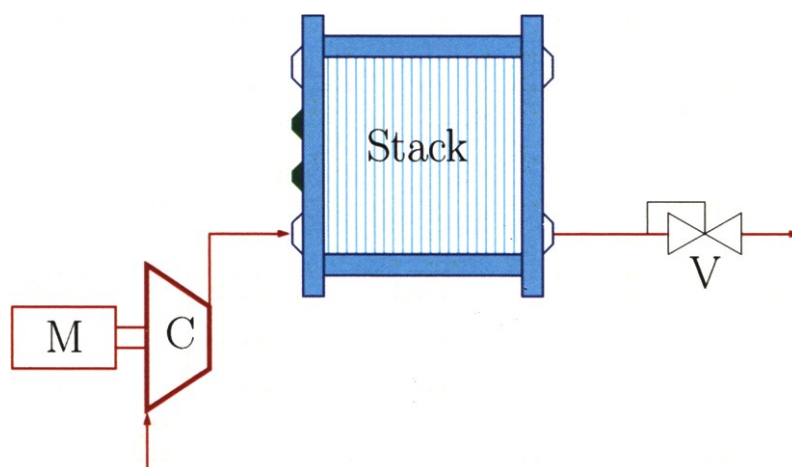


Figure 2.1: Single level compressor (electric compressor) [12]

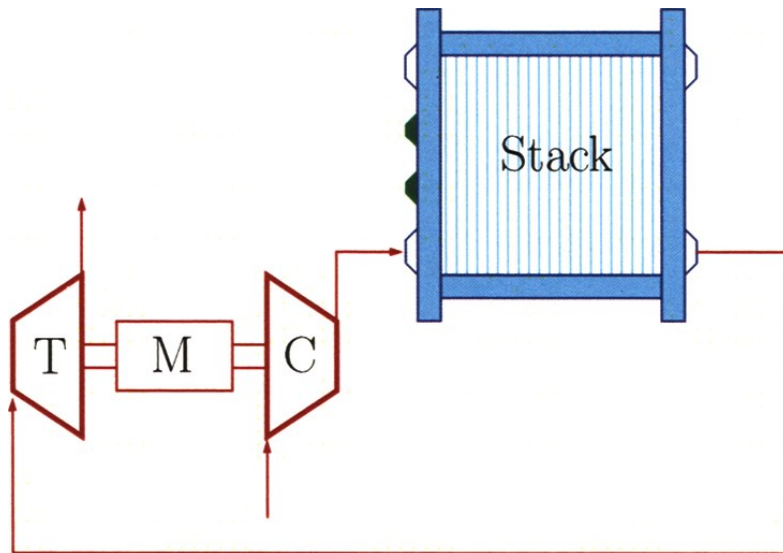


Figure 2.2: Electric turbocharger (volumetric/expander compressor or centrifugal turbine/compressor) [12]

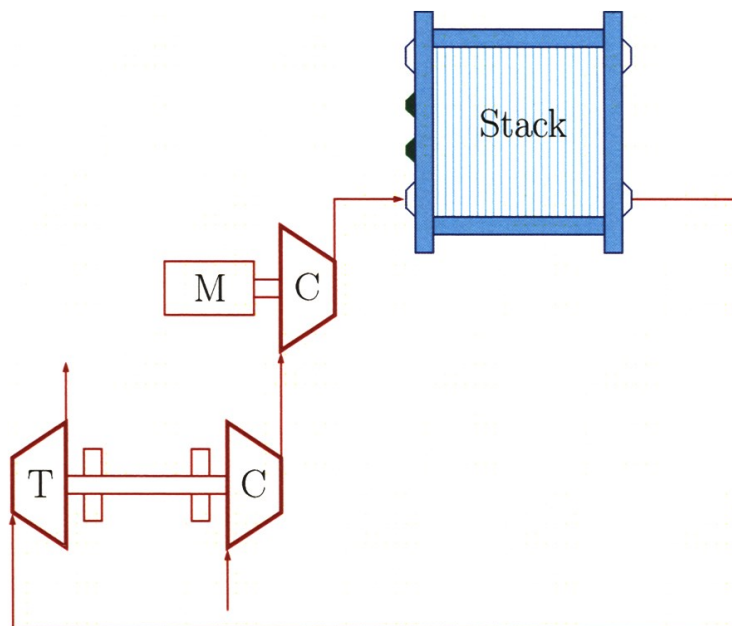


Figure 2.3: Serial booster (volumetric/centrifugal compressor and turbomachine) [12]

The architecture in figure (2.1) is of the electric compressor type, consisting of a compressor that draws air from the outside and is powered by an electric motor; it is the configuration with the simplest layout, but it is also the solution with the lowest efficiency as it does not include an energy recovery system for the combustion gases.

For this application, a control valve can be inserted at the cathode outlet coupled to the compressor to guarantee the pressure level at the stack and thus obtain the best system efficiency.

The second configuration, shown in figure (2.2) is an electric turbocharger (e-turbo).

It can be realised either with a volumetric expander and compressor or with a centrifugal turbine and compressor.

In this case, the compressor is coupled with a turbine, which allows energy to be recovered from the exhaust gases exiting the FC stack's cathode.

The article tells us that this architecture is certainly more complex and therefore implies lower system reliability and higher costs, but it can increase efficiency by 4-5% and net power capacity by 14% for the same stack size.

This solution also presents a complicated control by having both the turbine and the motor, which both feed the compressor, on the same shaft.

The third configuration, shown in figure (2.3), is a serial booster, in this solution there is a high-speed turbomachine that harnesses the energy of combustion gases, connected in series to an electric compressor, the total compression ratio is then divided into two compression lines.

Through this configuration, it is possible to increase the air pressure at the stack inlet and thus achieve higher pressures at the outlet of the latter.

This architecture can increase the efficiency of the system by 3%, however, it makes the system even more complex than the previous solution.

In the work Uhring et al.[16], it is stated that electric compressor, electric turbocharger, and serial booster architectures are the typical configurations used in the automotive industry for supplying air to a FCPS (Fuel Cell Power System). In the case of the electric compressor, a throttle valve can be employed to manage the incoming airflow to the fuel cell, thereby controlling both pressure and efficiency.

In the architecture of the electric turbocharger and serial booster, the pressure in the stack is regulated by balancing the turbine and compressor maps at a specific speed. To control the pressure in the fuel cell (FC), two valves are used: a backpressure control valve at the outlet of the FC and a bypass valve located before the turbine.

In the article it is mentioned how through the serial booster system it is possible to reduce the inertia of the turbocharger shaft through the compression stage performed by the electric compressor in series with the turbocharger, it is also possible to boost the system pressure through the compression ratio of both stages.

These three architectures are dimensioned, using a parameter optimisation method, and compared with each other. The study shows that for high operating conditions, i.e., for a high compression ratio, it is more convenient to use a serial booster system, since through the high speed of the turbocharger, which is not limited by the speed limits of the electric motor, it is possible to generate more mechanical power, which is used to increase the inlet pressure to the electric compressor.

In addition, with the serial booster-type architecture, it is possible to use a more efficient compressor. However, the system exhibits larger dimensions and greater inertia.

In the article of Bao et al.[17] are examined three different architectures for high-pressure air supply systems in fuel cell applications. Using a real-code genetic algorithm, it optimizes the air stoichiometric ratio and cathode outlet pressure. The three architectures include:

- Single-Stage Scheme, shown in figure 2.4 a): Utilizes a screw compressor.
- Serial booster Configuration, shown in figure 2.4 b): Involves a centrifugal turbocharger driven by exhaust gases and a screw compressor for the second-stage pressure ratio.
- Expander shown in figure 2.4 c): Employs an auxiliary motor to power a centrifugal compressor with partial exhaust energy recovery.

Utilizing exhaust recycling can enhance system efficiency by over 3% compared to using only a screw-based system. If we consider the adjustable nature of the centrifugal compressor, the serial booster configuration may achieve a higher system efficiency than the expander configuration. This advantage arises because compressor efficiency exhibits an exponential relationship with the pressure ratio and a linear relationship with the flow rate.

The system efficiency results obtained during the sizing, as a function of the net power generated, are shown in the figure 2.5.

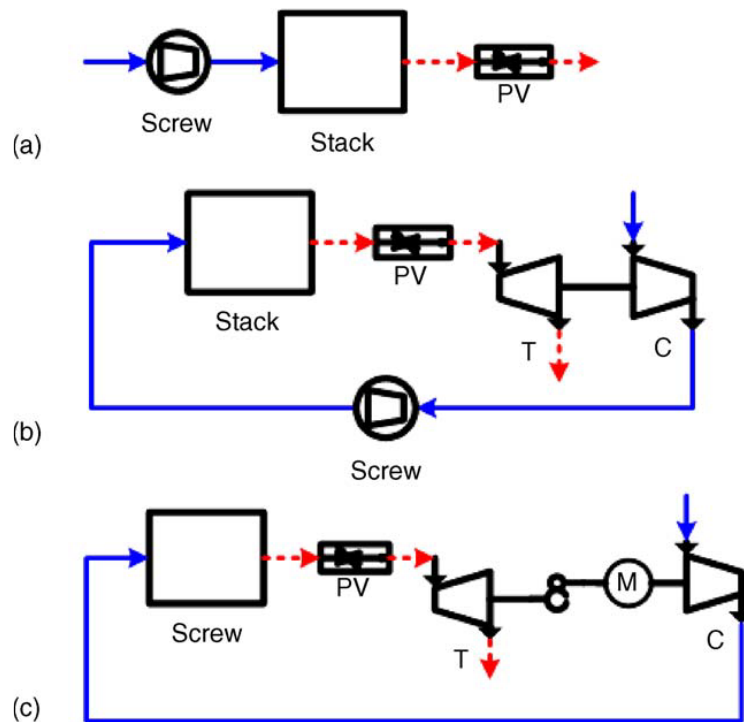


Figure 2.4: Different types of air supply system (a) single-level screw compressor, (b) serial booster and (c) expander. [17]

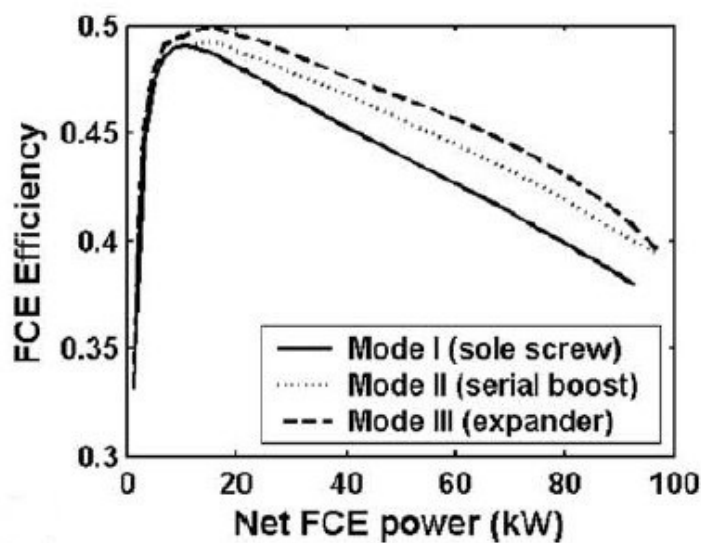


Figure 2.5: Overall efficiency for the three different configurations at varying net power output [17]

In the thesis work of Lukas Barchewitz [5], some preliminary calculations were carried out on a model PEMFC system, which feeds an aircraft, operating at a cathode pressure of 1.33 bar and an altitude of 12500 m, in which air has to be compressed from 0.179 bar to 1.33 bar, requiring a pressure ratio of approximately 7.5 for the compressor.

The cathode gas outlet temperature is 80°C and the relative humidity of the flow is 100%, which is typical for modern PEM-FCs.

Under these conditions, the use of a radial compressor with an efficiency of 75% would require a power input of about 40 kW, with the air supply system consuming about 50% of the power generated by the FC, making it an unsatisfactory solution. Therefore, to achieve optimal overall performance, two critical design criteria for the air supply must be met. Firstly, it is very important to use a highly efficient compressor. Secondly, it is crucial to further reduce the parasitic energy demand of the air supply in order to achieve optimal system efficiency.

To this end, the exhaust gas produced by the fuel cell can be utilised efficiently and a thermomechanical drive system implemented, further reducing the parasitic energy demand of the air supply and improving the overall efficiency of the system.

For the thermomechanical drive, two possible design alternatives are presented [5]: coupling a screw compressor and a screw expander or combining a screw compressor and a turbine. The first solution involves an extremely heavy system, considering the compensation tank, while the second requires a heavy and expensive gearbox with high gear ratios due to different shaft speeds.

Subsequently, it is suggested that the coupling of a radial compressor and a radial turbine, resulting in a turbocharger, may be an optimal solution in the aeronautical field.

This is a well-known and robust technology in stationary and mobile applications. The main advantage of radial turbines is their compactness and the possibility of applying variable turbine geometry (VTG), which allows the control of shaft speed and thus mass flow or pressure ratio. Although there are no turbochargers with the specified design requirements, the maturity of turbocharger technology suggests the possibility of adapting to the PEM-FC environment in flight.

2.3 Influence of operational parameters on Energy Recovery and alternative solutions

In this section, the importance and impact of operating parameters within an energy recovery system in a PEMFCPS (Proton Exchange Membrane Fuel Cell Power System) will be analysed. Particular attention will be paid to the influence of the operating pressure at which the fuel cell stack operates on the overall performance of the energy recovery system, as well as the importance of the turbine inlet gas temperature (TIT).

During this discussion, several solutions proposed in the scientific literature to increase the turbine inlet gas temperature (TIT) parameter will be exposed. This effort aims at making the turbocharger autonomous, completely feeding the compressor with energy from the turbine, improving the performance of the system but further increasing its complexity.

In the work of Campanari et al. [9], different PEMFC system architectures are considered, where the air supply system consists of an electrically driven compressor or a turbocharger, a system model is

presented for predicting the performance of the PEM fuel cell as the operating temperature and pressure change, in order to analyse the pros and cons of the different architectures and find the optimal operating conditions, in particular the operating pressure, compressor air delivery pressure and compression ratio, for each configuration.

The article provides guidance on how cost-effective it may be to use a turbine for energy recovery from flue gases and on which architectures and under which conditions.

In all cases, it is considered to design the fuel cell system to achieve a net electrical output of 60 kW at cruising conditions.

System performance is discussed under different operating conditions faced by an aircraft during flight, including ground operation, cruise conditions and the condition referred to as worst case, high altitude, and low speed.

These conditions, in fact, have very different operating conditions and therefore different compressor operating points, for example when operating at high altitude the atmospheric pressure is lower and therefore a higher compression ratio is required to operate at the same operating pressure, this also means more work from the compressor.

At high altitude, there is also a lower ambient temperature, a certain degree of pressurisation is necessary to allow the presence of liquid water at the typical operating temperatures of the cell.

Under such conditions, it becomes important to utilise the expansion of the cell exhaust gases with a turbine.

An increase in operating pressure allows the fuel cell to operate better, making it produce more energy with the same amount of hydrogen. However, this advantage comes at an energy cost, as it requires the compressor to work harder. Excess pressure could therefore have a negative impact on the entire system. For this reason, PEM fuel cells usually operate at a pressure of between 1.2 and 1.5 bar. If the pressure is to be increased, it may be convenient to recover energy from the fuel cell's exhaust gases.

The fuel cell considered is a low temperature type, so it operates at a maximum temperature of around 80-85 °C. Under these conditions, the minimum pressure should be 0.57 bar to avoid condensation; setting a margin, the minimum operating pressure below which the system must not fall is set at 0.8 bar.

The article considers three different architectures schematised in figure 2.6.

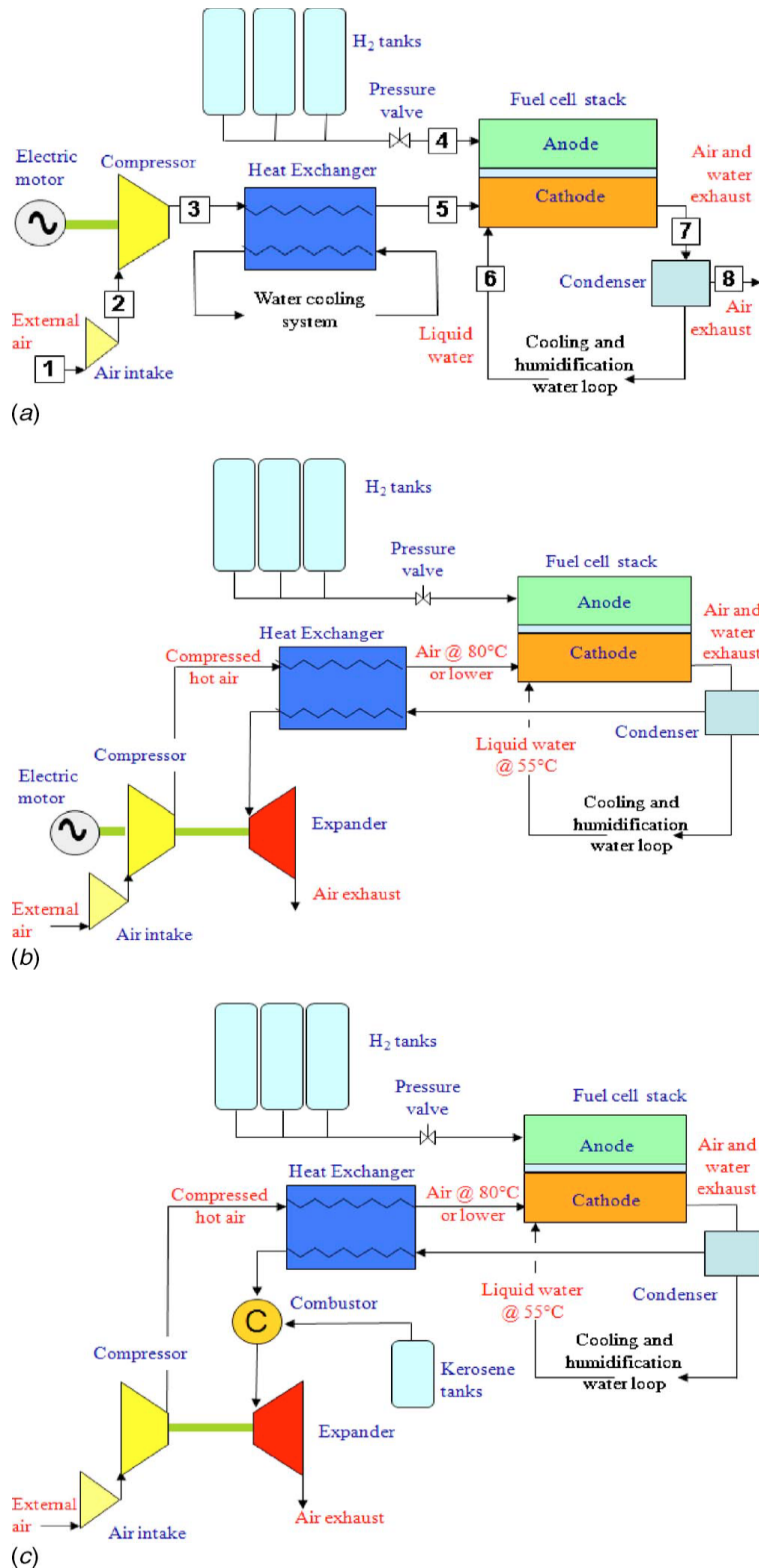


Figure 2.6: Different layout of air supply system (a) Schematic layout of the base case (b) Schematic layout of the case with turbocharger (c) Schematic layout of the case with combustor and turbocharger [9]

In the first case, i.e. case 2.6 a), the flow of air enters from outside and passes through a diffuser, in which the kinetic energy of the air is converted into pressure, the flow then passes into the compressor, where the air is compressed to the pressure required by the fuel cell; it is then cooled through a heat exchanger to reach the temperature required by the fuel cell; the air is mixed with

water required to humidify the fuel cell, this water required for humidification is separated directly from the combustion gases leaving the fuel cell through a condenser, the excess gases are directly expelled to the outside environment.

The optimisation model implemented in this work shows that with this type of architecture, which does not recover energy from the combustion gases, it is not convenient to supply the fuel cell with a higher operating pressure than the minimum pressure considered in cruise and high altitude and low speed conditions, while a slight increase in pressure may be convenient for the ground condition. The reported efficiency is 43.5 per cent during cruise conditions and 52.5 per cent during ground operation.

The article argues that with this configuration, it is not possible to insert a turbine that harnesses the energy of the combustion gases because the temperature of the gases entering the turbine would be too low and could lead to the formation of condensed water droplets during expansion, while if the expansion was stopped at a higher pressure, the power advantage would be too small to justify the complexity of the system.

The article says that to harness the energy of flue gases with a turbine, the architecture must be modified to achieve higher turbine inlet temperatures, as in cases b) and c).

In case b), the inlet temperature of the combustion gases arriving at the turbine is increased by passing the gases through a heat exchanger together with the pressurised air coming out of the compressor, which also eliminates an extra flow needed to cool the air.

With this system, the temperature of the gases is high enough to justify the insertion of a turbine, but the power generated by the turbine is in any case not enough to power the compressor, so an electric motor is also inserted on the same shaft as the turbine and compressor, which however consumes much less energy than in case a).

With this solution, the electrical efficiency rises to 50.5 per cent at cruising conditions and there is also an increase in the optimum operating pressure compared to the previous case.

Even in this case, for high altitude and low speed conditions, the optimum pressure is still the minimum of 0.8 bar. This is because the external pressure of the air taken from the compressor is very low and increasing the compression ratio too much is too expensive in terms of power.

This solution is very advantageous in terms of efficiency, but more complex control solutions may be required since the compressor is powered partly by the turbine and partly by the electric motor, each operating under significantly different conditions.

In the c) architecture, a combustor is inserted that gives off heat to the exhaust gases, so the turbine can completely power the compressor and there is no need to insert an electric motor.

Under all conditions, efficiency is slightly lower than in case B and significantly higher than in case a), reaching 48.7% in cruising conditions.

This solution makes it possible to eliminate the electric motor while saving on costs and solving control problems, but it is necessary to insert additional fuel to power the combustor.

The article therefore shows that the b) and c) architectures are more efficient and allow a lower power requirement for the CF than the a) case but require a more complex and expensive layout; however, the article hypothesises that, given the much higher PEMFC costs compared to the turbine costs, it may still be economically viable to use the b) and c) solutions.

Solution b) is preferable to solution c) due to the fact that it does not require additional fuel for the combustor.

In figure 2.7 is shown also a comparison of the energy balances obtained for cases b) and c) with those of a conventional APU, it can be seen how the efficiencies of the PEMFC systems are much greater and how the fuel flow rates used are much lower, also in terms of air flow rate.

Energy balances	PEM B	PEM C	GT
System net power output (kW)	60.0	60.0	60.0
PEM fuel heat input ($m_{\text{fuel,PEM}} \times \text{LHV}$) (kW)	118.7	111.3	0.0
GT fuel heat input ($m_{\text{fuel,GT}} \times \text{LHV}$) (kW)	—	11.8	349.3
Hydrogen consumption (kg/h)	3.56	3.34	—
Jet fuel consumption (kg/h)	—	0.99	21.43
m_{air} (kg/s)	0.068	0.064	0.30
Stack outlet temperature (K)	280	391	836
Electric efficiency η_{el}	50.53	48.73	17.75

Figure 2.7: Comparison of the energy balances obtained for cases b) and c) with those of a conventional APU [9]

In the work of Jiuxuan et al. [18]a performance prediction model of the PEMFC system is implemented, which utilises a radial turbine to recover energy from the fuel cell exhaust gas and partially drive the compressor, in an electric turbocharger type architecture, with the compressor being partly powered by the electric motor and partly by the turbine.

The impact of the average specific heat capacity of an exhaust gas mixture on turbine performance is suggested in this text.

There is also an interesting analysis of the efficiency of energy recovery by the turbocharger as certain factors vary, such as gas supply pressure, stoichiometric air ratio, current density, and operating temperature.

Figures 2.8 show the amount of energy recovered by the radial turbine indicated by the coefficient η_1 as the current density and operating pressure of the fuel cell vary while maintaining a constant operating temperature.

The coefficient is calculated as the ratio between the power generated by the turbine and the net power, i.e., power generated by the FC minus the power of the compressor and thermal management module.

η_1 increases gradually with increasing operating pressure and current density.

An increase in operating pressure corresponds to an increase in the partial pressure of oxygen at the cathode; this, with the same current density, leads to an increase in the voltage produced by the FC and also to an increase in the exhaust gas pressure and thus to more energy that can be used by the expansion in the turbine.

Figure 2.9 shows how the efficiency of the recovery system increases with higher current density at the same operating pressure; this happens because increasing the current density also increases the

power output of the fuel cell and therefore there is a greater demand for air flow, which also means an increase in the exhaust gas flow rate at the cathode outlet, hence greater recoverable energy. The research therefore shows how the performance of the energy recovery system increases with increasing operating pressure and current density, which obviously means an increase in the energy consumption of the compressor.

Figure 2.10 shows how the parasitic power absorbed by the air compressor and the power generated by the turbine vary as the operating pressure changes.

The recovered energy is 26% greater than the compressor's parasitic power consumption for all operating pressures considered and as already mentioned, increases with increasing operating pressure. Therefore, it is possible to decrease the power absorbed by the compressor while also improving the performance of the FC system.

Figure 2.11 shows a comparison of the overall efficiency of the PEMFC system in the presence or absence of the energy recovery turbine, varying the operating pressure and current density; it can be seen that the efficiency of the architecture with energy recovery is at least 1.87% higher than that of the architecture without the energy recovery system for all pressure and current density conditions.

The trend shows that the total efficiency drops as the operating pressure increases, but more slowly than in the non-turbine configuration, so it is convenient to use an energy recovery system when working with higher operating pressures.

As current density increases, however, the total efficiency of the system with recovery decreases linearly with that without recovery, so although increasing current density improves the efficiency of the energy recovery system and increases the power generated by the FC, the power absorbed by the auxiliary components increases more.

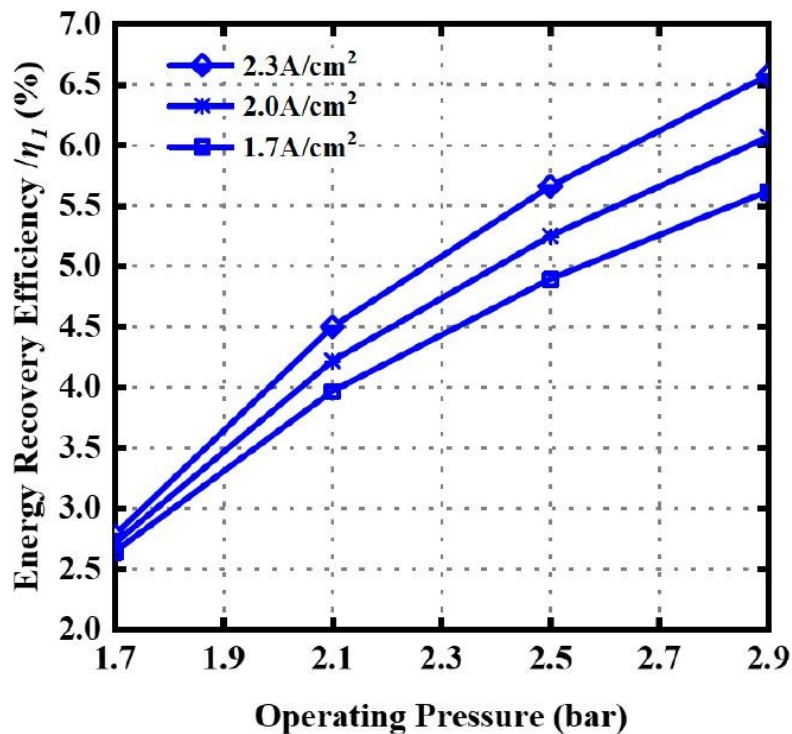


Figure 2.8: Efficiency of the recovery system at varying operating pressure and current density [18]

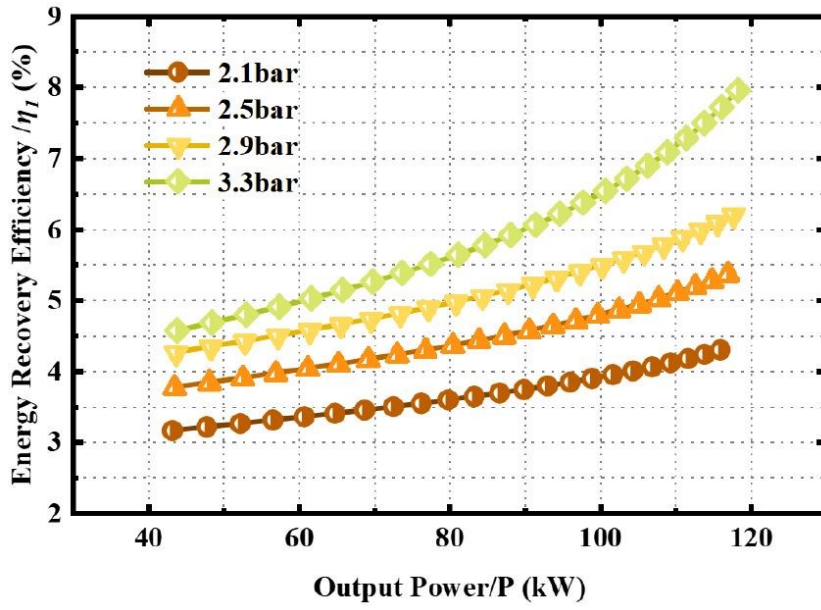


Figure 2.9: Efficiency of the recovery system at varying operating pressure and output power [18]

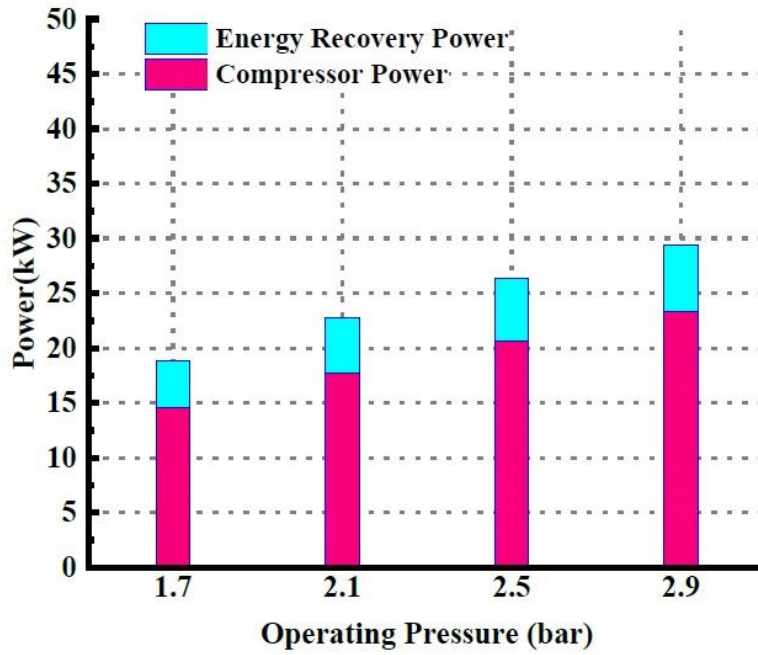


Figure 2.10: Power absorbed by compressor and power generated by the turbine [18]

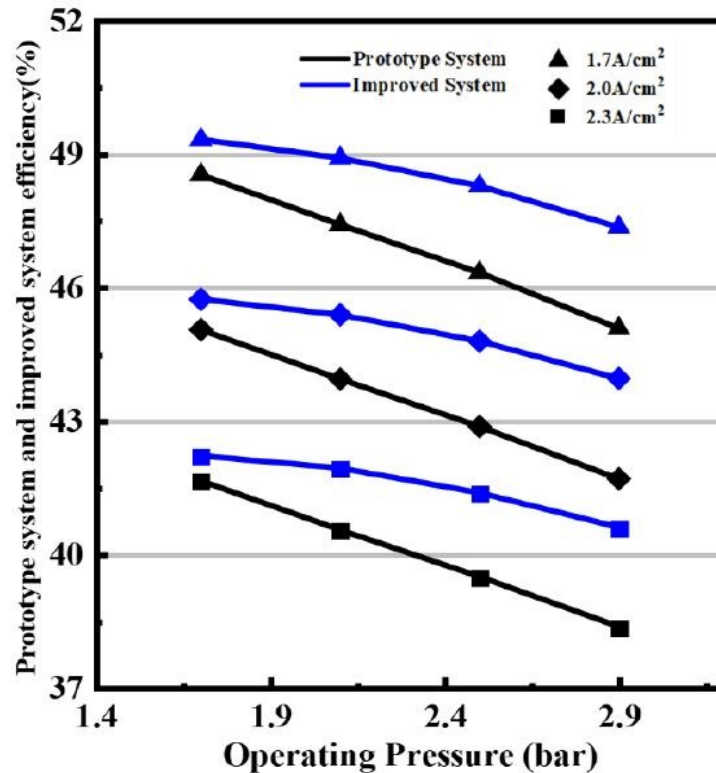


Figure 2.11: Comparison of the overall efficiency of the PEMFC system in the presence or absence of the energy recovery turbine [18]

In the work of Lukas Barchewitz [5], a simple calculation is performed for the power generated by a radial turbine recovering energy from the FC (Fuel Cell), under the analysed operating conditions.; assuming an isentropic efficiency of 60% and an inlet air temperature to the turbine of 80°C, which is identical to the stack exit temperature.

the calculated mechanical power generated by the turbine is 26 kW.

It is noteworthy that the output power is proportional to the inlet temperature. The article suggests utilizing the heat generated by the unused hydrogen combustion in the fuel cell exhaust, thereby increasing the turbine inlet temperature by 180K and enhancing the efficiency to 70%. With these values, the turbine power is calculated to be roughly 45 kW, which is 5 kW greater than the power calculated as absorbed by the compressor, resulting in a self-sustaining system.

2.4 Theses research decisions and next steps

Based on the solutions examined earlier in the chapter, the turbocharger system, comprising both a compressor and a radial turbine, is selected in this study as the most suitable choice for air supply in aeronautics. This technology is widely recognised and reliable and is commonly used in both stationary and mobile applications.

As a first analysis in this thesis work, electric turbocharger, and serial booster architectures, which are already widely used in the automotive sector, will be considered.

These will be the subject of sizing and a subsequent comparison with the electric compressor architecture previously analysed in Federico Fasiello's thesis [7].

For future research, an interesting potential solution could involve using the heat produced by the combustion of unused hydrogen in the fuel cell exhaust to increase the temperature of the gases exiting the FC stack and entering the turbine (TIT). This increase in TIT could allow the elimination of the auxiliary electric motor and improve the performance of the FCPS.

In the next chapter, a performance analysis will be carried out to preliminarily determine the optimal operating pressure of the fuel cell stack. As highlighted in the articles described in the preceding section, this parameter plays a significant role in the overall performance of the energy recovery system.

3 Performance Analysis

Following the thesis work of Federico Fasiello [13], which is the starting point for this research, the initial phase of the design procedure commences with an assessment of performance.

This entails a preliminary investigation conducted at a systemic level, with the objective of discerning the most advantageous arrangement of components and the operational factors of the FCPS. This pursuit is directed towards attaining a commendable degree of efficiency across the complete range of flight conditions.

This process can be regarded as a preliminary stage of static sizing for the air supply system; indeed, some of the outputs of this procedure will subsequently be employed as inputs for the static design process, which will be addressed in Chapter 4.

However, performance analysis and static design are not separate processes but are closely interconnected through iterative processes to achieve accurate results [13].

The assessment of performance relies on simplified steady-state models designed solely to evaluate crucial parameters for conducting system efficiency calculations. These models can be considered as the stationary counterparts of the dynamic ones introduced in Chapter 5.

The main objectives of this analysis are:

- Determining the design points for specific FCPS components, particularly focusing on optimizing the air supply system.
- Identifying design parameters that optimise the efficiency and performance of the FCPS.

3.1 Performance analysis model

As mentioned in the previous section, the model implemented for the performance analysis can be seen as the stationary counterpart of the dynamic fuel cell power system, which is detailed in Chapter 5.

This static model is intended to provide a simplified representation of the various elements constituting the fuel cell power system, thus enabling a preliminary performance analysis. Its implementation was carried out using MATLAB software, which made it possible to create this detailed model.

The organisation of the code reflects the basic physical configuration of the system, as well as the most significant interrelationships between the constituent parts [13]; in this regard, the code is

composed of several modules that are linked and interact with each other by being called up both in the code of the main module and within the codes of other modules.

Each module represents a modelling of a physical component of the fuel cell power system; consequently, all these subsystems combine to form the complete model of the fuel cell power system.

The structure of the code, with the different information flows, is depicted in Figure 3.1, while Figure 3.2 shows a schematic representation of the FCPS architecture that the performance analysis model reproduces.

The components that are part of the model include the atmosphere model, the air intake model, the fuel cell stack model, the intercooler, and the air supply system, which is responsible for ensuring the required amount of oxygen to the cathode of the stack for the reaction to occur.

In the previous thesis work, the air supply system included only a compression system powered by an electric motor.

In this study, an energy recovery system has been introduced through a turbine system, aiming to recuperate a portion of the exhaust gas energy exiting the fuel cell. This recovered energy is then used to partially power the compression system, thereby reducing the power demand on the electric motor, which is directly supplied by the fuel cell stack.

The performance analysis model works by inputting the desired net cruising power, P_{net_cruise} , which is a design requirement; this power is equal to the total power generated by the fuel cell's stacks, P_{gross_cruise} , from which the power required to power the auxiliary components of the FC power system is subtracted.

The gross power is correlated with the flows of reactants required to achieve this power; the necessary reactants, under static conditions, are calculated in the stack model.

However, the reactant value depends not only on the gross power desired but also on certain distinctive parameters of the stack, which will be discussed later.

In the stack model, the flow rate of dry air exiting the fuel cell is also calculated.

This will be directed towards the inlet of the turbine, which will harness its enthalpy energy, generating power P_t .

This power will partially drive the compressor mounted on the same shaft as the turbine in a turbocharging system.

The compression system is tasked with ensuring the proper flow rate of oxygen, contained in the air, required at the anode, and calculated within the stack model, subsequently bringing it to the operational pressure, p_{st} , of the stack itself.

In the context of the compression system model, the absorbed power is also calculated, referred to as P_c .

This power will be partially supplied by the turbine and the remaining portion by the electrical motor's energy source.

The power that the electrical motor must generate is termed P_{cm} . Additionally, a basic intercooler performance model has been integrated to evaluate the necessary thermal energy uptake from the airflow, aiming to lower its temperature to match the stack's operating temperature, denoted as T_{st} [13].

In the following paragraphs, the fundamental aspects of the performance analysis model components will be outlined. These aspects can be further detailed in Federico Fasiello's thesis [13]. Additionally, a more comprehensive explanation of the model concerning the air supply system and all aspects related to the integration of the turbine system within the same model will be provided.

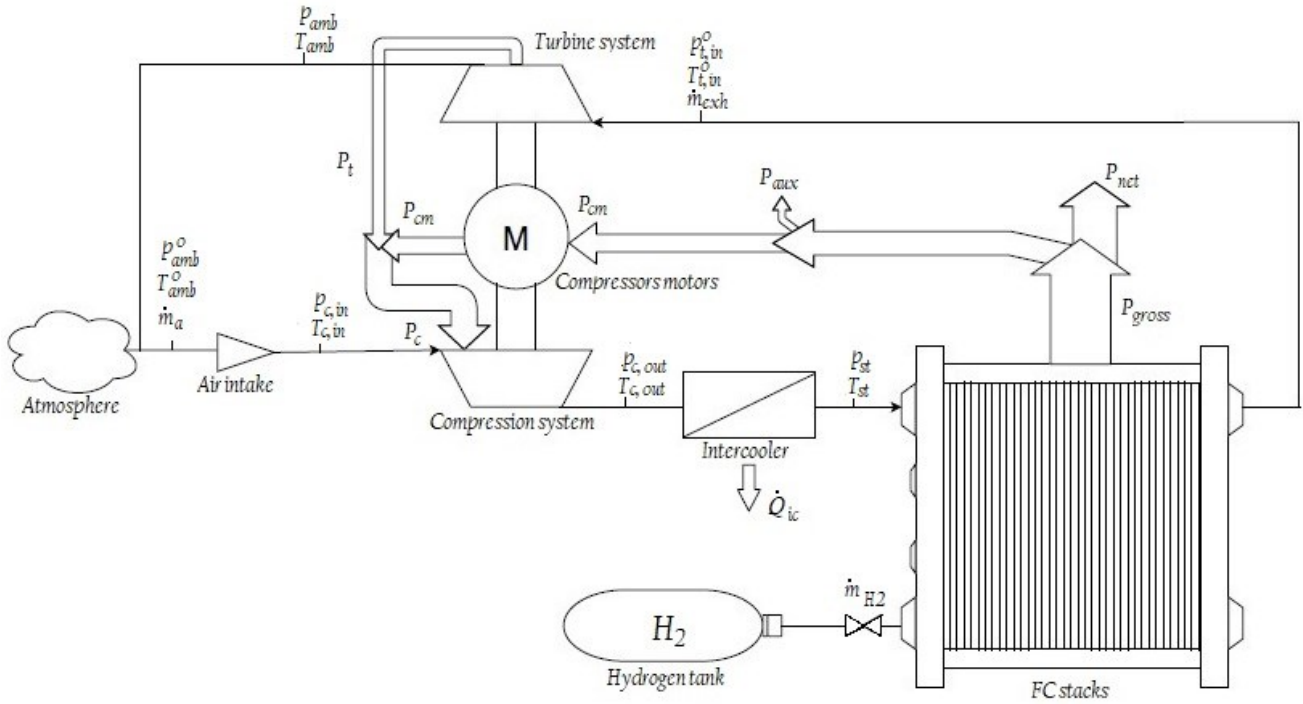


Figure 3.1: Schematic representation of the FCPS architecture.

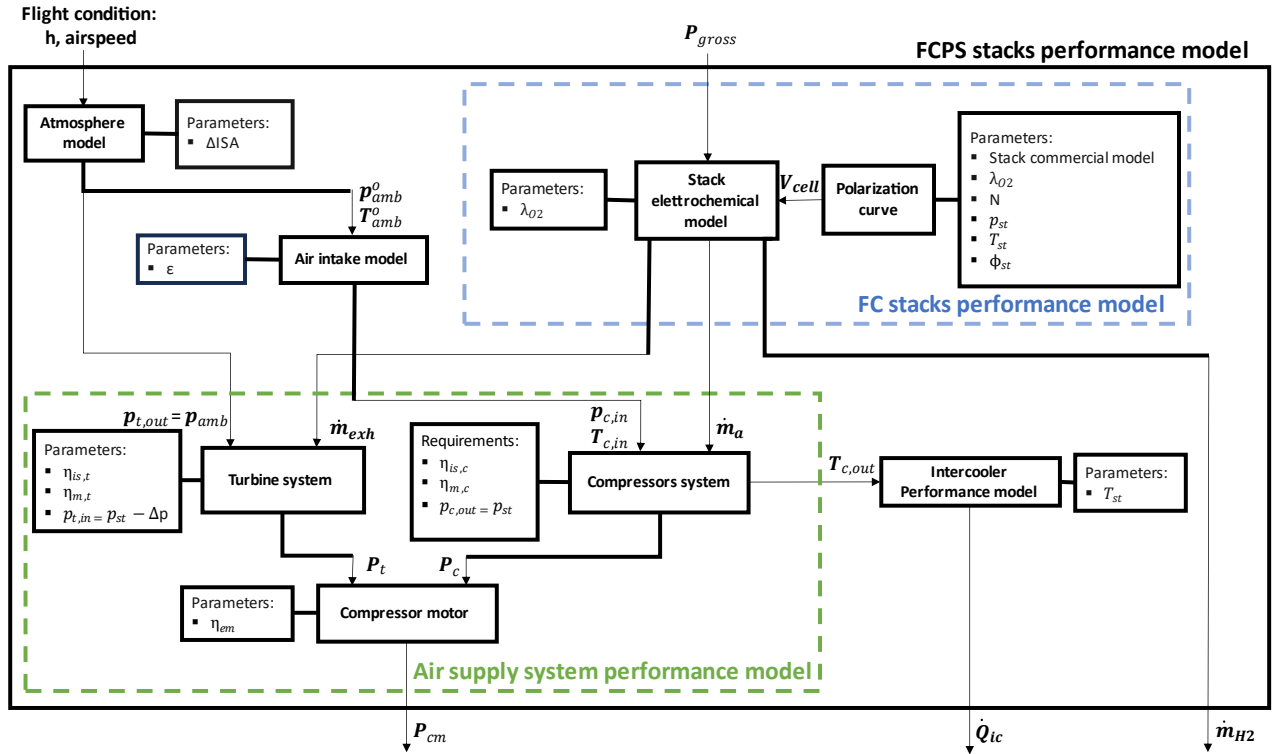


Figure 3.2: Structure of the FCPS performance model.

3.1.1 Efficiencies of the fuel cell power system

To perform an accurate assessment of a system's performance, it is essential to conduct a thorough analysis of the efficiencies that characterize it. This analysis aims to identify what influences these efficiencies, thus enabling optimal choices to be made regarding the parameters that can be changed in order to maximize the overall effectiveness of the system.

The key factor that defines how well the system performs is the overall efficiency of the FCPS.

This efficiency is calculated by comparing the net power output, P_{net} , to the energy content of the fuel, P_{H_2} .

The energy content of the fuel is determined by the product of the flow rate at which hydrogen is consumed, m_{H_2} , and the lower heating value of hydrogen, LHV_{H_2} , it is assumed to be 119.96 MJ/kg [13], [18]

$$\eta_{FCPS} = \frac{P_{net}}{P_{H_2}} = \frac{P_{net}}{LHV_{H_2} \dot{m}_{H_2}} \quad (3.1)$$

The net power output of the FCPS is calculated as the gross power generated by the FC stacks minus the power required to supply the Balance of Plant (BoP) components, which include the air supply system and other auxiliary components of the FCPS.

The largest amount of power absorbed is the power required to power the air supply system, i.e., the power required by the electric motor that powers the compression system.

However, if an energy recovery system is provided, the compressors are partly powered by the turbines that recover energy from the gases leaving the stacks of fuel cell.

The power absorbed by the electric motors is then equal to that required by the compressor system minus the power generated by the turbines, the latter then being added to the gross power when calculating the net power [19].

The rest of the power absorbed by the auxiliary components is denoted by P_{aux} , this is a significantly smaller part than that absorbed by the air supply system and is assumed to be 1% of P_{gross} [1].

$$P_{net} = P_{gross} - P_c + P_t - P_{aux} = P_{gross} - P_{cm} - P_{aux} \quad (3.2)$$

Another important efficiency parameter is the plant efficiency, denoted by η_{plant} , which reflects the ability of the FCPS to transform the gross power generated by the FC stacks into useful power; this parameter thus gives an indication of the amount of power absorbed by the BoP components in relation to the power generated.

This efficiency is calculated as the ratio between the net power and the gross power generated by the fuel cell; it depends on the system architecture and the characteristics of the BoP components.

$$\eta_{plant} = \frac{P_{net}}{P_{gross}} \quad (3.3)$$

Another characterising parameter of the FCPS is the efficiency of stacks η_{stack} , which indicates of the FC stacks' ability to transform chemical energy into electrical energy.

This efficiency is influenced by the structural attributes of the stacks as well as the conditions under which they operate [13]

It is calculated as the power generated by the stacks, P_{gross} , divided by the energy content of the fuel, P_{H_2} .

$$\eta_{stack} = \frac{P_{gross}}{LHV_{H_2} \dot{m}_{H_2}} \quad (3.4)$$

In light of the quantities introduced, the total efficiency of FCPS can be calculated using the following equations:

$$\eta_{FCPS} = \frac{P_{net}}{P_{H_2}} = \frac{P_{net}}{P_{gross}} \frac{P_{gross}}{LHV_{H_2} \dot{m}_{H_2}} = \eta_{plant} \eta_{stack} \quad (3.5)$$

The total efficiency of the FCPS is thus equivalent to the product of the efficiency of the plant and that of the stacks.

3.1.2 FC stacks performance model

The FC stacks model calculates the flow rates of air and hydrogen that must be supplied to the cathode and anode of the FC, under steady-state conditions, to produce a certain amount of gross power P_{gross} , input.

Under steady-state conditions, the oxygen flow required by the FC stacks must be equal to that consumed during the reaction at the cathode, but is in excess of this amount, depending on the excess oxygen ratio λ_{o_2} at which the fuel cell operates, to prevent reactant starvation.

The flow rate consumed during the reaction at the cathode is calculated, under steady-state conditions, using the following formula:

$$\dot{m}_{o_2} = \frac{mm_{o_2} P_{gross}}{4F V_{cell}} \quad (3.6)$$

Thus, the flow rate of air to be supplied to the FC stacks must be:

$$\dot{m}_a = \frac{mm_{o_2} \lambda_{o_2} P_{gross}}{4F x_{o_2} V_{cell}} \quad (3.7)$$

Where:

- λ_{o_2} is the oxygen excess ratio.
- x_{o_2} is the oxygen mass fraction and is defined by $x_{o_2} = \frac{m_{o_2}}{m_{dry\ air}}$.
- mm_{o_2} is oxygen molar mass.
- V_{cell} is the cell voltage.
- F is the Faraday constant.
- P_{gross} is the total power generated by the fuel cell, including the power generated to supply the auxiliary components of the FC power system.

The hydrogen flow rate is equal to the amount reacting at the anode and is calculated using the following formula:

$$\dot{m}_{H_2} = \frac{mm_{H_2} P_{gross}}{2F V_{cell}} \quad (3.8)$$

Where mm_{H_2} is hydrogen molar mass.

The steps to arrive at these formulas are explained in detail in Federico Fasiello's thesis [13]

The voltage of the cell is determined by the current density i , following the cell's polarization curve. The specific shape of this curve can differ among various commercial FC models and relies on several operational factors of the stack, come the oxygen excess ratio λ_{o_2} , the stack pressure p_{st} ; the stack relative humidity ϕ_{st} , the stack temperature T_{st} .

The current density, i , can be examined by means of an overcapacity factor v , calculated by dividing the expected current density for the measurement of this parameter at the peak power point of the cell [13]

With the inclusion of the turbine, it was also necessary to include in the FC stack model the calculation of the flow rate of dry air leaving the fuel cell and entering the turbine, denoted by \dot{m}_{exh} . The fuel cell stack produces as output products: electrical energy, humid air, and water.

The air needs to be dehumidified by removing the water vapor, as it could potentially condense during turbine expansion due to the relatively low temperatures at which the fuel cell operates, risking damage to the turbine blades.

The value of the dry air flow rate \dot{m}_{exh} exiting the fuel cell stack can be calculated as the sum of the nitrogen and oxygen flow rates exiting the cathode.

In steady-state conditions, it will be equal to the incoming air flow rate minus the amount of oxygen consumed in the reaction, following the principle of mass conservation. Therefore, the following formulas hold in steady-state conditions:

- $\dot{m}_{o_2,ca,in} - \dot{m}_{o_2,ca,out} - \dot{m}_{o_2,reacted} = 0$ (3.9)

- $\dot{m}_{N_2,ca,in} - \dot{m}_{N_2,ca,out} = 0$ (3.10)

In the assumption that the dry air flow rate remains constant from the inlet to the outlet of the dehumidifier, we obtain:

$$\dot{m}_{exh} = \dot{m}_{o_2,ca,out} + \dot{m}_{N_2,ca,out} = \dot{m}_{o_2,ca,in} + \dot{m}_{N_2,ca,in} - \dot{m}_{o_2,reacted} \quad (3.11)$$

$$\dot{m}_{exh} = \dot{m}_{a,ca,in} - \dot{m}_{o_2,reacted} \quad (3.12)$$

Inserting the equations 3.7 and 3.6 into 3.12, results in stationary conditions:

$$\dot{m}_{exh} = \frac{mm_{o_2} \lambda_{o_2} P_{gross}}{4F x_{O_2} V_{cell}} - \frac{mm_{o_2} P_{gross}}{4F V_{cell}} \quad (3.13)$$

3.1.3 Air supply system

The air supply system must guarantee the FC stacks, through the compression system, the air flow calculated through the equation (3.7) at the fuel cell's operating pressure.

The model implemented in the performance analysis deals with calculating the P_{cm} power that must be transferred to the electric motor that partially powers the compression system.

At this preliminary stage the architecture of the air supply system has not yet been established but will be decided in chapter 4, the compression system is therefore taken as a black box which must work a certain compression ratio and a certain air flow rate.

As mentioned above, the power absorbed by the electric motor must be equal to that required by the compression system minus the power generated by the turbine.

The compressor and turbine powers can be calculated using the following formulas [20]

$$P_c = \frac{\dot{m}_a c_p T_{c,in} \left(\left(\frac{p_{c,out}}{p_{c,in}} \right)^{\frac{\gamma-1}{\gamma}} - 1 \right)}{\eta_c} \quad (3.14)$$

$$P_t = \eta_t \dot{m}_{exh} c_p T_{1,exh}^\circ \left(1 - \left(\frac{p_{t,out}}{p_{t,in}} \right)^{\frac{\gamma-1}{\gamma}} \right) \quad (3.15)$$

Where:

c_p is the specific heat of the air, expressed in $\frac{J}{kgK}$; it depends on the temperature, pressure and moisture content of the air and is calculated using the following formula:

$$c_p = \frac{R\gamma}{\gamma - 1} \quad (3.16)$$

Where R is Gas constant (J/kg/K) and γ is the Ratio of specific heats (-).

η_c e η_t are the efficiency of the compressor and turbine system respectively, these can be calculated as the isentropic efficiency of the turbomachinery multiplied by the mechanical efficiency.

$$\eta_c = \eta_{is,c} \eta_{m,c} \quad (3.17)$$

$$\eta_t = \eta_{is,t} \eta_{m,t} \quad (3.18)$$

During this performance analysis phase, the values of these efficiencies cannot be precisely determined. Therefore, they are reasonably assumed and held constant in order to allow preliminary evaluations of the system with these stable values.

Following the static dimensioning process, it will be necessary to reintegrate them with the precise efficiency values obtained.

The rest of the parameters in the formulae represent the requirements for the air supply system.

These requirements depend on the demands of the fuel cell stack and external atmospheric conditions, which in turn depend on flight conditions.

$p_{c,in}$ and $T_{c,in}$ represent the pressure and temperature at the inlet of the compression system. These conditions depend on the external atmospheric conditions, specifically, the altitude reached by the aircraft during the flight mission.

The properties of air at different flight conditions are calculated using the International Standard Atmosphere (ISA) model, which is explained in detail in Appendix A of Federico Fasiello's thesis [13].

The flight conditions that are input to the atmosphere model are altitude h, airspeed, and deviation from ISA conditions ΔISA .

The inlet conditions to the compressor system are calculated through the air intake model using the following formulae [13]:

$$p_{c,in} = p_{amb} + \varepsilon(p_{amb}^\circ - p_{amb}) \quad (3.19)$$

$$T_{c,in} = T_{amb}^\circ \quad (3.20)$$

$p_{t,out}$ is the pressure at the turbine outlet, which is equal to the ambient pressure and therefore depends on the atmospheric conditions and the altitude of the aircraft, hence the flight conditions. $p_{t,in}$ is the gas pressure at the stack of fuel cell outlet and therefore the inlet to the turbine. It depends on the operating pressure required by the fuel cell stack minus the pressure losses within the cathode flow channel.

Since the pressure losses at the cathode are an uncertain value that depends on various factors such as the geometric characteristics of the cells, they were initially estimated as a constant value of $\Delta p = 0.5$ bar [5], [18], [21]–[24].

$$p_{t,in} = p_{st} - \Delta p \quad (3.21)$$

$T_{t,in}$ is the temperature of the air entering the turbine. It is assumed that this temperature remains constant throughout the internal processes of the stack; therefore, it is equal to the operating temperature required by the fuel cell stack.

$$T_{ca,out} = T_{ca,in} = T_{st} \quad (3.22)$$

$p_{c,out}$ is the pressure at the outlet of the compression system and therefore must be equal to the pressure required by the stack.

\dot{m}_a represents the air flow required by the fuel cell stack, it is calculated in the stack model via the equation (3.7)

\dot{m}_{exh} is the dry air flow rate exiting the fuel cell stack, calculated in the stack model using (3.13).

The power absorbed by the electric motor can be calculated as the ratio between the difference between the power required by the compression system and the power generated by the turbine and the electromechanical efficiency of the engine, estimated during the evaluation phase.

$$P_{cm} = \frac{P_c - P_t}{\eta_{em}} \quad (3.23)$$

Another output of the air supply system performance model is the temperature of the air leaving the compressor, this is important as the compressed air will have to be brought to the operating temperature of the stack.

The temperature of the air leaving the compressor is calculated using the following formula:

$$T_{c,out} = T_{c,in} + \frac{1}{\eta_{is,c}} T_{c,in} \left[\left(\frac{p_{c,out}}{p_{c,in}} \right)^{(\gamma-1)/\gamma} - 1 \right] \quad (3.24)$$

3.1.4 intercooler model

There is also a simple model of the intercooler in which the heat output, \dot{Q}_{ic} , from the air flow is calculated to bring it to the stack operating temperature T_{st} .

$$\dot{Q}_{ic} = \dot{m}_a c_p (T_{c,out} - T_{st}) \quad (3.25)$$

3.2 Calculation of optimal FC operating pressure

Through the presented model, it is possible to make a performance analysis by identifying the value of parameters, on which it is possible to intervene, that maximise the performance of the FCPS. In Federico Fasiello's thesis[13], evaluations were made for all parameters and optimal values were identified for the case under consideration from the ranges indicated in the literature.

The parameters chosen are shown in the table 3.1.

Model parameter	Symbol	Value
Oxygen excess ratio	λ_{o_2}	2
Oversizing factor	N	0.8
Stack pressure	p_{st}	1.2 atm
Stack relative humidity	ϕ_{st}	1
Stack temperature	T_{st}	80 °C
Compressor efficiency	η_c	0.75
Compressor mechanical efficiency	$\eta_{m,c}$	0.98
Motors electromechanical efficiency	$\eta_{em,c}$	0.95
Deviation from ISA condition	ΔISA	0 °C (standard day)
Pressure recuperation factor	ε	0.5

Table 3.1: parameters used in the performance analysis model in Federico Fasiello's thesis [13]

By adding the turbine, it is necessary to make new assessments of the optimum operating pressure of the stack while the assessments made on the other parameters remain valid.

The state of the art discussed in Chapter 2 shows that it is more cost-effective to increase the operating pressure of the stack if an energy recovery system is used.

The pressure range at which the fuel cell can work, chosen for the study in this thesis, is between 1 and 3 atm [13], [19].

Figure 3.3 shows the trend in fuel cell (FC) stacks efficiency and plant efficiency, calculated at varying operating pressure in the absence of an energy recovery system.

It can be seen that the stack efficiency, calculated using equation (3.4), rises with the increase in operating pressure. This improvement can be attributed to the higher cell voltage achieved at the same current density. This phenomenon is a consequence of the increase of reaction rate [19] and is illustrated in figure 3.4, where the polarisation curves of the stacks as the operating pressure changes is shown.

The increase in pressure, however, also leads to a decrease in the plant efficiency, calculated through the equation (3.3), since, under the same flight conditions, the compressor must work with a higher compression ratio and therefore consumes more power.

It is therefore important to find a compromise between these two aspects.

The main objective is to maximise the overall efficiency of the system, this is calculated as the product between the plant efficiency and the efficiency of the stack as shown in the formula (3.5) and therefore takes into account both effects of efficiency change due to pressure increase.

Figure 3.5 shows the trend of the total efficiency of the FCPS as the pressure varies without using an energy recovery system implemented in Federico Fasiello's thesis[13]; it can be seen that the efficiency increases with increasing pressure to a peak value around 1 atm.

Up to this value, in fact, the effect of the increase in stack efficiency is greater than the decrease in system efficiency, after which the effect of the decrease of plant efficiency prevails and the efficiency of the FCPS begins to decline.

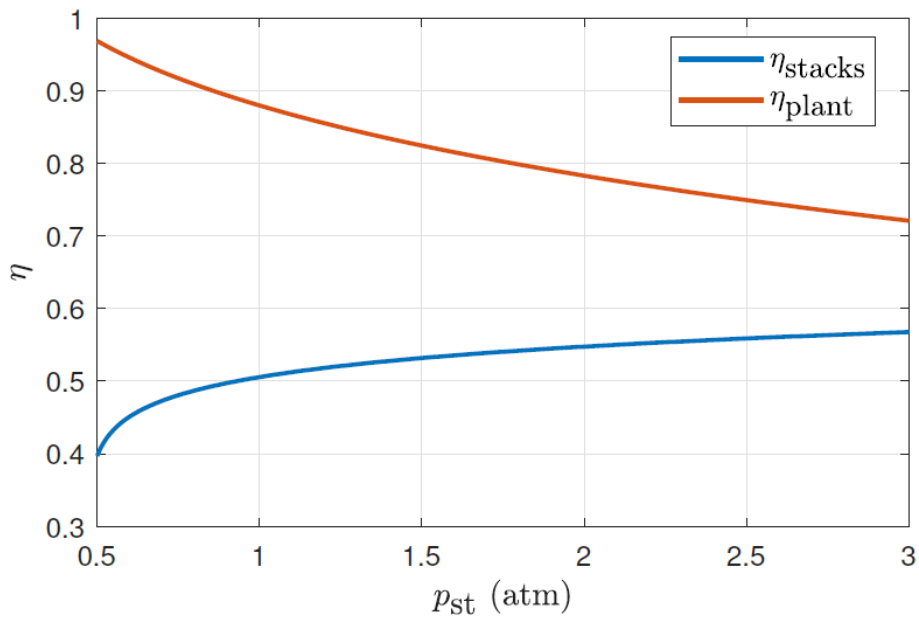


Figure 3.3: Effect of stack pressure on the stacks electric efficiency and the plant efficiency for architecture without turbocharger system.

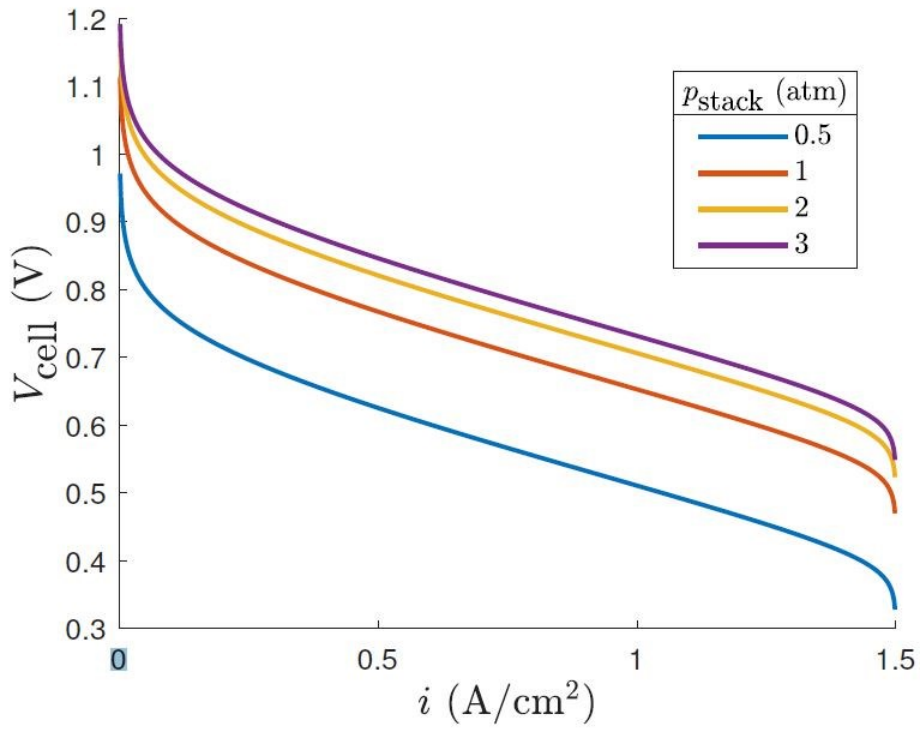


Figure 3.4: Effect of stack pressure on polarization curve.

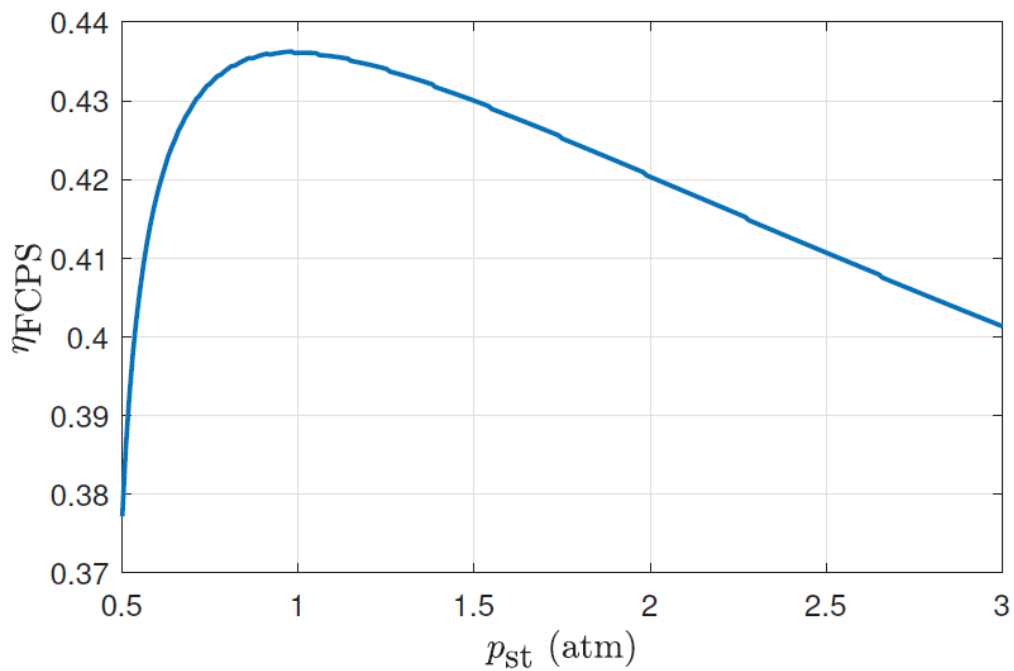


Figure 3.5 : Effect of stack pressure on the overall efficiency for architecture without turbocharger system.

Figure 3.6 Instead, shows the efficiencies of the stacks and of the plant at varying operating pressure in the case of an energy recovery system by means of a turbine system.

It can be seen that the efficiency trend of the stacks is the same as that of the architecture without the turbine system shown in the figure 3.3 while there is a smaller decrease in the efficiency of the system as the pressure increases.

This is due to the fact that, although as the pressure increases the power required by the compressor increases, the power generated by the turbine also increases, since the turbine inlet pressure is equal to the stack pressure minus the losses.

As the stack pressure increases, therefore, the turbine can take advantage of a higher expansion ratio under the same flight conditions.

Figure 3.7 shows the trend of the overall efficiency of the FCPS, it can be seen how the efficiency-maximising operating pressure increases compared to the case without a turbine system.

As the plant performance decreases less as the pressure changes, the effect of the stack efficiency increase prevails up to a pressure of 1.9 atm, so this value is chosen as the operating pressure of the FC in this work.

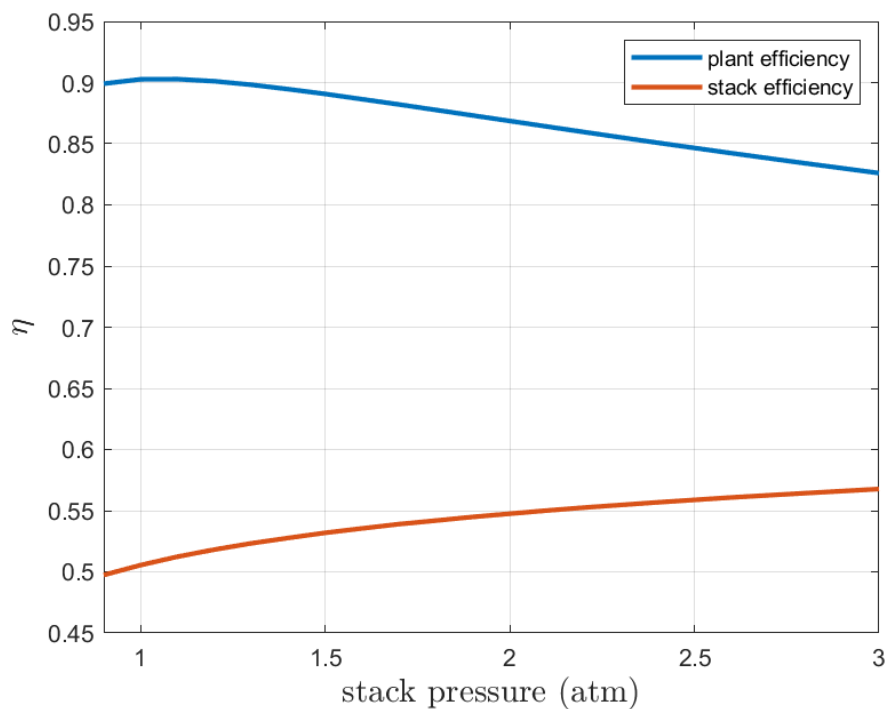


Figure 3.6: Effect of stack pressure on the stacks electric efficiency and the plant efficiency for architecture with turbocharger system.

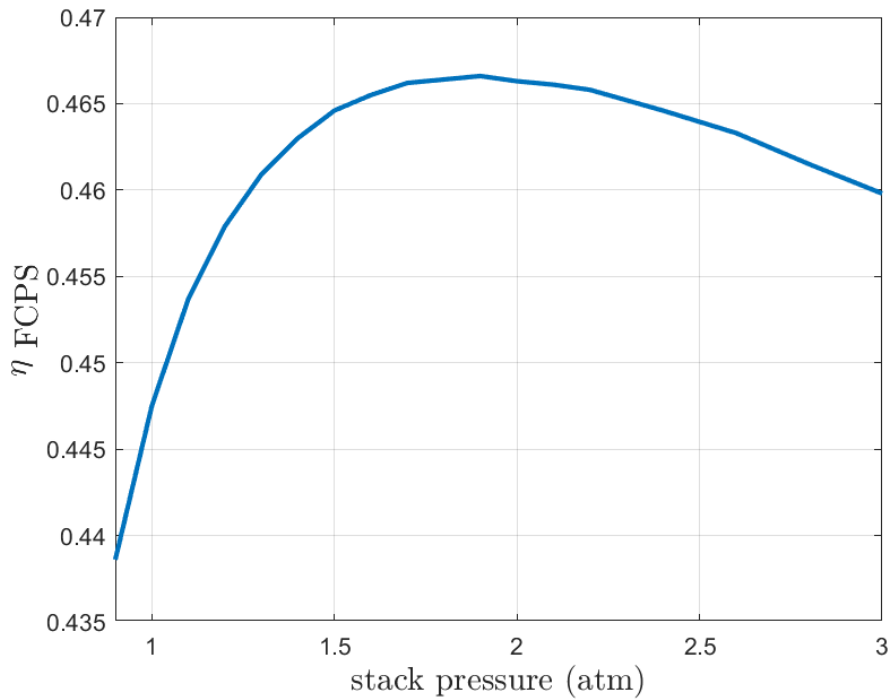


Figure 3.7: Effect of stack pressure on the overall efficiency for architecture with turbocharger system.

The effects described are also shown in figures 3.8 and 3.9 which show, respectively, the development, as the operating pressure changes, of the gross power and the power absorbed by the electric motor and the rest of the auxiliary components with the same net power generated, for the case without and with energy recovery.

It can be seen that as pressure increases, there is an increase in the gross power generated by the stack and also an increase in the power required by the motor.

If the recovery system is present, the increase in power to be produced by the electric motor (indicated as P_m) as the stack operating pressure increases is significantly lower, just as the value of P_m is also lower at the same pressure, precisely because the power generated by the turbine system partially feeds the compression system and reduces the power required from the engine.

Comparing figure 3.8 with figure 3.9, it can also be observed that, with the same stack operating pressure, the system with energy recovery has a lower ratio of gross power to net power, which justifies the increase in system efficiency for the system with energy recovery, at the same pressure, observed by comparing the figures 3.3 and 3.6.

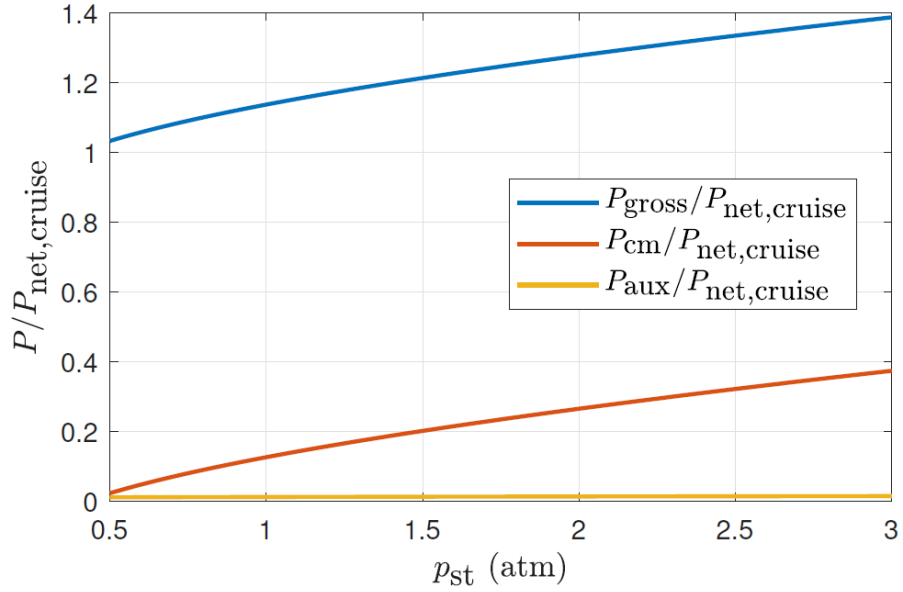


Figure 3.8: Effect of stack pressure on the different power term for architecture without turbocharger system.

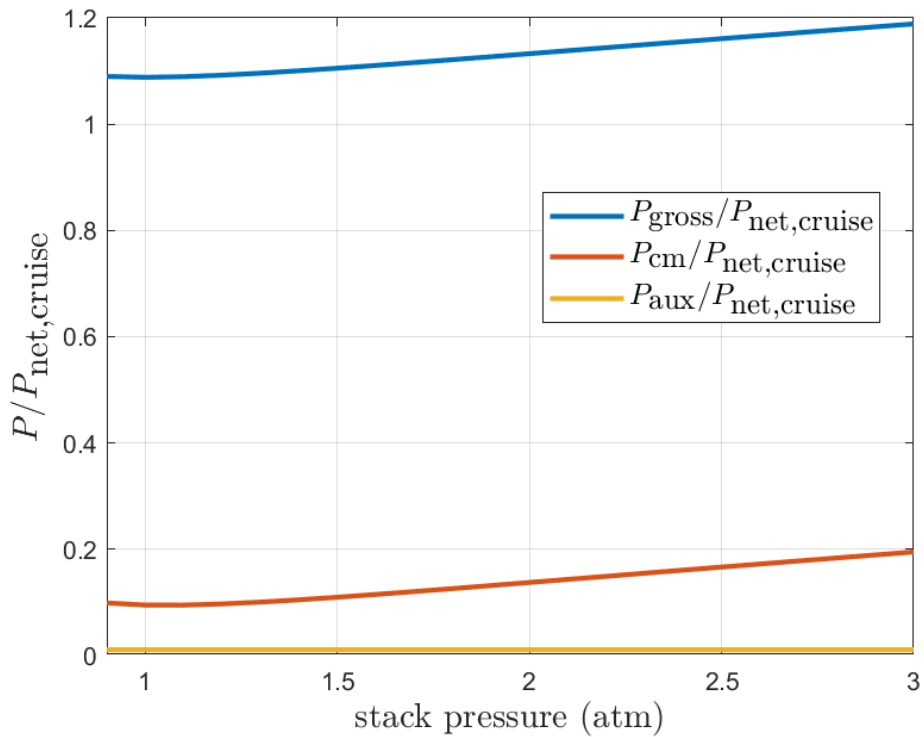


Figure 3.9: Effect of stack pressure on the different power term for architecture with turbocharger system.

Another relevant assessment concerns the air and hydrogen flow rates required by the fuel cell since reducing these leads to a decrease in the size of the compressor, turbine, and stacks, as well as a reduction in the stored hydrogen quantity. Of particular significance is the reduction in the hydrogen flow, as this is obtained through steam reforming processes of natural gas or other light hydrocarbons, resulting in CO_2 emissions.

From the figures 3.10, which depict the variations in air and H_2 flow rates with changing operating pressure for the system without energy recovery, and from figure 3.10, illustrating the same trend for the energy recovery architecture, it is evident that the optimal pressure for system efficiency also reduces reactant consumption. These flow rates, at constant net power generation, are indeed correlated with FCPS efficiency since they are directly proportional to gross power generation and inversely proportional to the voltage produced by a cell, which depends on the FC polarization curve, as shown in equations (3.1), (3.6), and (3.7).

Comparing the values in this first phase of performance analysis, a decrease in reagent flows of 8.11% was observed for the system with the energy recovery system compared to the system without recovery, both evaluated at their performance-optimising operating pressure.

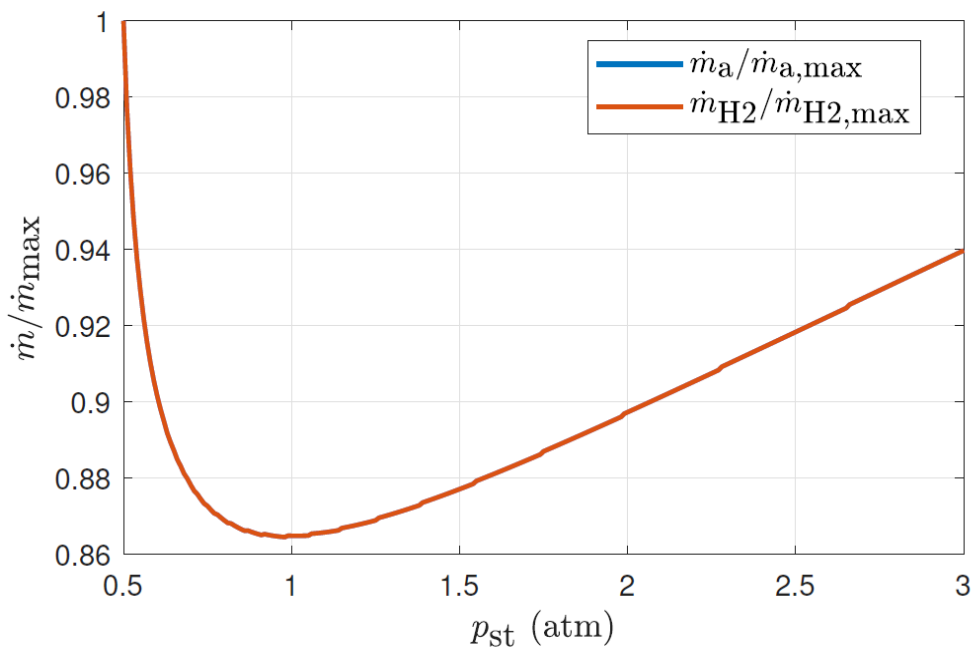


Figure 3.10 : Effect of stack pressure on the reactants consumption for architecture without turbocharger system.

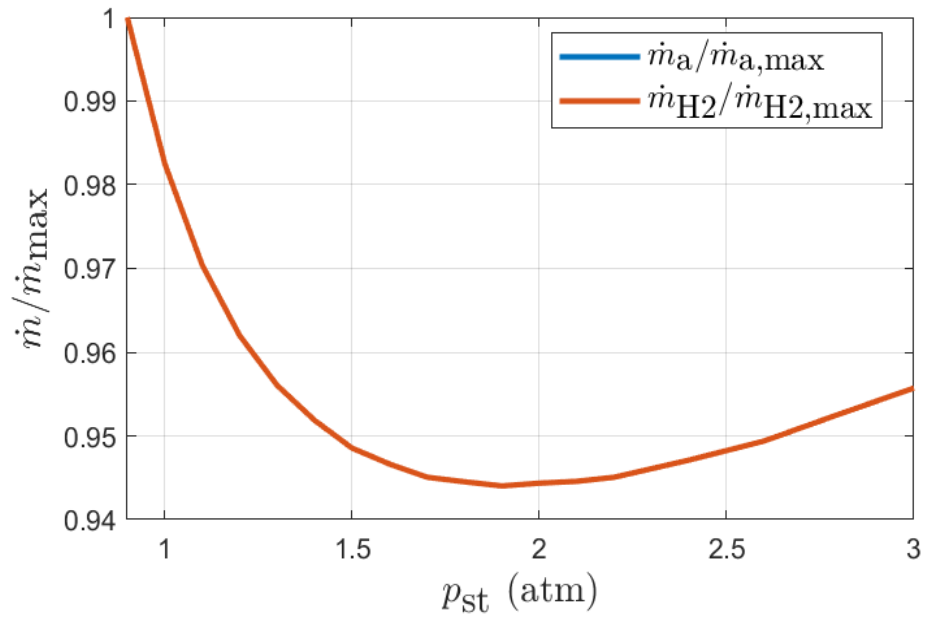


Figure 3.11: Effect of stack pressure on the reactants consumption for architecture with turbocharger system.

3.2.1 Performance Analysis Results

In this section, the performance analysis results are presented.

The results reported in this phase will serve as an indication for the choice of optimal operating parameters but are not definitive.

In Figure 3.12, the variations of the requirements for the compression system during the flight mission are displayed. It is observed that the compressor's outlet pressure must remain constant to optimize the FCPS performance.

Figure 3.13 illustrates the set of operating points at which the compressor is expected to work during the flight mission.

In Figure 3.14, the trends of the compressor's outlet temperature and the stack's required temperature are displayed. A notable temperature difference is observed, larger than in the optimal case for the system without energy recovery, as shown in Figure 3.15.

The temperature increase at the outlet is due to the higher operating pressure required by the compressor. However, this solution does not entail the challenges of cooling the air under certain flight conditions and heating it under others. Furthermore, an interesting solution could be to recover the thermal energy from the outgoing air of the compressor to heat the gas exiting the fuel cell, thereby increasing the TIT, as suggested in the article of Campanari et al.[9].

Figure 3.16 displays the requirements for the turbine system under different flight conditions. In this case, during the cruise phase, where atmospheric pressure is lower and the stack's outlet pressure remains constant, a higher gas expansion ratio can be exploited.

Figure 3.17 depicts the operating point of the fuel cell stacks for the chosen current density as a parameter. It is evident that this point represents a good compromise between stack efficiency and generated power, optimizing performance.

The flow rate of the reagents to be supplied, on the other hand, remains constant during the flight mission as the objective is to operate at a constant gross power throughout the mission, which is why it is not shown.

In Figures 3.18 and 3.19, an estimate of the performance is shown, indicating that the cruise phase is the most critical due to its higher expansion ratio, making it the chosen design point.

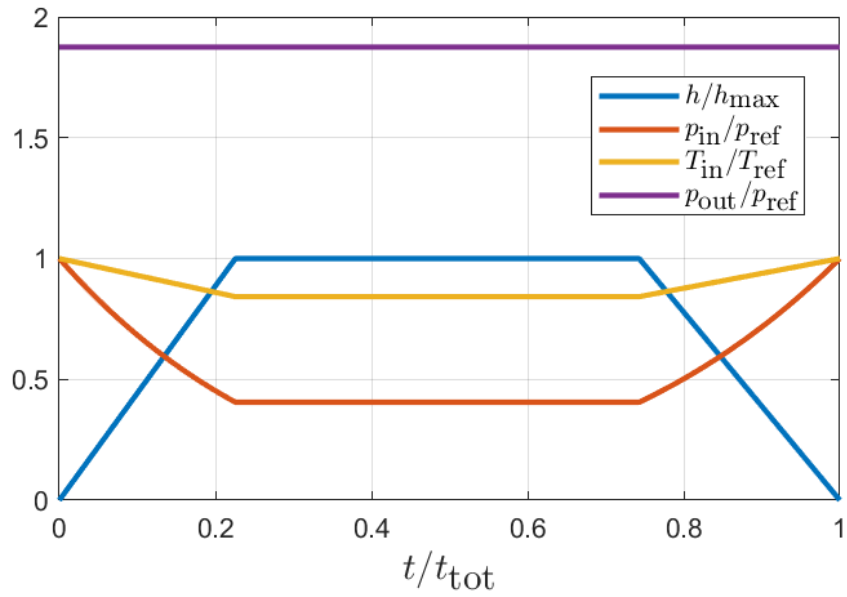


Figure 3.12: Trend of compressor inlet and outlet pressure and compressor inlet temperature during the mission.

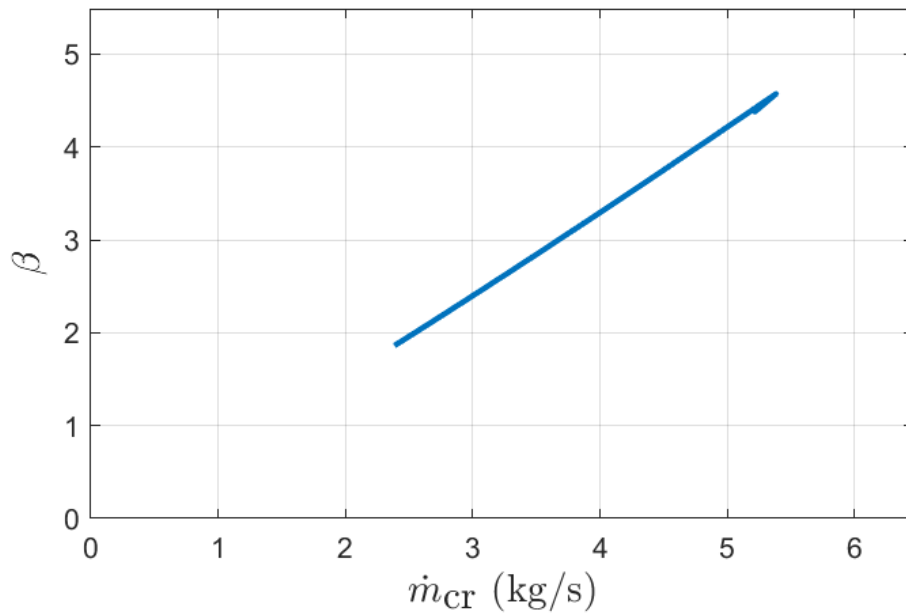


Figure 3.13: Trend of compressor working line during the mission.

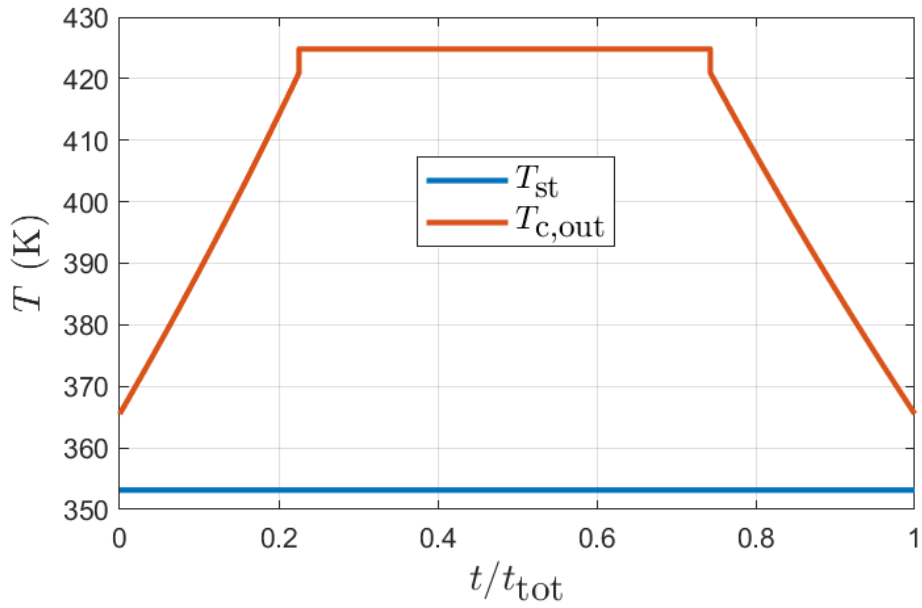


Figure 3.14: Trend of compressor outlet temperature during the mission for architecture with turbocharger system.

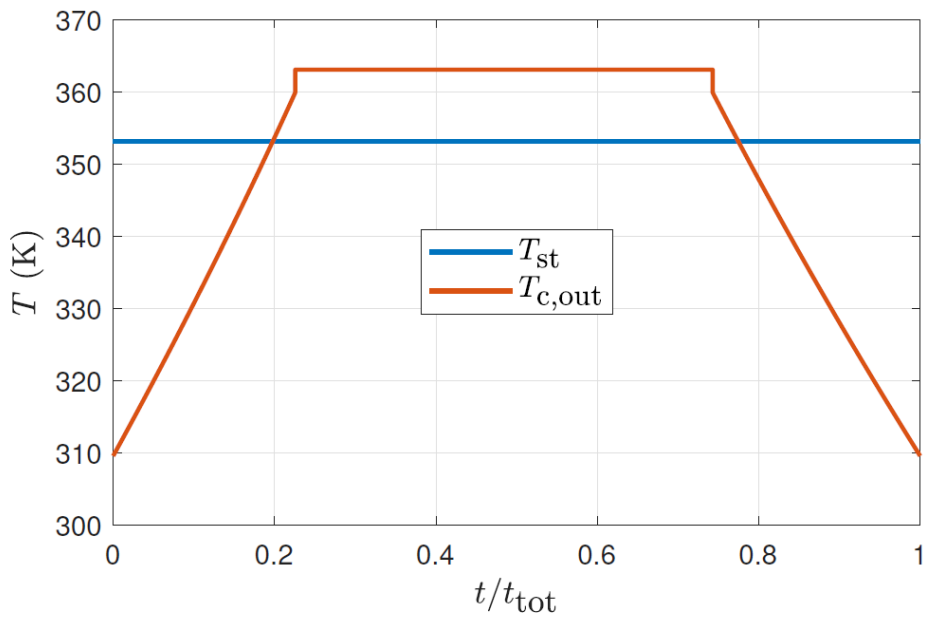


Figure 3.15: Trend of compressor outlet temperature during the mission for architecture without turbocharger system.

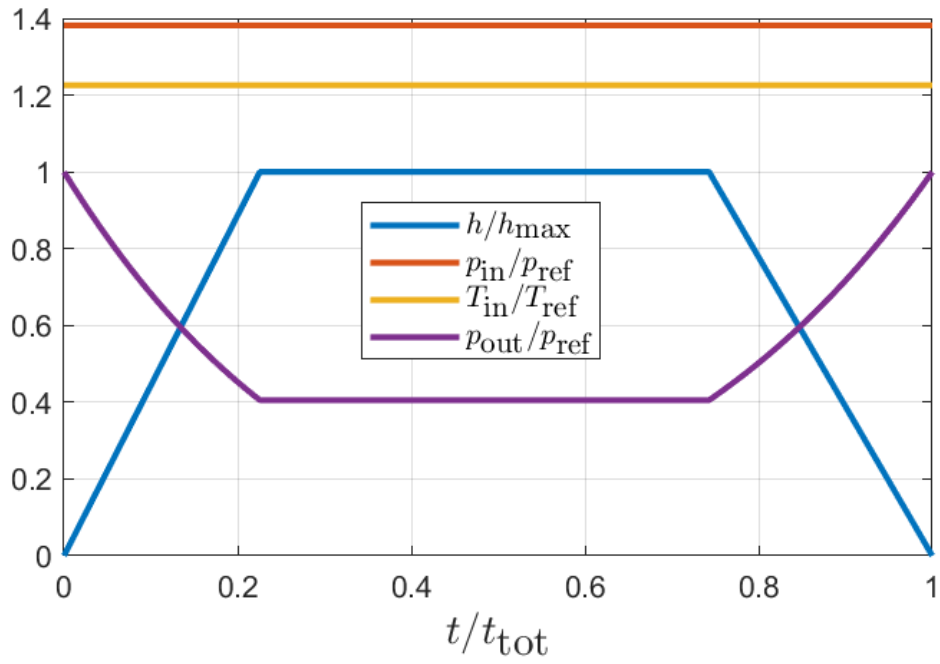


Figure 3.16: Trend of turbine inlet and outlet pressure and turbine inlet temperature during the mission.

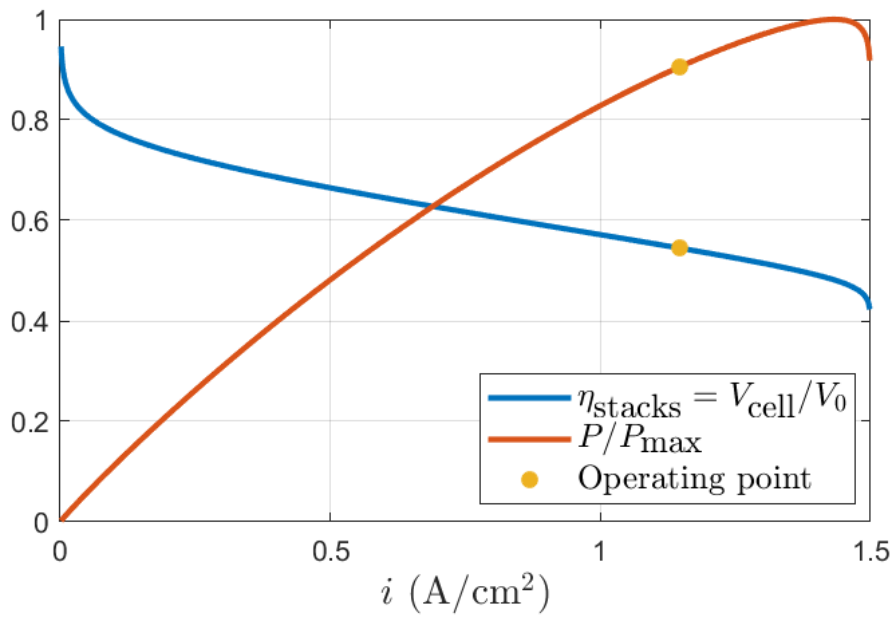


Figure 3.17: FC stacks stable operating point.

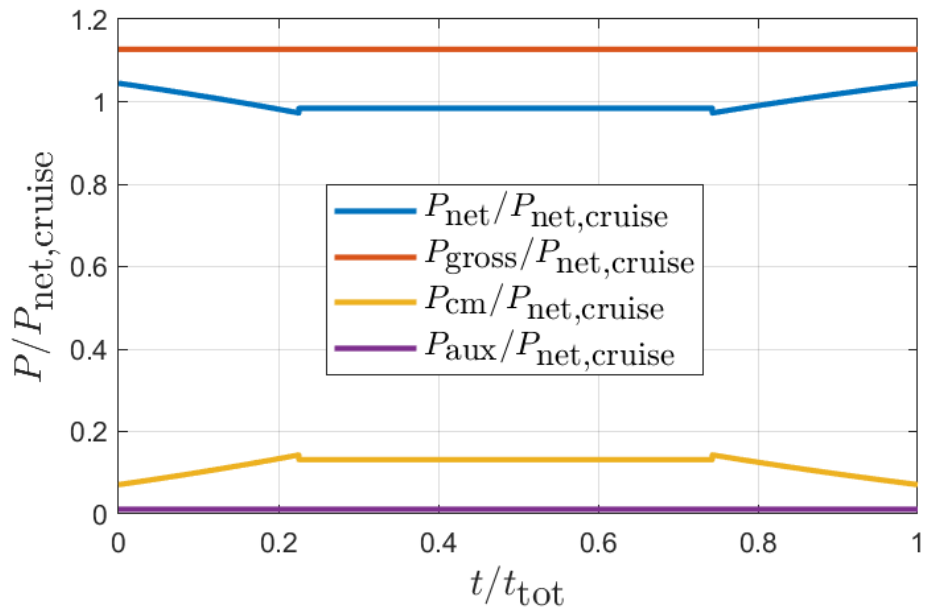


Figure 3.18: Trend of the power terms along the mission.

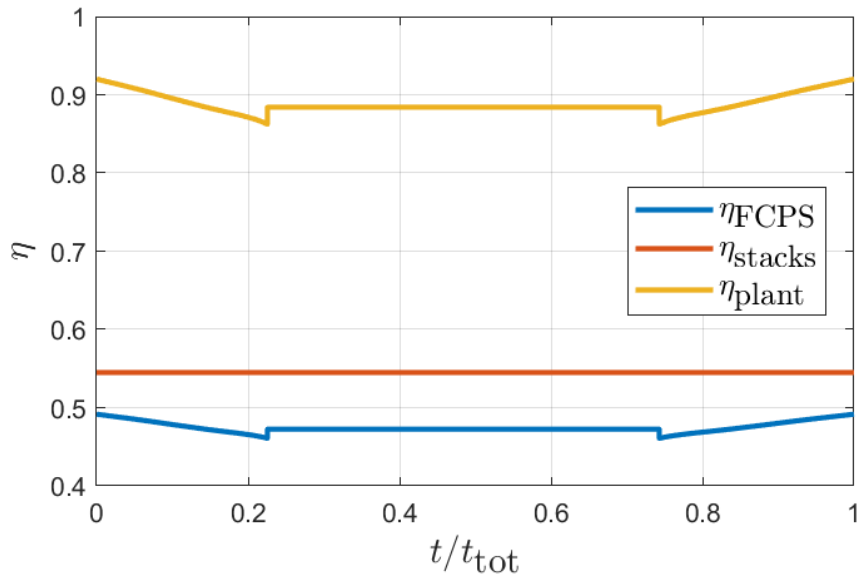


Figure 3.19: Trend of the system efficiencies along the mission

4 Sizing

4.1 Scaling method

In this chapter, an extensive overview is provided on the concepts of dimensional analysis and fluid dynamics similarity applied to turbomachinery.

These concepts are fundamental for the selection and preliminary design process of turbomachinery and will be used as support in the selection and sizing process of the compressor and turbine in this thesis work. This approach allows for the transfer of performance results obtained from an existing machine with known characteristics, considered as a reference model, to a new machine that needs to have similar characteristics to the base one.

In practice, the theory of similarity offers an efficient method to adapt and apply proven solutions in the field of turbomachinery, thereby simplifying the design process for new machines. This approach maximizes the utilization of previous knowledge and accelerates the development of optimal solutions for turbomachinery [25].

4.1.1 Dimensional analysis

In general, it is possible to describe a physical phenomenon based on the physical phenomena that influence it and have specific dimensions. Dimensional analysis allows for simplifying the description of the phenomenon by reducing the number of parameters through the use of "dimensionless" parameters obtained by a suitable combination of dimensional parameters [25].

Dimensional analysis represents a fundamental approach in engineering to simplify complex physical problems, enabling a deeper understanding and more efficient quantitative response. At its core lies the concept of similarity, which refers to the possibility of establishing a connection between different phenomena. For instance, considering a full-scale aircraft and a scaled-down model, under specific conditions, a direct relationship can be identified between the forces acting on both. By employing mathematical tools, similarity entails a transformation of the variables involved, reducing the number of independent factors characterizing the problem [26].

At the core of dimensional analysis lies the Buckingham's theorem, also known as the Π theorem. This theorem is based on the concept of dimensional homogeneity and asserts that it is possible to reduce any physical equation to an appropriate dimensionless form, i.e., one that does not depend on units of measurement[26]

Given a general dimensional equation:

$$F(x_1, x_2, \dots, x_n) = 0 \quad (4.1)$$

F depends on n physical parameters, where the n parameters are characterized by k independent fundamental quantities. It is possible to reduce the equation by expressing it through $n - k$ dimensionless groups indicated as Π_i .

$$F(\Pi_1, \Pi_2, \dots, \Pi_{n-k}) = 0 \quad (4.2)$$

The Buckingham's theorem allows us to determine the number of dimensionless groups that can be formed; however, it does not indicate how they can be constructed or provide information about the analytical form of the function F.

Indeed, it is well known that the creation of dimensionless groups on which the function F can depend does not have a definitive solution.

Ferrari [27] states that the construction of dimensionless groups is a task that requires a deep understanding of the physical phenomenon, along with a good amount of sensitivity and experience. It is necessary to experiment with different approaches before finding the optimal solution, that is, the one that allows the creation of dimensionless groups that are highly relevant from a physical perspective for the analysed phenomenon.

4.1.2 Fluid Dynamics Similarity

The concepts in this paragraph refer to Professor Claudio Dongiovanni's slides from the Machines course at the Politecnico di Torino [28]. Through similarity analysis, it is possible to predict the performance of an object, specifically a machine, using information regarding a similar object but operating under different conditions. To achieve this objective, it is necessary for the main equations describing the involved phenomena to have a common solution. However, this statement is theoretically valid only if the conditions of geometric, kinematic, dynamic, and thermal similarity are satisfied. Geometric similarity occurs when two objects have dimensions along the Cartesian axes with an equal linear ratio between them.

Geometric similarity is a fundamental requirement for achieving kinematic similarity, which pertains to the motion of objects. Kinematic similarity occurs when two objects have similar elements that occupy the same positions simultaneously.

On the other hand, dynamic similarity is based on the equality of ratios between forces, masses, and energies of the two objects and is constrained by geometric and kinematic similarities.

Thermal similarity requires that the temperature fields in the two objects are the same, and it also presupposes geometric similarity as a necessary condition to be fulfilled. To achieve thermofluid-dynamic similarity, all four similarities need to be satisfied; however, this condition is ideal and cannot be fully realized in practice.

On the other hand, fluid-dynamic similarity is attained by verifying only geometric, kinematic, and dynamic similarities.

4.1.3 Scaling laws

The objective of this section is to find laws that allow for sizing a turbomachinery, both turbine and compressor, starting from a base turbomachinery whose characteristics and performance map are known. This is achieved by leveraging the concepts of fluid-dynamic similarity and dimensional analysis discussed in the previous paragraphs, applying them to turbomachinery.

This approach proves highly advantageous in generating performance maps of sized turbomachinery, which can be easily integrated into dynamic models. By using the maps and

characteristic data of known turbomachinery as a basis, it is possible to scale such information according to the specific requirements of the project.

As mentioned in the previous section, the performance of a series of compressors and turbines with similar geometries, in terms of pressure ratio and efficiency, can be described using dimensionless groups, also known as similarity variables. These variables are derived from the combination of geometric and operational parameters that define a particular turbomachinery[29].

In this section, the classical principle of similarity, also known as the Π theorem, is applied to turbomachinery [29].

The first step in applying the principle of similarity is choosing the appropriate dimensional quantities that govern the problem under consideration.

This section on the construction of dimensionless groups is based on the works of Lakshminarayana B [30] and Dufour G, Carbonneau X [29].

The performance of a turbomachinery, including compressors, pumps, and turbines, can be represented by the following functions:

$$\beta^\circ = \beta^\circ(\dot{m}, n, p_{in}, T_{in}, \gamma, R, \mu, D, l_1, l_2) \quad (4.3)$$

$$\eta^\circ_{is} = \eta^\circ_{is}(\dot{m}, n, p_{in}, T_{in}, \gamma, R, \mu, D, l_1, l_2) \quad (4.4)$$

Where subscript “ $^\circ$ ” denotes the total quantities.

The dimensional quantities describing the phenomenon are divided into geometric variables, related to operational conditions and fluid properties.

The geometric variables are D , the diameter; l_1 , the blade height; and l_2 , the chord length.

The fluid properties are R , the universal gas constant; μ , the kinematic viscosity; and γ , the specific heat ratio.

The properties related to operational conditions are: \dot{m} , the mass flow rate of the fluid through the turbomachinery; T_{in} and p_{in} , the properties of the fluid at the inlet of the turbomachinery, namely the inlet temperature and pressure; and n , the rotational speed of the turbomachinery.

R and T_{in} are combined into a single dimensional group, RT_{in} , because they are the only variables dependent on temperature, yielding:

$$\beta^\circ = \beta^\circ(\dot{m}, n, p_{in}, RT_{in}, \gamma, \mu, D, l_1, l_2) \quad (4.5)$$

$$\eta^\circ_{is} = \eta^\circ_{is}(\dot{m}, n, p_{in}, RT_{in}, \gamma, \mu, D, l_1, l_2) \quad (4.6)$$

The fundamental units of measurement, independent of each other, are mass, length, and time, indicated as:

Mass=(M); Length=(L); Time=(t).

Therefore, the dimension of the dimensional groups is as follows:

$$p_{in} = [ML^{-1}t^{-2}]; R = \frac{p}{\rho T} = [L^2t^{-2}\theta^{-1}]; \dot{m} = [Mt^{-1}]; \quad (4.7)$$

$$T_{in} = [\theta^{-1}]; n = [t^{-1}]; D, l_1, l_2 = [L]; \quad (4.8)$$

For the equation (4.3), the function f that describes the properties of turbomachinery through dimensionless parameters can be written as:

$$0 = f(\dot{m}, n, p_{out}, p_{in}, RT_{in}, \gamma, \mu, D, l_1, l_2) \quad (4.9)$$

As stated in the previous paragraph, the Buckingham's theorem states that if a phenomenon described by a dimensional equation is characterized by n variables and k independent fundamental quantities, in the present case being length L , mass M , and time T , the equation can be expressed by $n-k$ dimensionless groups.

By using the Buckingham's theorem, the following dimensionless groups are derived:

$$\Pi_1 = \frac{p_{out}}{p_{in}}; \Pi_2 = \frac{\dot{m}\sqrt{RT_{in}}}{p_{in}D^2}; \Pi_3 = \frac{nD}{\sqrt{\gamma RT_{in}}}; \Pi_4 = \gamma; \quad (4.10)$$

$$\Pi_5 = \frac{l_1}{D}; \Pi_6 = \frac{l_2}{D}; \Pi_7 = \frac{ND^2 p_{in}}{\mu RT_{in}}; \quad (4.11)$$

Therefore, the performance of the turbomachinery is represented by the following equations:

$$0 = f\left(\frac{p_{out}}{p_{in}}, \frac{\dot{m}\sqrt{RT_{in}}}{p_{in}D^2}, \frac{nD}{\sqrt{\gamma RT_{in}}}, \gamma, \frac{ND^2 p_{in}}{\mu RT_{in}}, \frac{l_1}{D}, \frac{l_2}{D}\right) \quad (4.12)$$

In a similar manner, the following relationship is determined:

$$0 = f\left(\eta^{\circ}_{is}, \frac{\dot{m}\sqrt{RT_{in}}}{p_{in}D^2}, \frac{nD}{\sqrt{\gamma RT_{in}}}, \gamma, \frac{ND^2 p_{in}}{\mu RT_{in}}, \frac{l_1}{D}, \frac{l_2}{D}\right) \quad (4.13)$$

If we consider two machines in fluid dynamics similarity, they are geometrically similar, so the ratios $\frac{l_1}{D}$ and $\frac{l_2}{D}$ are constant and can be simplified.

$$\frac{p_{out}}{p_{in}} = f\left(\frac{\dot{m}\sqrt{RT_{in}}}{p_{in}D^2}, \frac{nD}{\sqrt{\gamma RT_{in}}}, \gamma, \frac{ND^2 p_{in}}{\mu RT_{in}}\right) \quad (4.14)$$

$$\eta^{\circ}_{is} = f\left(\frac{\dot{m}\sqrt{RT_{in}}}{p_{in}D^2}, \frac{nD}{\sqrt{\gamma RT_{in}}}, \gamma, \frac{ND^2 p_{in}}{\mu RT_{in}}\right) \quad (4.15)$$

The last dimensionless group represents the Reynolds number, $Re = \frac{ND^2 p_{in}}{\mu RT_{in}}$, which represents the ratio of inertial forces to viscous forces.

Considering that the two machines operate with the same fluid, the parameters γ , R e μ can also be simplified, resulting in:

$$\frac{p_{out}}{p_{in}} = f\left(\frac{\dot{m}\sqrt{T_{in}}}{p_{in}D^2}, \frac{nD}{\sqrt{T_{in}}}, Re\right) \quad (4.16)$$

$$\eta^{\circ}_{is} = f\left(\frac{\dot{m}\sqrt{T_{in}}}{p_{in}D^2}, \frac{nD}{\sqrt{T_{in}}}, Re\right) \quad (4.17)$$

The quantities of the dimensionless groups can be combined into the values of corrected flow rate and corrected velocity used in performance maps, which are typically calculated as:

$$\dot{m}_{cr} = \frac{\dot{m}\sqrt{T_{in}/T_{ref}}}{p_{in}/p_{ref}} \quad (4.18)$$

$$n_{cr} = \frac{n}{\sqrt{T_{in}/T_{ref}}} \quad (4.19)$$

For the theorem to be valid, it is necessary for all similarity variables to be exactly the same. However, it is known that the effects of Reynolds number can be negligible if the range of variation is not excessively wide [29]. Generally, turbomachinery is characterized by the presence of fully turbulent flows, with a Reynolds number (Re) greater than 10^6 . Under these conditions, it can be assumed that the effects of Reynolds number on performance are negligible (for very high Re , losses due to friction depend solely on surface roughness) [25].

According to these assumptions, if only Π_1 e Π_2 remain constant, it can be considered that the two turbomachines have similar performances. The assumption of neglecting the effects of Reynolds number is referred to as partial similarity assumption, and the following equations are obtained:

$$\frac{p_{out}}{p_{in}} = f\left(\frac{\dot{m}_{cr}}{D^2}, n_{cr}D\right) \quad (4.20)$$

$$\eta^{\circ}_{is} = f\left(\frac{\dot{m}_{cr}}{D^2}, n_{cr}D\right) \quad (4.21)$$

Considering two turbomachines in fluid dynamic similarity, we can therefore obtain that:

$$\frac{\dot{m}'_{cr}}{D'^2} = \frac{\dot{m}''_{cr}}{D''^2} \rightarrow \frac{\dot{m}'_{cr}}{\dot{m}''_{cr}} = \left(\frac{D'}{D''}\right)^2 \quad (4.22)$$

$$n'_{cr}D'^2 = n''_{cr}D''^2 \rightarrow \frac{n'_{cr}}{n''_{cr}} = \frac{D''}{D'} \quad (4.23)$$

If these equality conditions are satisfied, then the compressors exhibit the same performance in terms of pressure ratio and efficiency.

$$\beta^{o'} = \beta^{o''} \quad (4.24)$$

$$\eta^{o'} = \eta^{o''} \quad (4.25)$$

The scaling laws (4.22) and (4.23) derived from dimensional analysis for two turbomachines in fluid dynamic similarity, which form the basis of the compressor and turbine sizing process used in the turbocharger, are applied in several research works. Among these, the studies by Liu et al. [31], Bao et al. [17], Uhrig et al. [16], Tancrez et al. [32], and Lee B.[33] are mentioned.

In the context of this thesis, the mentioned scaling laws constitute the foundation of the sizing process for both the compressor and the turbine used in the turbocharger. Starting from a base turbomachine, whose performance is known, it can be appropriately resized or scaled using a scaling factor specifically identified to achieve the desired results.

The scaling laws are thus employed to determine the scaling factor required to meet a specific requirement requested from the design standpoint.

4.2 Turbocharger sizing procedure

A parametric model has been developed on the Matlab platform to automate the sizing of the turbocharger based on design parameters.

In this paragraph, the static sizing procedure used for the turbocharger is described. This procedure is based on the application of scaling laws derived from fluid dynamic similarity and dimensional analysis, as presented in the previous paragraph.

This procedure allows for leveraging technical data and performance maps of turbomachines available in the market and easily obtaining new data and performance maps for use in dynamic model simulations, enabling rapid and effective integration between static and dynamic models.

Both the selection of the base turbine and compressor is done through a specifically built database that contains all the characteristics of the machines provided by suppliers (e.g., geometry, dimensions, performance maps, technical data, etc.), which will be described in detail later. Within this database, machines that maximize efficiency according to the required design specifications are chosen.

The selected machines represent the base models that will be subsequently resized using scaling laws, depending on the project requirements. In this way, fluid dynamically similar turbomachines are obtained compared to the base models, maintaining the same performance but with a different size, capable of meeting the specific requirements of the design point.

What is described in this paragraph is the so-called turbomatching process [34], which involves selecting the compressor and turbine that can be coupled according to the project specifications.

It is a delicate operation that requires careful consideration of the conditions and requirements that both components must meet.

The turbine harnessed the exhaust energy from the fuel cell stack, leading to a decrease in the power consumption of the compressor motor. The turbomatching process therefore differs from that used for turbochargers in internal combustion engines and these three conditions must be met [35]:

1. Since the turbine, compressor and electric motor are mounted on the same shaft, they must rotate at the same rotational speed [35]

$$N_t = N_c = N_m \quad (4.26)$$

In the case of a serial booster-type architecture, the engine is not linked to the same shaft as the compressor, and therefore the following applies:

$$N_t = N_c \quad (4.27)$$

2. As mentioned earlier in Chapter 3, where the performance analysis model is presented, the law of conservation of mass must be followed if stationary conditions and no air accumulation are assumed. This means that the airflow entering the turbine, \dot{m}_{exh} , must be the same as the airflow exiting the compressor, $\dot{m}_{a,ca,in}$, minus the amount of oxygen used during the cathode reaction in the fuel cell stack[35].

$$\dot{m}_{exh} = \dot{m}_{a,ca,in} - \dot{m}_{o_2,reacted} \quad (4.28)$$

3. According to the principle of energy conservation, the power generated by the turbine must be equal to the power required by the compressor minus the power generated by the electric motor[35].

$$P_t = P_c - P_m \quad (4.29)$$

The turbocharging system needs to be coupled to the fuel cell stack while maintaining good efficiency across all flight conditions [35], in fact, the operating points in terms of pressure ratio, mass flow rate, and inlet temperature at which the two components operate depend on the characteristics and specifications required by the fuel cell, as well as external environmental conditions, which are dependent on flight conditions[36].

Both the turbine and the compressor need to be designed to operate at high efficiency at the operating points that adhere to the described conditions.

4.2.1 Project requirements and plant configuration

Before proceeding with the sizing process of an air supply system for an FC power system, it is necessary to consider two fundamental aspects[13]:

- Definition of project requirements
- Selection of the plant configuration

Regarding the first aspect, the sizing process of the compression system is carried out in order to meet the requirements of the design point, which is chosen as the most critical operating point for the air supply system, namely the cruise point. This point also represents the predominant phase of the aircraft's flight mission in terms of duration.

The cruise point is the most critical flight condition as it requires the maximum compression ratio. It is required, in fact, that the air pressure supplied to the FC stack remains constant, maximizing the performance of the FCPS, while the inlet pressure depends on ambient conditions. Since the cruise altitude represents the maximum height, the aircraft needs to reach, the inlet pressure will be as low as possible.

A crucial design objective is to ensure high performance along with an adequate stability margin during this critical phase.

The requirements for the air supply system were discussed at length in the presentation of the air supply system performance analysis model in section 3.1.3.

They include the flow rate of dry air at the turbine inlet, \dot{m}_{exh} , its temperature $T_{t,in}$ and pressure, $p_{t,in}$ as well as the pressure at the turbine outlet $p_{t,out}$. For the compressor, the design requirements include the air flow rate at the compressor inlet, \dot{m}_a , which is that required to supply the fuel cell stack, as well as the inlet pressure, $p_{c,in}$, and temperature, $T_{c,in}$, and the outlet pressure, $p_{c,out}$, at which the compressor must compress the air.

All these quantities, calculated in the cruise condition, constitute the design requirements that must be met for the static design of the air supply system.

About the choice of plant configuration, as mentioned in Chapter 2, the two architectures, Electric turbocharger type and serial booster type, shown in the figures 2.2 and 2.3 were considered.

Static dimensioning was carried out with both configurations and a comparison was made to determine the best solution for the case under consideration; the design strategies for both architectures are presented in the paragraphs 4.2.2 and 4.2.3.

In addition, it is possible to consider, as a first estimate, the use of a parallel configuration for the network of turbo-compressors feeding the fuel cell.

According to an analysis carried out in Federico Fasiello's thesis work [13], the starting point for this thesis, in fact, this system is the most convenient for achieving a reduction in the size of the compression system.

This involves several parallel turbo-compression lines, each serving a group of fuel cell stacks. Based on the examination performed by Federico Fasiello regarding the case study under consideration in this research, a fuel cell power system (FCPS) consisting of three identical power units has been taken into account.

Each power unit is supported by an independent air supply system. In this context, it is assumed that the total required mass flow rate for the entire system is evenly divided among the various compression lines, as shown in the figure 4.1.

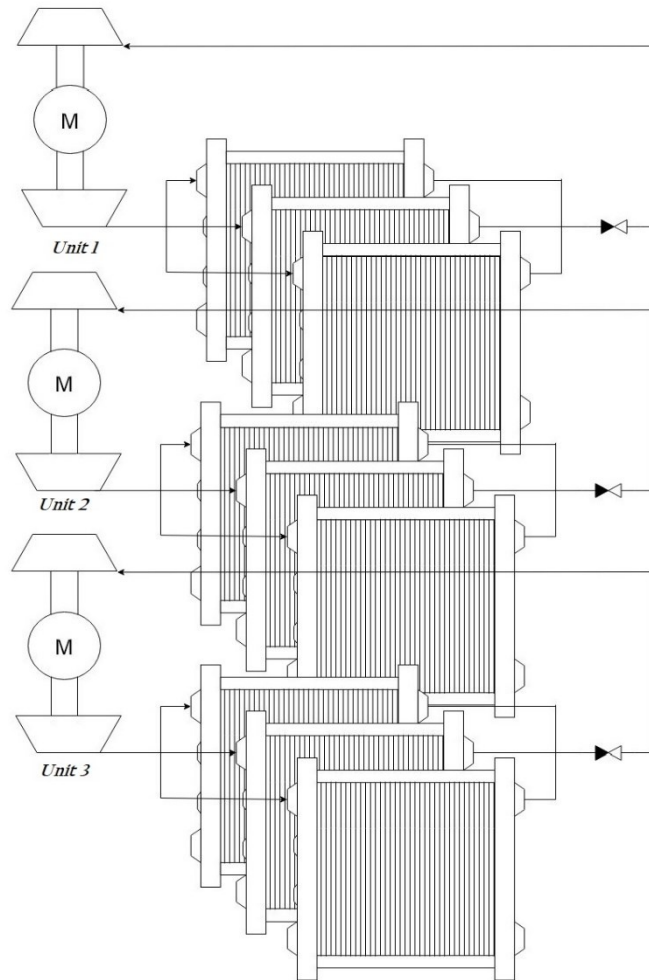


Figure 4.1: Parallel architecture for FCPS.

4.2.2 Turbomatching procedure for electric turbocharger (e-turbo) architecture

The matching procedure for the turbocharger inserted in the electric turbocharger architecture is shown in the flowchart in figure 4.2.

The process begins with the input requirements for the turbine and compressor, which are mounted on the same shaft.

The compressor sizing procedure, which includes the selection of the base compressor to be adapted and the subsequent scaling, is described in detail in chapter 4.2.4; to apply it, it is necessary to know the compression ratio and dry air flow required by the project.

Knowing the compression ratio that the compressor must provide, entered as input, the compressor with the best efficiency for that specific compression ratio is selected from the database.

At this point, knowing also the dry air flow required by the fuel cell stack, which is also an input requirement, it is possible to find the scaling factor of the compressor by means of the scaling laws described in section 4.1.3 and to scale the chosen compressor in the selection process; the procedure for selecting and scaling the base compressor with the best efficiency is described in detail in section 4.2.4.

The compressor scaling process returns as output the value of the efficiency of the chosen compressor (i.e. the maximum among the efficiencies found, for all compressors in the database, for

the considered design point), the scaling factor and the value of the rotational speed at which the compressor rotates for the considered design point; the rotational speed can be obtained through the appropriately scaled compressor performance map while the efficiency is equal to that of the base compressor as this does not vary during the scaling process.

As mentioned earlier, the rotational speed of the turbine will have to be the same as that of the compressor since they are fitted on the same shaft.

As input to the sizing of the turbine there are therefore the flow rate of dry pressurised air leaving the fuel cell and the expansion ratio which are assigned as requirements and the rotation speed which is found by the compressor sizing process; knowing therefore the speed and flow rate at which the turbine must work for the required expansion ratio, it is possible to find the scaling factor, so as to maximise efficiency, for each turbine in the database.

Of all the turbines scaled in the database, the one with the highest efficiency is then chosen.

The sizing process for the turbine is explained in detail in section 4.2.5.

Following the sizing of the turbocharger, it is possible to calculate the power absorbed by the compressor and the power generated by the turbine using formulae 3.14 and 3.15; the power required by the electric motor can then be calculated as the difference between the two powers divided by the electromechanical efficiency of the engine according to 3.23.

The design requirements for the electric motor are the torque and rotational speed it must provide; being keyed to the same shaft as the turbocharger it will have the same rotational speed, while torque is calculated as the ratio of power to rotational speed.

The motor sizing process is described in Federico Fasiello's thesis[13].

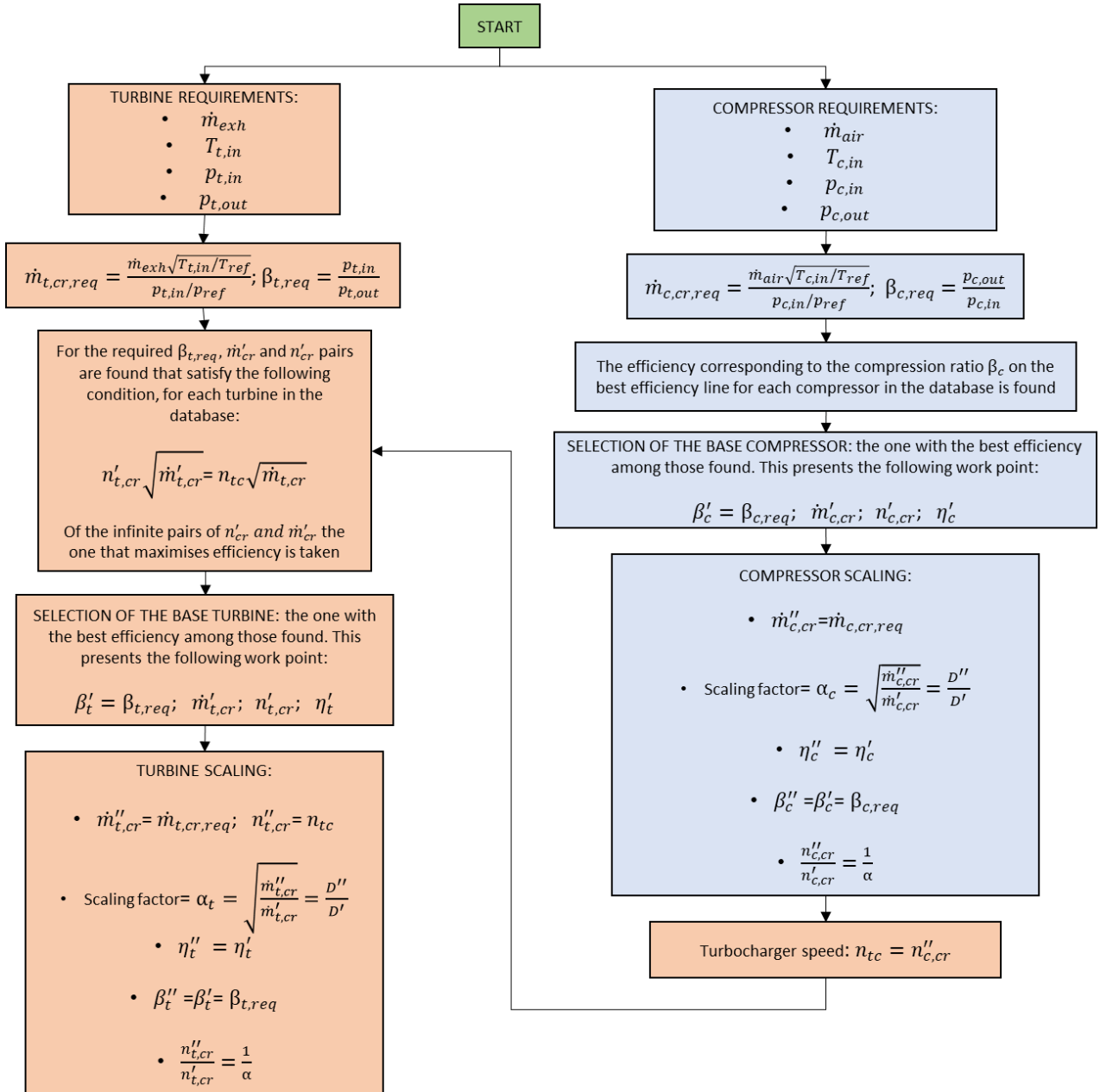


Figure 4.2: The matching procedure for the electric turbocharger architecture

4.2.3 Turbomatching procedure for serial booster architecture

In the serial booster architecture, the required compression ratio is divided into two compressors, one of which is completely fed by the turbine while the second is powered by the electric motor. The first compressor sucks in air from the external environment at the atmospheric pressure and temperature $p_{c,in}$ and $T_{c,in}$ and performs an initial compression; the air will then be sucked in by a second compressor, which must bring it up to the desired pressure $p_{c,out}$, which is the operating pressure of the fuel cell.

The design requirements for this architecture are illustrated in figure 4.3, it highlights the difference between the requirements of the first and second compressor. In particular, it can be seen that the

value of the output pressure of the first compressor is not an a priori known requirement but is a design degree of freedom.

The compression ratio performed by the first compressor and, consequently, the outlet pressure of the first compressor, in fact, is a parameter determined during the sizing process and is calculated in such a way as to utilize, through the turbine, the maximum enthalpy energy of the pressurized air exiting the stack.

In fact, the first compressor is powered by the turbine, which harnesses the energy of the air exiting the stack. The maximum achievable compression ratio of the first compressor can be calculated using a power balance equation [34]. Since the turbine and compressor are on the same shaft, the power absorbed by the compressor will be equal to the power generated by the turbine.

The two powers are calculated using the following expressions [20]:

$$P_t = \eta_{is,t} \dot{m}_{exh} c_p T_{exh}^{\circ} \left(1 - \beta_t^{\frac{k-1}{k}} \right) \quad (4.30)$$

$$P_{1,c} = \eta_{is,t} \dot{m}_a c_p T_{1,c,in}^{\circ} \left(\beta_{1,c}^{\frac{k-1}{k}} - 1 \right) \quad (4.31)$$

Where β_t is the turbine expansion ratio and β_c is the compression ratio of the compressor. calculated as:

$$\beta_t = \frac{p_{t,out}}{p_{t,in}} \quad (4.32)$$

$$\beta_{1,c} = \frac{p_{1,c,out}}{p_{1,c,in}} \quad (4.33)$$

By equating the two powers $P_t = P_{1,c}$ it is possible to determine the maximum achievable compression ratio of the first compression stage, effectively utilizing all the energy of the air exiting the fuel cell through the turbine:

$$\beta_{1,c} = \left(\frac{\eta_{is,c} \eta_{is,t} \dot{m}_{exh} c_p T_{exh}^{\circ} \left(1 - \beta_t^{\frac{k-1}{k}} \right)}{\dot{m}_a c_p T_{1,c}^{\circ}} + 1 \right)^{\frac{k}{k-1}} \quad (4.34)$$

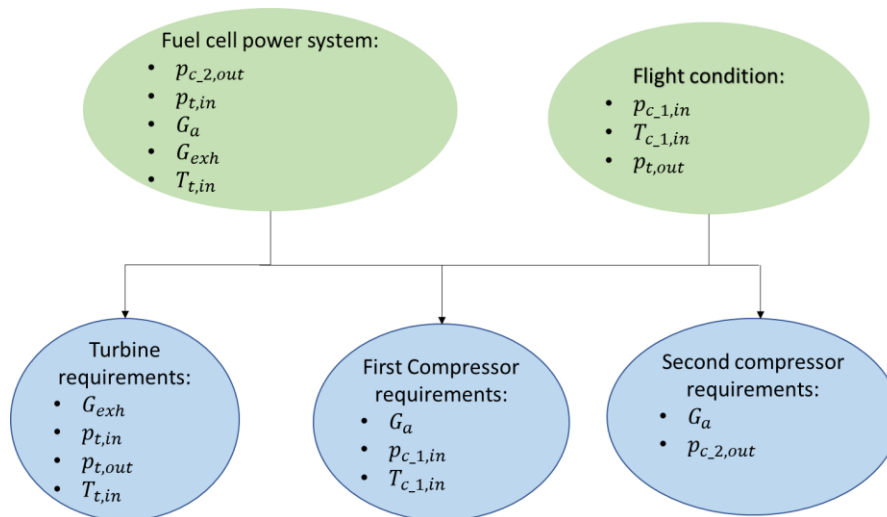


Figure 4.3 design requirements for serial booster turbocharger

The turbomatching procedure for the turbocharger included in this architecture is more complex than in the case of the e-turbo precisely because the compression ratio is not a design requirement but is calculated during the dimensioning procedure through the balance of powers; the matching procedure is depicted in the flowchart shown in Figure 4.4.

The process begins with inputting the requirements for the turbine and compressor of the turbocharger, which are mounted on the same shaft.

The compressor sizing procedure remains the same as that of the electric-turbocharger architecture illustrated in section 4.2.4; to apply it, the required compression ratio and the dry air flow rate for the project need to be known.

The air flow rate \dot{m}_a is given as an input, while the compression ratio is the maximum achievable ratio determined through the power balance on the shaft between the turbine and compressor; thus, it is an unknown value that can be calculated using equation (4.34).

In equation (4.34), all parameters except for the isentropic efficiencies of the turbine and compressor are known input of the model. The isentropic efficiencies are incorporated into the model directly through their product $\eta_{is,c}\eta_{is,t}$, which appears in the numerator of the formula.

An initial value for the efficiency product is then inserted, assuming it to be the maximum achievable value. For radial compressors and turbines, the efficiency typically does not exceed 80%, so starting with a product value of 64% can be a reasonable choice, although a higher value can also be used.

This value of the efficiencies will be checked at the end of the sizing process and adjusted for iterations. It is important to note that by iteratively changing the value of the efficiency product, the achievable compression ratio of the first compressor will also change with each iteration.

Once the achievable compression ratio value is calculated, the compressor with the best efficiency for the determined compression ratio is selected from the database.

Knowing the required dry air flow rate that the compression system must deliver to the fuel cell, which is an input requirement, it is possible to determine the compressor scaling factor using the scaling laws described in section 3.1.3 and scale the selected compressor in the selection process.

From the compressor scaling process, the output includes the isentropic efficiency value of the compressor indicated as $\eta'_{is,c}$ (which remains constant during the scaling process compared to the base compressor value) and the rotational speed at which it operates for the considered design

point. Both values are obtained from the performance map of the sized and appropriately scaled compressor.

As mentioned earlier, the rotational speed of the turbine must be equal to that of the compressor since they are mounted on the same shaft.

The turbine sizing procedure is also the same as that used in the e-turbo architecture and it is explained in section 4.2.3.

As inputs to the turbine sizing, the requirements are the flow rate of pressurized dry air exiting the fuel cell and the expansion ratio.

The rotational speed is determined from the compressor sizing process. With the known required speed and flow rate for the desired compression ratio, it is possible to find the scaling factor that maximizes the efficiency for each turbine in the database.

Among all the scaled turbines in the database, the one with the highest efficiency is selected.

After the turbine sizing process, it is possible to determine the isentropic efficiency of the turbine indicated as $\eta'_{is,t}$.

By knowing the isentropic efficiencies of both the turbine and the compressor, it is checked that the absolute value of their product, subtracted from the initially assumed product, is approximately zero, meaning it is smaller than a very small value indicated as ϵ .

A smaller value of ϵ indicates a higher precision of the sizing process.

If the condition is satisfied, the sizing process for the turbine and the compressor is completed. Otherwise, the assumed product of efficiencies is decreased by a certain percentage, dependent on the error and the sign of the error, and the maximum achievable compression ratio for the compressor, referred to as β_c , is recalculated. The compressor and turbine sizing process are then implemented again. The process is repeated until the value of the product of isentropic efficiencies reaches convergence.

The airflow exiting the first compressor is subsequently directed to the second compressor, which is connected in series with the first compressor and powered by an electric motor.

the second compressor and the electric motor that powers it will be further sized in the subsequent step of the sizing.

The detailed explanation of their sizing procedure can be found in Federico Fasiello's thesis[13]

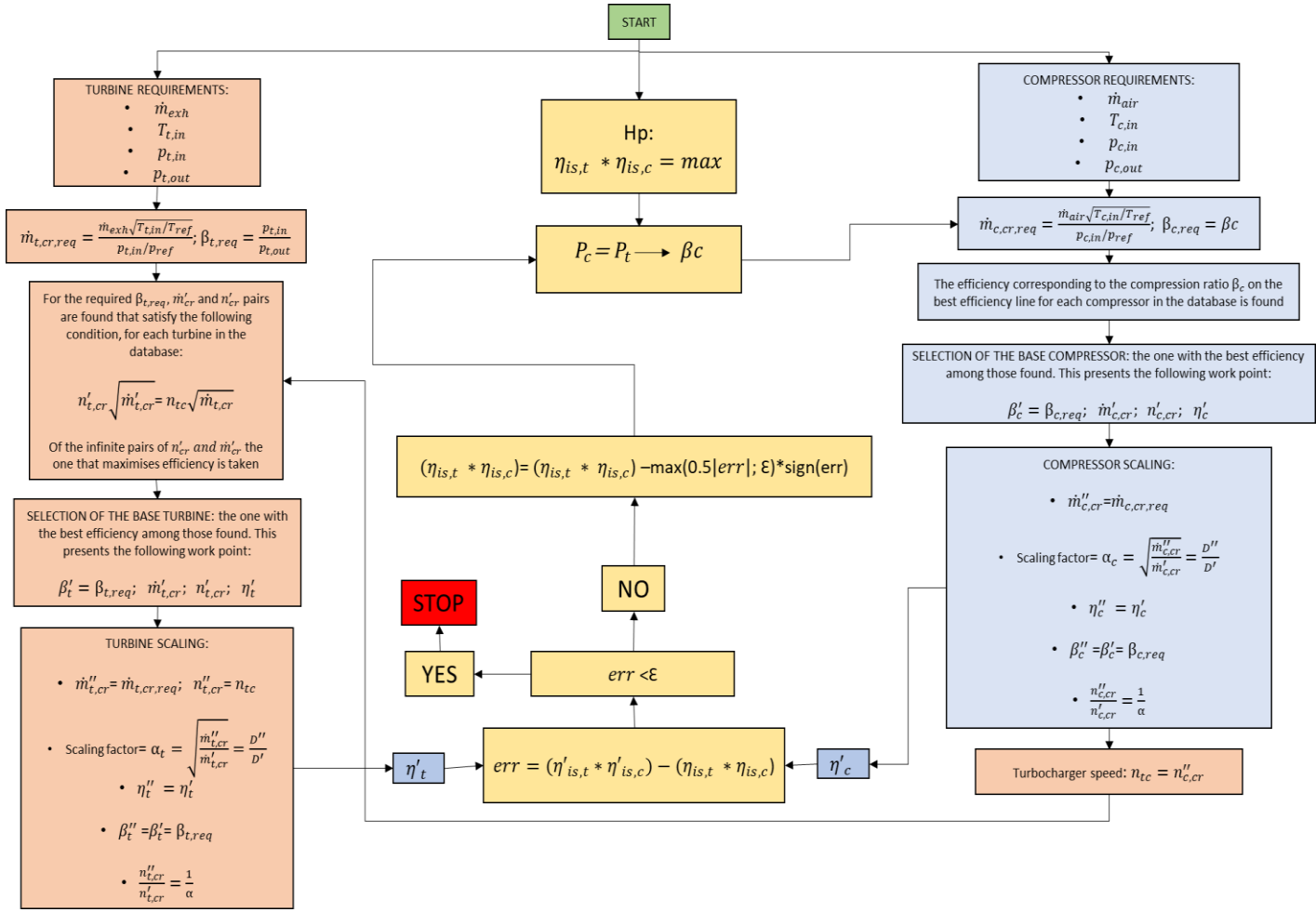


Figure 4.4: The matching procedure for serial booster architecture

4.2.4 Compressor sizing

This paragraph and the next describe in detail the compressor and turbine sizing procedures used in this thesis and presented in the previous paragraphs, these are the same for both architectures reported.

The compressor sizing procedure is well described in Federico Fasiello's thesis [13] and is based on the work of Dufour et al. [37]. This section will summarize its key points.

The sizing procedure for the compression system cannot be carried out without the preparation of a compressor database to be used as a baseline for compressor scaling. This database contains all the characteristic data and performance maps of commercial compressors obtained from suppliers. Within the database, potential candidate points are identified for each compressor to serve as references for the scaling process. These points lie on the maximum efficiency curve (BEL).

The BEL (Best Efficiency Line) represents the ideal position of the compressor on the performance map in terms of efficiency. For each compression ratio value, there is a corresponding operating point of the compressor on the best efficiency line.

After the scaling process, performed using scaling laws under the assumption of partial similarity, the pressure ratio and efficiency remain unchanged.

Therefore, in this process, the base compressor chosen as the reference for scaling is the one that exhibits the highest efficiency value among all compressors in the database for the desired compression ratio at the design point.

The selected compressor will then be scaled at the identified maximum efficiency point, referred to as the "point-to-be-scaled" (PTBS), and is denoted with a colon ‘

$$PTBS: \dot{m}'_{cr,PTBS}, n'_{cr,PTBS}, \beta'_{PTBS}, \eta'_{PTBS}$$

The PTBS selection procedure is shown in image 4.5.

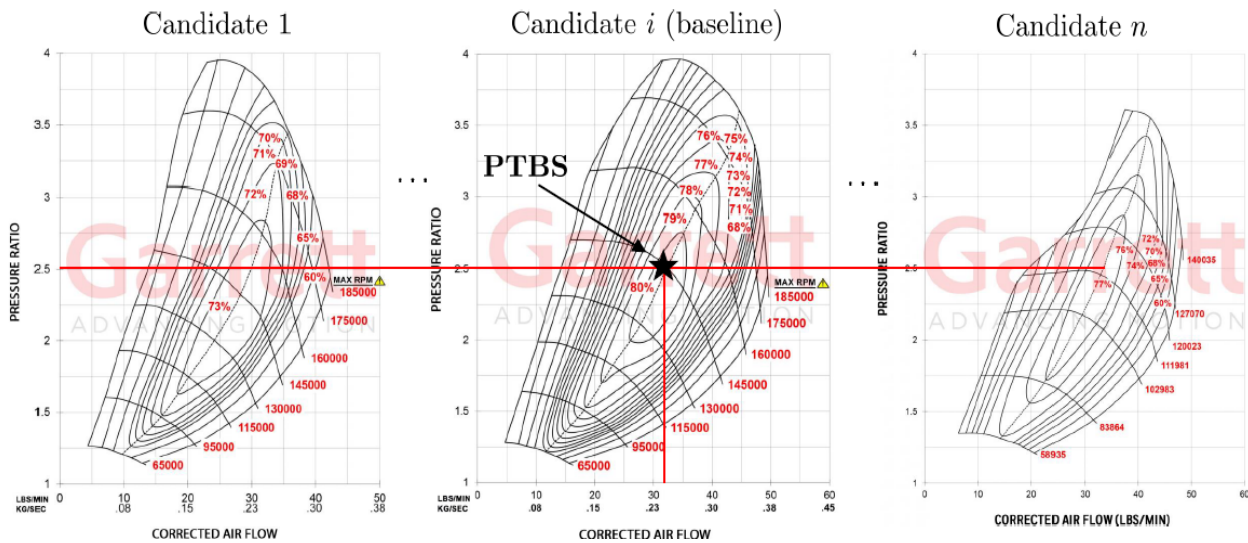


Figure 4.5 Representation of the compressor selection process[13], [38]

The scaling laws are applied to the PTBS to determine the geometric scaling factor that enables meeting the design requirements. It is determined how much the base compressor needs to be scaled, under the assumption of fluid dynamic similarity, to ensure the desired design requirements in terms of required airflow.

The scaling factor is the ratio between the characteristic quantities of the base compressor and the scaled compressor. Since the two compressors are geometrically similar, this ratio remains constant for all geometric quantities of the compressors[13].

Typically, the rotor's external diameter is used as the characteristic length, which is the inlet diameter for radial turbines and the outlet diameter for radial compressors[25]

$$\alpha = \sqrt{\frac{\dot{m}'_{cr}}{\dot{m}'_{cr,PTBS}}} \quad \frac{D''}{D'} = \alpha \quad (4.35)$$

In this context, the exponent ‘ is used to denote quantities related to the scaled configuration.

The scaled performance map is then determined by calculating all points in fluid dynamic similarity with those present in the original map. For each point in the original map, are applied the formulas described in the section 4.1.3, i.e. (4.22), (4.23), (4.24) and (4.25), to find the corresponding point on the scaled map.

4.2.5 Turbine sizing

In this thesis work, the turbine is sized downstream of the compressor because it is necessary for the turbine's rotational speed at the considered design point to be the same as that of the compressor since they are fitted on the same shaft.

The value of the turbocharger's rotational speed is therefore an output of the compressor sizing and an input for the turbine sizing. The other inputs are the dry air flow rate exiting the fuel cell stack and entering the turbine, and the total-to-static expansion ratio, defined as the ratio between the total pressure at the inlet and the static pressure at the outlet:

$$\beta_t^\circ = \frac{p_{t,in}^\circ}{p_{t,out}^\circ}, \text{ where the symbol } ^\circ \text{ indicates that the magnitudes refer to total properties.}$$

The same laws used for the compressor, described in section 4.1.3, also apply to the turbine.

After the scaling process, the expansion ratio and efficiency of the turbine at a point on the performance map remain the same as those of the base turbine map, provided that the assumptions of partial fluid dynamic similarity are met.

While the corrected mass flow rate and corrected speed scale according to the following formulas (4.22) and (4.23).

Unlike the compressor sizing process, in this case, both the corrected mass flow rate and the corrected speed at which the turbine must operate are known, in addition to the desired expansion ratio.

Therefore, an additional constraint must be satisfied in the scaling process compared to the compressor case.

By observing the scaling formulas (4.22), (4.23), (4.24), (4.25), it can be noted that both the scaling formulas for the corrected mass flow rate and the corrected rotational speed depend on the scaling factor. Thus, it is possible to establish a correspondence between them by following these steps:

$$\dot{m}_{cr}'' = \alpha^2 * \dot{m}_{cr}' \quad (4.36)$$

$$n_{cr}'' = \frac{n_{cr}'}{\alpha} \quad (4.37)$$

$$\alpha = \sqrt{\frac{\dot{m}_{cr}''}{\dot{m}_{cr}'}} \quad (4.38)$$

$$\frac{n_{cr}''}{n_{cr}'} = \sqrt{\frac{\dot{m}_{cr}'}{\dot{m}_{cr}''}} \quad (4.39)$$

$$n_{cr}' * \sqrt{\dot{m}_{cr}'} = n_{cr}'' * \sqrt{\dot{m}_{cr}''} \quad (4.40)$$

Where n_{cr}' e \dot{m}_{cr}' are the corrected rotational speed and corrected airflow rate of the base turbine, while n_{cr}'' e \dot{m}_{cr}'' are the values we want to achieve after the scaling process, i.e., the design inputs.

It is necessary to find the pair of values for n'_{cr} e \dot{m}'_{cr} for the base turbine that satisfy the equation (4.40), where n''_{cr} e \dot{m}''_{cr} are known. This equation is indeterminate, meaning it has infinite solutions. By fixing the expansion ratio equal to the design value, which will remain unchanged after the scaling process, there are infinite pairs of n'_{cr} e \dot{m}'_{cr} that satisfy the condition (4.40).

In other words, there are infinite scaling factors that allow sizing the turbine in such a way that it can operate under the required design conditions.

Among these pairs, the ones with the maximum efficiency are selected. It is important to note that in this sizing process, the turbine may not operate at maximum efficiency for the desired expansion ratio, as in the case of the compressor. Instead, the point on the turbine's performance map that satisfies the condition of the equation (4.40) and has the highest efficiency is chosen. This efficiency will remain the same after the scaling process.

The scaling procedure described is applied to all the turbines in the database, and subsequently, the turbine with the highest efficiency among them is selected.

If, at the end of the matching procedure, the turbine operates with low efficiency, it indicates that there is no turbine in the database that performs well under the considered design conditions. In such cases, it would be advisable to include new turbines in the database that are suitable for the specific requirements.

4.2.6 Sizing output, masses, and moments of inertia

Through the scaling of the turbine and compressor under the assumption of fluid dynamic similarity, it is also possible to make a preliminary assessment of two important design specifications: mass and moment of inertia of the turbomachinery.

These assessments are of fundamental importance for proper design. The accurate estimation of the mass of the turbocharger is particularly significant as it allows evaluating the impact of its weight on the system. Furthermore, such estimation enables meaningful assessments regarding changes in power density compared to the case of an air supply system without energy recovery.

On the other hand, estimating the moment of inertia of the machines is crucial for characterizing the rotor shaft dynamics during the dynamic simulation of the Fuel cell power system.

Under the assumption of fluid dynamic similarity between the scaled turbomachinery and the base machines, and considering that the material and, consequently, their density remain unchanged, the validity of the following relationships can be easily demonstrated:

$$\frac{m''}{m'} = \alpha^3 \quad (4.41)$$

$$\frac{I''}{I'} = \alpha^5 \quad (4.42)$$

In other words, the mass and moment of inertia of the compressor increase proportionally to the cube and fifth power of the geometric scaling factor [13]. The above assumption about density

brings further implications. First, it can be demonstrated that, while maintaining the same operating conditions, the stress field remains unchanged.

$$\sigma'' = \sigma' \quad (4.43)$$

As a result, scaling laws ensure the structural integrity of the compressor and turbine. Another significant result is related to the power density of turbomachines:

$$\frac{P''}{m''} \frac{m'}{P'} = \frac{1}{\alpha} \quad (4.44)$$

According to the above relationship, the power density increases proportionally to the inverse of the geometric scale factor. In other words, smaller machines with higher speed have higher power density [39].

4.3 Off-design validation

After sizing the components through the scaling process, it is necessary to validate the air supply system even under off-design conditions.

If the verification phase is not successfully passed, it is possible to consider changing the chosen base compressor and turbine, selecting others with different performance maps, or implementing a control system capable of avoiding the exceedance of stability limits.

The turbocharger is designed to operate at maximum efficiency during cruise, which is the longest flight phase, and also an energy-critical phase as the one requiring the highest compression ratio.

However, it is essential for the turbocharger, along with the entire air supply system, to be capable of operating in conditions outside of the design range, encompassing all other flight mission phases. Furthermore, it must be able to handle specific situations, thus ensuring stability under such circumstances.

4.3.1 Adjustment for off design

In off-design operating conditions of the air supply system in a fuel cell power system, the use of a turbocharging system requires the adoption of appropriate control devices to ensure proper integration with the fuel cell [4].

In fact, only at the design point, i.e., the cruising point, the turbine can work in perfect agreement with the fuel cell and the compressor, i.e., with the required air flow, expansion ratio and rotational speed, precisely because it has been designed to meet these requirements.

If the working conditions change, the system will find a new equilibrium point in which to work.

Other flight conditions, other than the cruise condition, also represent off-design points as the atmospheric properties of the air at different altitudes change; in fact, both the turbine and the compressor will have to work at a new point in their map while the fuel cell will always have to receive the same amount of air flow and at the same pressure, i.e. the operating pressure of the

stack. There will probably not be a point on the turbine map that works under the new conditions of air flow, expansion ratio and rotational speed (which must be the same as the compressor), in other words, the turbine will not be able to work with all three requirements at the same time. Therefore, the use of a control system is essential to modify the operating conditions of the turbine and move within the performance map.

In a fuel cell power system, it is not possible to fully recover all the enthalpy energy from the exhaust gases under off-design operating conditions. This means that it is not feasible to match the fuel cell stacks using only a fixed-geometry turbine [40].

The article by Uhrig et al. [16], as shown in Figure 4.6, presents three air supply system architectures used in the automotive sector. Case a) features an electric compressor that does not involve energy recovery in the turbine, while cases b) and c) respectively involve an electric turbocharger (ETC) and a serial booster (SB) that utilize the turbocharging system.

In all three cases, there is an initial throttle valve that controls the mass flow of released air. This allows for the control of the operating pressure of the system and, consequently, enhances the efficiency of the fuel cell.

For cases b) and c), where energy recovery through the turbocharger is present, a second valve is introduced to regulate the airflow entering the turbine. Both throttle valves exert pressure control.

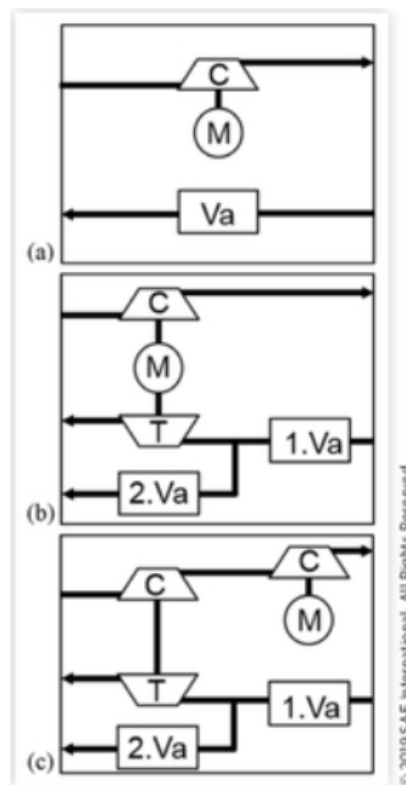


Figure 4.6: Different air supply system architectures with respective valve control modes [16]

The article by Zhang et al. [40] presents three different control systems for an air supply system's supercharging system in a fuel cell power system used in the automotive industry, as shown in Figure 4.7.

In Figure 4.7(a), a control system is employed using a turbine with a fixed-geometry stator that operates in coordination with a back-pressure control valve (BPV). The optimal operating condition of the fuel cell is defined as the turbine's design point. Under these conditions, the turbine is able to fully recover the exhaust energy from the fuel cell stack.

However, in other operating conditions, it is necessary to adjust the BPV to match the supercharging system to the fuel cell stack. The exhaust energy that is not recovered by the turbine is released directly into the environment through the BPV.

In figure 4.7(b), the turbine operates in synergy with a By-Pass Valve (BV). The BV, commonly known as a wastegate, is a widely used component in automotive turbochargers. It is a pressure-controlled valve designed to open at a specific predetermined pressure value, allowing the discharge of excess flow at pressures above that point.

In Figure 4.7(c), a Variable Nozzle (VN) is used within the turbine. The nozzle vanes can rotate, allowing for the modification of flow passage through the nozzle itself. The aerodynamic performance of the turbine can be adjusted to adapt to different operating conditions of fuel cell vehicles by varying the angle of the nozzle vanes.

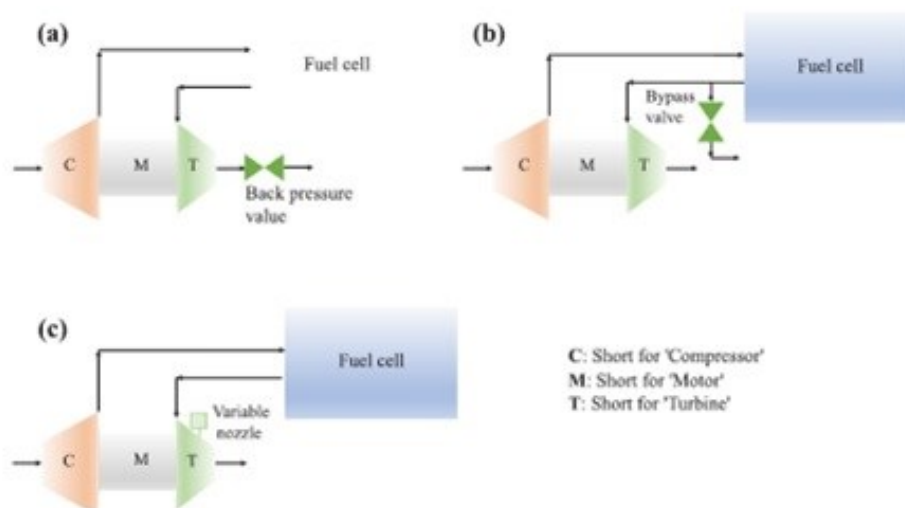


Figure 4.7: Different valve control modes for electric turbocharger architecture [40]

The article by Filsinger et al. [36] analyses the performance of an energy recovery system within an air supply system used in the aeronautical context, with an Electric Turbocharger architecture. Two options were considered: a Fixed Geometry Turbine (FGT) and a Variable Geometry Turbine (VGS). The article states that the maximum efficiency design conditions can be achieved using exclusively a fixed geometry turbine. However, for operating conditions outside the design, adjustment is required to match the turbine configuration to the specifications.

For the fixed geometry turbine, two types of off-design operating conditions are considered. One condition requires a reduction in the turbine expansion ratio to meet the demands of the fuel cell and the compressor. In this case, a flow restriction-type control valve is used. These operating

conditions are shown in Figure 4.8, indicated as L1 and H1, where L and H refer to low-altitude and high-altitude flight conditions.

The other operating condition occurs when there is a higher mass flow rate compared to the maximum efficiency condition. The article suggests that in this case, the adoption of a simple bypass valve is a suitable choice. The operating points are represented in Figure 3.7 as L2 and H2.

The article notes that, for most operating points, there is minimal difference between the two turbines, both the fixed geometry turbine and the variable stator turbine. However, under optimal recovery conditions, the fixed geometry turbine (FGT) produces higher assist power by eliminating some clearance losses. On the other hand, the variable stator turbine (VGS) offers advantages in terms of output power for specific operating points, thanks to its higher usable pressure ratio. The recovery efficiency varies depending on the operating conditions, but the use of the fixed geometry turbine seems appropriate to simplify the design phase. Additionally, it is emphasized that operating the turbocharger at half-flow, assisted by the more efficient turbine, represents an advantage in reducing electrical energy consumption.

In the light of this analysis and with the aim of simplifying the design phase, a fixed-configuration turbine is believed to be suitable and appropriate for the regulation of turbochargers utilized in the air supply system in fuel cell-based systems.

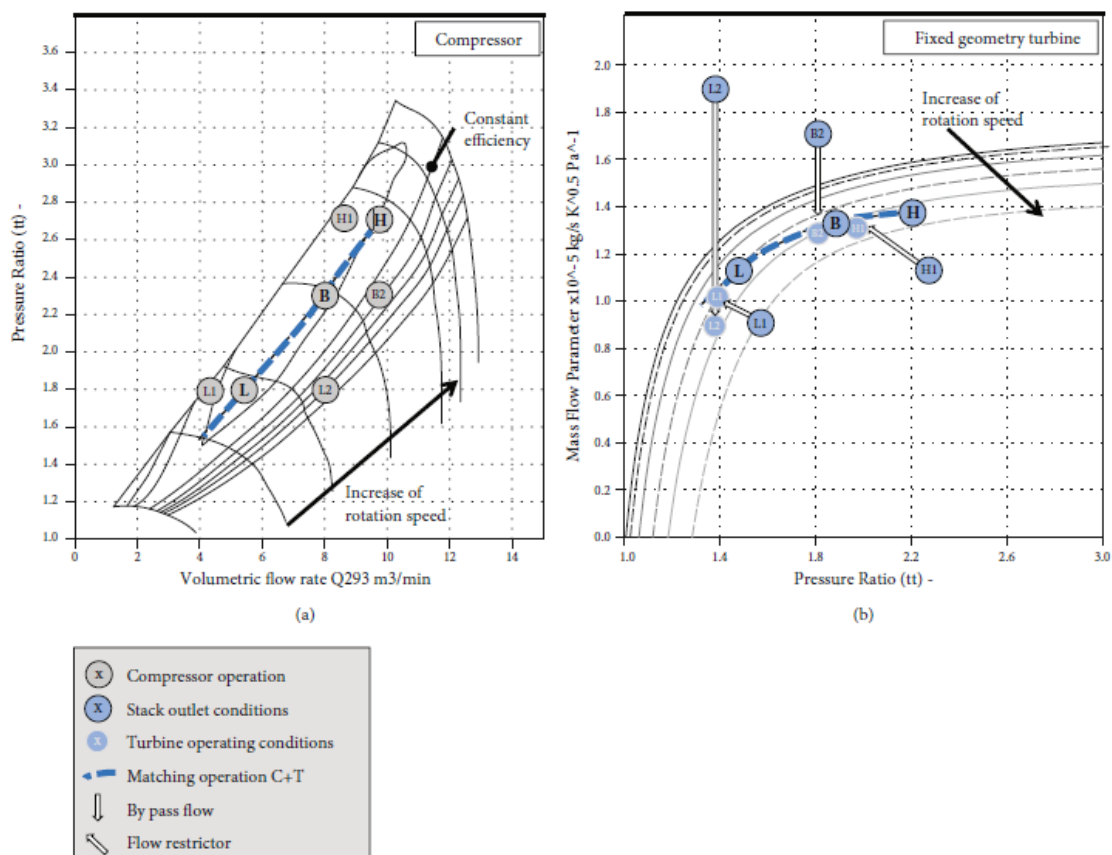


Figure 4.8: Different adjustment modes on the turbine map [36]

Based on the information presented in the state of the art of this thesis, a control system using a fixed geometry turbine (FGT) was considered, which includes a black-pressure valve for controlling

the gas pressure exiting the fuel cell, and a bypass valve (wastegate) that opens to regulate the gas flow exiting the fuel cell under non-standard operating conditions.

In the context of static sizing, it was assumed that there are no pressure losses in the flow passing through the turbine when the wastegate is opened. This assumption is also supported by the study by Filsinger et al. [36], as shown in Figure 4.8.

This is a reasonable assumption because the major pressure losses will occur in the flow passing through the wastegate, while the pressure losses for the flow passing through the turbine, caused by flow discontinuity when the wastegate opens, can be considered negligible.

To calculate the airflow passing through the turbine under static conditions, the airflow passing through the wastegate was simply subtracted from the airflow exiting the fuel cell.

$$G_{exh,t} = G_{exh} - G_{exh,w} \quad (4.45)$$

4.4 Fitting method

The common approach to modelling turbomachinery characteristic maps in turbochargers is to integrate turbocharger performance data directly into the model using look-up tables [20].

As pointed out by Moraal et al.[20], this mode has limitations, as the standard linear interpolation used is not continuously differentiable and can lead to apparent discontinuities during simulations. It is also important to emphasise that this type of model cannot adequately handle operating conditions outside the range of the mapped data.

Due to the non-linear nature of compressor and turbine characteristics, standard interpolation methods such as polynomial regression and look-up tables do not produce reasonable results outside the region of available experimental data.

Indeed, interpolation via look-up tables has been found to cause unacceptable performance in simulations. Therefore, it becomes necessary to adopt different approaches to obtain more reliable results outside this region.

Various regression models have been proposed to fit turbomachinery performance maps over time, some of these models are based on physical principles that could extend performance characteristics into areas not usually mapped [20].

In this thesis work, the formulations provided by Jensen et al. [41] were used, which were also implemented in the work of Moraal et al.[20].

This method represents a common approach based on mean values and the fitting of dimensionless parameters already discussed in Section 4.1; such an approach leads to simpler and more general relationships in the entire model.

An element of great importance in modelling with mean values is the use of models that are based on physical principles; the relationships used are therefore derived directly from physical and thermodynamic principles.

When it is necessary to use empirical relationships, the basic principles of physics and thermodynamics are applied to accurately determine the independent and dependent variables.

4.4.1 Curve fitting of turbine mass flow.

In a turbine, the mass flow rate through it can be modelled as the flow passing through an adiabatic nozzle where the effective flow area is a parameter that depends on the independent variables that are the expansion ratio and the turbine speed[20], [41].

It can be modelled with the following equations:

$$\phi = A_t \sqrt{\frac{2\gamma}{\gamma-1} \left(\left(\frac{p_{out}}{p_{in}} \right)^{\frac{2}{\gamma}} - \left(\frac{p_{out}}{p_{in}} \right)^{\frac{\gamma+1}{\gamma}} \right)} \text{ for } \frac{p_{out}}{p_{in}} > p_{crit} \quad (4.46)$$

$$\phi = A_t \sqrt{\frac{2\gamma}{\gamma-1} \left((p_{crit})^{\frac{2}{\gamma}} - (p_{crit})^{\frac{\gamma+1}{\gamma}} \right)} \text{ for } \frac{p_{out}}{p_{in}} < p_{crit} \quad (4.47)$$

$$A_t = k_{t1} \left[\frac{p_{in}}{p_{out}} \right] + k_{t2} \quad (4.48)$$

$$K_{ti} = k_{1,i} \frac{N_t}{\sqrt{T_{in}}} + k_{2,i} \quad i = 1; 2. \quad (4.49)$$

The flow equations are the standard ones for the flow passage through an adiabatic nozzle, where for expansion ratios less than the critical ratio (which varies depending on the chemical composition of the gas with which the turbine is working, in the case of air this ratio is about 0.528) the phenomenon of choking occurs.

However, the equations for the flow passage in an adiabatic nozzle are based on the assumption of an isentropic expansion, whereas for the turbine it is not possible to make this assumption; therefore, the isentropic efficiency value, which is a value known from the turbine performance maps, could be used [20];

As pointed out by the work of Moraal et al. [20], however, the inclusion of this parameter in the flow modelling would not lead to better fits of the model curve than the experimental one; therefore, it will not be considered in this thesis work.

In the formulas 4.46 and 4.47 the parameter that is fitted is the effective flow area of A_t , i.e., the area of flow passage through the turbine, this depends on the expansion ratio and the speed of the turbine, as mentioned above.

The parameters K_{ti} are determined using the mean value method implemented on the Matlab software, in order to obtain the values that best fit the flow model curve to the experimental data.

In Moraal et al. [4] it is pointed out that the behaviour of the turbine is more similar to that of two nozzles in series representing the flow passage in the stator and rotor, and that therefore the value of the pressure ratio at which choking occurs is lower than the typical air ratio used in the model.

However, it is pointed out that, in the presented model, the mass flow continues to increase even beyond the critical air pressure ratio; this is possible because the pressure ratio is included within

the formula of the effective area, which is the fitted parameter, so that the modelled curve is able to follow the real one well even beyond the critical pressure ratio.

4.4.2 Curve fitting of turbine efficiency.

With regard to the modelling of efficiency curves, two different approaches were taken and compared, namely the method of Jensen et al. [41] and Andersson [42].

In the model of Jensen et al.[41], the efficiency of a turbine depends mainly on the blade speed ratio (BSR) which is a parameter that represents the relationship between the circumferential speed of a turbine wheel and the ideal spouting velocity of the working gas during an isentropic expansion between the entry and exit pressures of the stage [43].

It is calculated using the following formula (4.50):

$$BSR = \frac{U}{C_0} = \frac{\pi D \frac{n}{60}}{\sqrt{2c_p T_{in}^{\circ} \left(1 - \frac{p_{out}}{p_{in}^{\circ}}\right)^{\frac{\gamma-1}{\gamma}}}} \quad (4.50)$$

Where T_{in}° [K] signifies the initial total temperature at the inlet, p_{in}° [Pa] represents the initial total pressure at the inlet, p_{out} [Pa] indicates the static pressure at the outlet, γ [-] represents the heat-specific ratio, U [m/s] represents the rotational speed of the turbine wheel, C_0 [m/s] denotes the isentropic exit velocity, D [m] stands for the wheel's diameter, n [rpm] is the rotation frequency, and c_p [J/kg/K] represents the specific heat capacity at constant pressure.

The efficiency is adjusted as a quadratic function with respect to the BSR and a function of the turbine rotation speed N_t [41].

$$\eta_t = b_0 + b_1 N_t + (b_2 + b_3 N_t) \frac{U}{C_0} + (b_4 + b_5 N_t) \left(\frac{U}{C_0}\right)^2 \quad (4.51)$$

The parameters b_0, b_1, b_2, b_3, b_4 and b_5 are found by fitting the efficiency curves to the experimental values.

In Andersson's work[42], on the other hand, the efficiency is again a function of the BSR, and can be calculated by knowing the maximum efficiency value for each rotational speed and its corresponding BSR, denoted by $BSR_{\eta_{t,max}}$ [42]:

$$\eta_t = \eta_{t,max} \left(1 - \left(\frac{BSR - BSR_{\eta_{t,max}}}{BSR_{\eta_{t,max}}}\right)^2\right) \quad (4.52)$$

This is a semi-empirical formula and has the advantage that efficiency curves can be estimated even in the absence of experimental points.

4.4.3 Fitting results

The fitting formulas for the flow and efficiency curves were implemented on the Matlab software using the mean value method.

The performance maps taken as reference are examples of turbine performance maps used for turbochargers in the automotive sector.

In figure 4.9 is shown an example of a performance map provided by BorgWarner[44], [45] in the absence of available data from suppliers.

Figure 4.10 and 4.11 show performance maps of the flow and efficiency curves at varying expansion ratio and speed, these were taken from the web site of Sa-charging solutions[46], where commercially available turbochargers are tested.

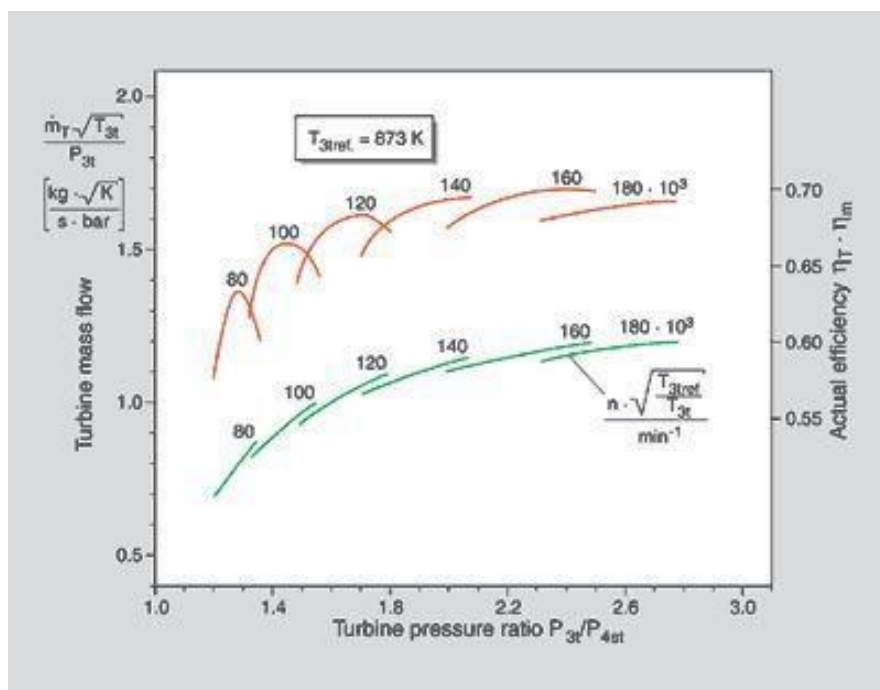


Figure 4.9: Example of a BorgWarner turbine flow curve map [44], [45]

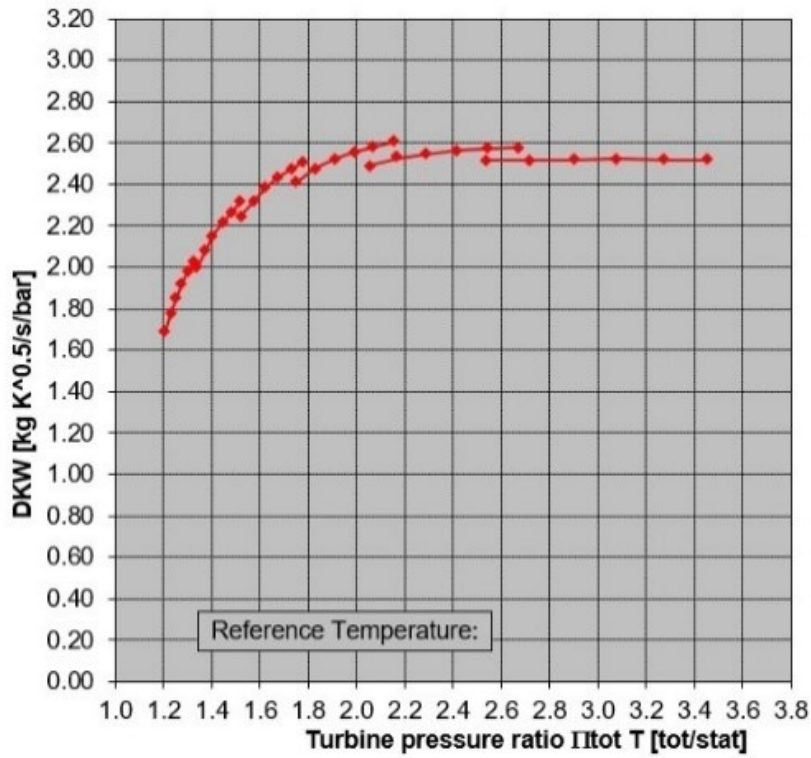


Figure 4.10: Sa-charging solution turbine flow curves map [46]

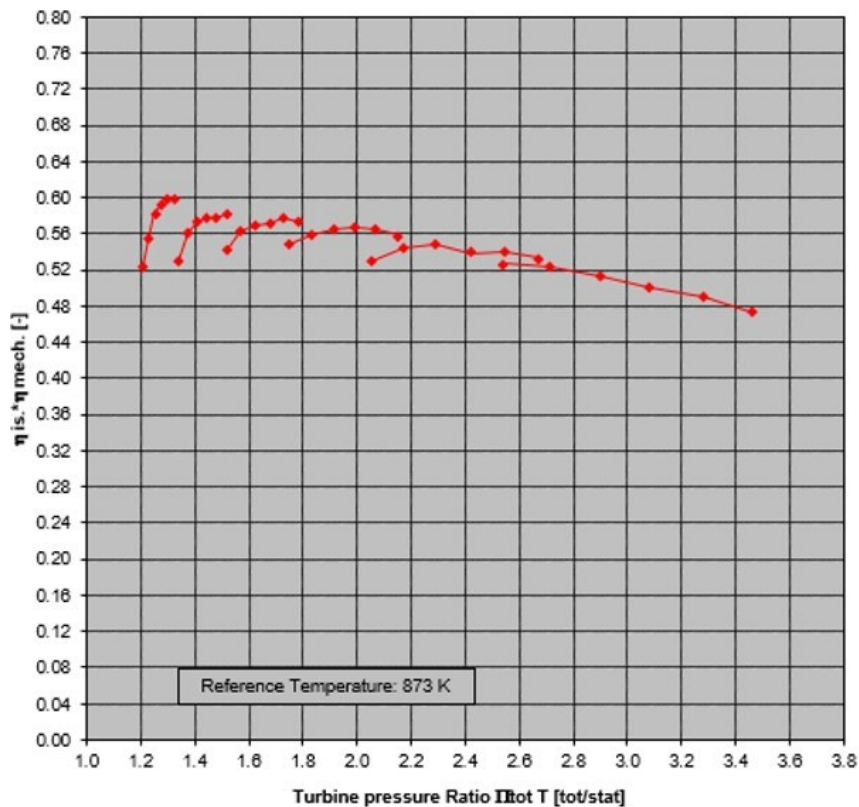


Figure 4.11: Sa-charging solution turbine efficiency map [46]

This section shows the results of the fitting process for the two performance maps.

Figure 4.12 and 4.13 shows the trend of the flow curves as the expansion ratio and corrected velocity change, in 3D, where the values of total to static expansion ratio and corrected velocity are indicated

on the x and y axes while the values of corrected flow rate on the z axis. In figure 4.14 and 4.15 the same result is shown in 2D where the expansion ratio is plotted on the x-axis and the corrected flow rate is plotted on the y-axis for each corrected velocity curve shown in the legend.

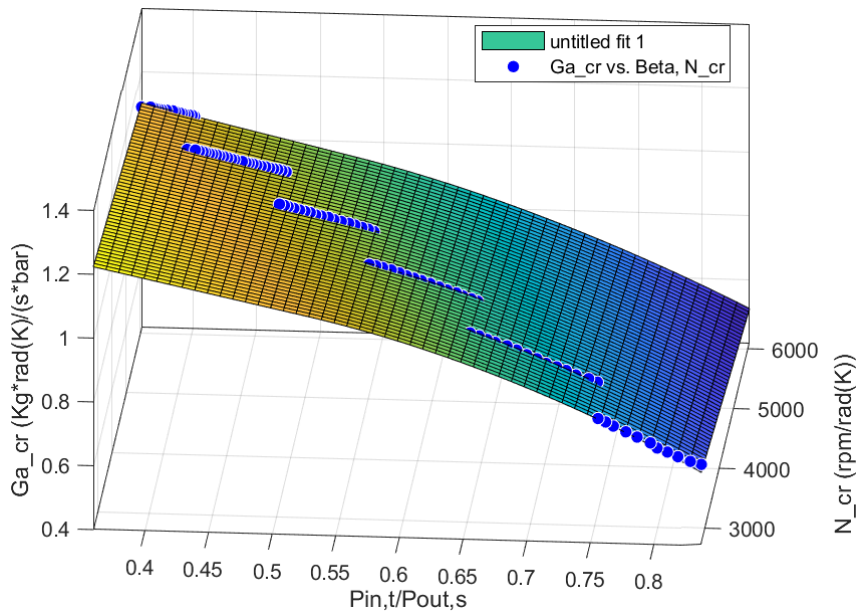


Figure 4.12: 3D fitting results against experimental data for BorgWarner turbine flow curves

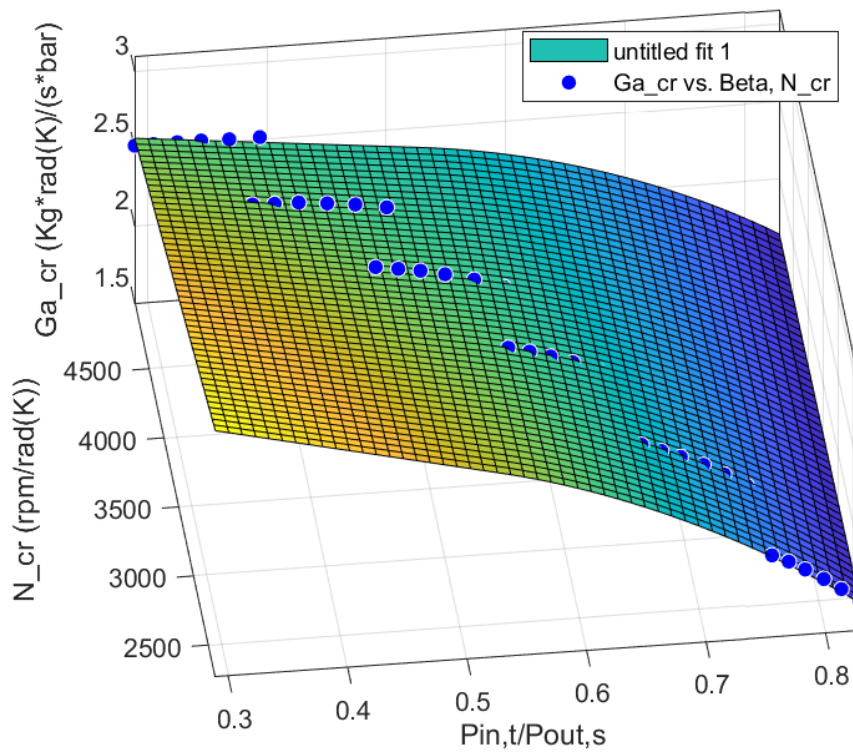


Figure 4.13: 3D fitting results against experimental data for Sa-charging solutions turbine flow curves

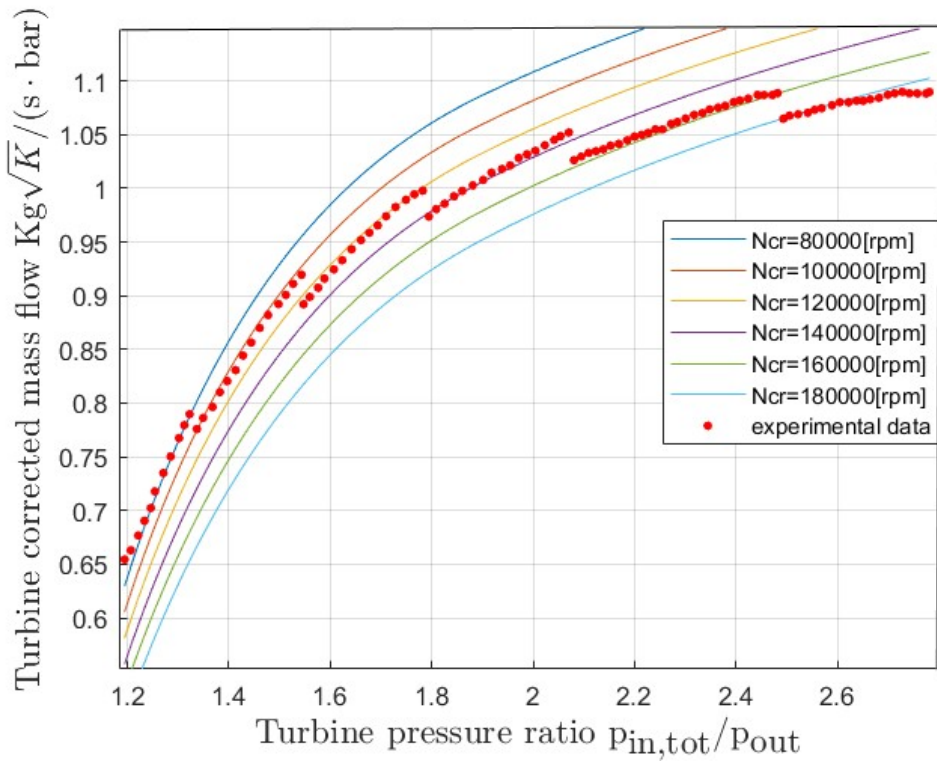


Figure 4.14: 2D fitting results against experimental data for BorgWarner turbine flow curves

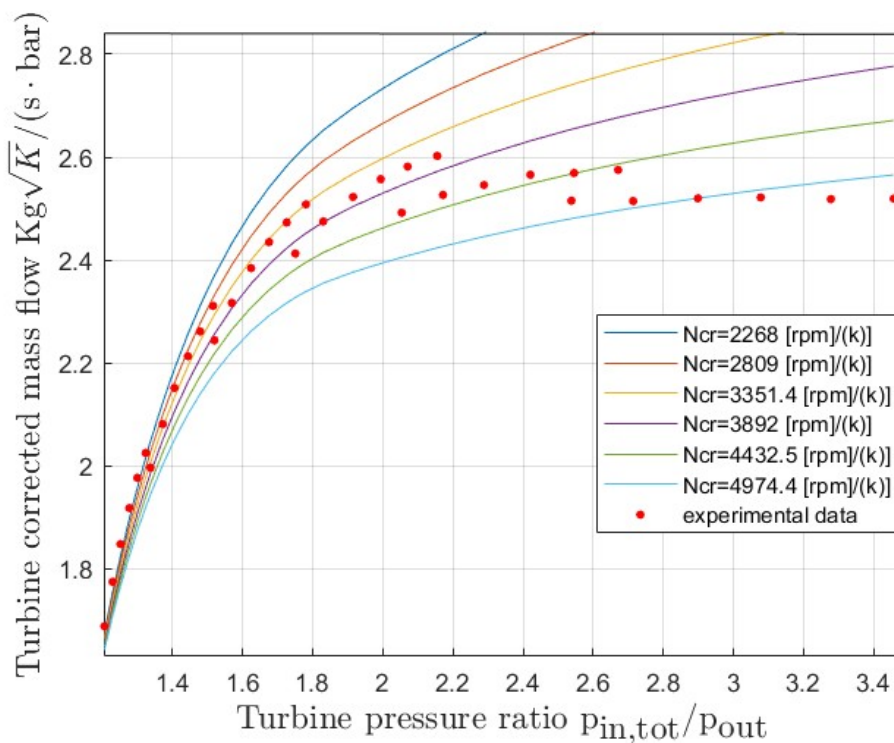


Figure 4.15: 2D fitting results against experimental data for Sa-charging solutions turbine flow curves

A significant success in fitting the model to the experimental values is shown as the flow curves of the analysed turbochargers accurately follow the experimental points with a very small error, for both performance maps.

Figures 4.16 and 4.17 shows the trends of the efficiency curves as the expansion ratio and rotational speed change obtained using Andersson's formula [42].

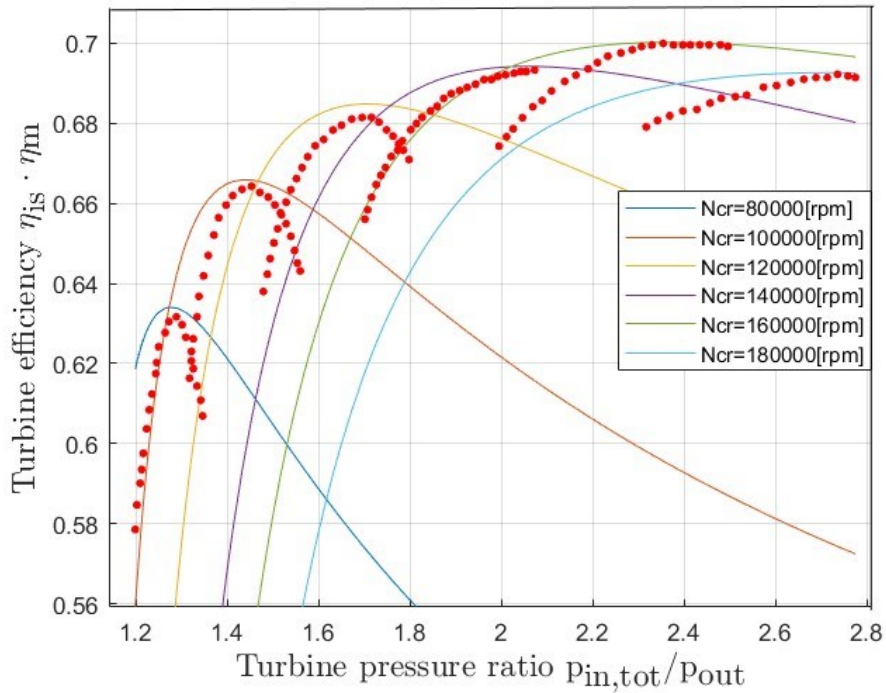


Figure 4.16: Efficiency curves for BorgWarner turbine obtained using Andersson's formula.

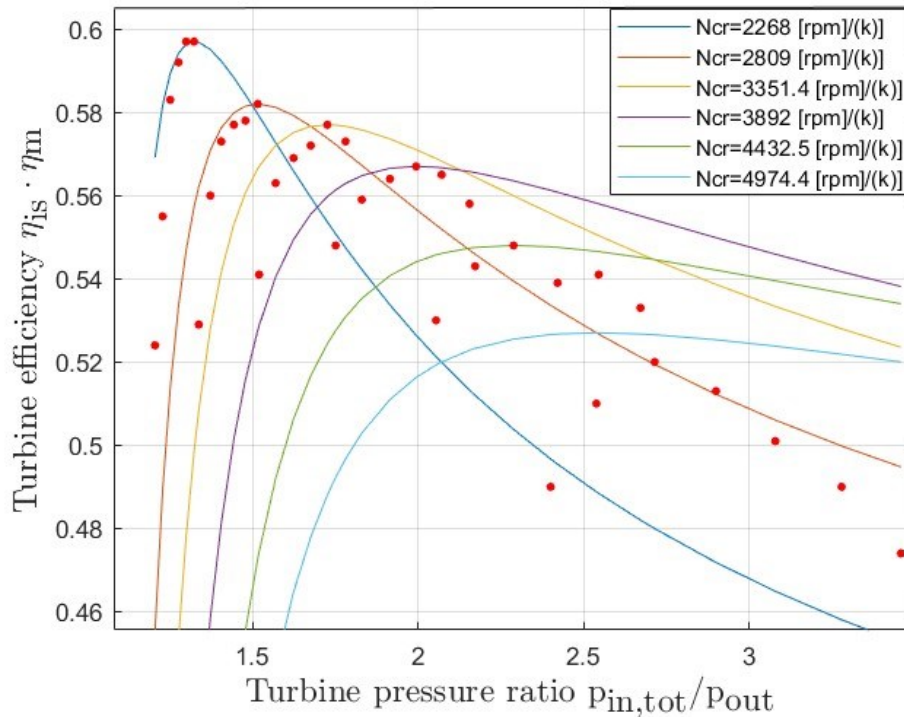


Figure 4.17: Efficiency curves for Sa-charging solution turbine obtained using Andersson's formula.

Using the formula of Jensen et al. [41], the trends shown in 3D in figure 4.18 and 4.19 and in 2D in figures 4.20 and 4.21 are obtained.

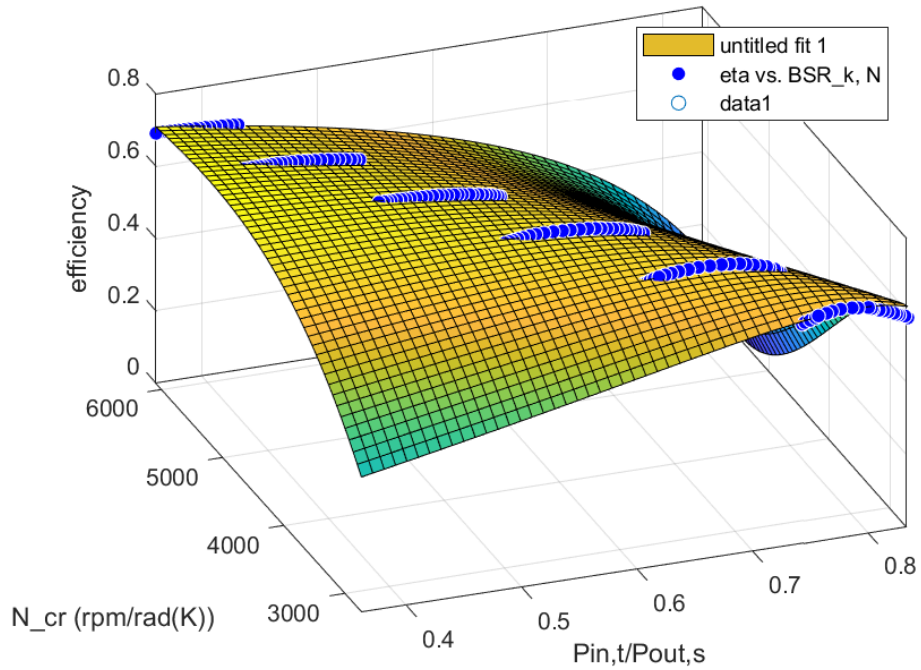


Figure 4.18: 3D fitting results against experimental data for BorgWarner turbine efficiency curves using Jensen et al. method.

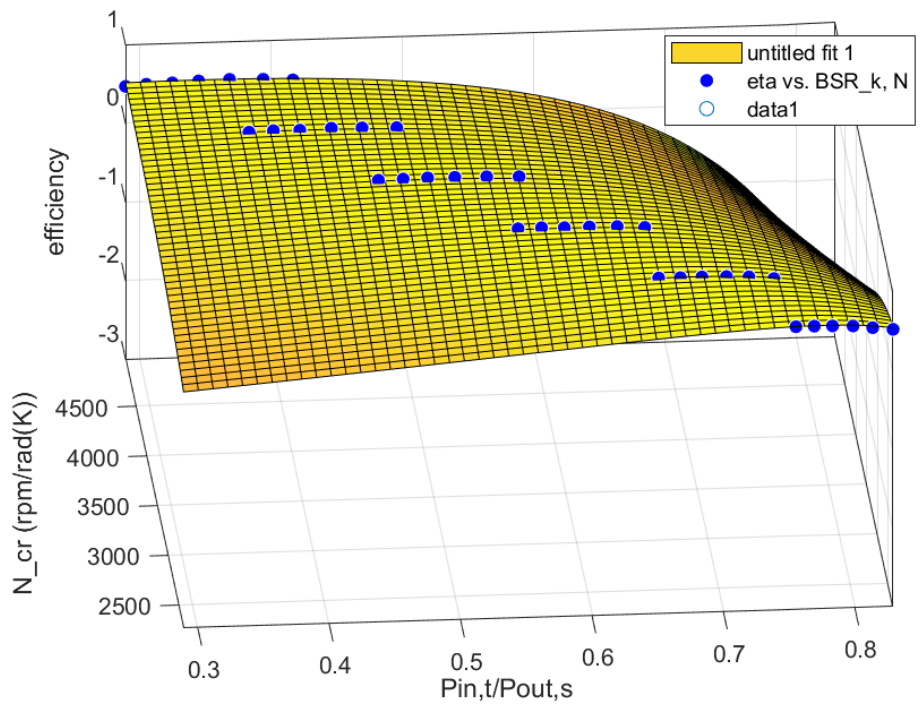


Figure 4.19: 3D fitting results against experimental data for Sa-charging solutions turbine efficiency curves using Jensen et al. method.

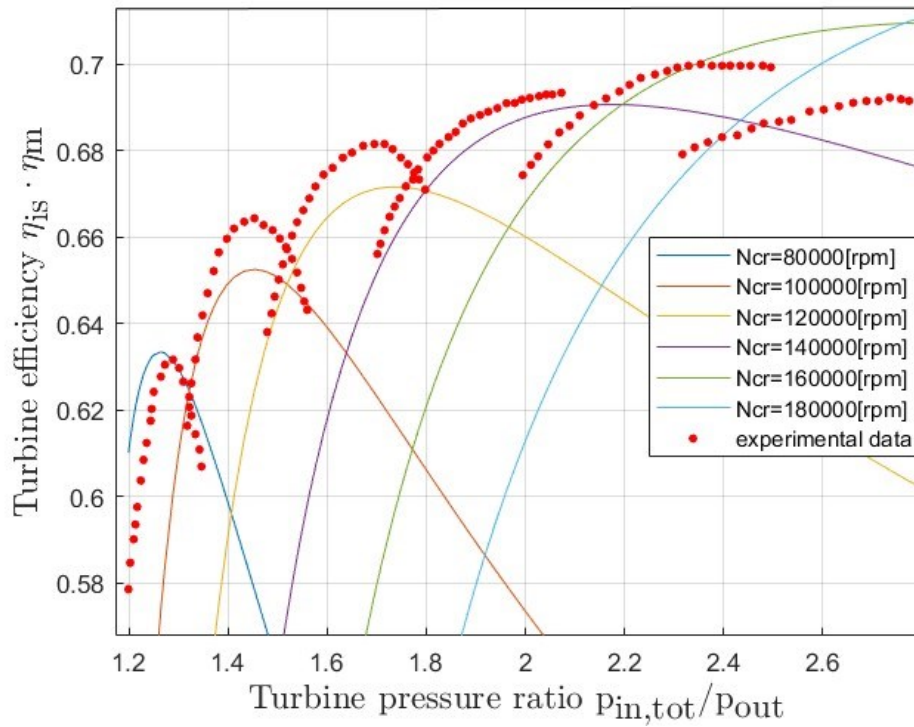


Figure 4.20: 2D fitting results against experimental data for BorgWarner turbine efficiency curves using Jensen et al. method.

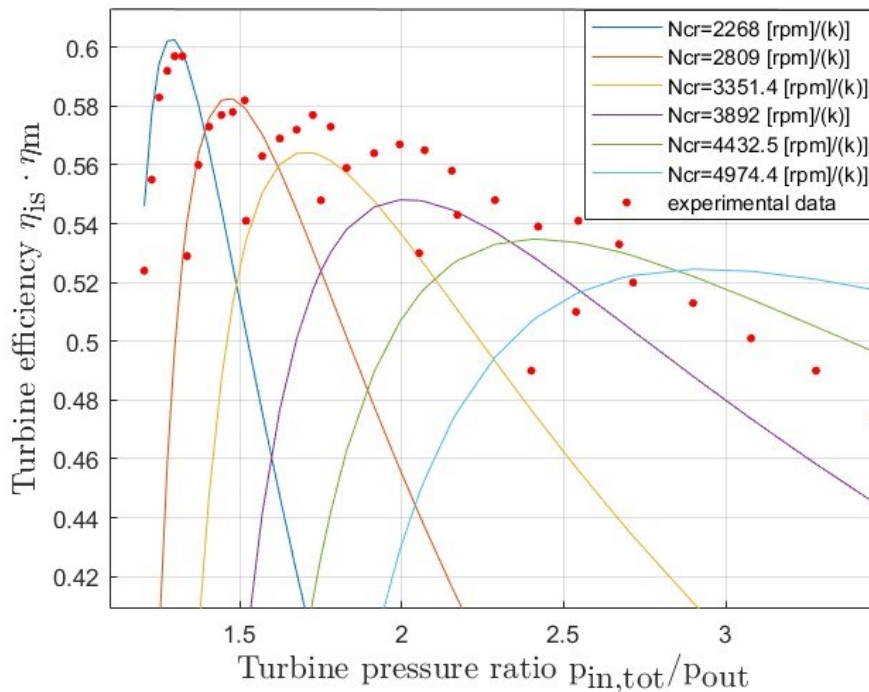


Figure 4.21: 2D fitting results against experimental data for Sa-charging solutions turbine efficiency curves using Jensen et al. method.

As far as this fitting process is concerned, the results obtained show a greater error between the modelled efficiency curves and the actual values than the fitting of the flow curves.

It is found, however, that the efficiency curves obtained by the formula of Jensen et al. follow the average course of the turbine's experimental curves better than those obtained by Andersson's formula, which, on the other hand, are more accurate in the ranges of the curves around the maximum efficiency, since the formula includes the point of maximum efficiency.

This is also found in the article by Fang et al.[47], where a comparison is made between different fitting methods for the turbine efficiency curves; in the article, Jensen et al.'s method is indicated as the one that best follows the experimental trend while he recommends Andersson's method when only the value of the maximum efficiency and the BSR that maximises it is known.

A better average fit for the Jensen et al. formulae was to be expected since these formulae involve a mean value fitting method in which constants are calculated so that the fitting curve comes as close as possible to the average trend of the experimental values.

Based on these considerations, the formulae of Jensen et al. were used for the static and dynamic turbine model.

4.5 Sizing results

In this section, the results of the static sizing process of the air supply system for the case under consideration are presented, considering both architectures. Subsequently, a detailed comparison of these results will be carried out, through which the architecture best suited to the study context will be selected. Once the optimal architecture has been identified, it will be integrated exclusively into the dynamic model for further analysis.

The results will also be compared with the electric compressor architecture, which does not have the turbocharger energy recovery system.

The operating conditions of the stacks were evaluated in the performance analysis presented in Chapter 2, in which the gross power to be generated by the FC stacks is also calculated from the net power requirement to be generated in cruise condition.

The three architectures are evaluated with the same net power generated by the FCPS while the gross power generated by the stacks to achieve the same net power will have slightly different values for the 3 architectures, depending on plant efficiency, η_{plant} .

The operating conditions of the stacks and the gross power they must generate, different for each architecture, are shown in the table 4.1.

Operating conditions		
Oxygen excess ratio	λ_{o_2}	2
Oversizing factor	ν	0.8
Stack pressure	p_{st}	1.9 atm
Stack relative humidity	ϕ_{st}	1
Stack temperature	T_{st}	80 °C
Power requirements		
Ratio between gross and net power of the electric compressor	P_{gross}/P_{net}	2316 kW
Ratio between gross and net power of the electric turbocharger	P_{gross}/P_{net}	2263 kW
Ratio between gross and net power of serial booster	P_{gross}/P_{net}	2243 kW

Table 4.1: Fuel cell stacks requirements for each architecture considering the same net power

In Federico Faiello's thesis [13]. the static stack model is explained, in this the inputs required for the dynamic model are calculated and the number of total parallel stacks required to generate the desired gross power is calculated; these will then be divided by the number of parallel compression lines used to obtain the number of stacks served by a single unit of the air supply system, from the number of total stacks calculated it is also possible to obtain an estimate of the total weight of the stacks.

4.5.1 Sizing results for electric turbocharger architecture

For the electric turbocharger architecture, the turbocharger and the electric motor are mounted on the same shaft, as explained in the previous paragraphs the main outputs of the turbocharger sizing are the scaled performance maps of the turbine and compressor, an estimate of the mass, moment of inertia and characteristic dimensions of the turbocharger.

The power generated by the turbine and that required by the compressor to compress the air needed to feed the FC stacks.

The requirements for the air supply system are summarised in table 4.2 and 4.3 are divided between requirements for the turbine and the compressor.

\dot{m}_a (Kg/s)	-
$p_{c,in}^\circ$ (Pa)	44000
$p_{c,out}$ (Pa)	192500
$T_{c,in}^\circ$ (K)	252
\dot{m}_a^* (Kg/s)	-
β_c (-)	4.38

Table 4.1: Compressor requirements

\dot{m}_{exh} (Kg/s)	-
$p_{t,in}^{\circ}$ (Pa)	160000
$p_{t,out}$ (Pa)	41200
$T_{t,in}^{\circ}$ (K)	367
\dot{m}_{exh}^* (Kg/s)	-
β_t (-)	3.89

Table 4.2: turbine requirements

The base compressor chosen to scale is the Garrett G55-2100 [48], part of the Garrett G-series turbochargers, is a centrifugal compressor that is part of a turbocharger designed for supercharging engines used in the automotive sector with displacements between 3.0L-12.0L and the capacity to deliver between 1000-2900 hp.

This compressor was chosen from the database as the one that can work at the highest efficiency, at the high compression ratio required, among the many compressors considered and researched in suppliers' catalogues.

Figure 4.22 shows the performance map of the compressor provided by the supplier and the main characteristic data are listed in table 4.4; the values of the geometric characteristics have been taken from the online catalogue provided by the supplier, while the values of mass and moment of inertia have been estimated using a cad available online.

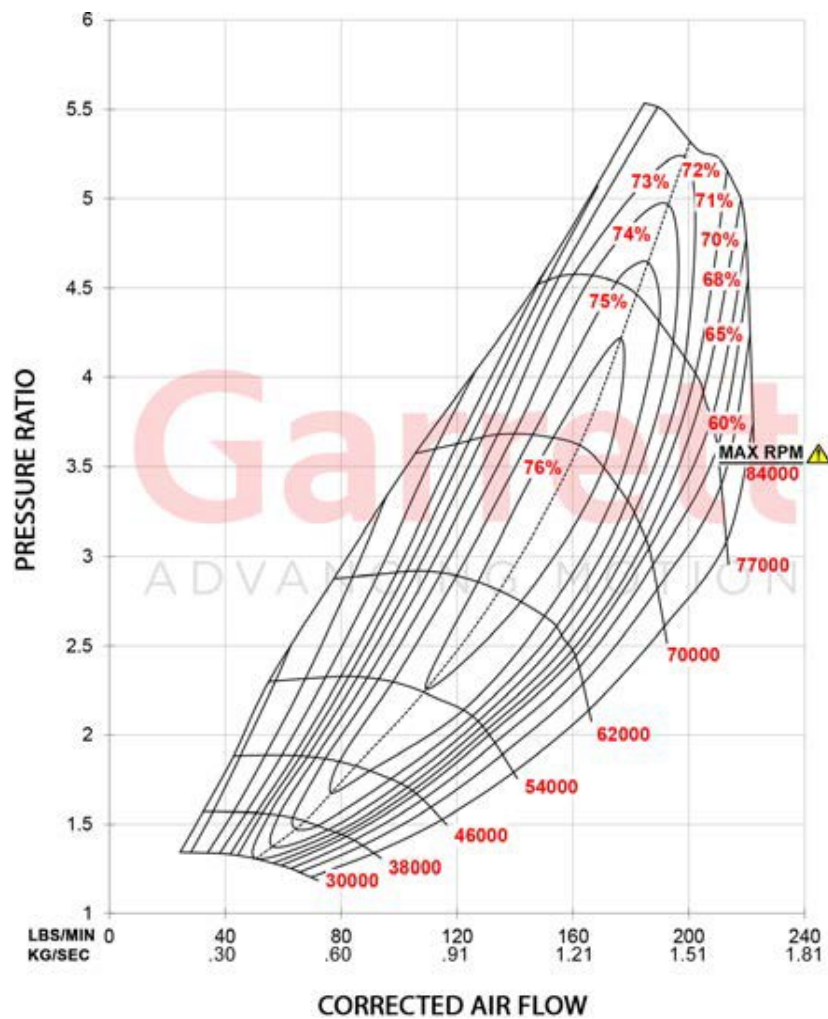


Figure 4.22: Garrett G55-2100 compressor performance map [48]

Inducer (m)	0.085
Exducer (m)	0.133
Diametral footprint (m)	0.321
Axial footprint (m)	0.162
Mass (Kg)	16.53
Moment of inertia ($Kg \cdot m^2$)	$2.67 \cdot 10^{-4}$

Table 4.3: Technical data of a turbocharger Garrett G55-2100 [48]

The performance map is fitted using the regression model discussed in Federico Fasiello's thesis [7], and the result is shown in figure 4.23.

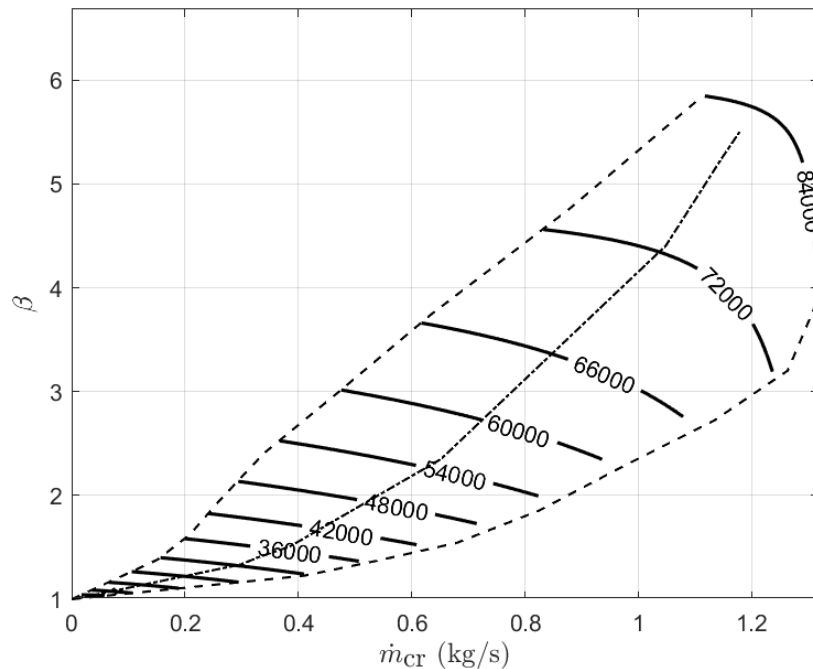


Figure: 4.23 Fitted compressor map (Garrett G55-2100).

The compressor performance map scaled through the procedure described in paragraph 4.2.4 is shown in figure 4.25, on which the working line of the compressor is projected in red.

This line consists of all the working points of the compressor during the flight mission while the working point in cruise conditions, i.e., at the design point, is highlighted in green.

Figure 4.24 shows the main working conditions of the compressor during the flight mission, i.e., the inlet pressure and temperature, the outlet pressure, the rotational speed of the turbocharger while h indicates the height the aircraft reaches during the mission.

The reference values are the International Standard Atmosphere conditions, i.e., $T_{ref} = 288.15 \text{ K}$ and $P_{ref} = 101325 \text{ Pa}$, while the rotational speed was normalised to the speed of 50000 rpm.

The working line of the compressor has been shown to verify that all points reside within the turbomachinery avoiding choking and surge zones; however, it is important to emphasise that the calculated working points are only a first approximation; these will be determined more precisely in the context of the dynamic model.

The outputs of the compressor sizing process are summarised in table 4.5.

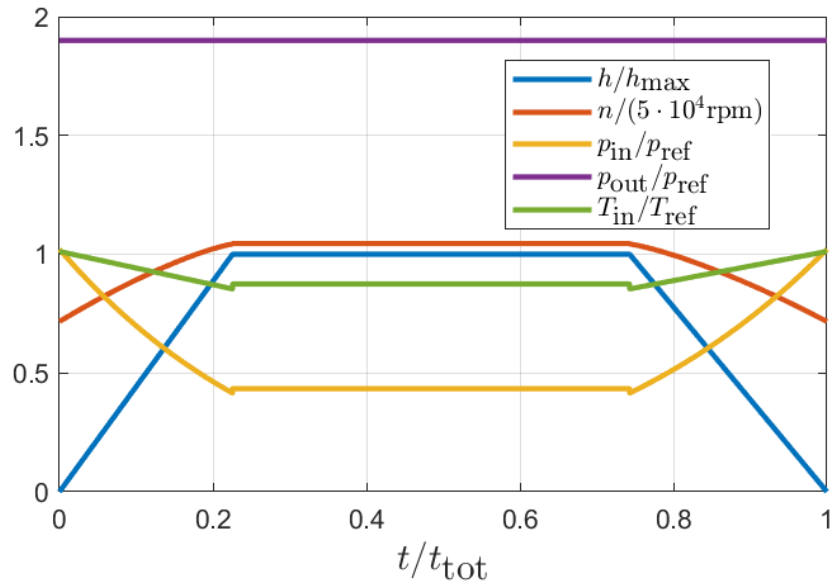


Figure 4.24: Trends in inlet and outlet pressure, inlet temperature and compressor rotation speed during the flight mission

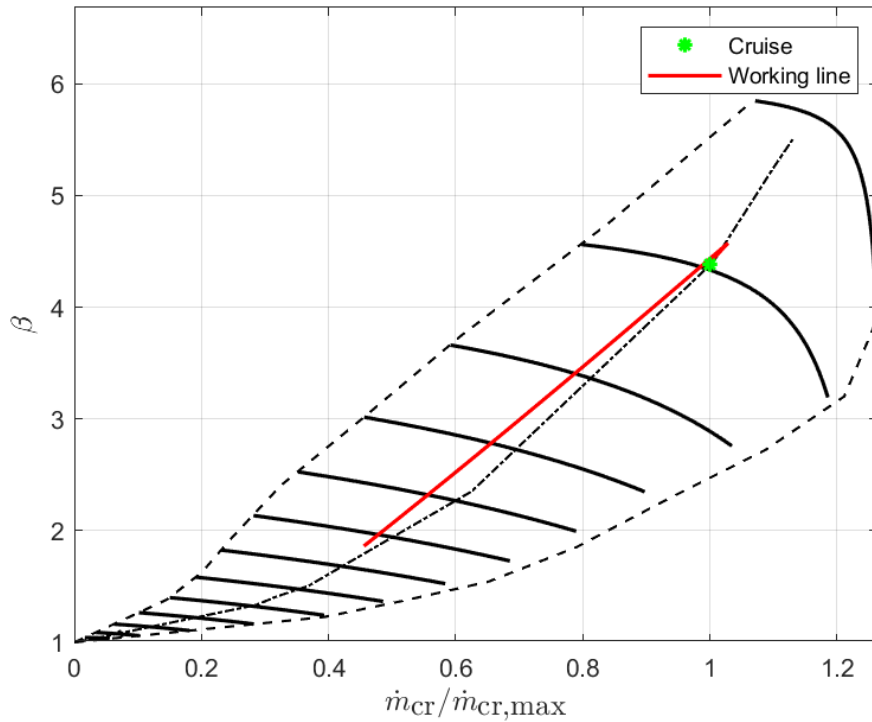


Figure 4.25: Scaled compressor performance map

Inducer (m)	0.110
Exducer (m)	0.171
Diametral footprint (m)	0.414
Axial footprint (m)	0.209

Table 4.4: Technical data of scaled compressor

For turbines, it was not possible to find performance maps with complete data directly from suppliers, these were obtained from research articles in the literature and sites available online.

In the present case, the base turbine performance map chosen in the database comes from the article of Adam Vondrák [49] in which studies are done on the fitting of performance maps of turbines produced at the Garrett Motion Inc. whose experimental data were acquired through tests on a hot gas bench or obtained on a turbine dynamometer.

By fitting the experimental data through the regression models explained in section 4.3, the base turbine performance maps, shown in figures 4.26 and 4.27 were obtained.

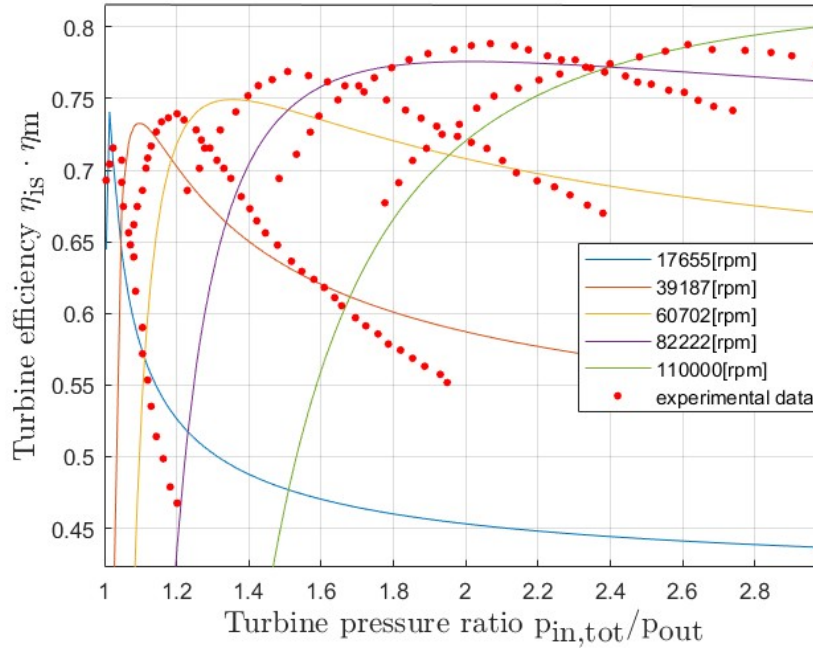


Figure 4.26: Performance map fitting of turbine efficiency curves

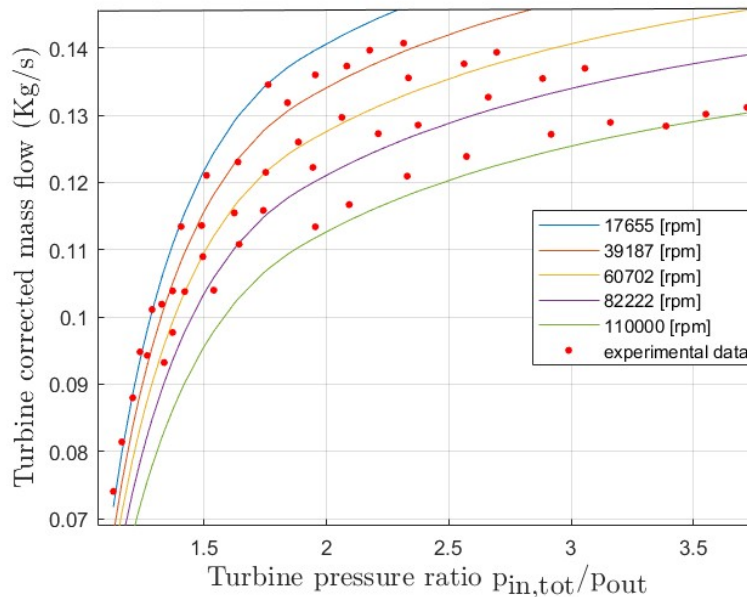


Figure 4.27: Performance map fitting of turbine flow curves

Inducer (m)	0.054
Exducer (m)	0.049
Diametral footprint (m)	0.082
Axial footprint (m)	0.141
Mass (Kg)	2.13
Moment of inertia ($Kg \cdot m^2$)	$1.479 \cdot 10^{-5}$

Table 4.5 Technical data of turbine Garrett G25-550 [38]

Not having enough information on the characteristic data of the turbine presented in the article, the characteristic data of the Garrett G25-550[38] turbine, available on the supplier's website, was taken as a reference.

This turbine is part of the Garrett G-series turbochargers and has a similar performance map to the one considered in terms of flow rate, expansion ratio range and efficiency; it was not possible to use this map directly in the model as only a single envelope line of flow curves is provided without giving any indication of the correct rotational speeds, and only a single maximum efficiency value is given. For this too, mass and moment of inertia values were estimated using a cad available online.

The main characteristic data of turbine are listed in table 4.6.

The scaled turbine performance maps are shown in Figure 4.29 and 4.30 The first one displays the flow curves as a function of the expansion ratio, while the second one illustrates the efficiency curves. Similarly, to the compressor, the cruise point and the working lines of the turbine have been projected for initial verification purposes; just like for the compressor, these lines will be calculated more accurately in the dynamic model.

Figure 4.28 shows the main working conditions of the turbine during the flight mission, it can be seen that the speed of the turbine is the same as that of the compressor as they are splined to the same shaft.

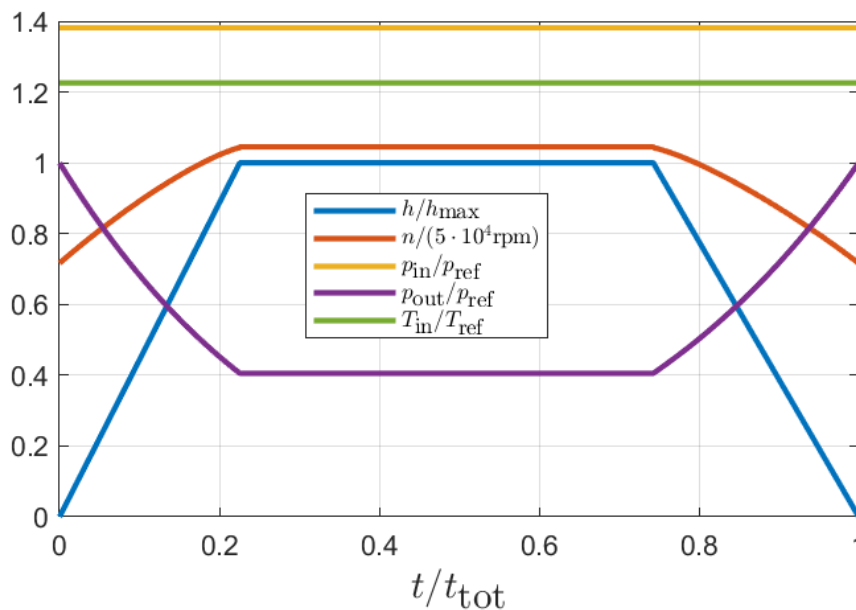


Figure 4.28: trends in inlet and outlet pressure, inlet temperature and turbine rotation speed during the flight mission

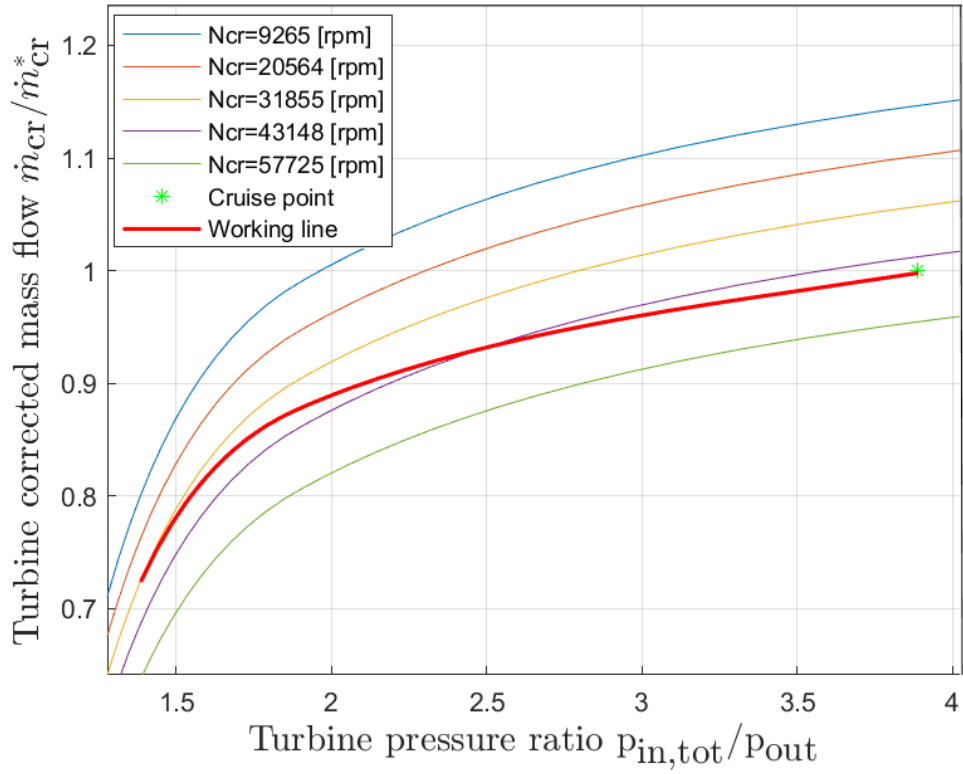


Figure 4.29: scaled turbine flow performance map

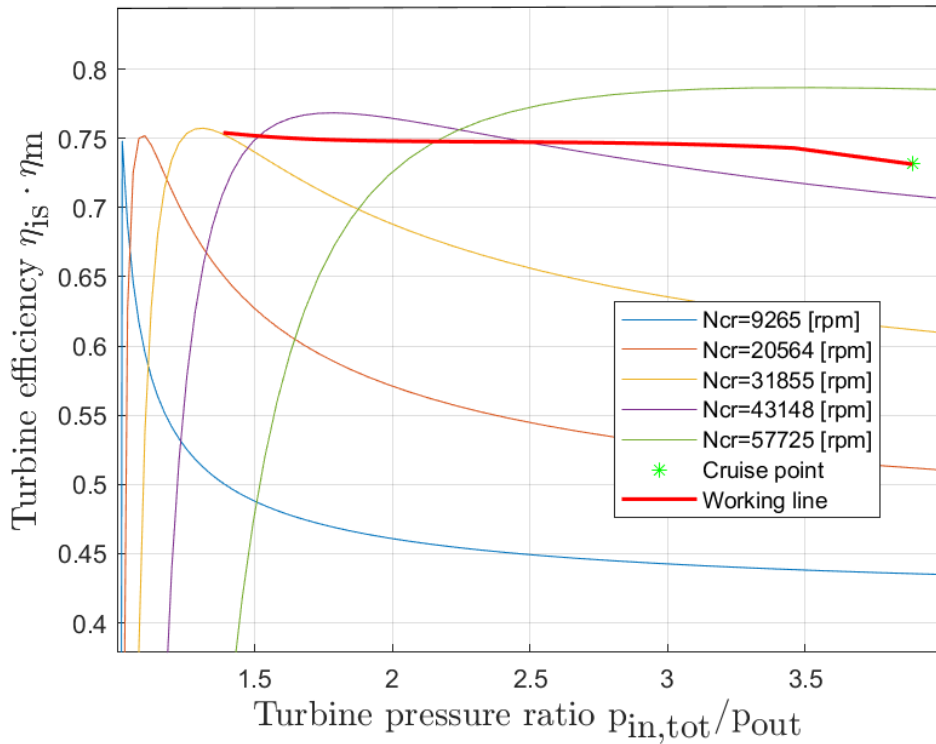


Figure 4.30: scaled turbine efficiency performance map

The outputs of the static turbine sizing process are shown in table 4.7, while table 4.8 summarises the main outputs of the electric motor sizing process.

Inducer (m)	0.103
Exducer (m)	0.093
Diametral footprint (m)	0.1563
Axial footprint (m)	0.269

Table 4.6: Technical data of scaled turbine

Maximum armature voltage (V)	670.04
Armature voltage (V)	478.60
Armature resistance (Ohm)	0.74
Armature inductance (H)	$7.4 \cdot 10^{-4}$
Voltage constant (Vs/rad)	0.500
Torque constant (Nm/A)	0.500

Table 4.7: Motor parameters

4.5.2 Sizing results for serial booster architecture

As explained above, in the serial booster architecture, the turbocharger is first sized.

This performs a first compression stage, then the electric compressor is dimensioned, which performs the second compression stage, compressing the air to the operating pressure of the stack. The requirements for the turbocharger are shown in Tables 4.9 and 4.10, in this case the required output pressure of the turbocharger is not the operating pressure of the FC stacks because the turbocharger only performs a first compression stage.

The compression ratio β_c is therefore not a fixed input but is found through the power balance and downstream of the iterative process, with the procedure described in section 4.2.3

\dot{m}_a (Kg/s)	-
$p_{c,in}^\circ$ (Pa)	44000
$T_{c,in}^\circ$ (K)	252
\dot{m}_a^* (Kg/s)	-
β_c (-)	2.18

Table 4.8: First compressor requirements

\dot{m}_{exh} (Kg/s)	-
$p_{t,in}^\circ$ (Pa)	160000
$p_{t,out}$ (Pa)	41200
$T_{t,in}^\circ$ (K)	367
\dot{m}_{exh}^* (Kg/s)	-
β_t (-)	3.89

Table 4.9: Turbine requirements

The turbocharger sizing process is described in section 4.2.3, returns the same turbocharger sizing outputs as the electric turbocharger architecture described.

The base compressor chosen from the database, i.e., the one with the best efficiency for the required compression ratio, is the Garrett G25-550[38].

This compressor is extremely high-performance, reaching a peak efficiency of 80 %, and is used in the automotive sector, coupled to a turbine within a turbocharging system, to turbocharge engines with a displacement of between 1.4 and 3.0 litres and which can generate a maximum power output of 550 hp.

It can be seen that this compressor has a higher efficiency for the design compression ratio than the compressor chosen for the electric turbocharger type architecture.

By dividing the compression ratio into two stages, it is possible to use compressors working with lower compression ratios that generally have higher peak efficiencies.

The main characteristics and the performance map are summarised in the table 4.11 and in the figure 4.31, the data on mass and moment of inertia are not shown on the supplier's website, which is why their values are estimated by means of a CAD model found on the net.

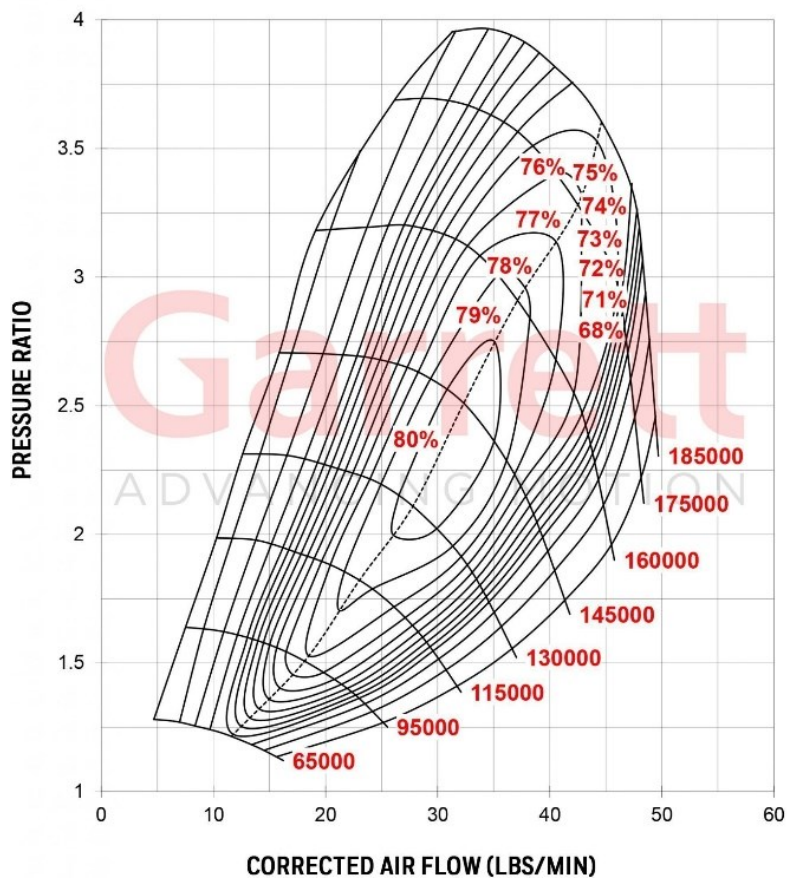


Figure 4.31: Garrett G25-550 performance map [38]

Inducer (m)	0.048
Exducer (m)	0.06
Mass (Kg)	2
Moment of inertia	$4.457 \cdot 10^{-5}$

Table 4.10: Technical data of a compressor of turbocharger Garrett G25-550 [38]

In figure 4.33 is shown the performance map, reconstructed through the fitting method, of the base compressor while in figure 4.34 is shown the performance map of the scaled compressor with the projection of the compressor work line, i.e., the set of all the compressor work points during the flight mission, in green is shown the cruise point, which is the design point.

Figure 4.32 shows the main working conditions of the compressor during the flight mission.

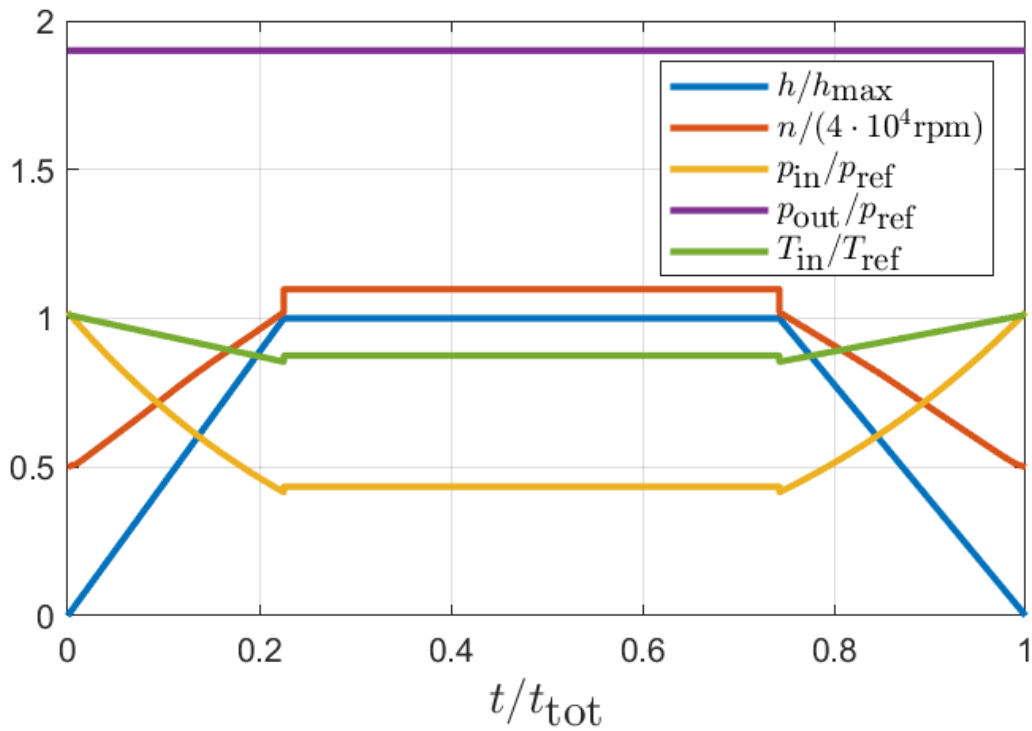


Figure 4.32: Trends in inlet and outlet pressure, inlet temperature and compressor rotation speed during the flight mission

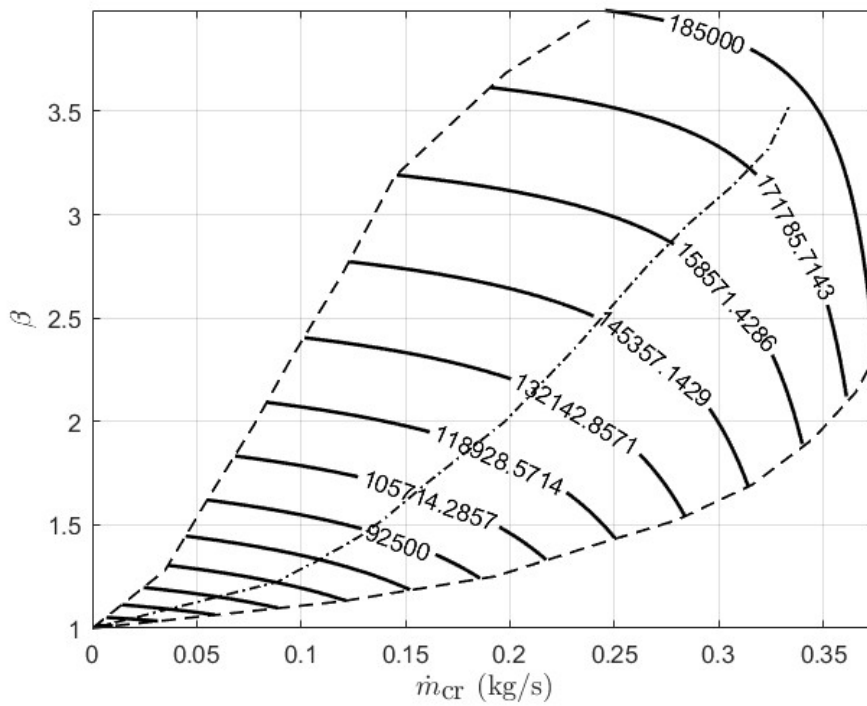


Figure 4.33: Fitted compressor performance map (Garrett G25-550)

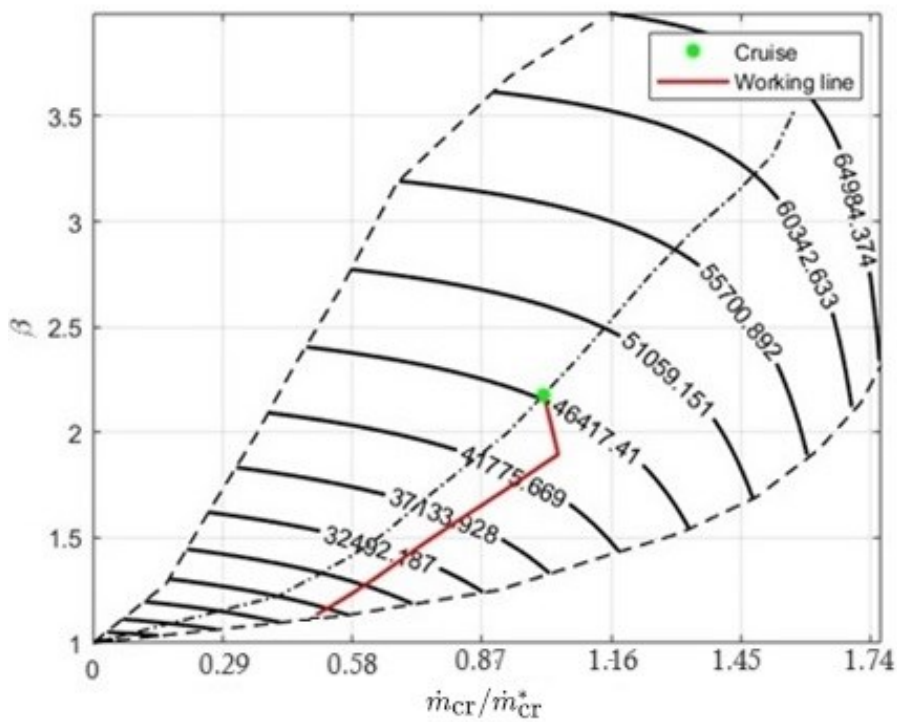


Figure 4.34: Scaled compressor performance map

Table 4.12 shows the characteristic data of the scaled compressor.

Inducer	0.136
Exducer	0.170
Axial footprint	0.479
Diametral footprint	0.232

Table 4.11: Technical data of scaled compressor

In this case, the performance map of the base turbine chosen from the database is the one shown in figure 4.9, which has already been discussed in the chapter on fitting procedures.

Also, for this turbine, not having enough data on its characteristics, those of the turbine GBC14-200 [50] have been taken as reference; the characteristics are shown in table 4.13.

The maps resulting from the scaling process are shown in figures 4.36 and 4.37, the first is the performance map which shows the flow rate curves as a function of the expansion ratio and as the speed varies, while the second shows the efficiency curves as a function of the expansion ratio, again as the speed varies.

Again, the turbine operating curves during the flight mission are shown in red, and the point in green indicates the cruise point, which is also the design point.

Figure 4.35 shows the main working conditions of the turbine during the flight mission.

Inducer (m)	0.039
Exducer (m)	0.036
Diametral footprint (m)	0.087
Axial footprint (m)	0.108
Mass (Kg)	1.24
Moment of inertia ($Kg \cdot m^2$)	$7.6 \cdot 10^{-6}$

Table 4.12: Technical data for turbine GBC14-200 [40]

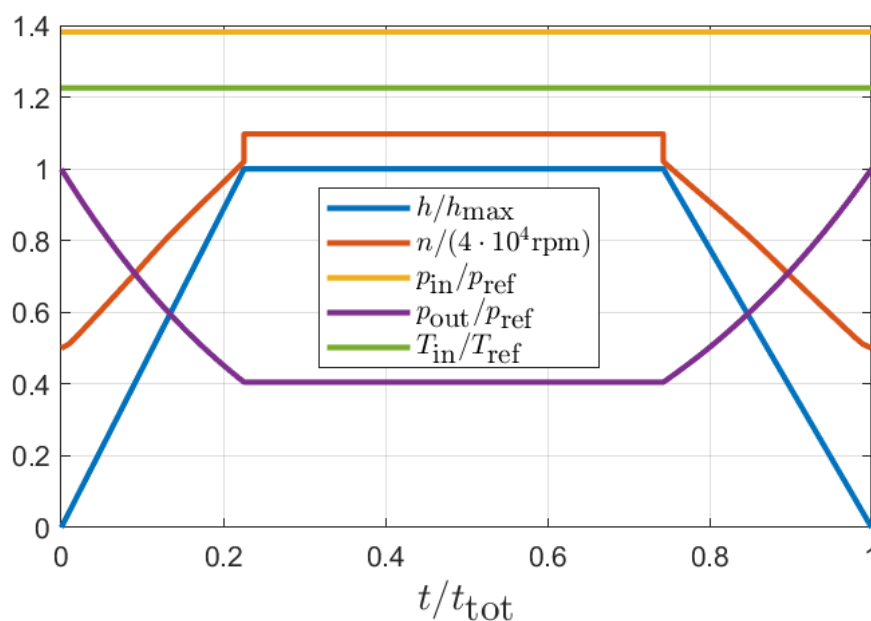


Figure 4.35: Trends in inlet and outlet pressure, inlet temperature and compressor rotation speed during the flight mission

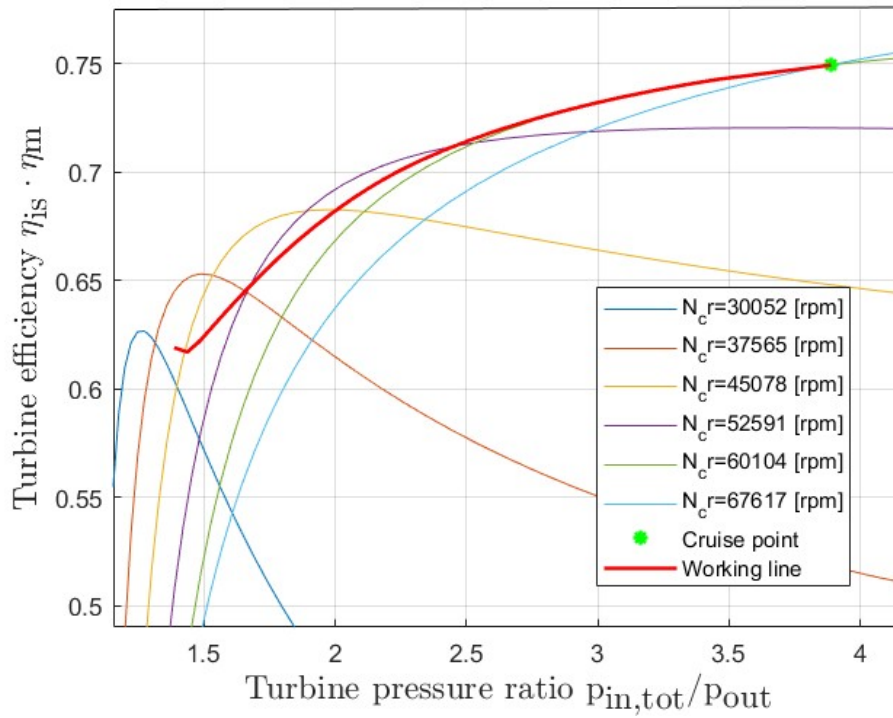


Figure 4.36: Scaled turbine efficiency performance map

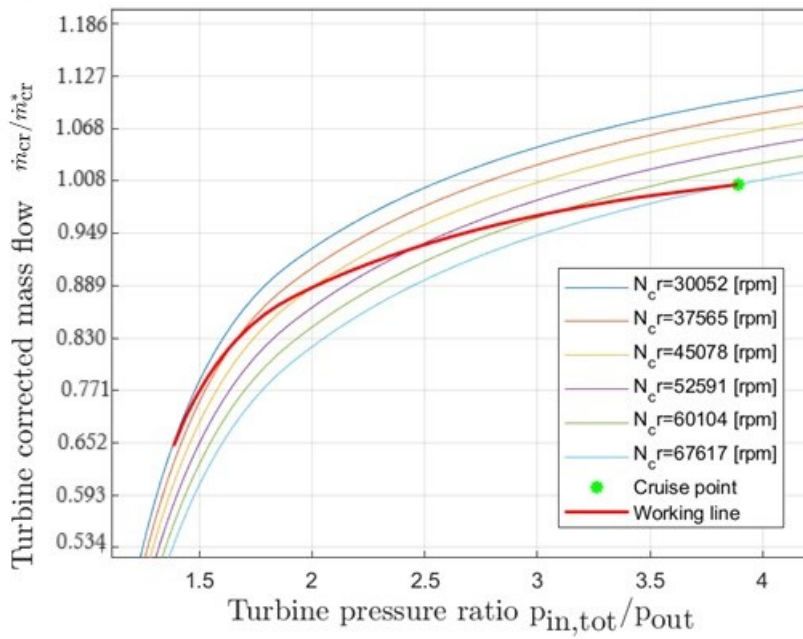


Figure 4.37: Scaled turbine flow performance map

The outputs of the turbine sizing process are shown in the table 4.14.

Inducer (m)	0.104
Exducer (m)	0.096
Diametral footprint (m)	0.231
Axial footprint (m)	0.287

Table 4.13: Technical data for scaled turbine

At this point, it was possible to size the compressor powered by the electric motor which performs the second stage of compression; the requirements for the compressor are shown in the table 4.15.

\dot{m}_a (Kg/s)	0.796
$p_{c2,in}^\circ$ (Pa)	95813
$p_{c2,out}$ (Pa)	192518
$T_{c,in}^\circ$ (K)	330.26
\dot{m}_a^* (Kg/s)	0.904
β_{2c} (-)	2.01

Table 4.14: Requirements for second compressor

The inlet air flow rate is the same as that sucked in by the first compressor, while the inlet pressure and temperature are the same as the conditions under which the air leaves the first compressor. and are calculated using the following formulae:

$$T_{c2,in} T_{c1,out} = \frac{P_c}{G_a c_p} + T_{c1,in} \quad (4.53)$$

$$p_{c2,in} = p_{c1,out} = \frac{p_{in}}{\beta_{1c}} \quad (4.54)$$

Also, for the electric compressor, the compressor chosen from the database is the Garrett 550-250, the performance map of the scaled compressor is shown in figure 4.38.

In table 4.16 The outputs of the compressor scaling are shown, while in table 4.17 those of the electric motor.

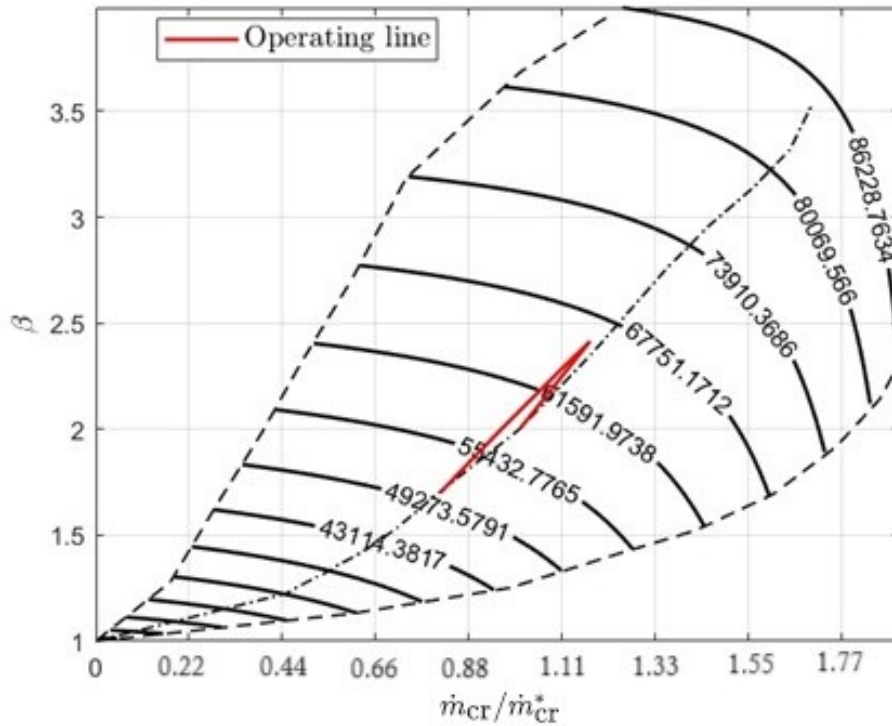


Figure 4.38: Scaled compressor performance map

Inducer (m)	0.102
Exducer (m)	0.128
Diametral footprint (m)	0.361
Axial footprint (m)	0.232

Table 4.15: Technical data for scaled compressor

Maximum armature voltage (V)	690.54
Armature voltage (V)	493.24
Armature resistance (Ohm)	0.738
Armature inductance (H)	7.38
Voltage constant (Vs/rad)	0.501
Torque constant (Nm/A)	0.501

Table 4.16: Electric motor parameters

4.5.3 Architecture comparison

This section analyses and compares the sizing results of the two architectures given in the previous paragraphs and the sizing results of the electric compressor architecture in which there is no energy recovery system through a turbocharger system.

Figure 4.41 compares the fuel cell stack efficiencies of the 3 architectures, these are calculated through the equation (3.4) shown in the performance analysis chapter.

As mentioned in Chapter 2, this efficiency is strictly related to the operating pressure of the FC stack and is higher for the architectures with energy recovery system since they are designed to work at a higher operating pressure, 1.9 atm, than the operating pressure that optimises the electric compressor type architecture which is 1.2 atm.

Since there are no differences in the operation of the stacks between the two architectures with the energy recovery system, the efficiency of these components is the same.

Figure 4.42 compares the plant efficiencies calculated by equation (3.3) and shows that the efficiency of the serial booster and electric turbocharger architectures is about 2% higher than that of the electric compressor architecture. This is due to the energy recovery of the gases coming out of the fuel cell through the turbine, which partially powers the compressor system, reducing the power required to power the electric motor.

This increase in efficiency is not particularly high because the recovery of power via the turbine is mitigated by the additional power required from the compressor for systems with the turbocharger to bring the intake air to an operating pressure of 1.9 compared to 1.2 for the electric compressor system.

The serial booster architecture has a higher plant efficiency. This is because by dividing the compression ratio into two stages, it is possible to use a compressor that works at a higher efficiency than the electric compressor architecture, but this difference is only 0.05% per cent.

In the picture 4.43 is shown the FCPS efficiency trend during the flight mission, this is calculated through the (3.1).

This is the most relevant data as it quantifies the performance of the entire system, and it can be seen that there is a clear improvement in the efficiency of architectures with an energy recovery system compared to the electric turbocharger.

In cruising, the efficiency improvement is about 3.4% this was desirable and is within the values read in the literature[12], [17], [31].

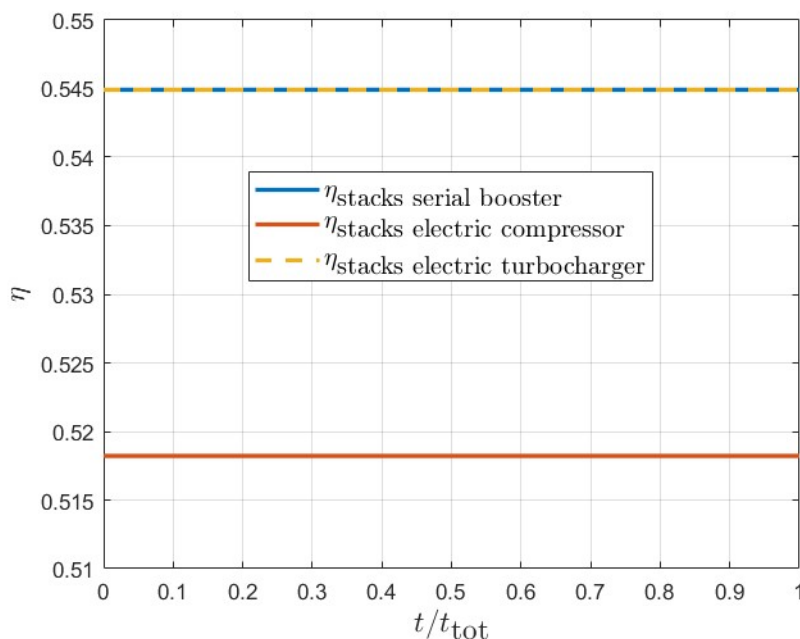


Figure 4.39: Comparison of stacks efficiency trends for the three architectures during the flight mission

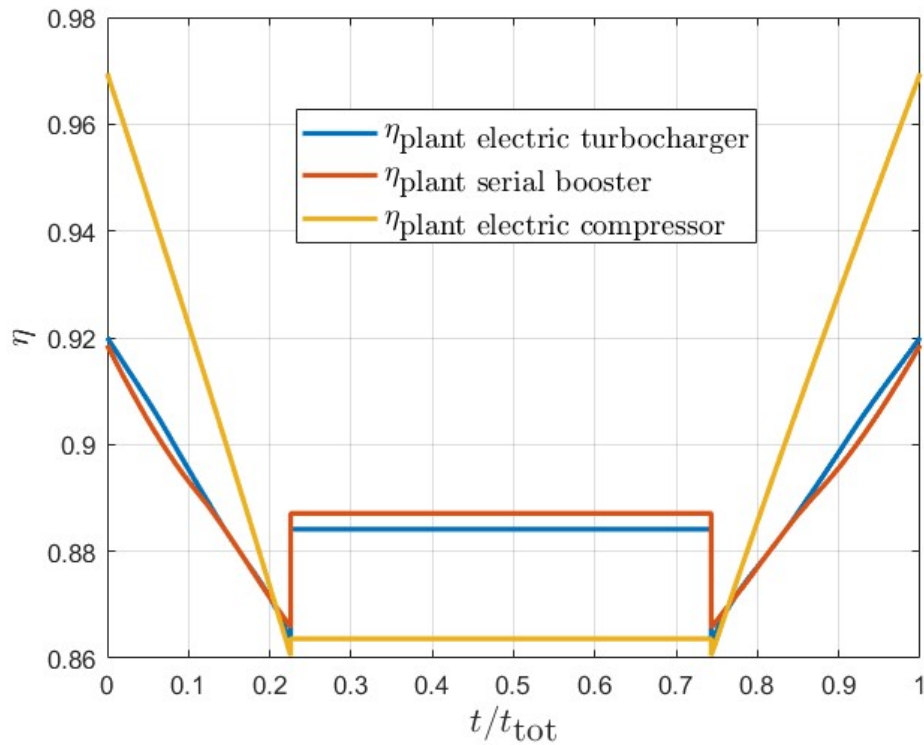


Figure 4.40: Comparison of plant efficiency trends for the three architectures during the flight mission

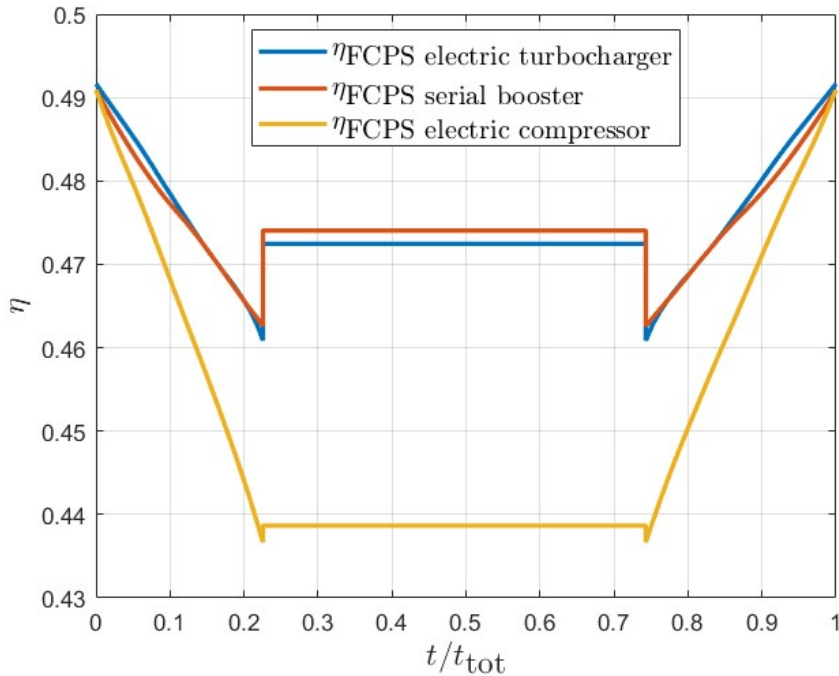


Figure 4.41: Comparison of overall FCPS efficiency trends for the three architectures during the flight mission

By the static sizing of the different architectures, an estimative analysis of the weight and dimensions of the air supply system and fuel cell stacks was conducted. It is emphasised that these values are preliminary approximations and reflect the initial nature of the model itself, which cannot provide

definitive data. However, by exploiting such data, it is possible to understand the influence of the components on the overall weight of the aircraft and make an initial comparison regarding weight and power density between the various architectures and identify the best architecture for the case study considered.

Figure 4.44 shows the total masses of the air supply system which includes the compressor system, the turbine system, and the electric motors.

It can be seen that the weight of the air supply system for the electric turbocharger type architecture is about 3.2% less than the electric compressor type system despite the inclusion of an additional component, i.e., the turbine, in the system.

This can be explained by the fact that the turbine partially powers the compressor, thus reducing the power generated by the electric motor.

In addition, there is also a reduction effect on the size of the compressor system since in order to generate the same amount of net power, the gross power produced by the stacks in cases where there is the energy recovery system must be greater due to the greater power required to feed the electric motor; a greater gross power produced by the stacks means in a greater demand for reactants that the supply systems must guarantee and in particular a greater demand for compressed air that the air supply system must guarantee as shown in equation (3.7).

The serial booster architecture, on the other hand, despite these aspects, has a much greater overall weight since it has two compression stages and consequently an additional component in addition to the turbine.

It is evident, however, that the sizing model applied to turbomachinery within the air supply system is oriented towards maximising system efficiency, neglecting the size and weight of the individual components. Further analysis, including detailed consideration of component dimensions, could probably allow a reduction of the compression system, which is very impactful for this architecture. As mentioned earlier, the electric compressor architecture, without energy recovery through the turbine, requires more gross power to have the same net power output, which implies a greater demand for reagents and also an increase in the size and weight of the stacks (i.e., an increase in the number of stacks arranged in parallel).

Figure 4.45 shows the overall weights of the air supply system and the stacks; it can be seen that the electric turbocharger architecture reduces the overall weight of the system by about 7.4%, while the other two architectures have very similar values.

Figure 4.46 shows the power density values of the three systems over the entire flight mission; this has been calculated as the net power generated by the FCPS during the flight mission divided by the overall mass of the system and is measured in W/Kg; since the net power generated in cruise is the same for the three architectures, the power density during this phase is directly proportional to the mass of the system.

The power density for the electric turbocharger type architecture in cruise is 0.1 kW/Kg greater than the electric compressor type architecture and 0.13 kW/Kg greater than the serial booster type architecture.

It is observed that the electric turbocharger architecture has a higher power density than the other architectures not only during the cruise phase but over the entire flight mission.

In view of the lower power density and weight in the electric turbocharger architecture compared to that of the serial booster, which, on the contrary, presents a higher FCPS efficiency of only 0.03%, the electric turbocharger architecture is chosen as the optimal solution for the case study under consideration. The latter will then be implemented in the dynamic model.

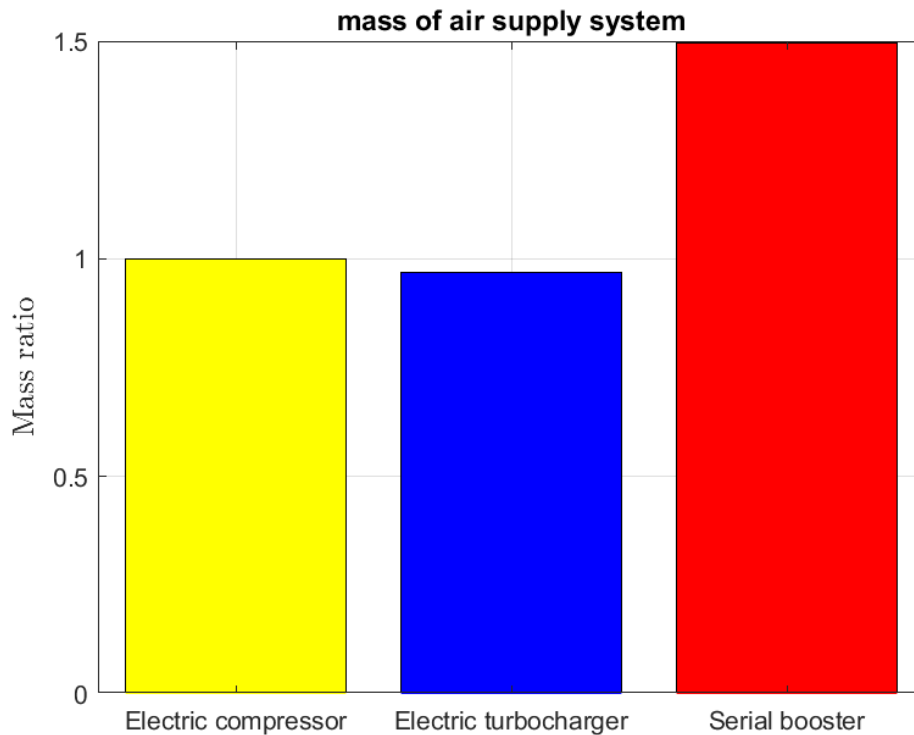


Figure 4.42: comparison of the overall air supply system mass of the three architectures

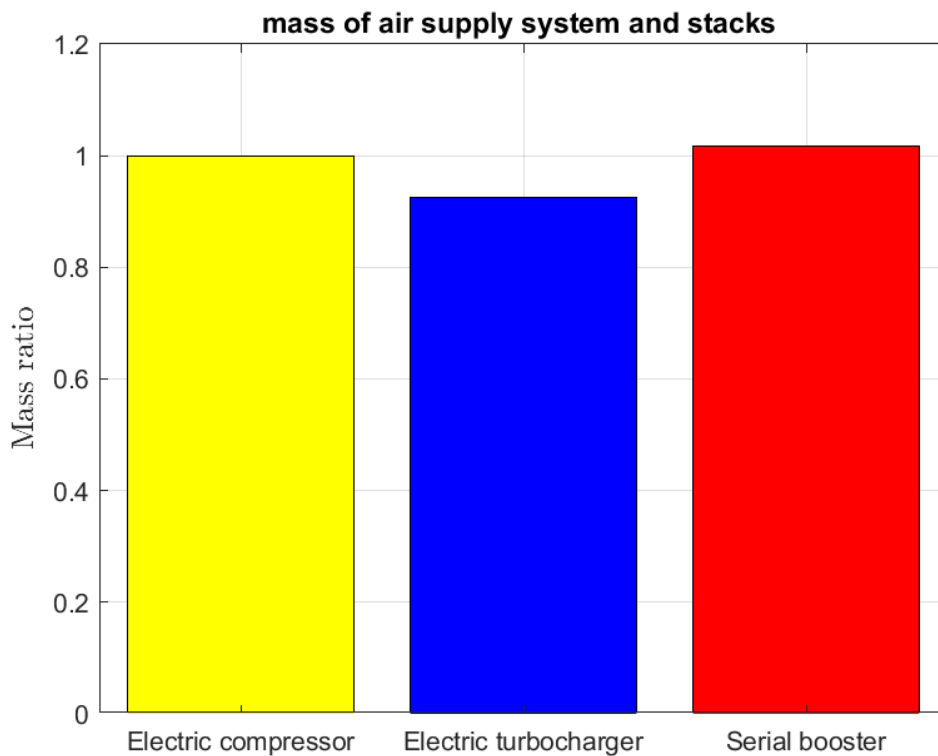


Figure 4.43: comparison of the sum of the mass of the air supply system and the mass of the FC stacks of the three architectures

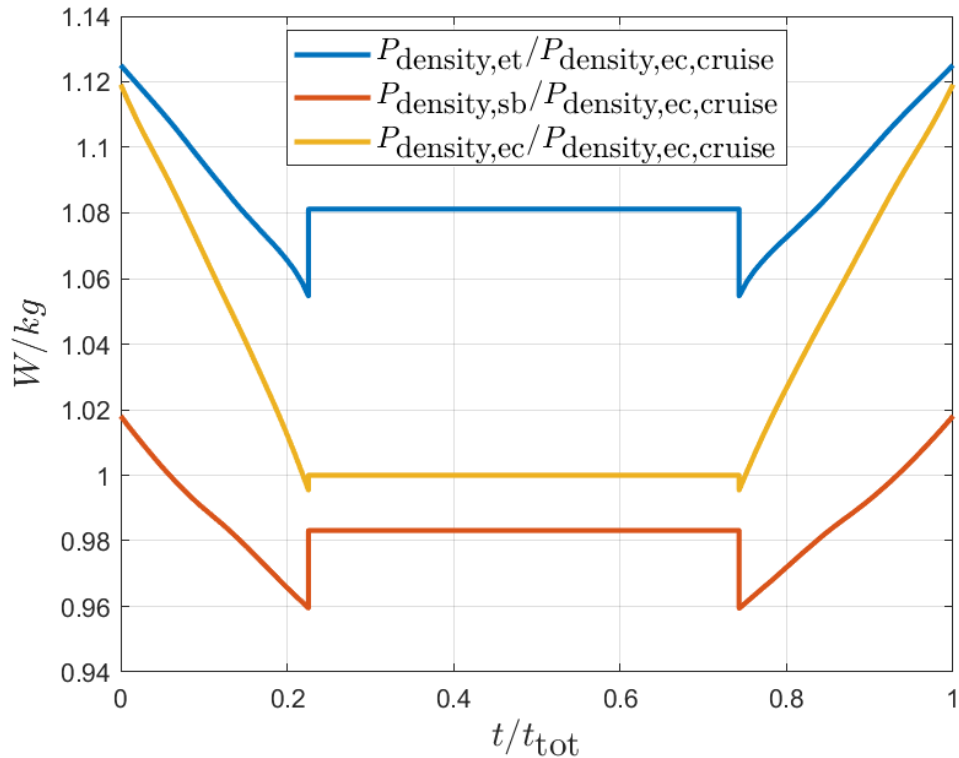


Figure 4.44: comparison of power density between the three architectures, calculated over the entire flight mission.

5 Dynamic model

In this chapter, models are presented of the various components concerning the air supply system with an electric turbocharger type architecture, i.e. one that has a turbine that recovers the energy of the gases exiting the FC stacks, coupled with a compressor to form a turbocharger residing on the same shaft as the electric motor; these models were integrated into the entire FCPS model used in Federico Fasiello's thesis[13], which takes its inspiration from the research of Pukrushpan, Stefanopoulou and Peng[3], in the context of the dynamic simulation of a single power unit.

As mentioned earlier, the static counterpart of some of these dynamic models was used as a model for the performance analysis of the FCPS and static sizing of the air supply system.

Figure 5.1 shows a simplified diagram of the entire modelled FCPS, while Figure 5.2 shows the corresponding dynamic model realised on the Simulink platform.

The dynamic model is represented by a series of blocks, where each block corresponds to a component of the FCPS and is modelled through physical laws describing the behaviour of the component. A crucial part of the modelling process for each individual component is the definition of a component-specific control volume in which these laws are applied.

Each control volume is then characterised by an inlet and outlet flow rate, with the characteristics of the outgoing flow varying from those of the incoming flow due to the thermo-fluid-dynamic phenomena taking place within it.

The model is based on these fundamental assumptions:

- Simplifications of behaviour are adopted for all gases, treating them as ideal gases, including oxygen, nitrogen, hydrogen, and water vapour.
- Simplified modelling is used for all balance-of-plant components except the air supply system, treating these devices as first-order systems with ideal control. This makes it possible to focus exclusively on dynamic air management, which is the goal of this thesis.
- The anode is configured without the use of purification processes and adopting a dead-end approach [13]

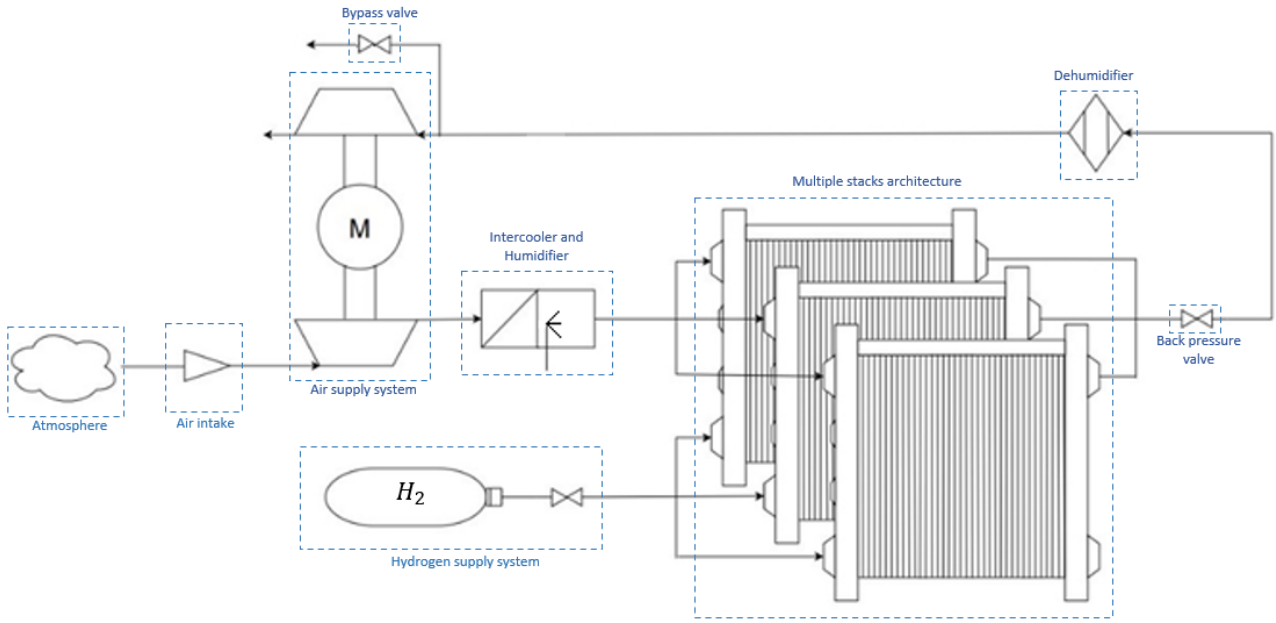


Figure 5.2: Diagram of the FCPS structure

5.1 Cathode model

This section presents the key concepts of the stack cathode model developed in Federico Fasiello's thesis[13]. This part of the model is of fundamental importance for this thesis work, as it illustrates the behaviour of the air flow within the stacks and is based on the assumptions made in the work of Pukrushpan, Stefanopoulou and Peng[3]. Its relevance is highlighted by its implication in the determination of airflows at the turbine inlet and compressor outlet, as well as in the control of the stack's operational flow rate and pressure, essential tasks entrusted to the air supply system.

The assumptions made for this model are as follows:

- In order to facilitate modelling, the air flow conduction paths, the base and cathode layers of the stack are united in a single control volume, i.e. that of the cathode[13].
- The assumption of ideal mixing is made, i.e. that the air properties are uniform, and it is assumed that the following properties of the outgoing air flow do not vary during the reaction and passage through the cathode [13]:

$$T_{ca,out} = T_{ca} = T_{st}$$

$$\phi_{ca,out} = \phi_{ca}$$

$$\gamma_{ca,out} = \gamma_{ca}$$

In the previous thesis, an assumption was made that there was no pressure loss within the stack. However, this assumption was found to be unsuitable for the

objectives of this thesis as it would have resulted in a hypothetical over-estimation of the outlet gas pressure, which would have led to an over-estimation of the enthalpy energy recoverable from the system, affecting the overall performance of the fuel cell power system.

Accurately determining the cathode pressure losses is complex as these depend on the different operating scenarios and the characteristics, shape and size of the stack and MEA; as explained in section 3.1.3 concerning the performance analysis, a constant value for pressure losses of 0.5 bar was considered as reasonable for the specific case under consideration.

$$p_{ca,out} = p_{ca} - \Delta p_{ca}$$

- The water formed as a result of condensation in the cathode region collects in the stack and turns into vapour when the relative humidity falls below saturation conditions[13].

By applying the principle of conservation of mass and the perfect gas law, the following dynamic equations can be obtained in the cathode control volume for the three main constituents of the air flow, i.e. nitrogen, water vapour and oxygen:

$$\frac{V_{ca}}{R_{O_2}T_{st}} \frac{dp_{O_2,ca}}{dt} = \dot{m}_{O_2,ca,in} - \dot{m}_{O_2,ca,out} - \dot{m}_{O_2,react} \quad (5.1)$$

$$\frac{V_{ca}}{R_{N_2}T_{st}} \frac{dp_{N_2,ca}}{dt} = \dot{m}_{N_2,ca,in} - \dot{m}_{N_2,ca,out} \quad (5.2)$$

$$\frac{V_{ca}}{R_{O_2}T_{st}} \frac{dp_{v,ca}}{dt} = \dot{m}_{v,ca,in} - \dot{m}_{v,ca,out} + \dot{m}_{v,react} + \dot{m}_{v,membr} - \dot{m}_{v,ca,out} \quad (5.3)$$

While the values of the reacting flow rates can be calculated from the electrochemical relationships of the cell, in particular the oxygen flow rate consumed during the reaction is given by:

$$\dot{m}_{O_2,react} = mm_{O_2} \frac{n_{cell}I_{st}}{4F} \quad (5.4)$$

Where:

- $\dot{m}_{O_2,ca,in}$ denotes the oxygen mass flow rate entering the cathode.
- $\dot{m}_{O_2,ca,out}$ represents the oxygen mass flow rate exiting the cathode.
- $\dot{m}_{O_2,ca,react}$ signifies the oxygen mass flow rate consumed by the cathode reaction.
- $\dot{m}_{N_2,ca,in}$ stands for the nitrogen mass flow rate entering the cathode.
- $\dot{m}_{N_2,ca,out}$ indicates the nitrogen mass flow rate leaving the cathode.
- $\dot{m}_{v,ca,in}$ is used for the vapor mass flow rate entering the cathode.
- $\dot{m}_{v,ca,out}$ represents the vapor mass flow rate leaving the cathode.
- $\dot{m}_{v,react}$ denotes the vapor mass flow rate generated by the cathode reaction.

- $\dot{m}_{v,membr}$ refers to the vapor mass flow rate due to water transfer phenomena across the membrane.
- $\dot{m}_{l,ca,out}$ is the mass flow rate of liquid water accumulating and leaving the cathode.

The partial pressures of oxygen, nitrogen, and steam, within the stack, are then calculated by solving the dynamic equations 5.1, 5.2 and 5.3.

The inlet flow rates to the stacks can be deduced through knowledge of the inlet flow conditions, while the outlet air flow rate can be calculated through the back pressure valve model and the flow conditions can be determined by formulating an appropriate method for calculating the air properties within the cathode.

As anticipated, in order to further study air handling, it was chosen to neglect the effects on FCPS performance resulting from dynamic variations in humidity levels. Therefore, the assumption is made that the relative humidity at the cathode is kept constant under saturation conditions.

$$\phi_{ca} = 1;$$

The total pressure at the cathode, p_{ca} , can be calculated as the sum of the partial pressures.

$$p_{v,ca} = p_{sat}(T_{st}) \quad (5.5)$$

$$p_{a,ca} = p_{O_2,ca} + p_{N_2,ca} \quad (5.6)$$

$$p_{ca} = p_{a,ca} + p_{v,ca} \quad (5.7)$$

5.1.1 Back pressure valve

To effectively control the air pressure at the stack cathode, a back pressure servo-valve is used, which connects the cathode outlet with the turbine inlet manifold.

It is modelled as a linearised nozzle [13], using the following formula.

$$\dot{m}_{bpv} = k_{bpv}(p_{ca,out} - p_{man,in}) \quad (5.8)$$

Where k_{bpv} is the valve constant and \dot{m}_{bpv} is the flow rate passing through the valve, this value is used to calculate the continuity equations in the cathode model.

After the back pressure valve the fluid passes through a dehumidifier, this component is included as the temperature of the fluid leaving the stack is relatively low and, under these conditions, steam could condense during expansion in the turbine, potentially creating water droplets that could damage the turbine blades.

In this thesis work, the dehumidifier has not been the subject of detailed modelling but is treated as an ideal component. In practice, the steam flow is simply subtracted from the total flow exiting the back pressure valve, neglecting the variation of fluid conditions during the process.

5.2 Air supply system

The components of the air supply system are the turbine and compressor, which form the turbocharger, and the electric motor that resides on the same shaft as the turbocharger.

There is a bypass valve, also known as wastegate, and an exhaust manifold before the turbine that collects the gases leaving the back pressure valve and going to the turbine and partly to the bypass valve if the latter is open.

In the context of this thesis, the turbocharger model was developed from models used in internal combustion engines[51], [52] , where the turbocharger rotational speed is deduced from the dynamic equation of mechanical equilibrium at the shaft of the electric turbocharger. This speed is then used as input into the mass turbine and compressor modules, in which the torque generated by the turbine and the compressor's resisting torque are calculated. These torques, in turn, are introduced as input into the model describing the mechanical equilibrium at the shaft of the electric turbocharger. It is important to note that there is also a mechanical motor in the same turbocharger shaft; therefore, its torque and inertia are added into the mechanical balance equation for the shaft. The details of the models for the compressor and the mechanical motor are discussed extensively in Frederick's thesis [7].

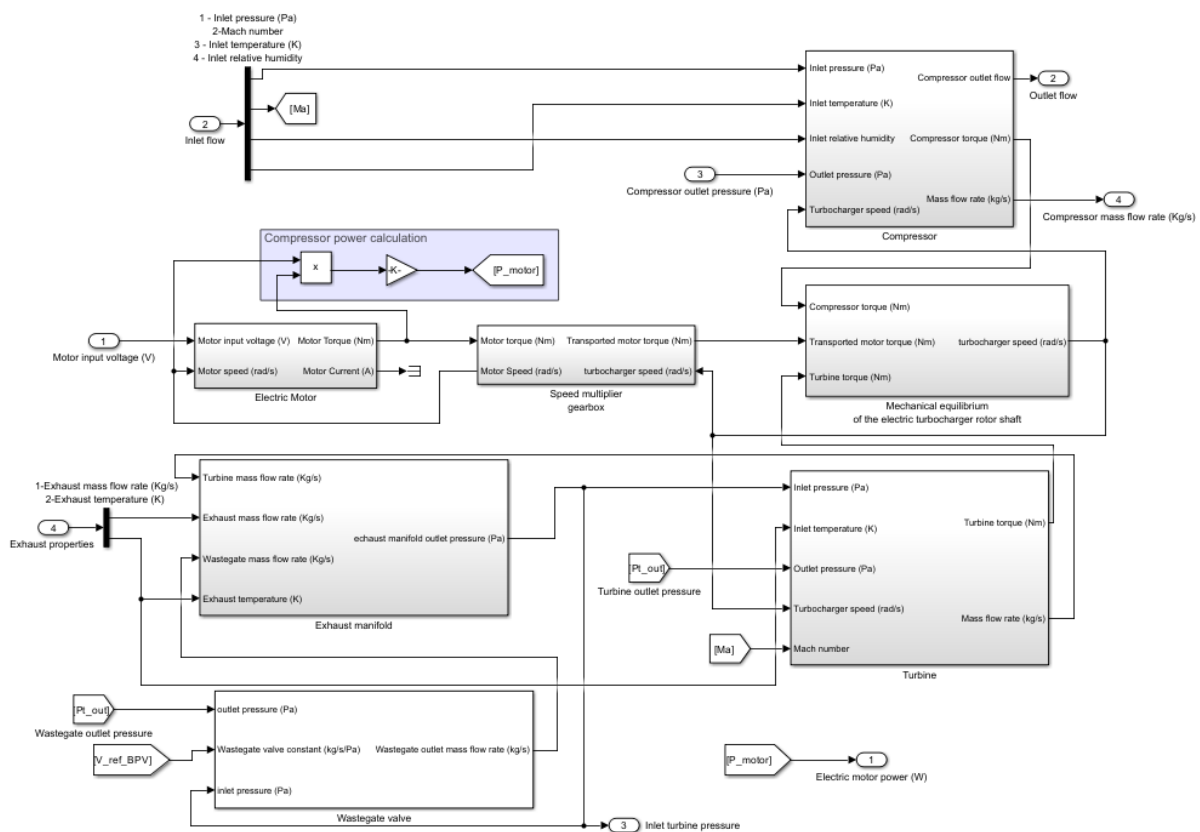


Figure 5.3: Simulink model of air supply system

5.2.1 Turbine

The dynamic model of the turbine is based on the performance maps dimensioned in the static sizing process explained in Chapter 4.

Using the turbine map, it is possible to know the flow rate at which the turbine can work and the efficiency at that working point, if the other parameters at which the turbine has to work are known, i.e., the expansion ratio and the rotation speed, which are inputs to the turbine model.

The expansion ratio shown on the turbine map is equal to the turbine's outlet pressure divided by the inlet pressure; the outlet pressure is the ambient pressure and is calculated using the atmosphere model explained in Federico Fasiello's thesis [7]. while the inlet pressure is given by the dynamic equilibrium at the manifold that collects the gases exiting the back pressure valve; this is calculated as the total pressure by knowing the Mach number of the gases; while the rotation speed is that at which the turbocharger rotates and is calculated through the mechanical equilibrium at the shaft of the electric turbocharger, which will be discussed later.

The flow rate and rotational speed values shown on the turbine performance map are the so-called "correct" values, i.e., normalised with respect to the reference pressure and temperature values. Therefore, it is necessary to calculate the value of the corrected rotation speed by means of formula 5.10; conversely, the flow rate at the output of the map will be the value of the corrected flow rate, the actual flow rate at which the turbine works can therefore be calculated by means of formula 5.11.

The temperature of the gases entering the turbine is considered to be the same as that of the stack since temperature variations at the manifold can be considered negligible, again the total temperature of the fluid is taken into account in the formula.

$$\beta_t = \frac{p_{t,out}}{p_{t,in}^\circ} \quad (5.9)$$

$$n_{cr} = n \sqrt{\frac{T_{ref}}{T_{t,in}^\circ}} \quad (5.10)$$

$$\dot{m}_{t,cr} = \dot{m}_t \frac{p_{ref}}{p_{t,in}^\circ} \sqrt{\frac{T_{t,in}^\circ}{T_{ref}}} \rightarrow \dot{m}_t = \dot{m}_{t,cr} \frac{p_{t,in}^\circ}{p_{ref}} \sqrt{\frac{T_{ref}}{T_{t,in}^\circ}} \quad (5.11)$$

The turbine map is modelled by means of the Jensen and Kristensen formulae [41] already explained in detail in chapter 4.4, in this paragraph they are shown again.

The flow rate is modelled using formulae 4.46 and 4.47, depending on whether the expansion ratio is greater or less than the critical air ratio, in this formula The parameter that is adapted with respect to the experimental values is the effective area of A_t , i.e. the area of the flow passage through the turbine, through the determination of the parameters k_{t1} and k_{t2} . The map was then scaled using the method illustrated in the chapter 4.2.5, all corrected flow values on the turbine performance map are then multiplied by the flow scaling factor found in the static sizing.

$$\phi = A_t \sqrt{\frac{2\gamma}{\gamma-1} \left(\left(\frac{p_{out}}{p_{in}} \right)^{\frac{2}{\gamma}} - \left(\frac{p_{out}}{p_{in}} \right)^{\frac{\gamma+1}{\gamma}} \right)} \text{ for } \frac{p_{out}}{p_{in}} > p_{crit} \quad (4.46)$$

$$\phi = A_t \sqrt{\frac{2\gamma}{\gamma-1} \left((p_{crit})^{\frac{2}{\gamma}} - (p_{crit})^{\frac{\gamma+1}{\gamma}} \right)} \text{ for } \frac{p_{out}}{p_{in}} < p_{crit} \quad (4.47)$$

$$A_t = k_{t1} \left[\frac{p_{in}}{p_{out}} \right] + k_{t2} \quad (4.48)$$

$$K_{ti} = k_{1,i} \frac{N_t}{\sqrt{T_{in}}} + k_{2,i} \quad i = 1; 2. \quad (4.49)$$

Efficiency is calculated as a function of blade speed ratio and turbocharger speed through 4.51 and is fitted against experimental values by determining parameters $b_0, b_1, b_2, b_3, b_4, b_5$.

$$BSR = \frac{U}{C_0} = \frac{\pi D \frac{n}{60}}{\sqrt{2c_p T_{in} \left(1 - \frac{p_{out}}{p_{in}} \right)^{\frac{\gamma-1}{\gamma}}}} \quad (4.50)$$

$$\eta_t = b_0 + b_1 N_t + (b_2 + b_3 N_t) \frac{U}{C_0} + (b_4 + b_5 N_t) \left(\frac{U}{C_0} \right)^2 \quad (4.51)$$

The efficiency shown on the map includes both the isentropic and mechanical efficiency of the turbine through the following formula:

$$\eta_t = \eta_{is,t} \eta_{m,t} \quad (3.18)$$

The maps of the flow and efficiency curves for the turbine were dimensioned in the static sizing and already shown in Section 4.5.1, in Figures 4.29 and 4.30.

The parameters determined through the fitting are shown in table 5.1 and 5.2, where the calculated scaling factor for the corrected flow rate is also indicated.

k_{11}	$1.08 * 10^{-6}$
k_{12}	-0.12
k_{21}	$-7.51 * 10^{-6}$
k_{22}	0.27
Corrected flow scaling factor	3.63

Table 5.1: Fitting parameters of flow curves performance maps

b_0	0.34
b_1	$9.03 * 10^{-6}$
b_2	0.63
b_3	$1.18 * 10^{-4}$
b_4	-0.19
b_5	$-1.51 * 10^{-4}$

Table 5.2: Fitting parameters of efficiency performance maps

Once all the parameters with which the turbine works have been determined, it is possible to calculate the power generated by the turbine using formula 3.15 already presented in Chapter 3.

$$P_t = C_t w_t = \eta_t \dot{m}_t c_p T_{t,in}^{\circ} \left(1 - (\beta_t)^{\frac{\gamma-1}{\gamma}} \right) \quad (3.15)$$

Knowing the turbocharger speed at which the turbine rotates, transformed into rad/s via 5.12, it is possible to calculate the torque generated by the turbine via 5.13.

$$w_t = \frac{2\pi n_{tc}}{60} \quad (5.12)$$

$$C_t = \frac{\eta_t \dot{m}_t c_p T_{t,in}^{\circ} \left(1 - (\beta_t)^{\frac{\gamma-1}{\gamma}} \right)}{w_t} \quad (5.13)$$

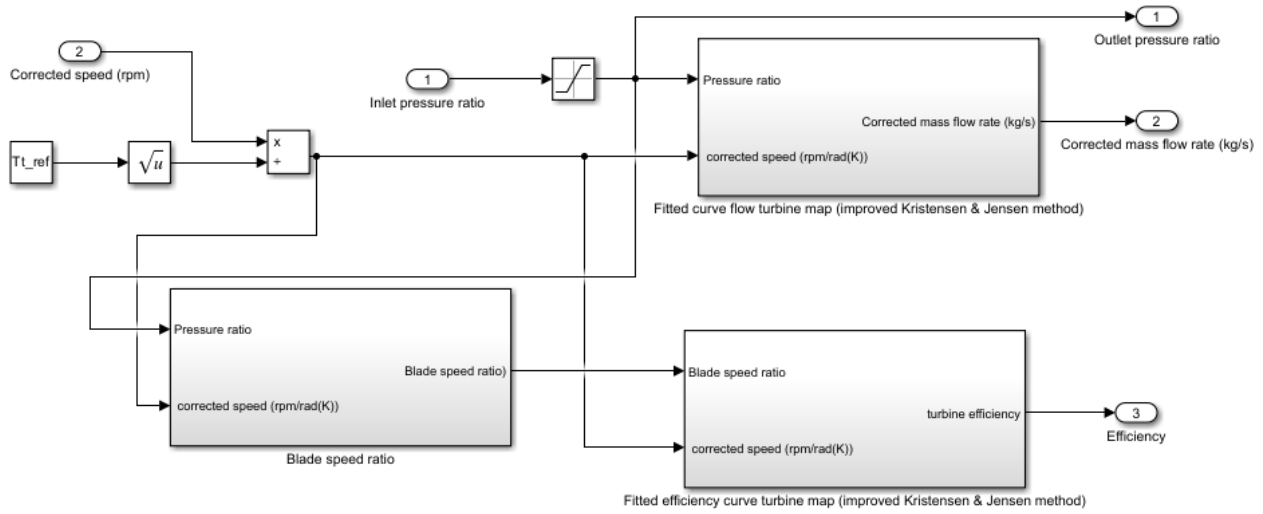


Figure 5.5: Simulink model of turbine maps

5.2.2 Mechanical equilibrium at the shaft

Turbocharger speed dynamics is described by applying Newton's second law for rotating systems that include a dissipative contribution from friction[51], illustrated in the following formula:

$$C_m - I_m \dot{w}_m = -C_t + I_t \dot{w}_t + C_c + I_c \dot{w}_c - C_f \quad (5.12)$$

Where I_m , I_t and I_c are the inertias of the motor, turbine and compressor calculated from static dimensioning, C_m is the motor torque of the motor, C_t the torque of the turbine and C_c the resistant torque of the compressor while C_f is the friction torque component; the latter can be taken into account assuming a plausible transmission efficiency value of 0.95.

$$\eta_{tras} = \frac{P_m}{P_t - P_c} = 0.95 \quad (5.13)$$

Considering that

$$w_c = w_t = w_{tc} = w_m \tau \quad (5.14)$$

Where tau is the transmission ratio from the turbocharger to the motor, the following equation of motion is obtained:

$$\left(\eta_{tras} \frac{I_m}{\tau^2} + I_t + I_c \right) \frac{dw}{dt} = C_m + C_t - C_c \quad (5.15)$$

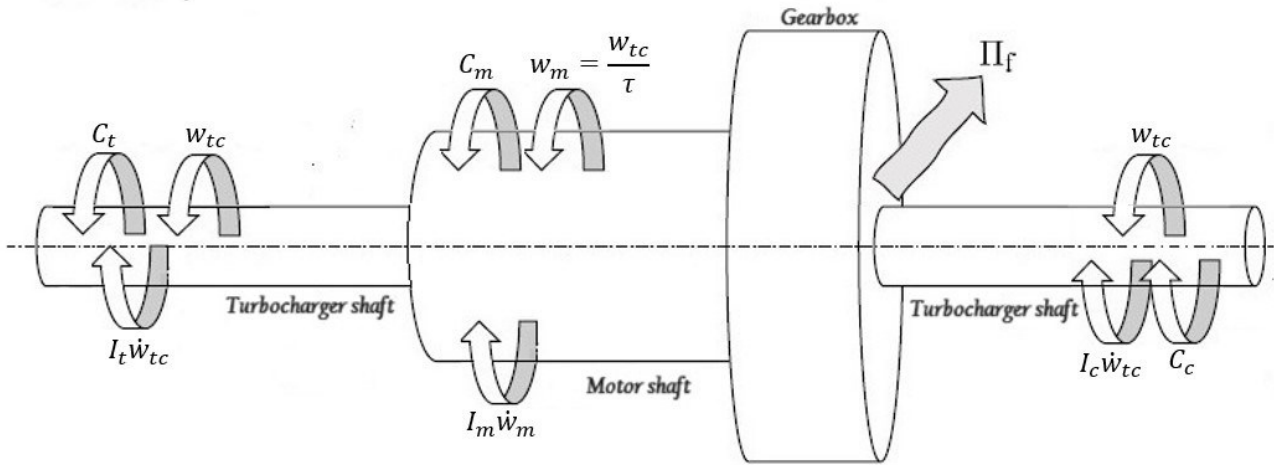


Figure: 5.6: Free body diagram of electric turbocharger shaft

The torque values are obtained in the respective turbine, compressor, and electric motor models as an output, and are an input to this block, as an output to this block the rotational speed of the electric turbocharger unit can be obtained by solving the dynamic equation, this value will go as an input to the turbine, compressor, and motor models.

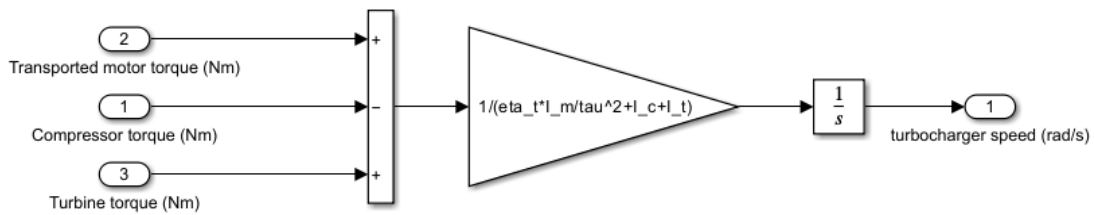


Figure 5.7: Simulink model of mechanical equilibrium at the shaft

5.2.3 Turbine inlet manifold

Gases exiting the back pressure valve before entering the turbine pass into the turbine inlet manifold, the capacitive effects of which are not neglected.

The flow entering the manifold consists of the flow coming from the valve, i.e. from the stack, while the flow leaving the manifold includes the air passing through the turbine and the air passing through the wastegate when the latter is open.

Applying the principle of conservation of mass and the law of perfect gases (under the assumption that the air leaving the stack is an ideal gas) to the manifold, it is possible to obtain the following dynamic equation for the pressure variation.

$$\frac{dp_{em}}{dt} = \frac{RT_{em}}{V_{em}} (\dot{m}_{ex} - \dot{m}_t - \dot{m}_{ppv}) \quad (5.16)$$

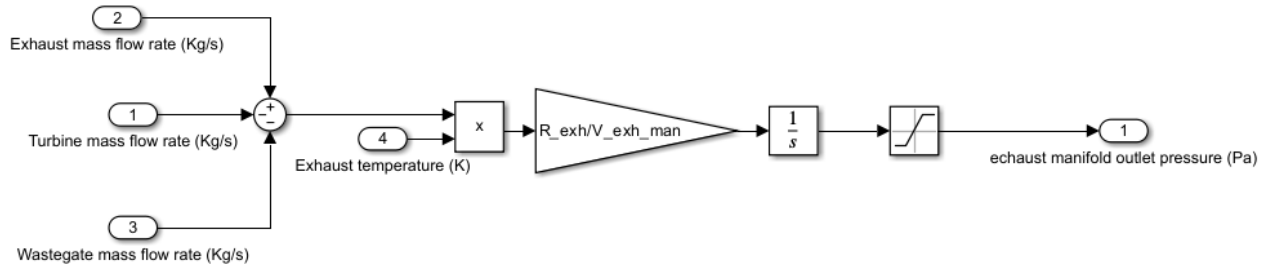


Figure 5.8: Simulink model of turbine inlet manifold

By solving the equation, it is possible to determine the gas pressure at the turbine inlet and wastegate if the latter is open.

The effects of temperature variation at the manifold, however, are neglected.

5.2.4 By-pass valve

As mentioned in section 4.3.1, regulation for off-design conditions is done both through the back pressure valve which regulates the flow of air leaving the stack and through the by-pass valve, this works in synergy with the back pressure valve to adapt the turbine to the different operating conditions of the stack, opening it allows the discharge of excess flow to the flow required by the turbine for the operating conditions to be obtained by lowering the pressure, this too, like the back pressure valve, has been modelled as a linearised nozzle.

$$\dot{m}_{bv} = k_{bv}(p_{man,in} - p_{amb}) \quad (5.17)$$

Where $p_{man,in}$ is the pressure at the turbine inlet manifold and bypass valve while p_{amb} is the outlet pressure from the wastegate i.e., ambient pressure, k_{bv} is the valve constant.

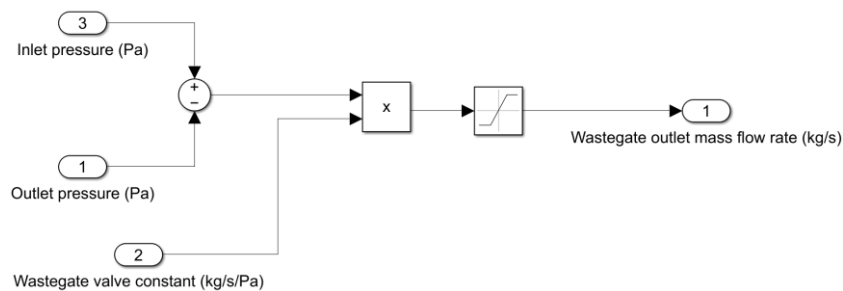


Figure 5.9: Simulink model of bypass valve

6 Control and simulation

In the context of a fuel cell power system, four main control sub-systems can be identified: a system for regulating air, and thus oxygen, at the cathode, a system for regulating the flow of fuel, in this case hydrogen, a system for regulating water, and one for managing temperature[3].

In this thesis the focus is on the air supply system, in order to concentrate mainly on the dynamics of this component, as mentioned above, the other subsystems have been modelled ideally as zero-order systems, and with ideal control [13].

The air supply system is mainly concerned with ensuring the necessary amount of oxygen at the cathode and compressing the air to bring it to the pressure required by the stack; in order to avoid malfunctions, make the system work safely and optimise the performance of the FCPS, two fundamental variables are identified on which to control:

- the excess oxygen ratio must be kept constant and equal to the value that maximises the net power of the FC system identified in the performance analysis. It is essential to maintain an adequate value for this parameter in order to prevent the phenomenon of oxygen starvation. This is a complex phenomenon that occurs when the oxygen partial pressure falls below a critical value at any point during the air flow path within the cathode; this causes an abrupt drop in cell voltage and, under severe conditions, a short circuit can occur [3]
- It is necessary to keep the pressure at the cathode constant equal to the value identified in the performance analysis chapter in order to optimise the performance of the stack and ensure that the compressor works in safe zones on its performance map, avoiding the phenomena of surge, choking and not exceeding the maximum speed values above which the compressor could be damaged.

In the context of this thesis, the current drawn by the load connected to the fuel cell is considered an external disturbance, i.e. a perturbation to which the system must respond appropriately. In reality, this parameter allows the power generated by the system to be regulated; its regulation allows the energy demands to be balanced. However, as far as this thesis is concerned, it can be considered an external disturbance for the air supply system, which is the main component of interest [7].

The values of the required excess oxygen ratio and pressure value, which must be controlled so that they are kept constant during the flight mission, and the current disturbances are shown in the table 6.1.

Oxygen ratio oxygen ratio, λ_{O_2}	2
Cathode pressure, p_{ca}	1.9 bar

Table 6.1: Reference values for control

In the previous thesis work, a control system was implemented that can guarantee the requirements. The excess air parameter is controlled by acting on the voltage signals to the compressor motor $V_{ref,m}$, which is the electric motor responsible for powering the compressor. The pressure, on the

other hand, is controlled via the servo back pressure valve by adjusting the voltage signals $V_{ref,bpv}$, sent to it.

Both control systems used are feedforward controls; that is, a control in which external disturbances are measured and taken into account before they have the opportunity to affect the system. In this type of control, the adjustment of the control variable is not based on error, but rather on knowledge of the process through a mathematical model of the process and the acquisition of data on process disturbances.

To be reliable, the disturbance signal and its effect on the system output must be well known[53] This type of control is considered to best respond to the effects of the current disturbances considered in the thesis work.

In this thesis, by adding the turbine that partially feeds the compressor together with the electric motor, it is necessary to include an additional control component to handle off-design conditions and adapt the turbine to the stack and the compressor under all operating conditions.

The stack pressure is the result of balancing the characteristic operating points of the compressor and turbine, identified on the performance maps, at a specific turbocharger speed [16]

For pressure control, the configuration of the thesis of Uhrig et al.[16] discussed in Chapter 4 is used, where the operating pressure is controlled synergistically through two valves, the back pressure valve inserted downstream of the stack allows the flow of air exiting the stack to be reduced by increasing the pressure, while the bypass valve, opening, allows the gases exiting the stack to be increased by decreasing the operating pressure at the cathode of the stack.

The bypass valve can be used in a similar way to the way it is used for internal combustion engines; when it opens, it allows part of the outgoing air flow from the stack to be discharged by bypassing the turbine, in this way it is possible to lower the pressure of the flow exiting the compressor and entering the stack when it exceeds the reference pressure value that is to be kept constant.

Feed-forward control is maintained through the back pressure valve by means of which an effective and rapid response to current disturbances can be achieved.

The system is simulated in various scenarios in order to test the control system.

First, the entire flight mission of the aircraft is simulated, in which changes in environmental conditions are considered dynamic effects to which the system must respond appropriately; then several simulations are carried out in which the system's response to dynamic changes in the current absorbed by the stacks, which is entered as a disturbance, is evaluated.

6.1 Control design

In this thesis, a control system is proposed based on the system considered in Federico Fasiello's thesis [7], suitably modified to adapt it to specific requirements. In particular, an additional pressure control was integrated through the use of a bypass valve, in order to adapt the behaviour of the turbine to the different operating conditions of the system.

To control the flow of air sucked by the compressor, a closed-loop control with a static feed forward was used, in which the set value is estimated from the current drawn from the stack, inserted as an external disturbance, knowing the value of excess oxygen that is to be kept constant, according to formula 6.1 which models the air flow required by the stack.

$$\dot{m}_{c,SET} = \frac{\lambda_{O_2,SET} m m_{O_2}}{4F x_{O_2}} n_{cell} n_{stacks} I_{st} \quad (6.1)$$

The flow sucked by the compressor is measured via a flow sensor and the value is feedbacked to the loop; through the difference between the set value and the feedback value, an error is generated which is compensated by a PI controller, which generates a reference voltage signal to the electric motor, increasing or decreasing the motor torque, thus influencing the balance at the shaft of the electric turbocharger in such a way as to adjust the compressor speed and thus the flow sucked by the latter, moving on the performance map.

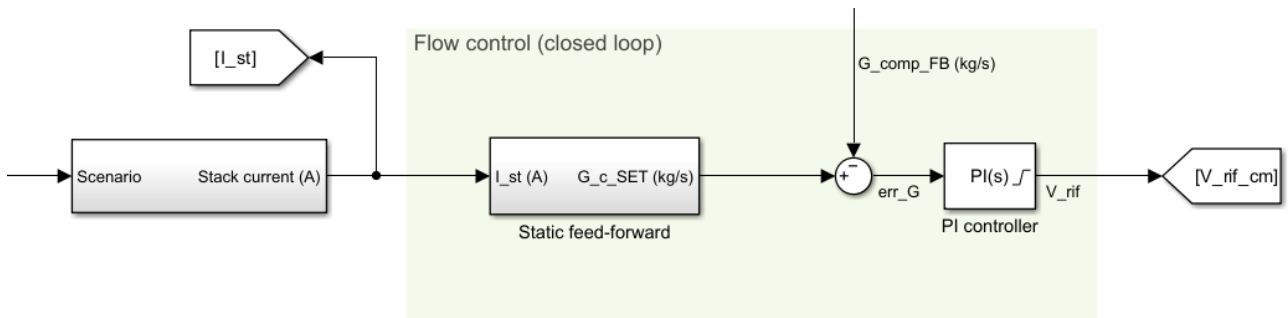


Figure 6.1: Closed loop flow control

As mentioned, pressure control is done both through the back pressure valve and the bypass valve. For the back pressure valve, the control based on a static feedforward with open-loop control proposed in Federico Fasiello's cit... has been maintained, in which the flow rate that must exit the stack under steady-state conditions is calculated from the current drawn from the load, inserted as a disturbance, through formula 6.2; if this flow rate is maintained at the exit of the stack, then the pressure remains constant according to the law of continuity applied to the stack in formula 5.1.

$$\dot{m}_{bpv}^* = (1 + w_{ca}^*)(\dot{m}_{ca,in}^* - m_{O_2,react}) \quad (6.2)$$

Where:

- \dot{m}_{bpv}^* is the estimated flow rate to pass through the back pressure valve under steady-state conditions, denoted by an asterisk.
- w_{ca}^* is the humidity ratio, i.e., the ratio of the vapour flow rate in the air to the air itself, also calculated at steady-state conditions.
- $\dot{m}_{ca,in}^*$ is the inlet flow rate at the cathode under steady-state conditions calculated via 6.1.
- $m_{O_2,react}$ is the amount of oxygen consumed during the reaction, calculated via 5.4.

By dividing the flow by the pressure gradient at the valve ends, the reference voltage value sent to the back pressure valve is calculated; the pressure gradient is calculated by entering the desired stack pressure as the set pressure upstream of the valve, also considering the assumed constant

losses at the cathode, while the downstream pressure is the pressure at the turbine inlet manifold, which is measured.

As mentioned, pressure control is done both through the back pressure valve and the bypass valve. For the back pressure valve, the control based on a static feedforward with open-loop control proposed in Federico Fasiello's thesis [7] has been maintained, in which the flow rate that must exit the stack under steady-state conditions is calculated from the current drawn from the load, inserted as a disturbance, through formula 6.2; if this flow rate is maintained at the exit of the stack then the pressure remains constant according to the law of continuity applied to the stack in formula 5.1.

$$\dot{m}_{bppv}^* = (1 + w_{ca}^*)(\dot{m}_{ca,in}^* - m_{O2,react}) \quad (6.2)$$

Where:

- \dot{m}_{bppv}^* is the estimated flow rate to pass through the back pressure valve under steady-state conditions, denoted by an asterisk.
- w_{ca}^* is the humidity ratio, i.e. the ratio of the vapour flow rate in the air to the air itself, also calculated at steady-state conditions.
- $\dot{m}_{ca,in}^*$ is the inlet flow rate at the cathode under steady-state conditions calculated through 6.1.
- $m_{O2,react}$ is the amount of oxygen consumed during the reaction, calculated via 5.4.

By dividing the flow by the pressure gradient at the valve ends, the reference voltage value sent to the back pressure valve is calculated; the pressure gradient is calculated by entering as the set pressure upstream of the valve the pressure of the stack to be obtained, also considering the assumed constant losses at the cathode, while the downstream pressure is the pressure at the manifold.

$$k_{bppv}^* = \frac{\dot{m}_{bppv}^*}{p_{ca,SET} - p_{t,in}} \quad (6.3)$$

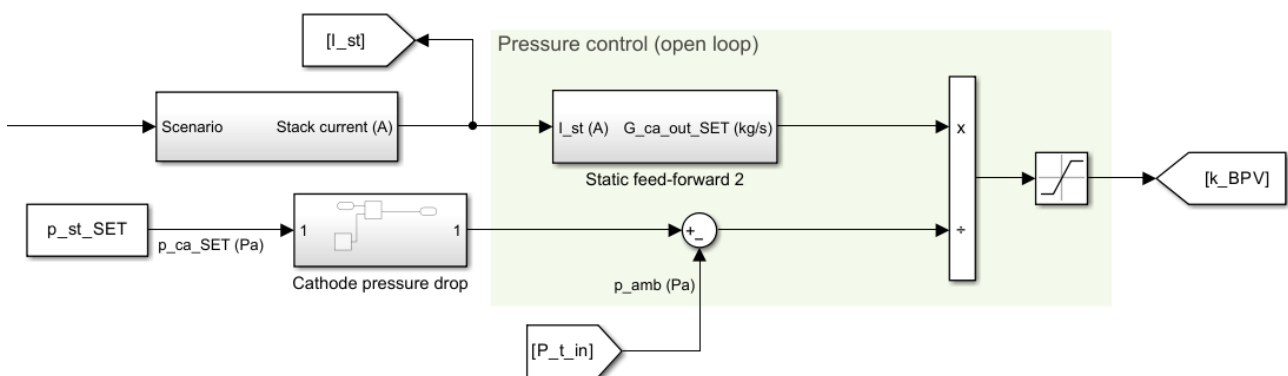


Figure 6.2: Open loop pressure control

The pressure at the turbine inlet manifold is controlled by the bypass valve so that it does not exceed the value of the pressure required by the reference stack to be controlled.

A closed-loop control system has been implemented in which the pressure in the turbine inlet manifold is measured and used as feedback in the control system. When the pressure exceeds the desired value in the stack, considering the losses at the cathode (which, as mentioned, in this thesis work are considered constant, to a first approximation) an error is generated, which the controller compensates for by means of a PI control by issuing a reference signal to the bypass valve that opens, thus reducing the pressure.

Opening the bypass valve allows the flow of gas out of the stacks to be increased, allowing the operating pressure to be lowered when necessary.

When the amount of air leaving the stack is greater than that required by the turbine to rotate at the turbocharger's rotational speed and the required expansion ratio, there is an increase in pressure at the turbine inlet, according to the dynamic manifold model presented in the previous chapter.

If the by-pass valve were not present, the pressure would increase until a new equilibrium point is found on the performance curves of the compressor and the turbine, which must rotate at the same speed, where the flow coming from the stack coincides with that required by the turbine. At this new equilibrium point, the pressure exiting the compressor would exceed the required pressure at which the stack is to work, making control with the bypass valve alone ineffective.

In addition, the bypass valve also allows the compressor to operate in safe zones, below the maximum permitted speeds.

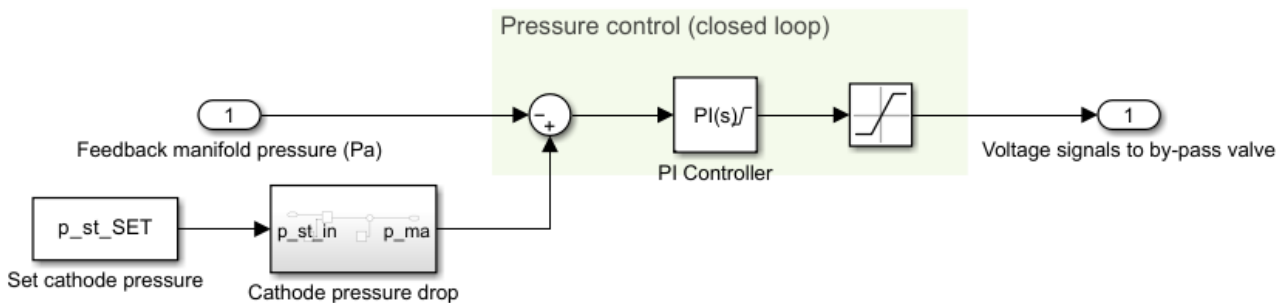


Figure 6.3: Closed loop pressure control

6.2 Simulation

6.2.1 Flight mission

Initially, a simulation is carried out to evaluate the behaviour of the system during the entire flight mission; for this simulation, the changes in atmospheric conditions, temperature, and pressure, which vary with the altitude reached by the aircraft (shown in figure 6.4) can be considered as dynamic effects to which the system must respond.

Figure 6.4 shows the trend of the variables controlled, small variations are observed from the set conditions, for all three variables, in the climb and descent phases; these are due to the variation of

environmental conditions during the mission, however they are insignificant, less than 1%, and do not compromise the correct functioning of the system.

Figures 6.5, 6.6, 6.7 and 6.8 show the performance maps of the turbine and compressor and the map of the electric motor; the red lines indicate the union of the operating points of the three components during the flight mission.

It can be seen that the compressor always operates within the safe conditions of the performance map; both the compressor and the turbine also show high efficiencies throughout the flight mission, indicating a good result for the static sizing of these component maps. It can be seen that the operating lines are very similar to those assumed in the static sizing.

Figure 6.11 shows the trend of the reference signal that controls the bypass valve; it can be seen how the valve opens in the climb and descent phases, since in these phases there is an imbalance between the flow rate arriving at the turbine and that required by the turbine in order to work at the rotational speed dictated by the dynamic equilibrium at the shaft of the electric turbocharger.

If the valve did not open, the imbalance between the two flow rates would lead to an increase in the turbine inlet pressure until the flow rate arriving at the turbine is equal to that required for the operating conditions under which it is working. This would modify the conditions at the balance of the torques at the turbocharger shaft, thus increasing the compressor outlet pressure and therefore the operating pressure of the stack, exceeding the set pressure value which is to be maintained.

It is shown, however, how in the cruise phase the valve remains closed; this was a desired result since the turbine was sized specifically to work at the operating conditions dictated by the compressor and the stack in this phase, so as to be able to exploit all the energy of the gases exiting the stack.

Figure 6.12 shows the trend of the torques generated by the electric motor from the turbine and compressor. As the altitude increases, the resistant torque of the compressor increases as more power is required to compress the air to a greater pressure ratio; therefore more torque is required from the electric motor to make the compressor turn at the required speed, however, the increase in torque that the motor must generate is compensated for by the increase in torque generated by the turbine, which is able to exploit a greater expansion ratio and also greater flow rate at the exit of the stack.

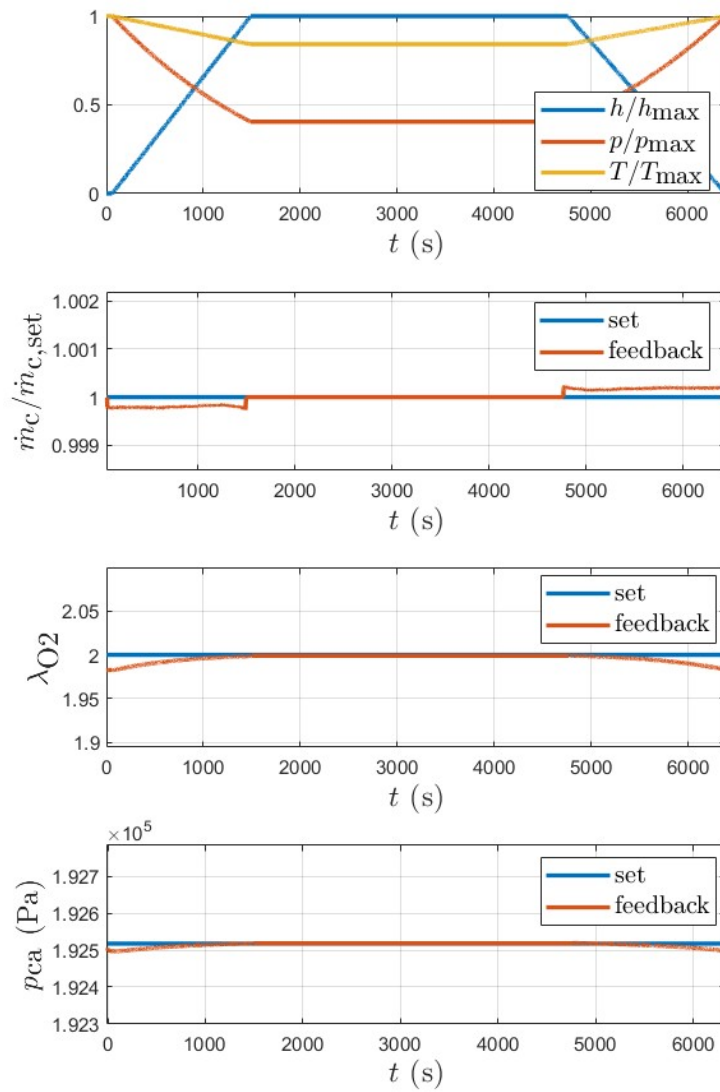


Figure 6.4: trend of controlled variables

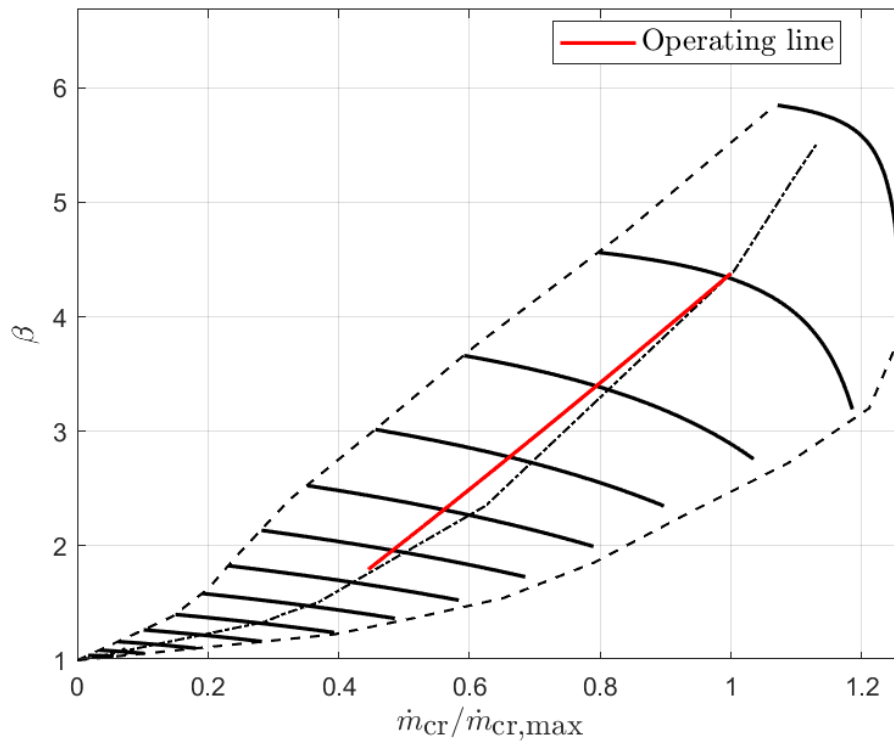


Figure 6.5: Compressor performance map

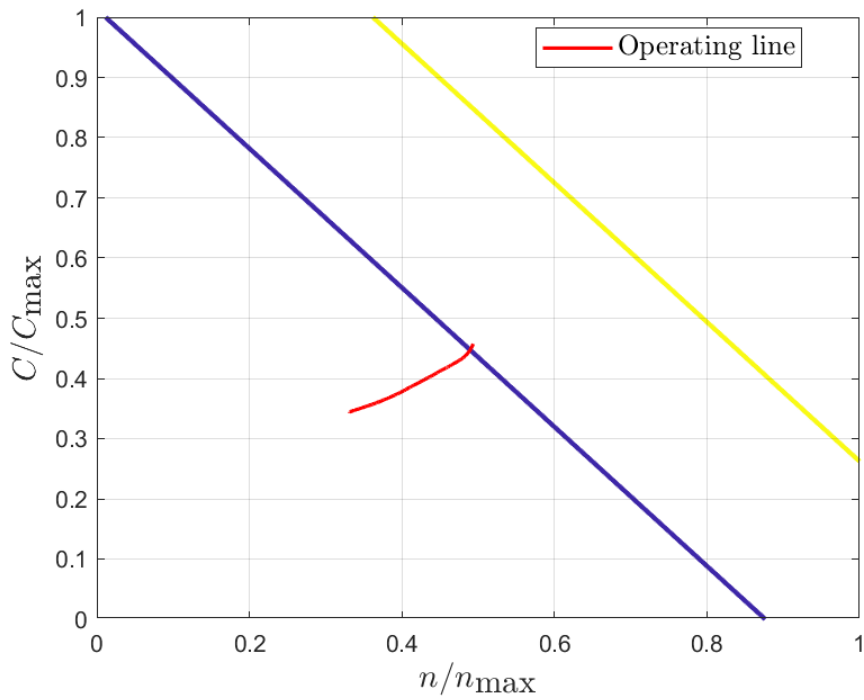


Figure 6.6: Motor map

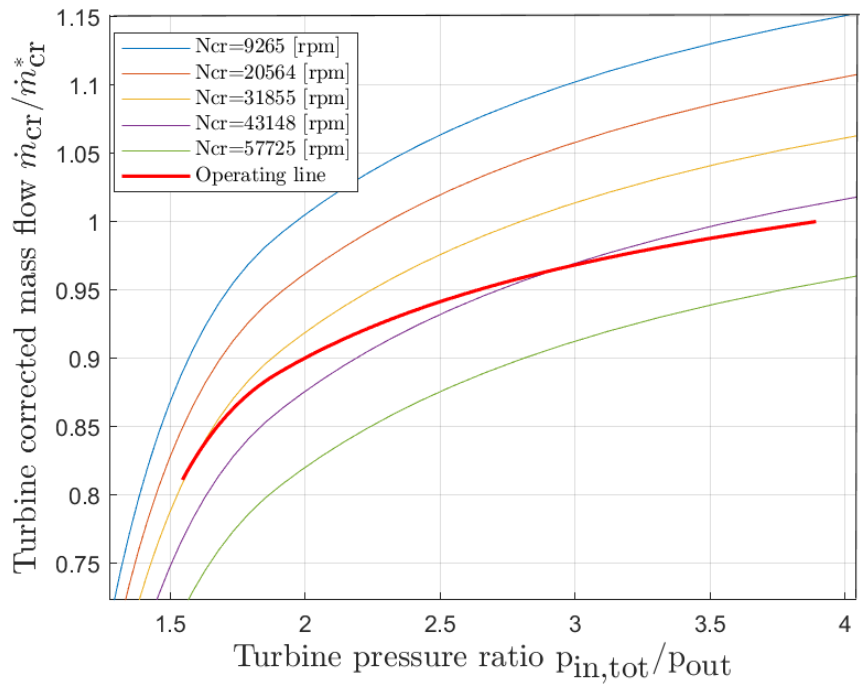


Figure 6.7: Performance map for turbine flow curves

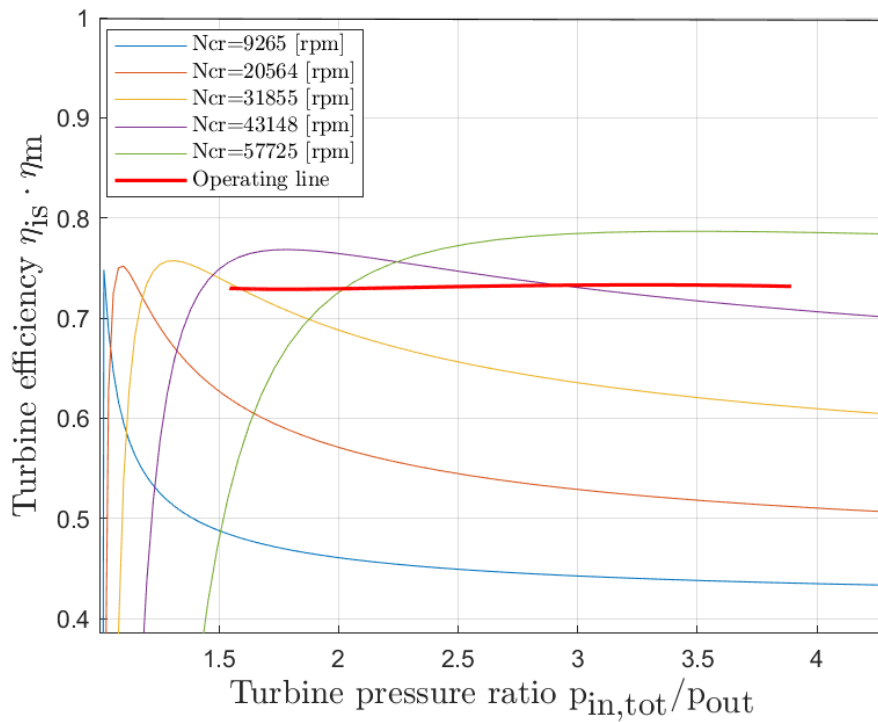


Figure 6.8: Performance map for turbine efficiency

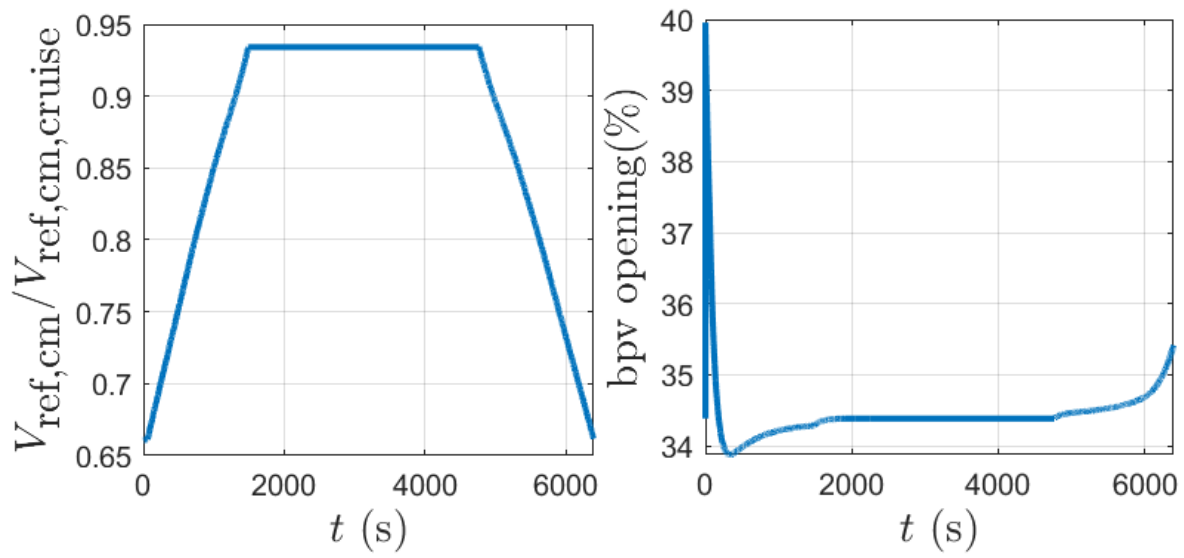


Figure 6.9: Reference voltage signals for the motor and the back pressure valve

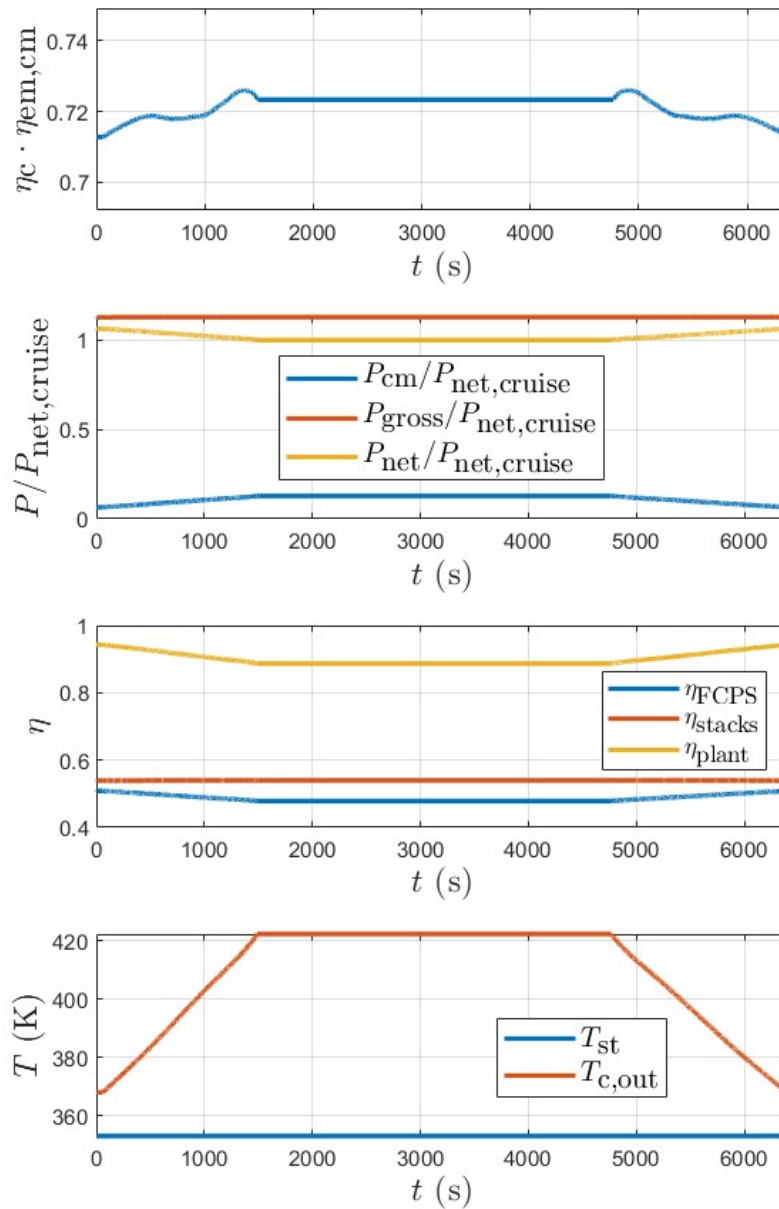


Figure 6.10: Trend of the performance parameters

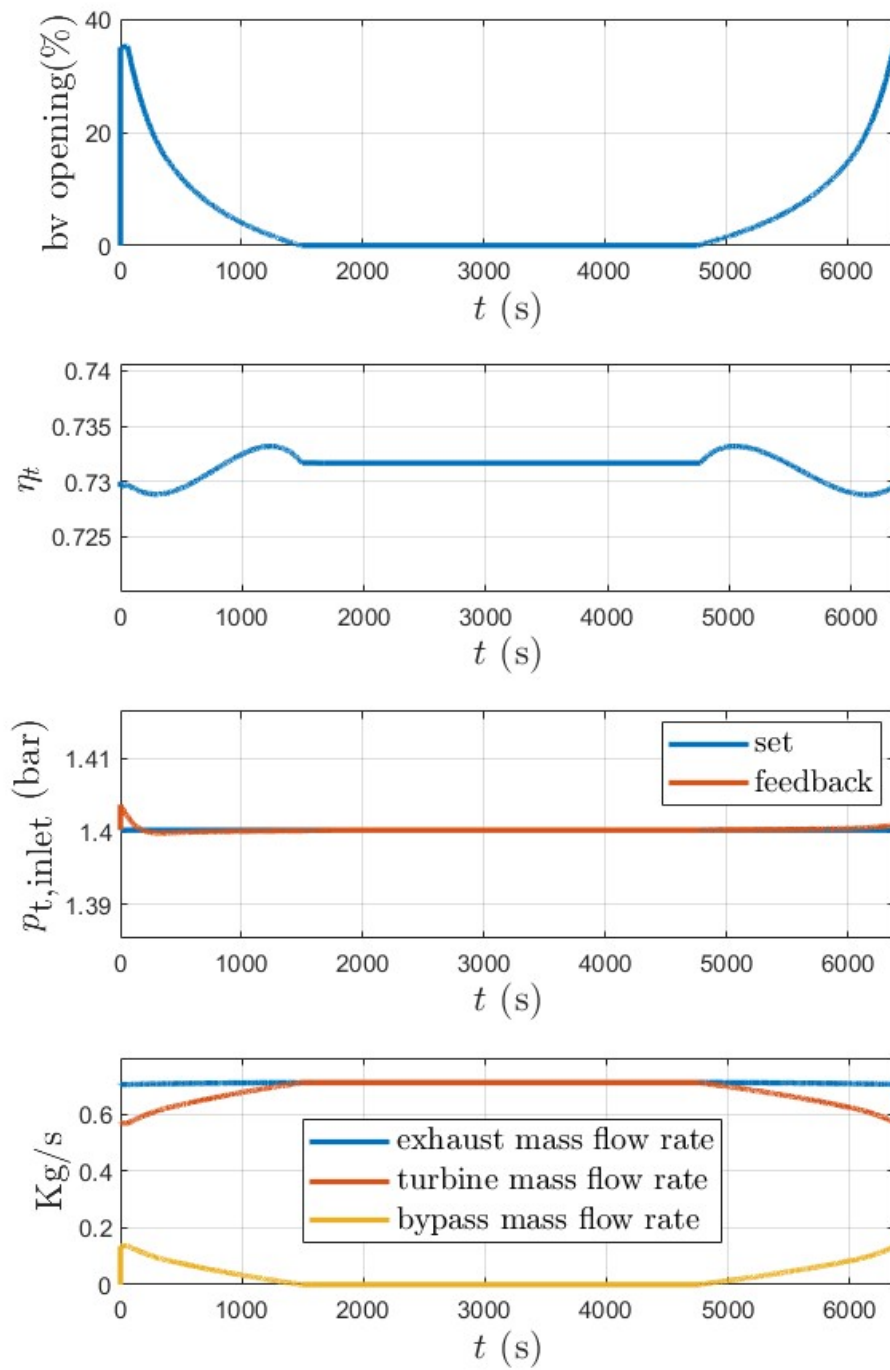


Figure 6.11: Control parameters for the bypass valve and turbine efficiency

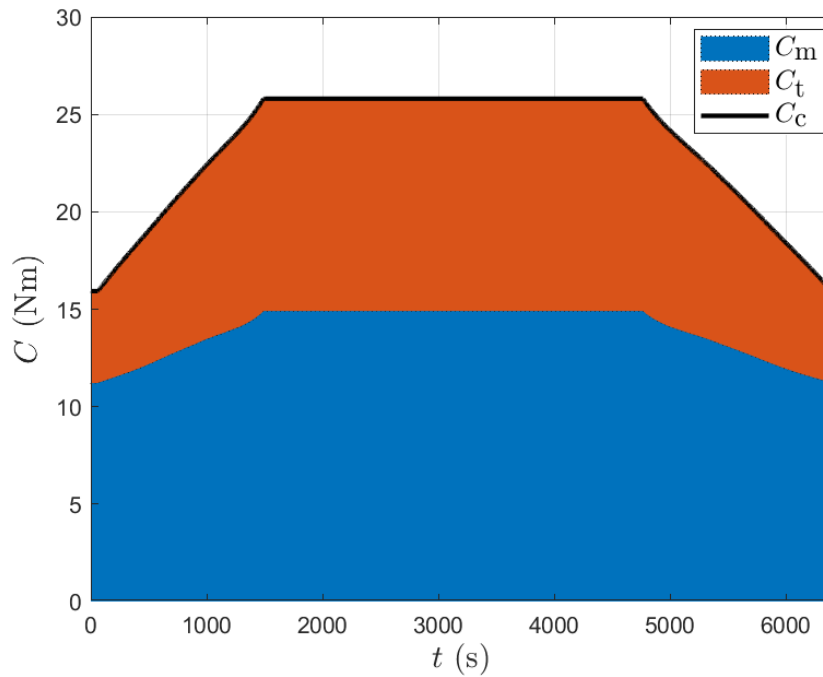


Figure 6.12: Trend of motor, compressor and turbine torques

6.2.2 Current disturbances

The system response to dynamic changes due to the application of the current disturbance was then evaluated.

Initially a positive step current disturbance of 50 A, about 15% of the nominal value, is applied at the time of 60 seconds; the value of oxygen flow reacting in the redox reaction increases with the current because it is directly proportional to the current absorbed by the cell; since the air supply system has its own dynamics it responds with a certain delay to the disturbance, and fails to instantly follow the increased air demand that the compressor must suck, this causes a decrease in the ratio of excess oxygen, this effect is observed in Figure 6.14.

The back pressure valve, instead, is controlled in feedforward; in figure 6.13 it is shown the course of the reference signal sent to the valve, is noticed as the valve is opened answering immediately to the noise, second formula 6.2; This increases the flow rate from the stack, which causes an instantaneous decrease in cathode pressure as seen in Figure 6.12

The increase of flow in exit from the stack directed in entrance to the turbine, provokes a difference between the flow in entrance to the turbine and that demanded from the turbine when it turns to the spin speed of the electric turbocharger group, and for the required expansion ratio; this imbalance brings an increase in pressure to the manifold of entry to the turbine generating an error that the controller of the bypass valve compensates, sending a reference signal to the bypass valve that, opening, lowers the pressure, balancing the flow that comes from the stack and that required by the turbine in the operating conditions that you want to maintain. These effects are visible in Figure 6.20.

It is observed that the bypass valve remains open following the application of the current step, this allows to maintain a new equilibrium condition between the characteristics of the compressor, stack

and turbine, obviously in the new equilibrium condition it is not possible to exploit all the energy of the gases coming out of the stack in the turbine, with a consequent lowering of the performances; the condition in which it is possible to exploit all the energy of the gases coming out of the stack and in fact obtainable are at the project point.

The feed forward control on the flow allows to increase the value of the set air flow that the compressor must suck according to the formula 6.1, thus generates an error between set and feedback (i.e. the flow sucked by the compressor measured) that the controller compensates by increasing the reference voltage to the motor; the increase in voltage to the motor armature causes an increase in the current of the armature, generating a greater torque.

The greater torque generated by the engine wins the inertia of the turbocharger and generates an imbalance to the turbocharger shaft accelerating it; a new equilibrium point is obtained on the compressor and turbine map, allowing the compressor to suck the required amount of air; this effect causes an increase in the values of excess oxygen and pressure at the cathode that return to the reference values that you want to keep constant.

The course of the torques of motor, compressor and turbine is visible in figure 6.21; it is observed as the torque of the motor increases as a result of the increase of the signal V_{ref} , with a certain delay due to the dynamics of the motor. As a result of the acceleration a new balance is found to the shaft of the electric turbocharger that returns to turn at constant speed, with the algebraic sum of the pairs acting on the shaft equal to zero.

The resistant torque of the compressor increases because processing greater flow requires more power while the torque generated by the turbine decreases slightly because there is a slight decrease in the flow exploited by the turbine at the new speed, even if this effect is minimal. In the new equilibrium position, therefore, the electric motor must generate a greater torque, and this provokes an increase of the power demanded from the motor and a decrease of the efficiency of the system as visible in figure 6.19.

There is also a decrease in stack efficiency following the current step, this is due to the increase in voltage losses as the current density increases as observed by the polarization curve and consequently the decrease in the overall efficiency of the FCPS.

Then, the system response to the application of a train of steps is evaluated, several pulses have been applied that have a duration of about 5 seconds with step values of about 15% of the nominal current load.

In this simulation it is observed in figure 6.22 that, when a negative step of current is applied, the back pressure valve is closed in order to maintain constant the pressure to the stack, through the control in feedforward; in this case, an imbalance is created between the inlet flow to the turbine and that required by the turbine, which is greater.

This causes a lowering of the pressure at the manifold at the inlet to the turbine, (and then a lowering of the expansion ratio to the turbine) until the flow required by the turbine on its performance map reaches the output from the stack; In this condition the bypass valve remains closed, since it is only used to open by lowering the pressure, this can be seen in Figure 6.27.

The pressure at the stack, however, does not decrease thanks to the presence of the back pressure valve that keeps the pressure upstream of it, constant.

Finally, the system response to a noise situation closer to reality was simulated, applying a Gaussian noise signal on the current absorbed by the load connected to the fuel cell system.

For all simulations performed, an appropriate system response shall be observed, in which the reference variables checked are kept at the desired value with rapid response and overshoot not exceeding the allowed values, not affecting the functioning of the system.

The pre-set conditions have been fully met: the compressor always works under safe conditions, that is, at stability points of its performance map, the excess oxygen value does not fall below the critical value of 1,2 which may lead to the phenomenon of reagent starvation and pressure fluctuations at the cathode do not exceed the indicative safety values of 100-200mbar.

6.2.2.1 Positive step

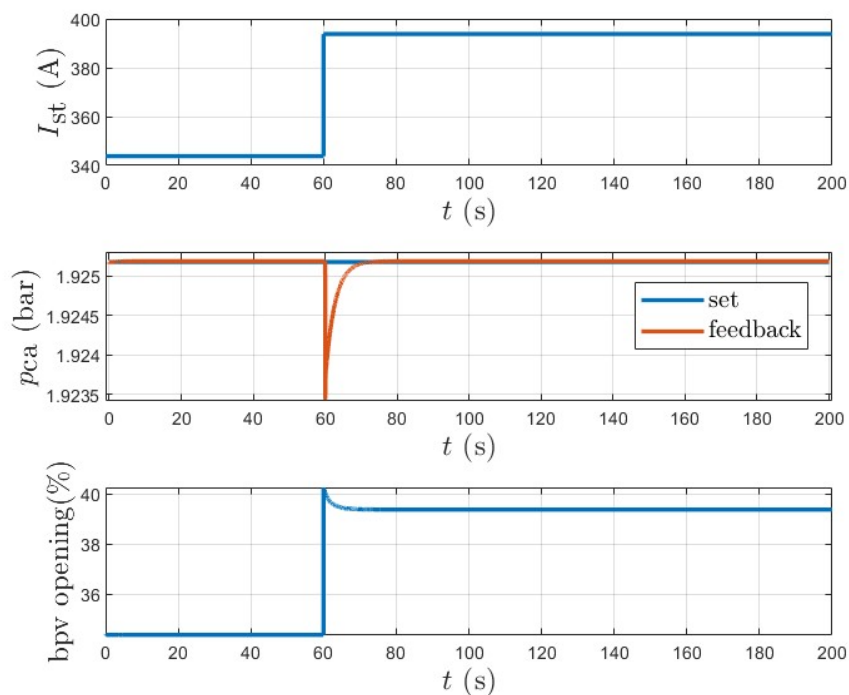


Figure 6.13: Effects of positive current step on pressure control

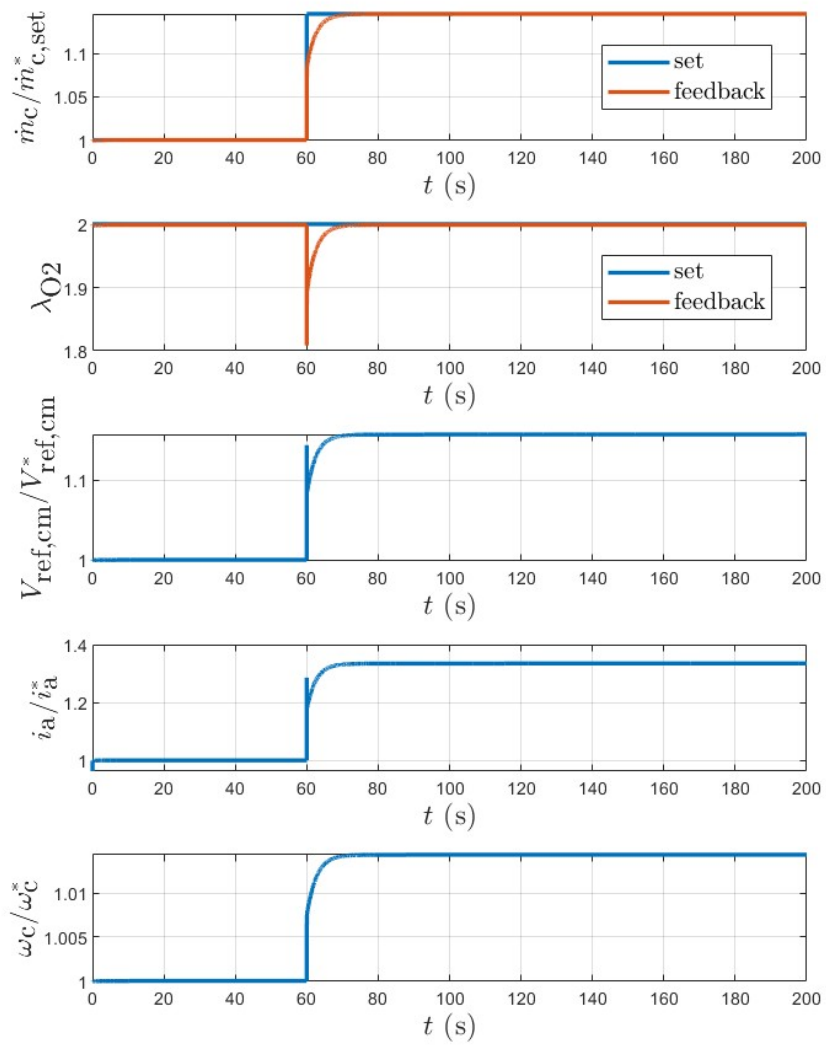


Figure 6.14: Effects of positive current step on mass flow control

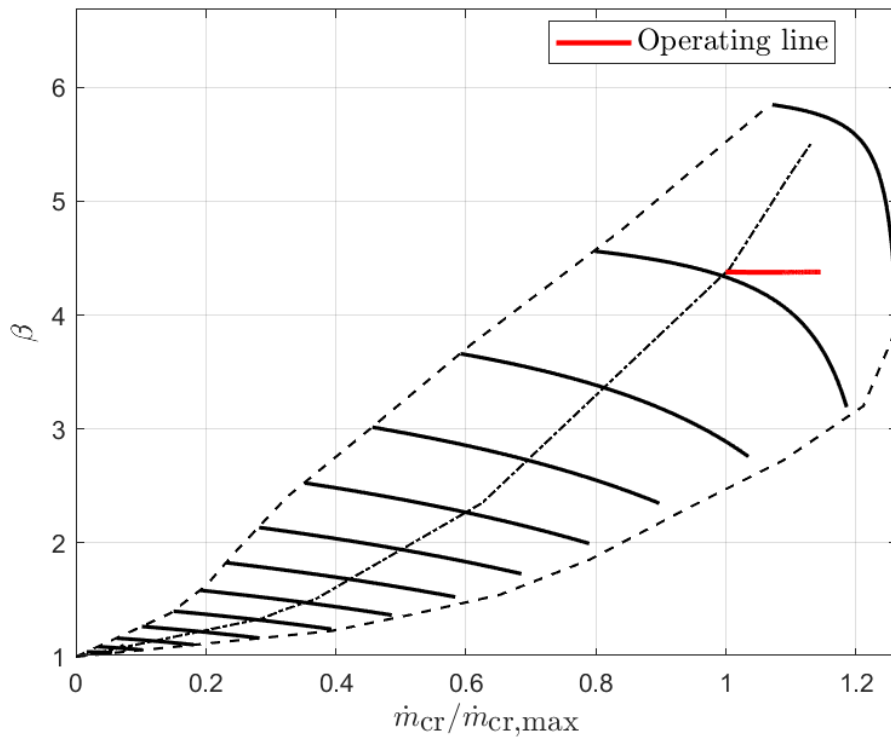


Figure 6.15: Effects of positive current step on compressor performance map

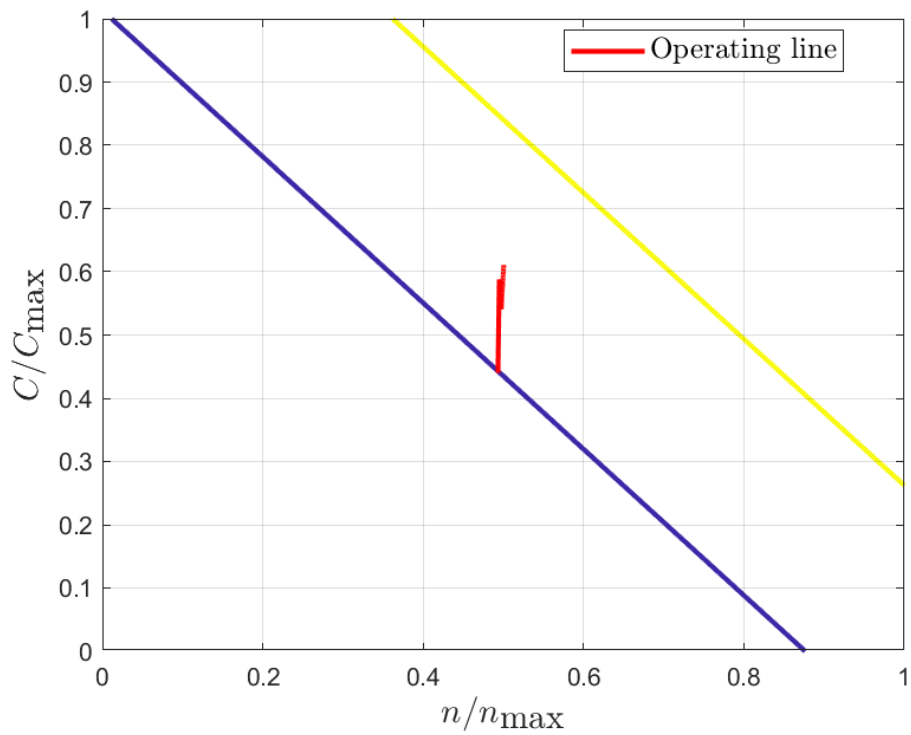


Figure 6.16: Effects of positive current step on motor map

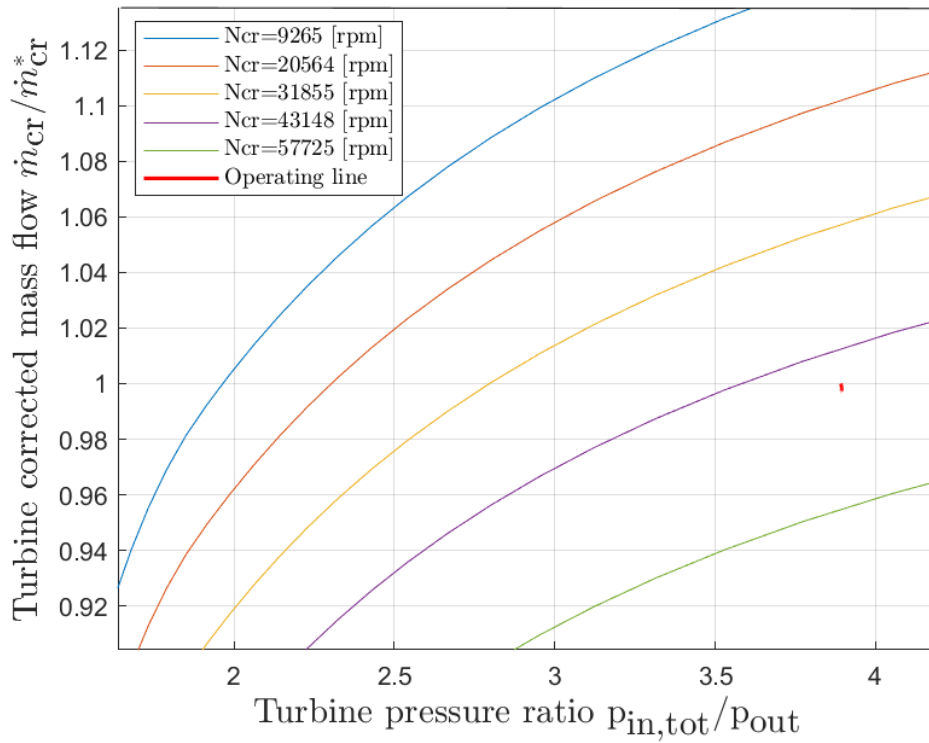


Figure 6.17: Effects of positive current step on turbine performance map (flow map)

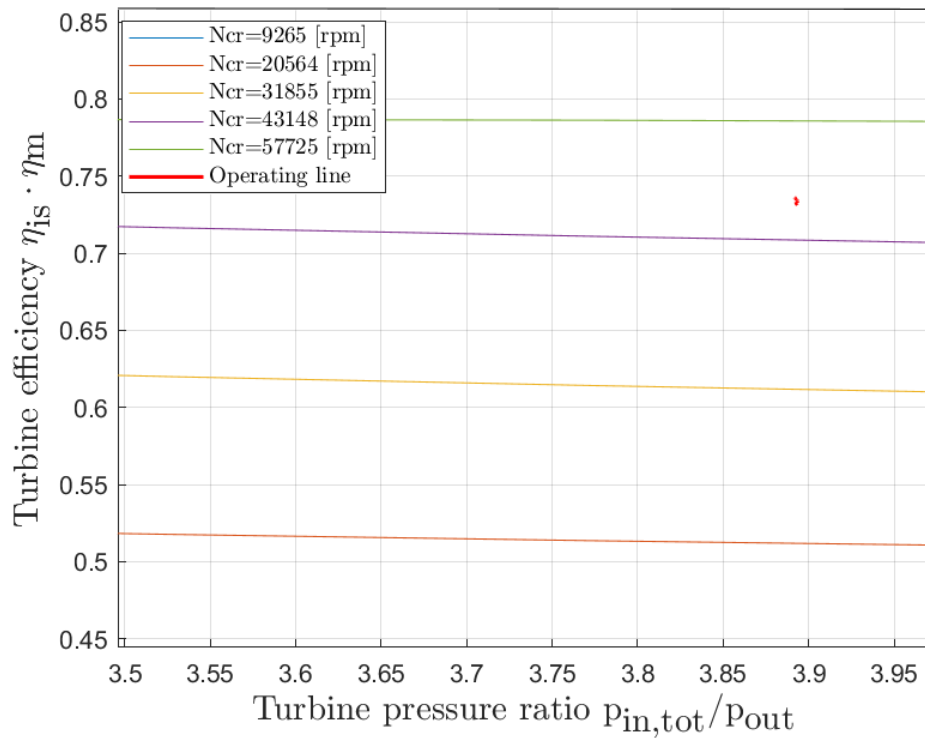


Figure 6.18: Effects of positive current step on turbine performance map (efficiency map)

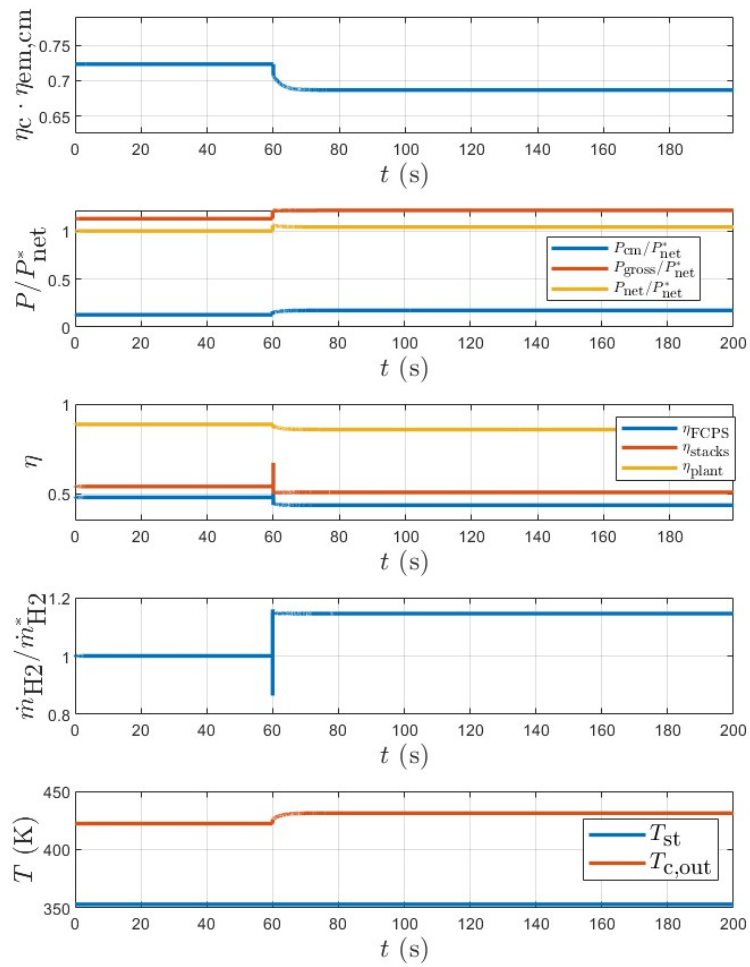


Figure 6.19: Effects of positive current step on performance parameters of the system

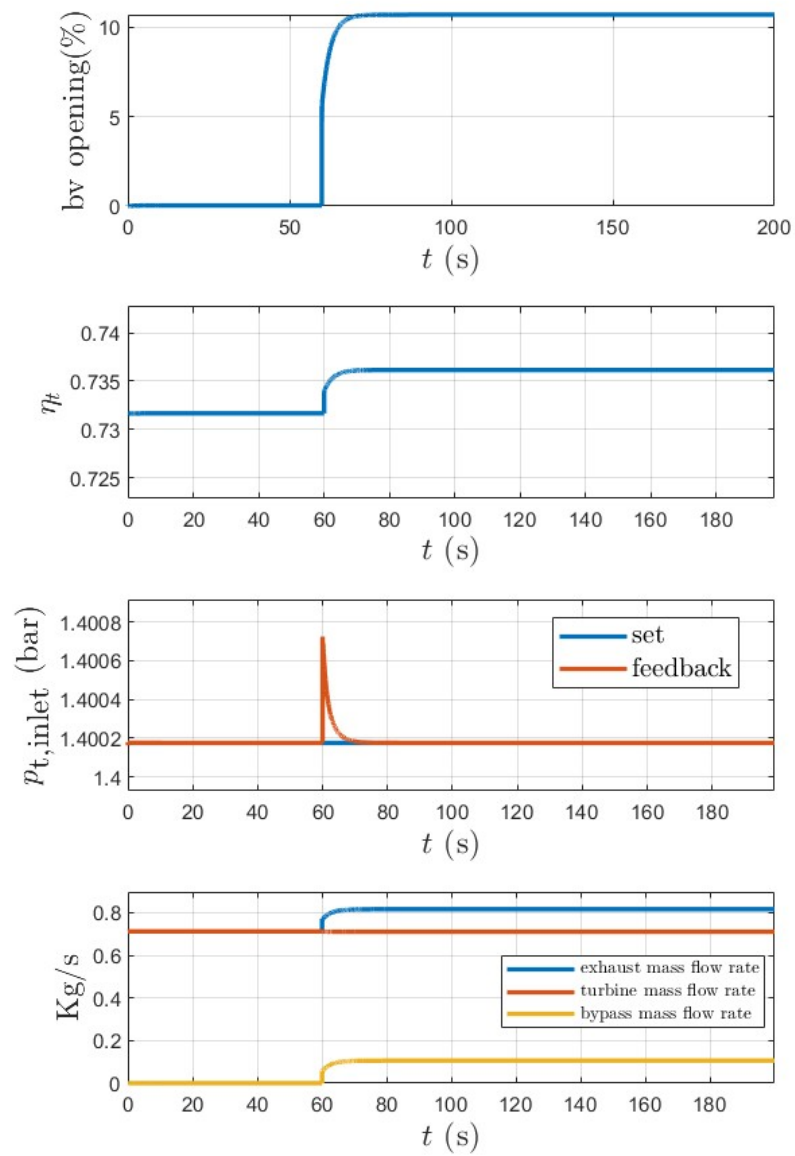


Figure 6.20: Effects of positive current step on bypass pressure control and turbine efficiency

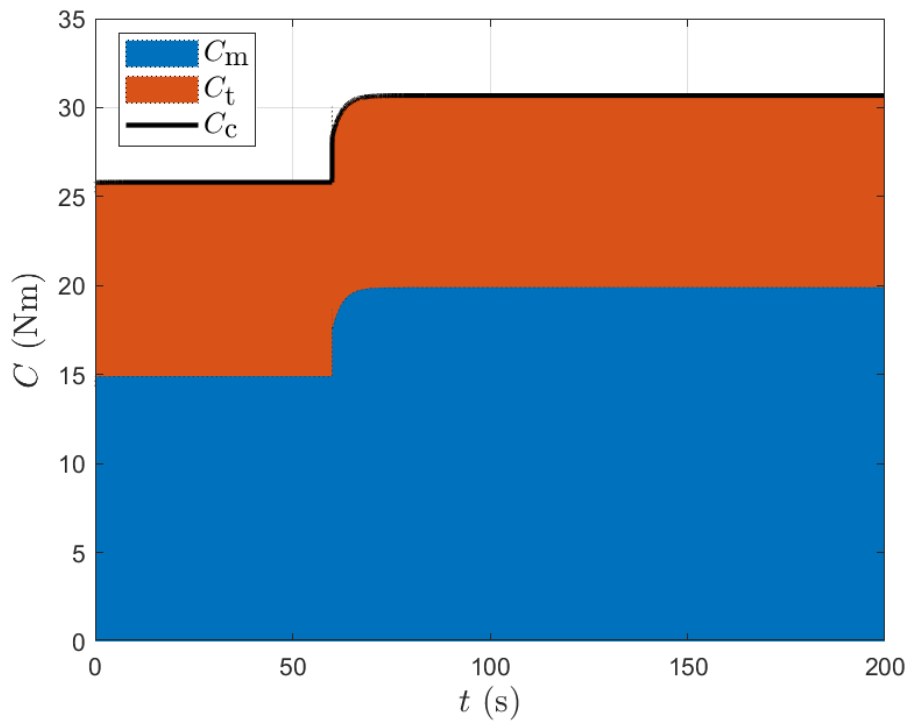


Figure 6.21: Effects of positive current step on motor, compressor and turbine torques

6.2.2.2 Train of steps

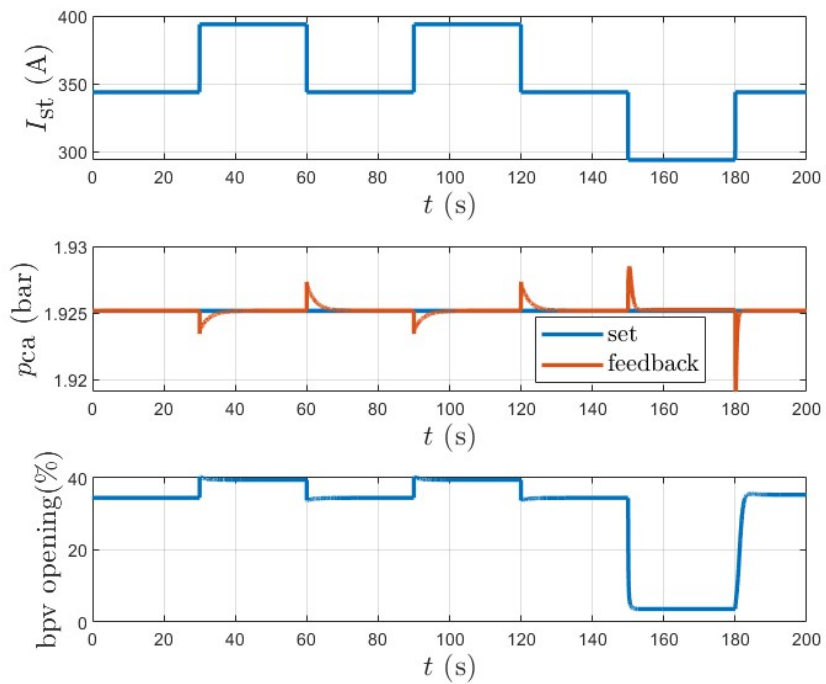


Figure 6.22: Effects of train of steps on pressure control

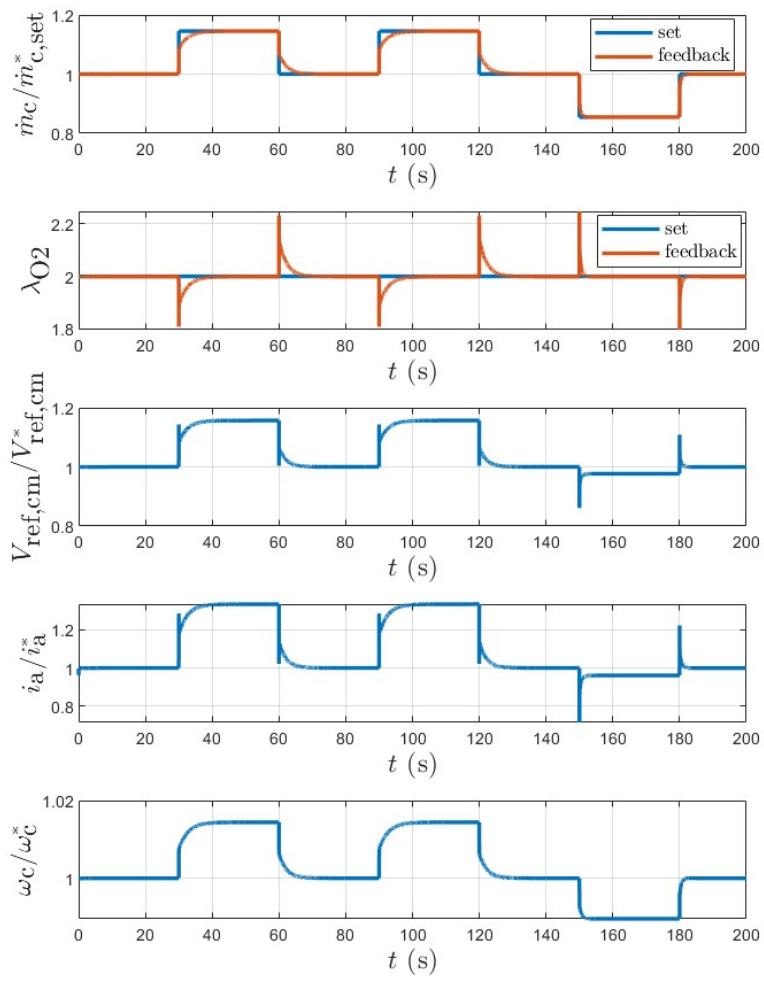


Figure 6.23: Effects of train of steps on mass flow control

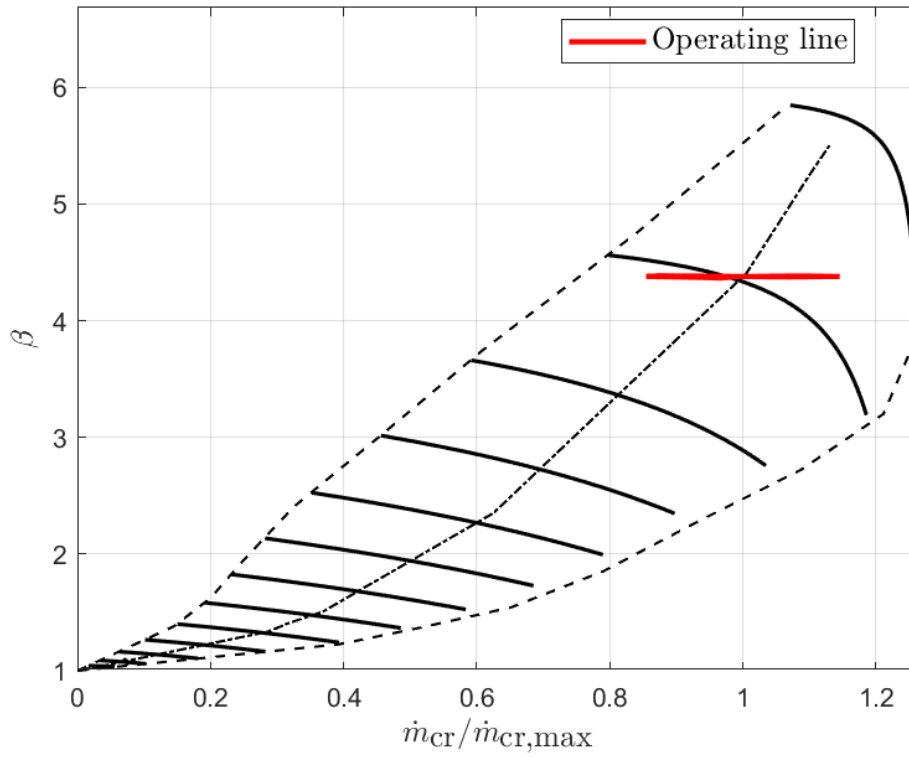


Figure 6.24: Effects of train of steps on compressor performance map

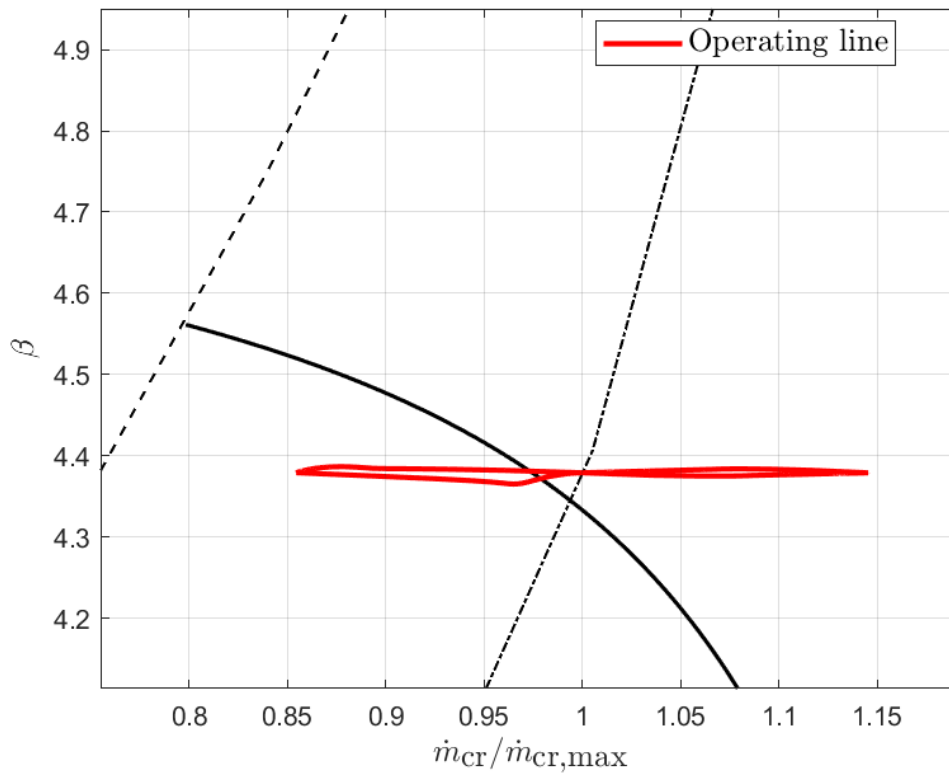


Figure 6.25: Zoom on effects of train of steps on compressor performance map

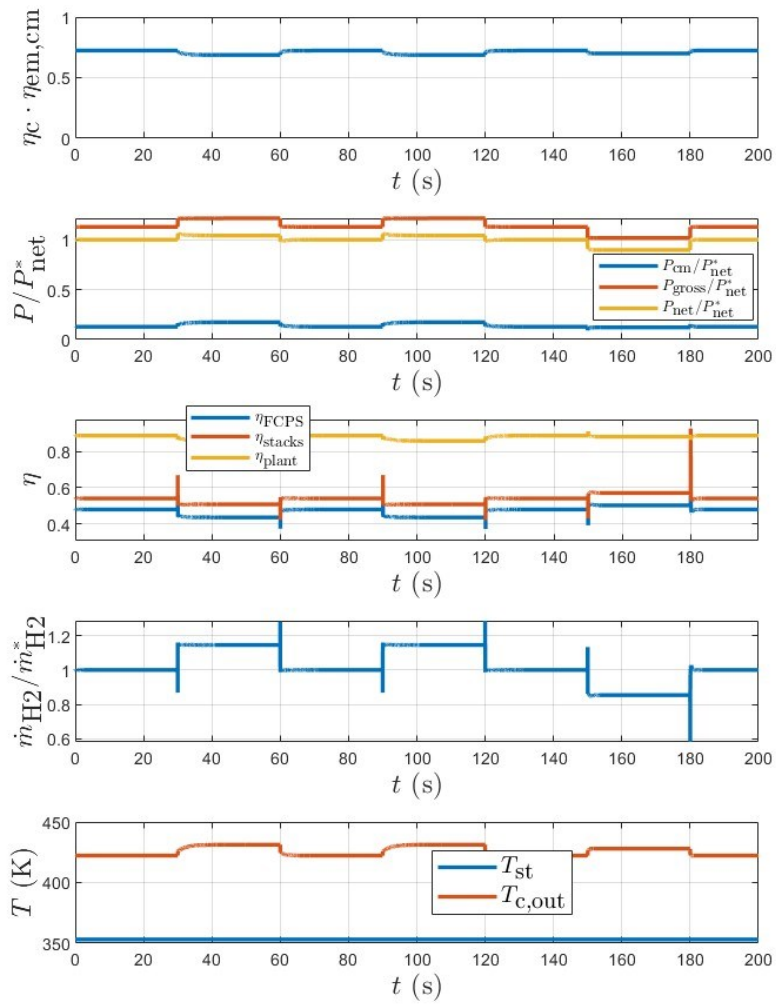


Figure 6.26: Effects of train of steps on system performance parameters

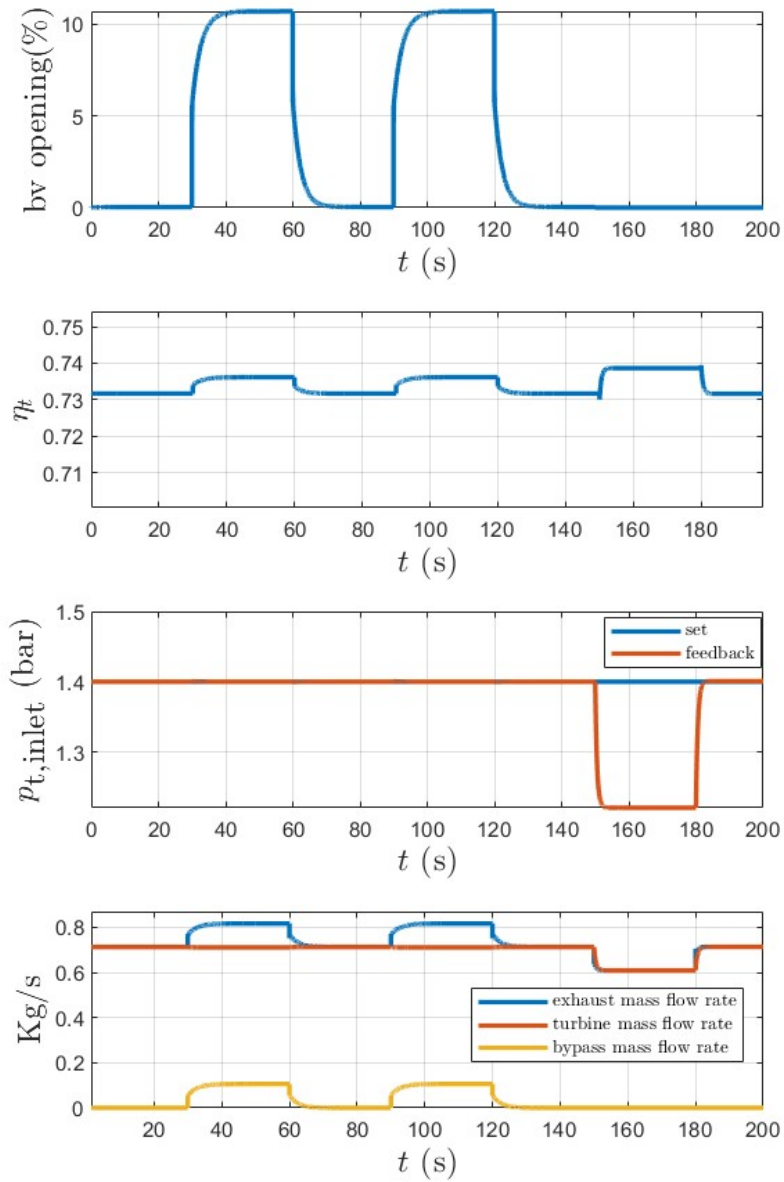


Figure 6.27: Effects of train of steps on bypass pressure control and turbine efficiency

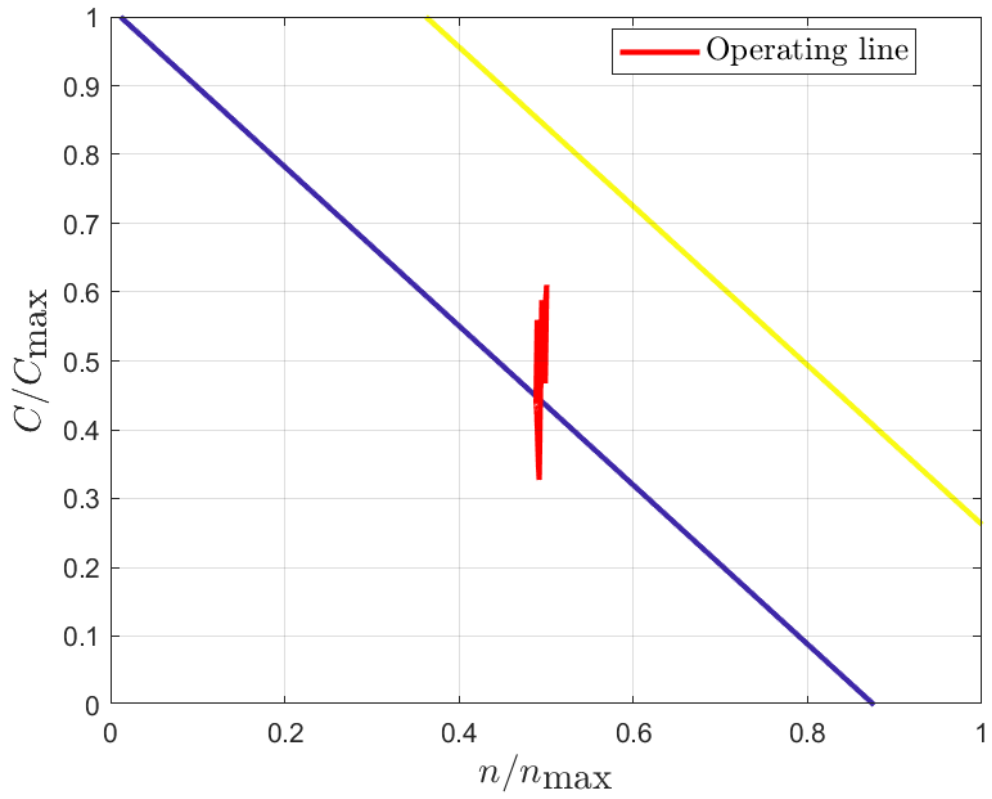


Figure 6.28: Effects of train of steps on motor map

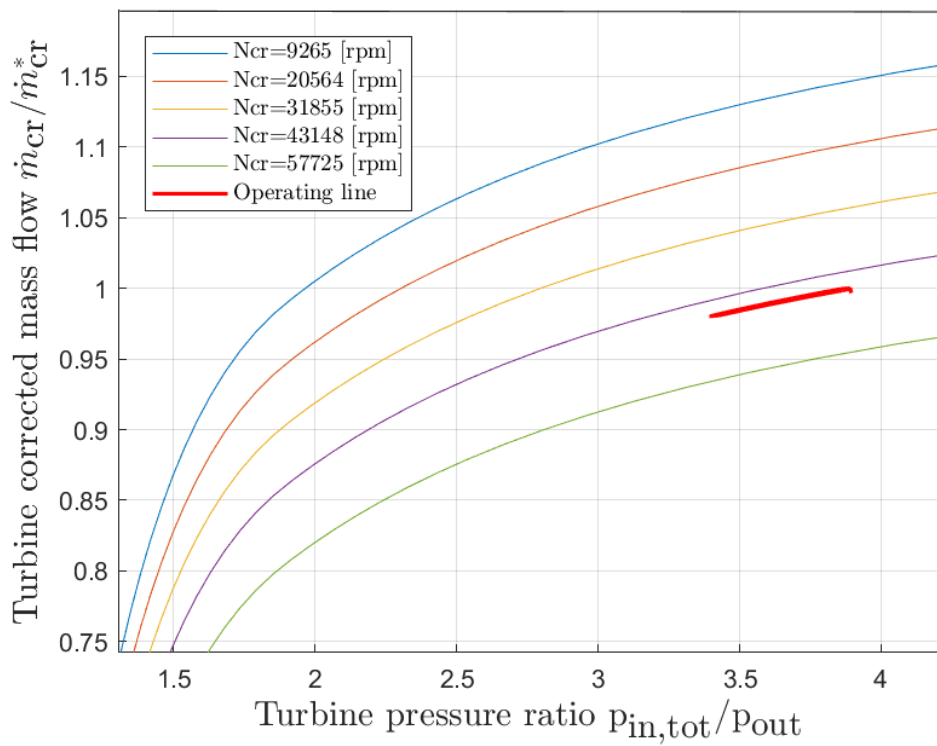


Figure 6.29: Effects of train of steps on turbine map (flow map)

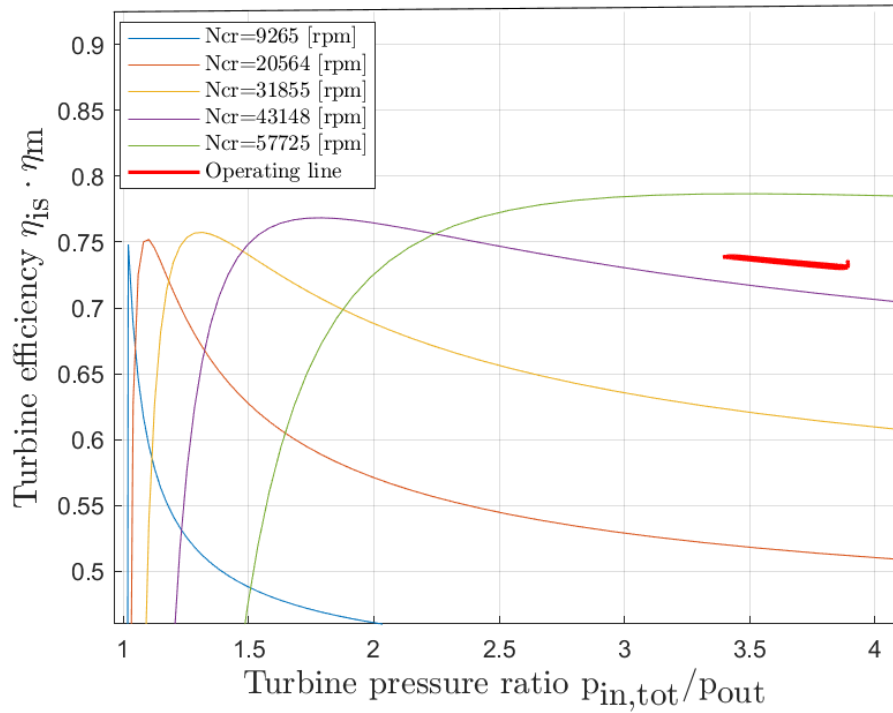


Figure 6.30: Effects of train of steps on turbine performance map (efficiency map)

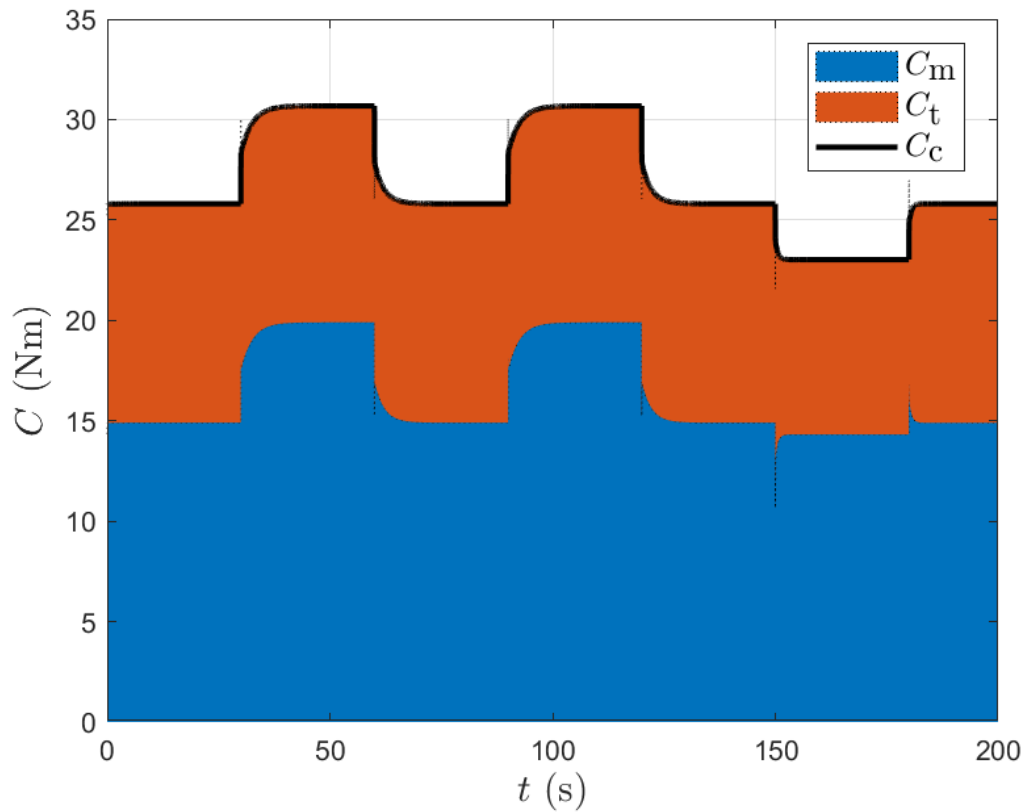


Figure 6.31: Effects of positive current step on motor, compressor and turbine torques

6.2.2.3 Gaussian noise

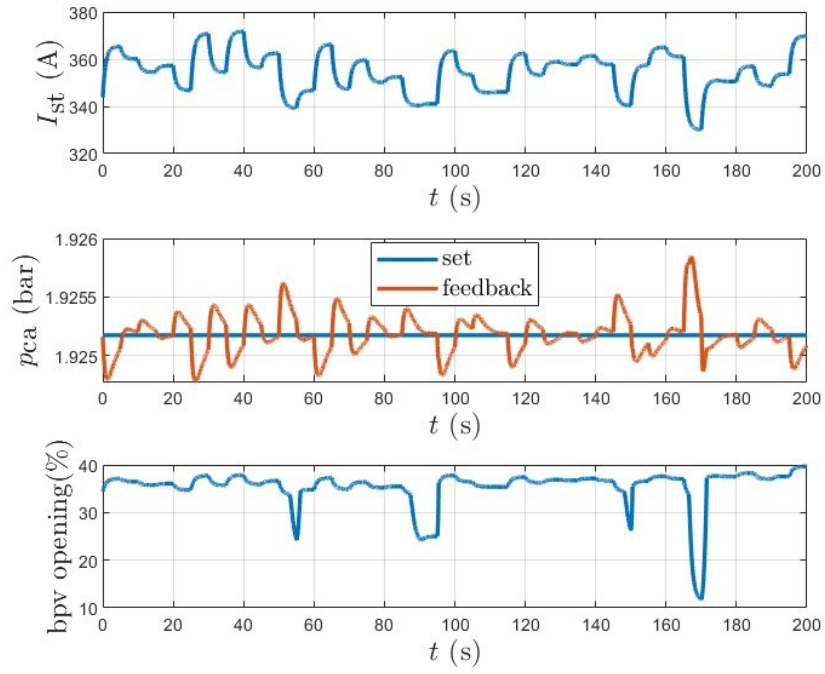


Figure 6.32: Effects of Gaussian noise current on pressure control

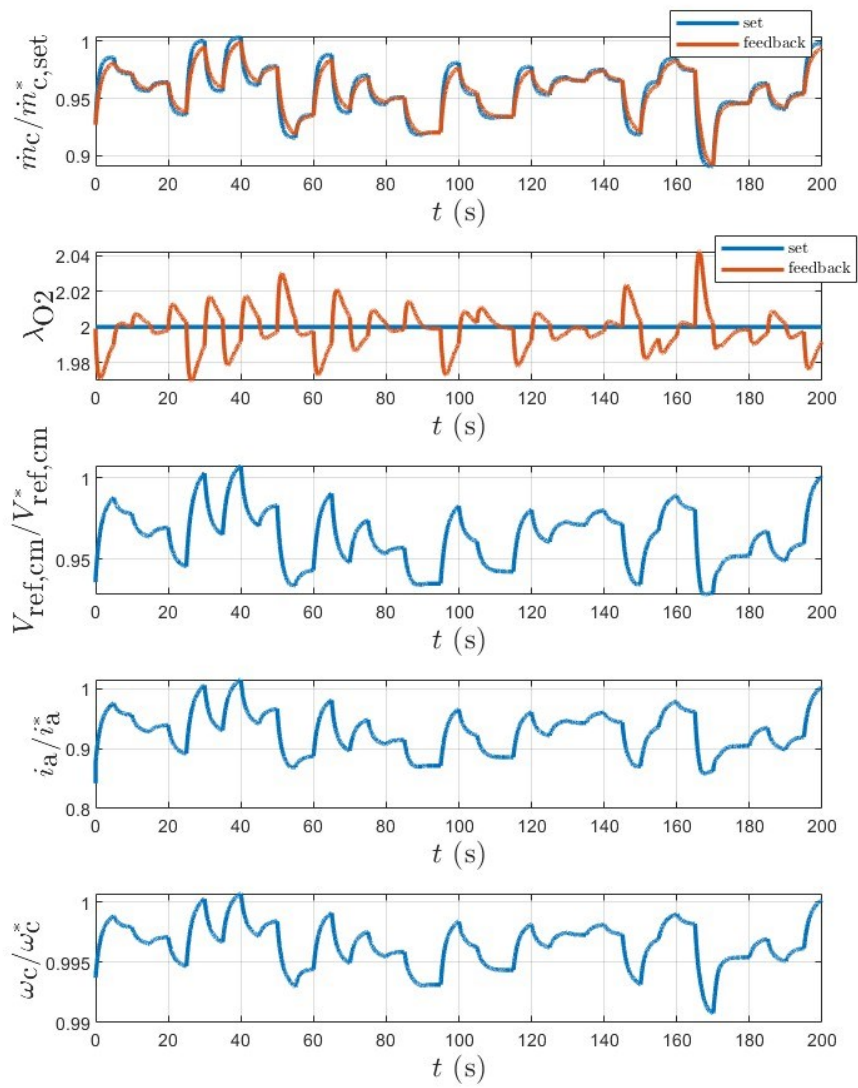


Figure 6.33: Effects of Gaussian noise on flow control

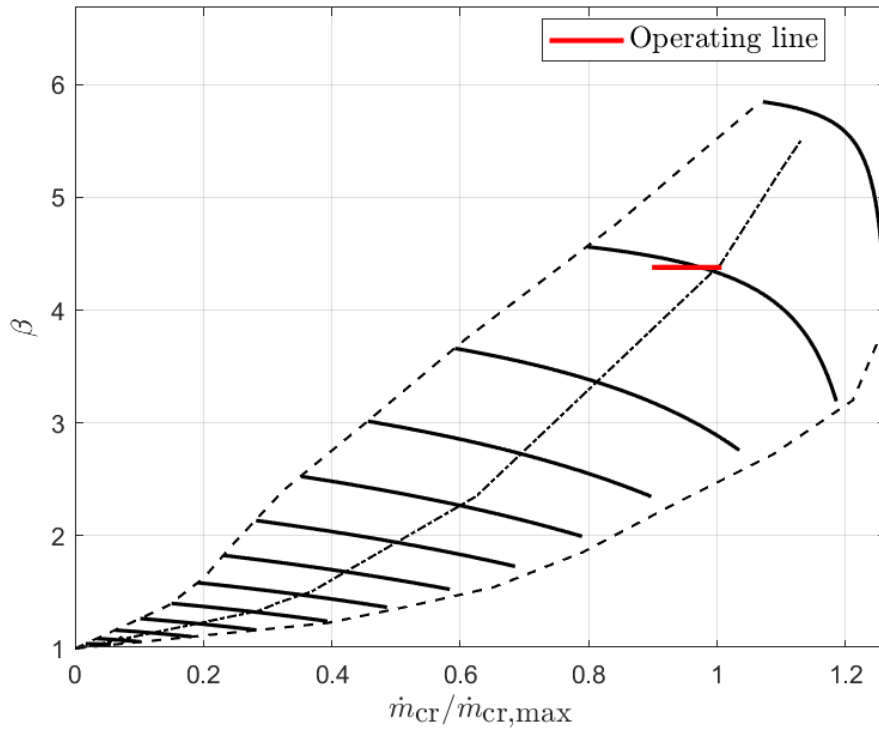


Figure 6.34: Effects of Gaussian noise on compressor performance map

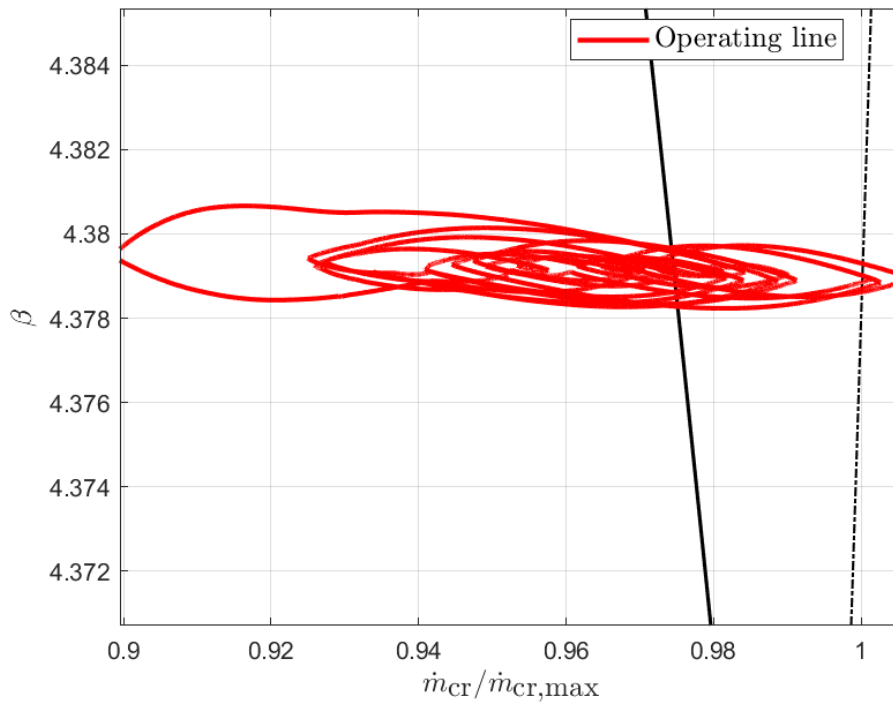


Figure 6.35: Zoom on Effects of Gaussian noise on compressor performance map

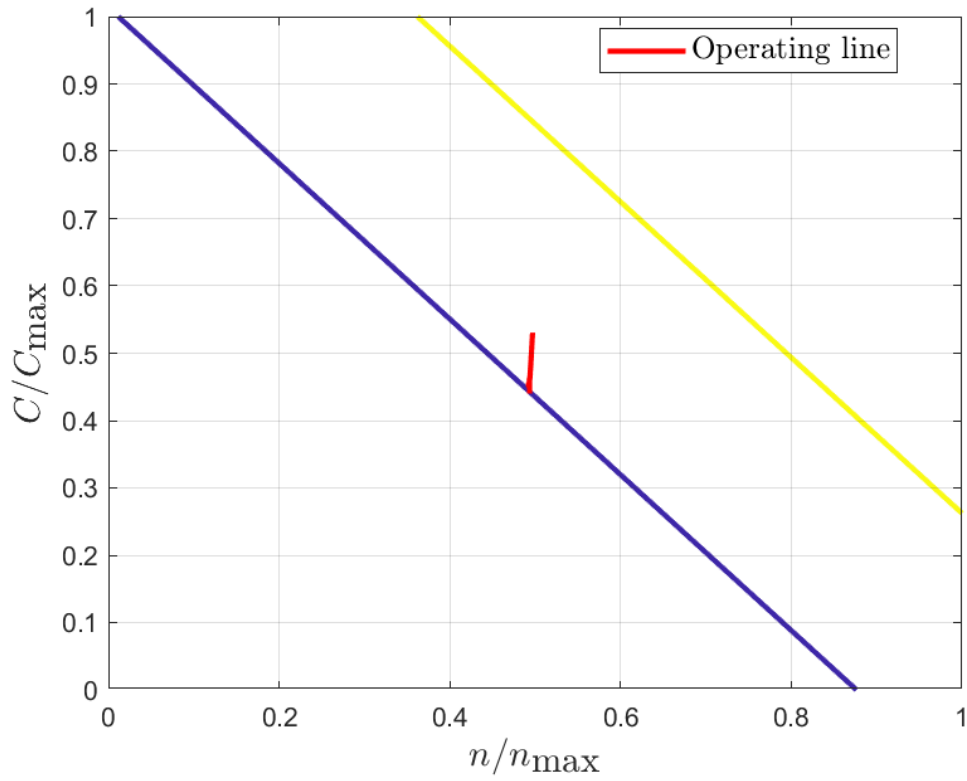


Figure 6.36: Effects of Gaussian noise on motor map

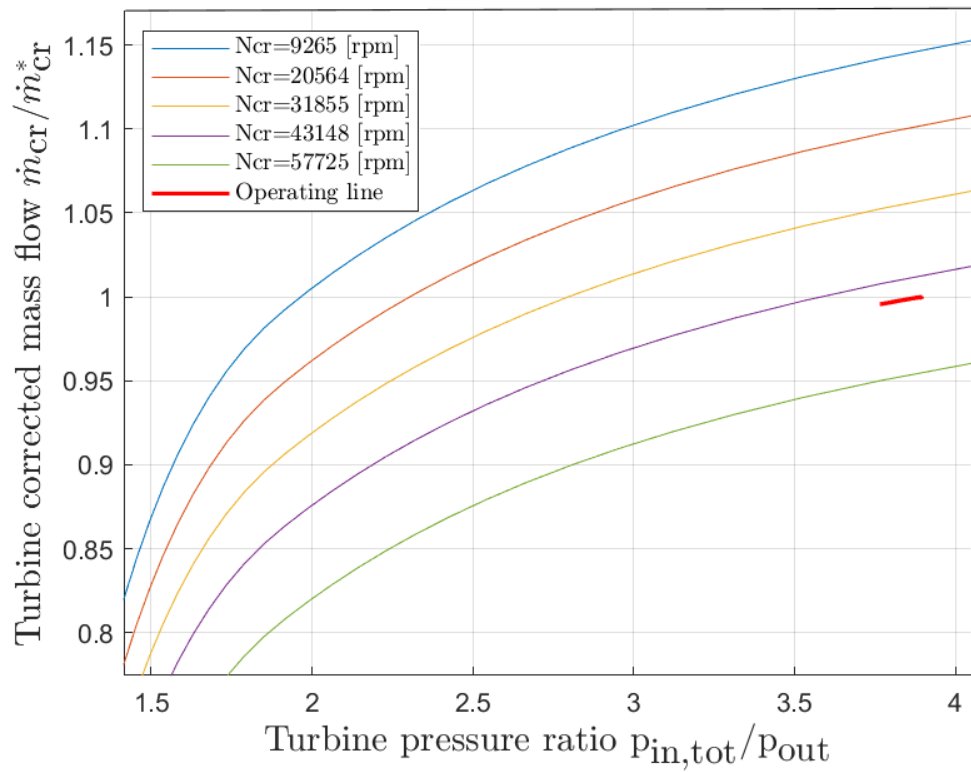


Figure 6.37: Effects of Gaussian noise on turbine performance map (flow map)

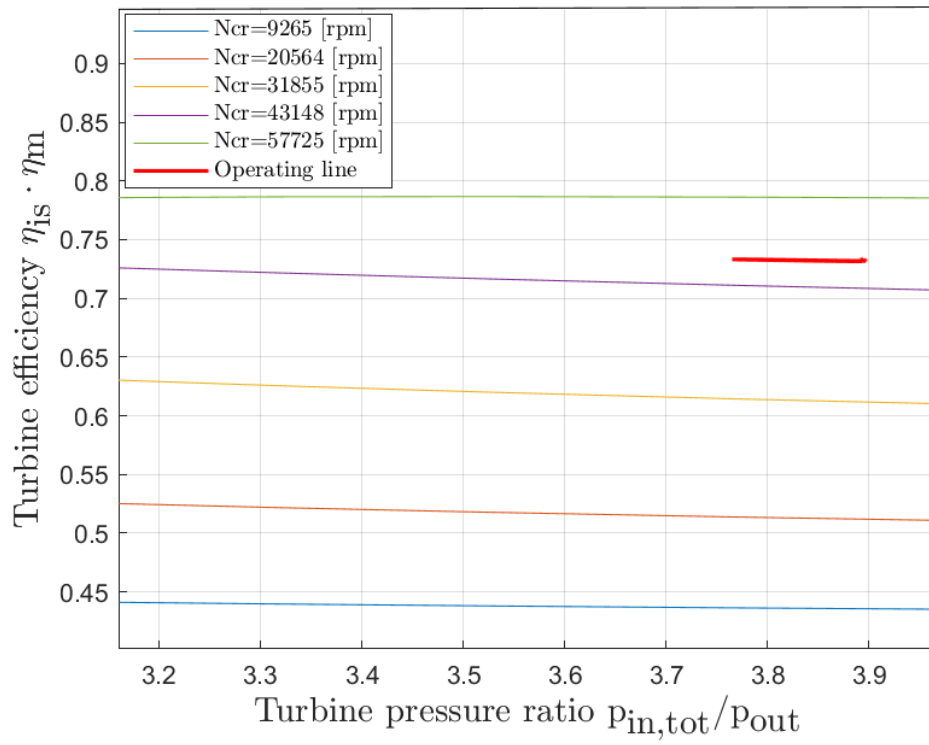


Figure 6.38: Effects of Gaussian noise on turbine performance map (efficiency map)

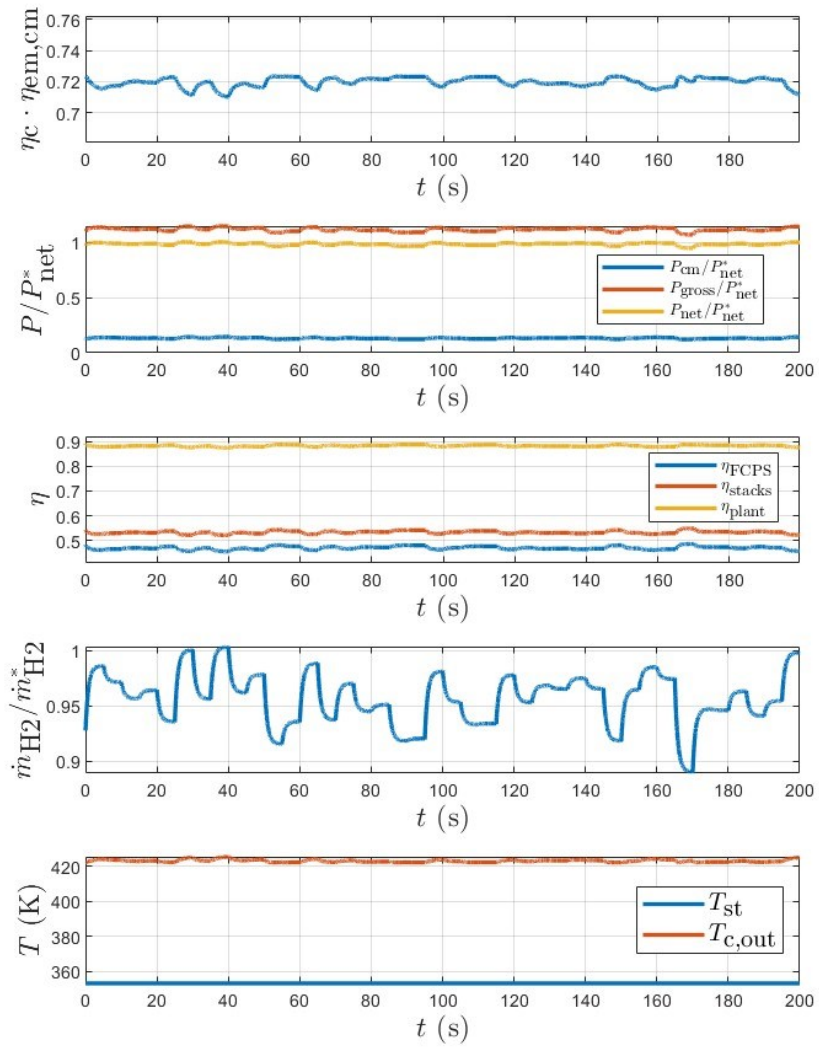


Figure 6.39: Effects of Gaussian noise on system performance parameters

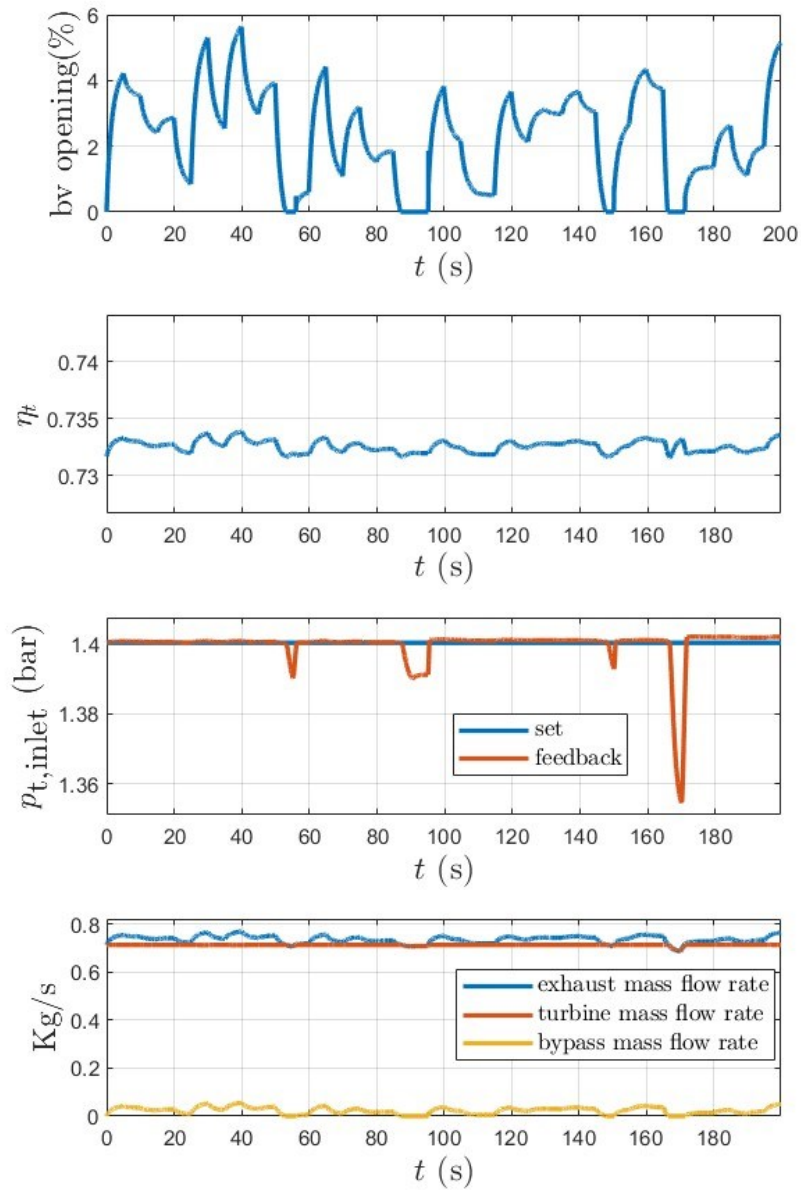


Figure 6.40: Effects of Gaussian noise on bypass pressure control and turbine efficiency

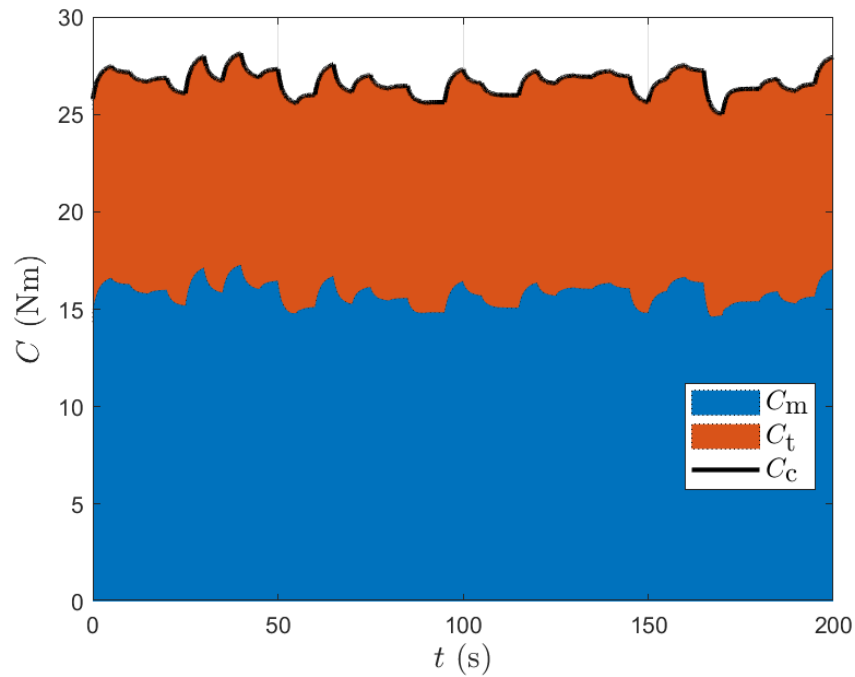


Figure 6.41: Effects of Gaussian noise on motor, compressor and turbine torques

6.2.3 Comparison of results with and without the energy recovery system

This section compares the results of the flight mission simulation and the current disturbance response for the FCPS with and without energy recovery.

In this comparison, the two systems designed to work under optimum conditions are evaluated, in particular the system with energy recovery is designed to work at an operating pressure of 1.9 bar while the one without energy recovery is designed to work at a pressure of 1.2 bar.

Figure 6.42 shows the power trends of the electric motor powering the compressor and the net and gross power of the FCPS, for the system with and without energy recovery through the turbine during the flight mission; all these are normalised with respect to the gross power value generated by the FCPS without the turbine.

As mentioned in the previous paragraphs, the sizing is done assuming that the FCPS generates constant gross power throughout the flight mission; furthermore, the sizing of the two systems was done starting from equal net power generated during cruise.

It can be seen that, for the same net power generated under cruising conditions, the gross power is 3.22% lower for the system with energy recovery than for the system without recovery; this value is justified by the lower power required by the electric motor, since the turbine partially powers the compressor.

The power required by the electric motor of the system with the turbine is 13.44% less than that required in the system without the turbine; this is despite the fact that in the system without energy recovery the power required by the compressor is less, since the latter is sized to work at the optimum pressure of 1.2 bar compared to the 1.9 bar of the system with energy recovery.

During the uphill and downhill phases, on the other hand, the power absorbed by the electric motor for the system with energy recovery is greater because the increase in power required by the compressor, to work at a higher compression ratio, prevails over the energy recovered by the turbine; this also leads to an increase in net power in these phases.

The decrease in gross power makes it possible to lower the reagent consumption by approximately 8%, as can be seen in figures 4.2 and 4.3; a lowering of reagent consumption, in addition to an improvement in efficiency, also means that a smaller stack size can be dimensioned.

In figure 4.2 it can also be observed that by lowering the compression ratio required of the compressor, it is possible to use a compressor working at a slightly higher efficiency.

Figure 4.3 shows the trends of the system's efficiencies, the system's efficiency is calculated as net power over gross power, the fact that the net power is greater in the up and down phases for the system without energy recovery also leads to an improvement in the system's efficiency in these phases; while in the cruise phase, the system's efficiency with the system with energy recovery is greater since more energy can be recovered in the turbine.

The efficiency of the stack is constant throughout the flight mission since the stack operating variables are kept constant through the control systems; the efficiency of the stack for the system with energy recovery is higher since it operates at a higher pressure.

The overall efficiency of the FCPS can be calculated through the multiplication of the efficiency of the system and that of the stack; it is observed that by inserting a system with energy recovery

through the turbine the efficiency increases by 3.5%, this is a good result consistent with the values indicated in the literature.

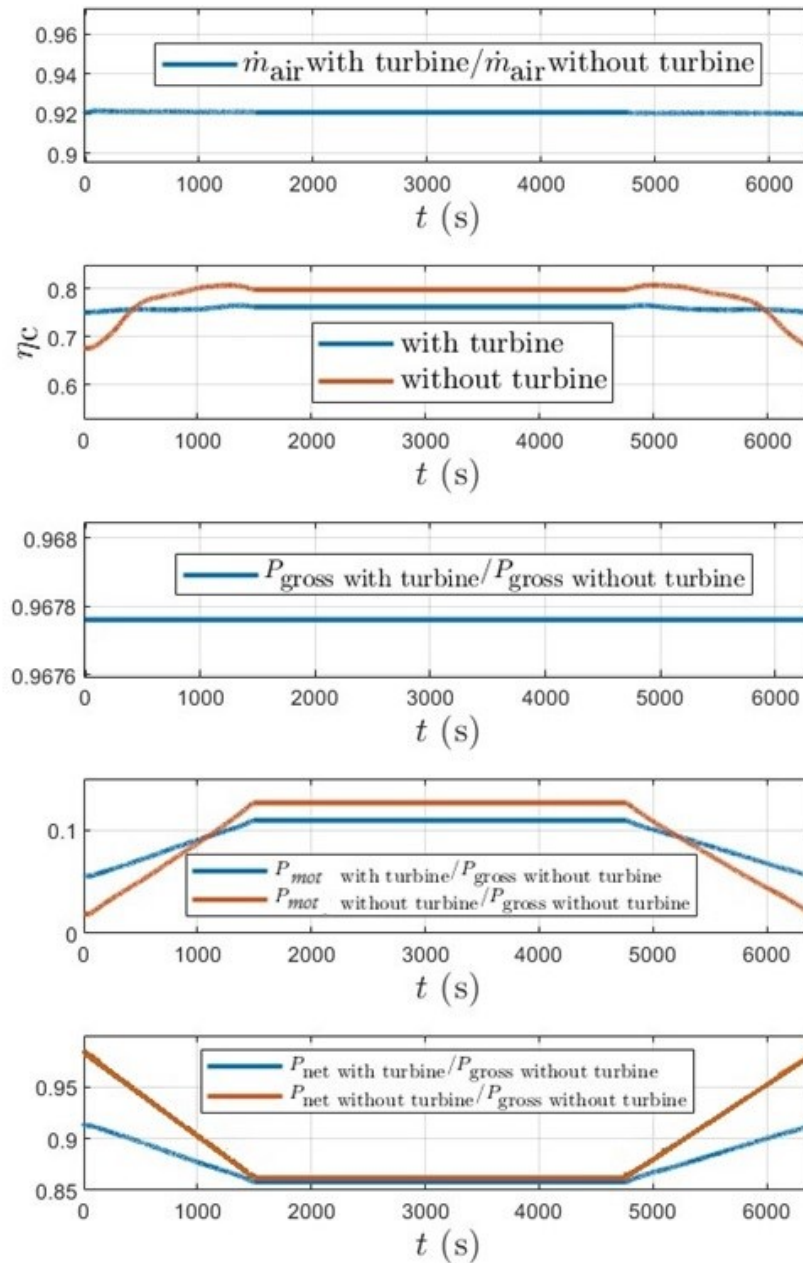


Figure 6.42: comparison of flight mission simulation results for the system with and without energy recovery

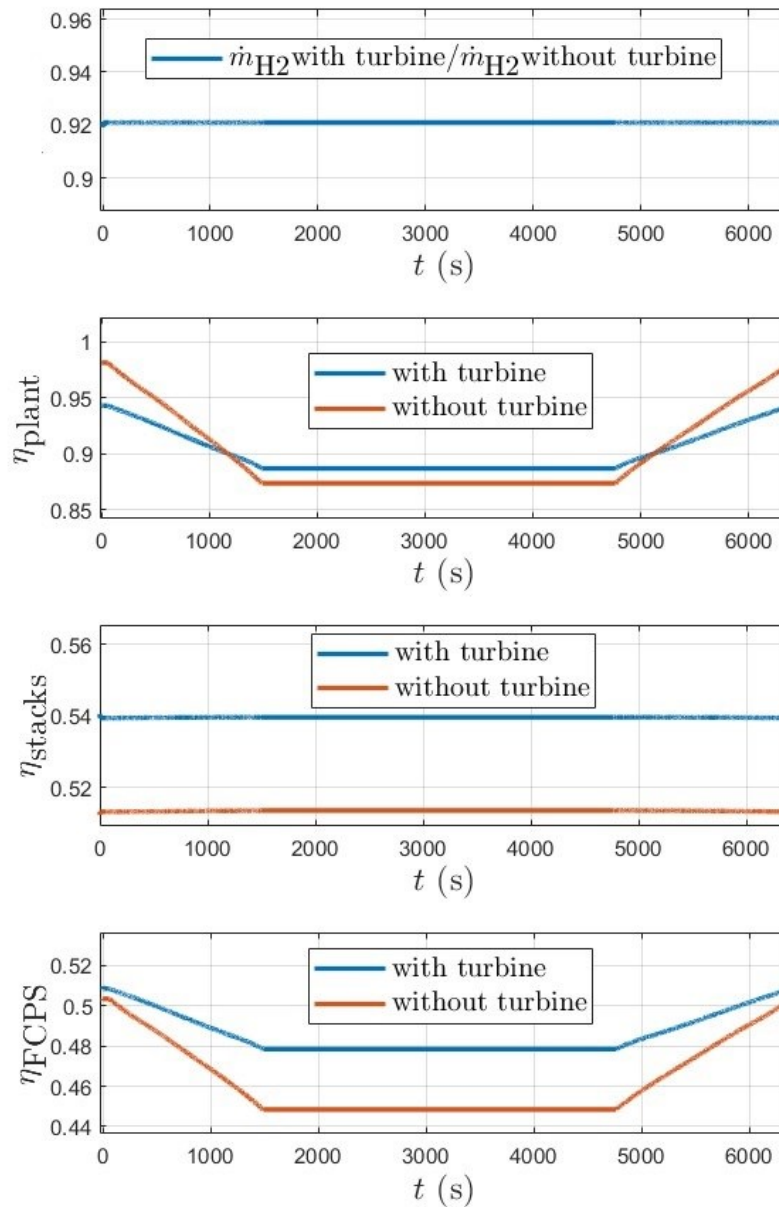


Figure 6.43: comparison of flight mission simulation results for the system with and without energy recovery

Figure 6.44 shows the efficiency trends for systems with and without energy recovery when current disturbances are applied with the train of steps indicated in paragraph 6.2.2; it can be seen that when steps are applied, the efficiency of the system with the energy recovery system decreases more than the one without recovery, while the stack efficiency trends are very similar, which also leads to a greater variation in the overall system efficiency when steps are applied for the system with energy recovery.

This effect is due to the losses of energy recovered by the turbine, under conditions where current disturbances are applied, due to the opening of the bypass valve.

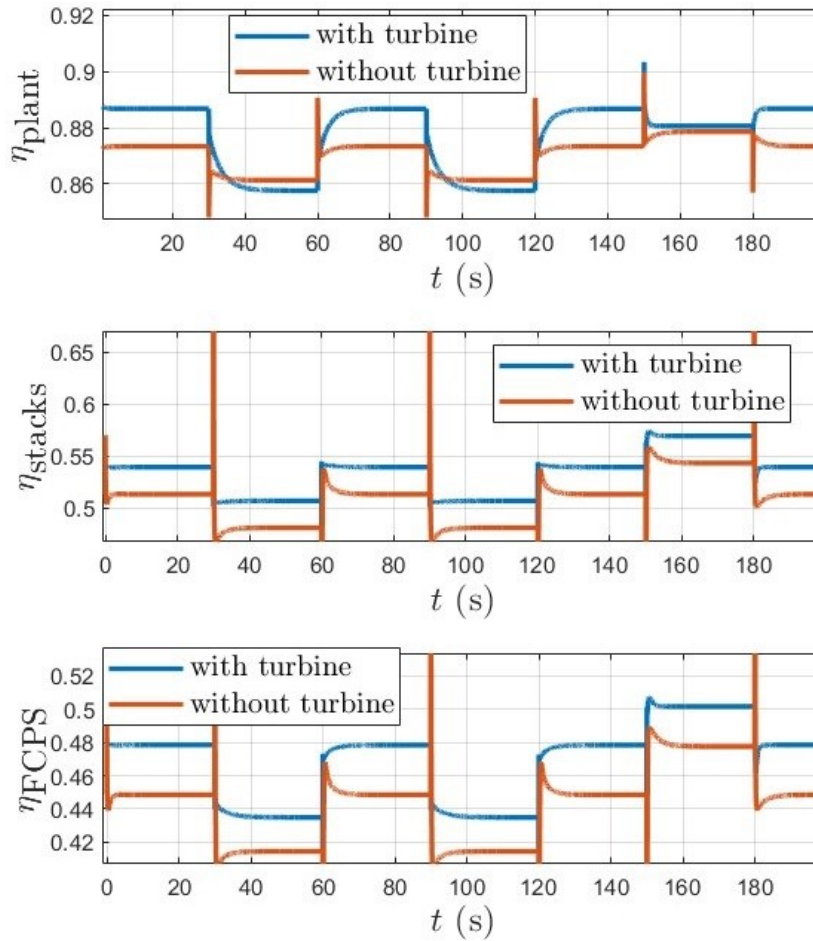


Figure 6.44: Comparison of simulation results of the application of a pulse train for the system with and without energy recovery

6.2.4 comparison of the same system with and without turbine

In this analysis, a comparison is made between the system sized and described in the previous chapters, with and without a turbine. The system is the same with or without the turbine, and thus operates at the same 1.9 bar cathode pressure.

It can be seen from the figures that, for the same gross power generated, the system without the turbine has a significant increase in the power required by the electric motor, which occurs precisely because there is no contribution from the turbine to the compressor.

The increase in power required by the motor is greater than in the case shown in section 6.2.3, this is because increasing the operating pressure increases the compression ratio that the compressor must guarantee.

The increase in power required by the engine is the cause of the decrease in net power for the system without a turbine, with the same gross power generated between the system with and without a turbine.

As can be seen in Figure 6.46, these effects lead to a decrease in system efficiency of almost 9% and a decrease in overall system efficiency of 4.5%.

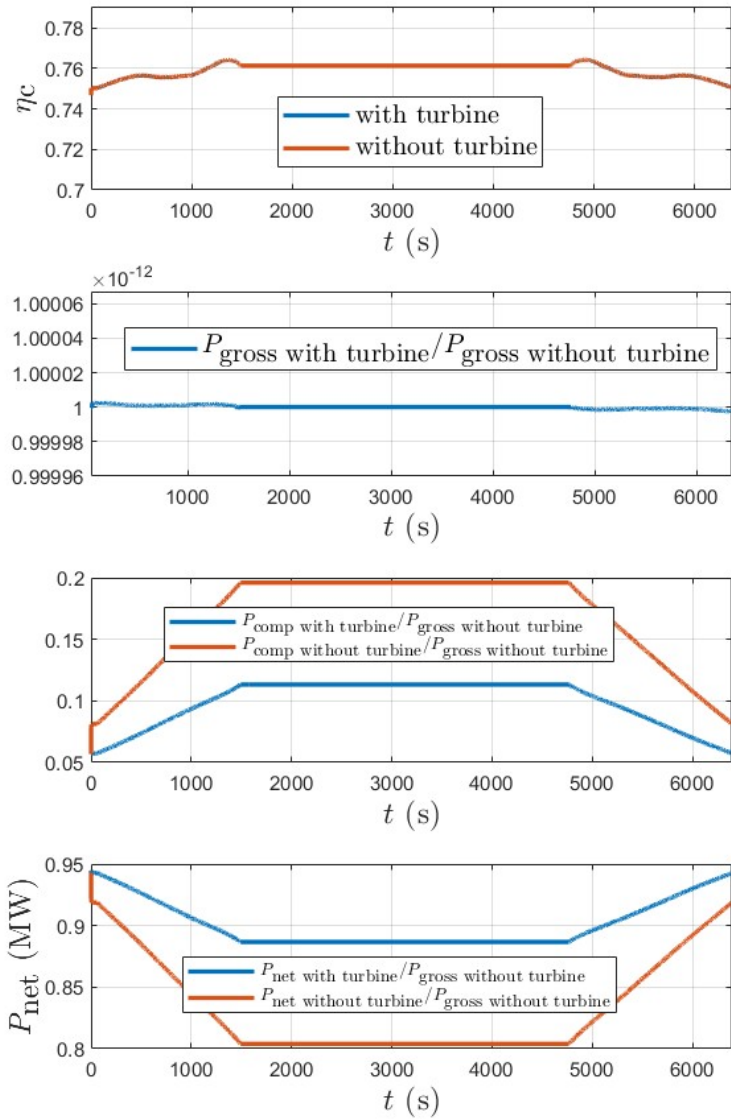


Figure 6.45: comparison of flight mission simulation results for the system with and without turbine

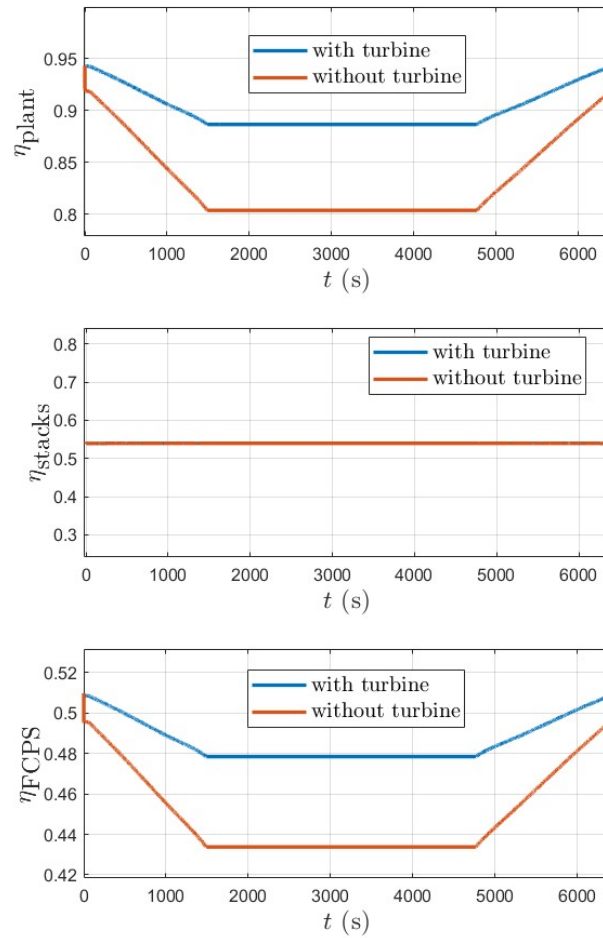


Figure 6.46: comparison of flight mission simulation results for the system with and without turbine

6.2.5 comparison of the system with and without pressure control via the bypass valve

In this section, the comparison is made between the system with and without pressure control via the bypass valve.

In figure 6.47, it is observed, how during the up and down phases, the pressure rises until a new equilibrium is reached in the system.

This has a negative effect on the efficiency of the compressor and turbine, as can be seen in figure 4.49.

However, the pressure rise is small and does not cause the compressor to work outside its safety zone.

The increase in the compression ratio, being limited, does not lead to an excessive increase in the power required by the engine, and the positive effects of being able to exploit all the energy of the gases coming out of the stack, without opening the turbine has a slightly improving effect on system efficiencies.

From the analysis, therefore, it can be seen that it may be advantageous to control the system with higher operating pressures, during the rise and fall phases.

This is because the optimum system pressure, found in the performance analysis, was only evaluated, to a first approximation, during the cruise phase.

However, the inclusion of a bypass valve or other turbine regulation system is essential to prevent the compressor from operating outside its safety zone.

Figure 6.50 shows the effect of a positive step current disturbance on the pressure at the cathode for the system without a bypass valve.

Figure 6.51 shows how the pressure increase does not cause the compressor to operate outside its safe condition, however, in figure 6.52 it can be seen that, in this case, the pressure increase in the cruise phase leads to a decrease in system efficiency and overall system efficiency, albeit only by about 0.4%.

Finally, figures 6.53 and 6.54 show the effect of a Gaussian current disturbance on the system without pressure control by means of the bypass valve, also in this case, the compressor continues to work in the safety zones; however, pressure oscillations of about 300 mbar are observed, exceeding pressure oscillation values of 200 mbar, this could lead to diaphragm damage and the generation of voltage pulsations.

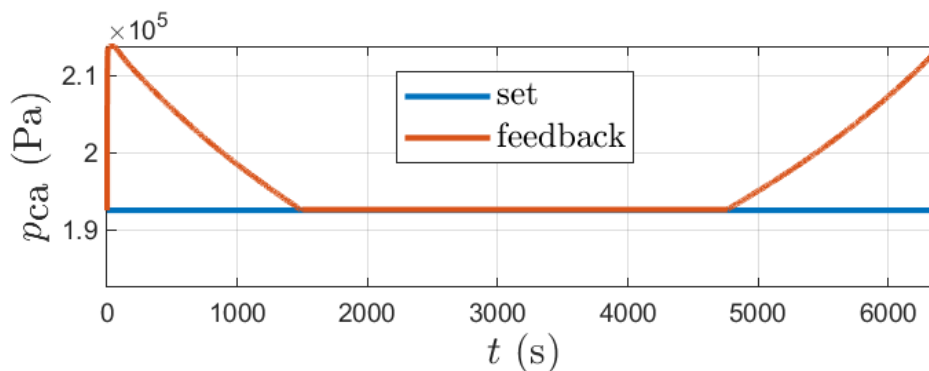


Figure 6.47: pressure trend during the flight mission for the system without bypass valve

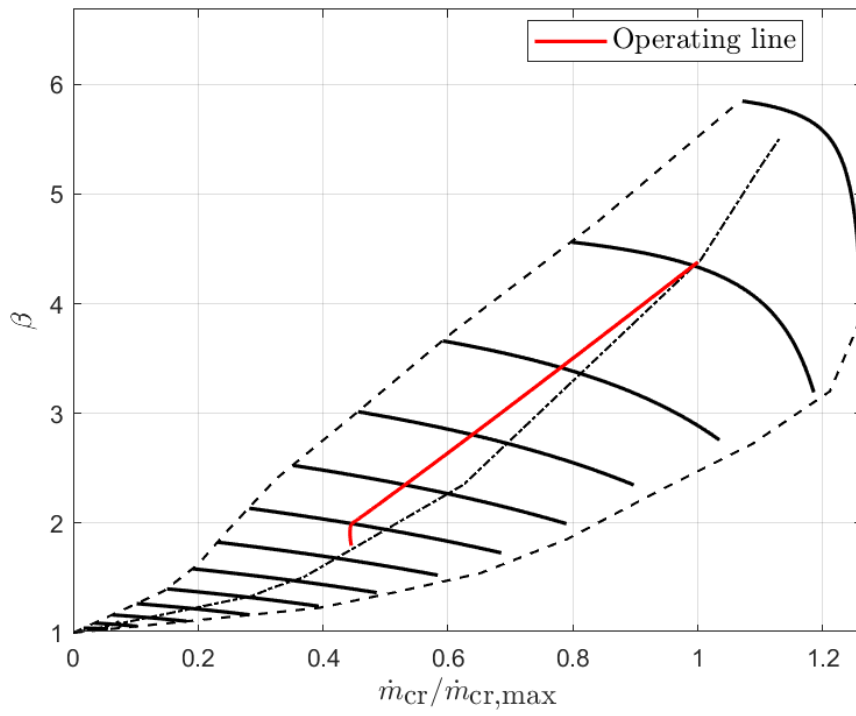


Figure 6.48: compressor operating line during the flight mission for the system without bypass valve

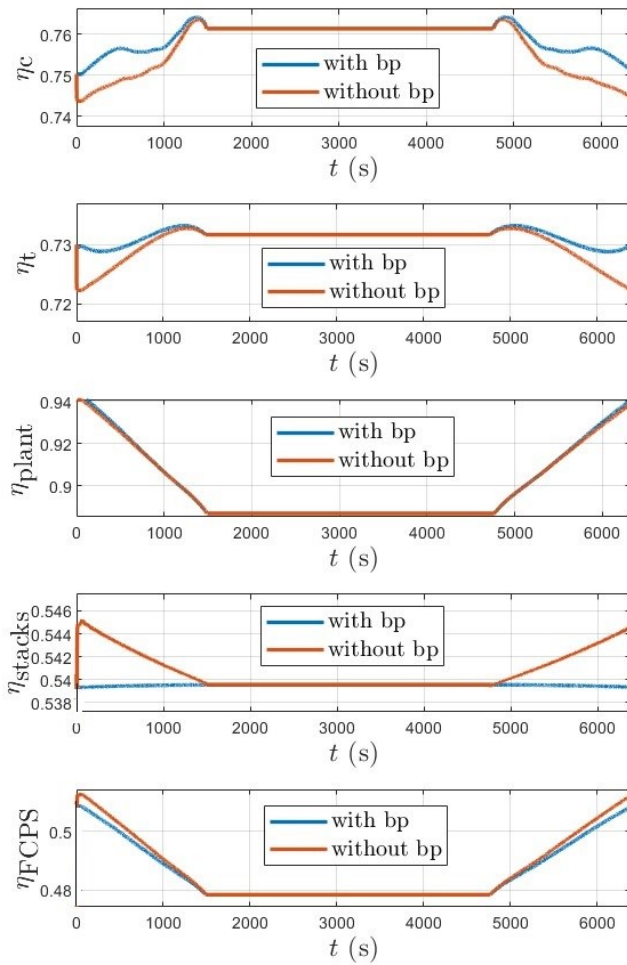


Figure 6.49: efficiencies trend during the flight mission for the system without bypass valve

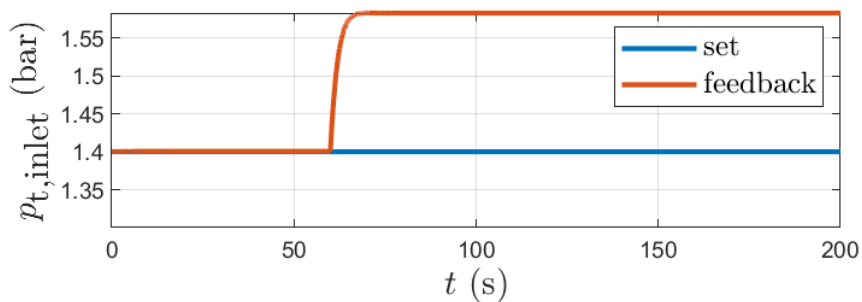


Figure 6.50: effect of a positive step disturbance on cathode pressure for the system without bypass valve

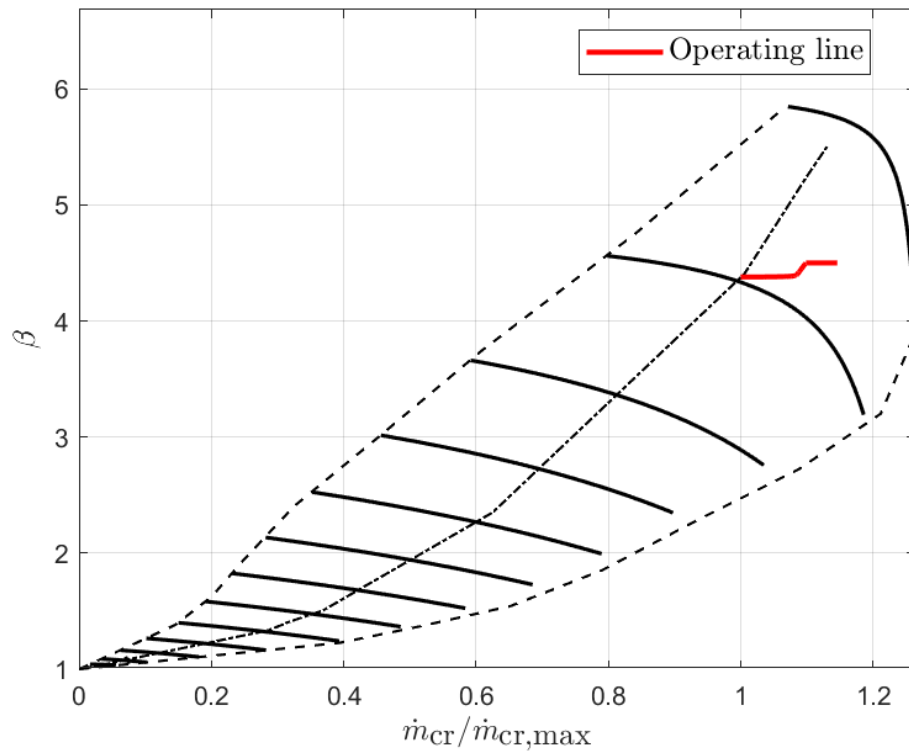


Figure 6.51: effect of a positive step disturbance on compressor operating line for the system without bypass valve

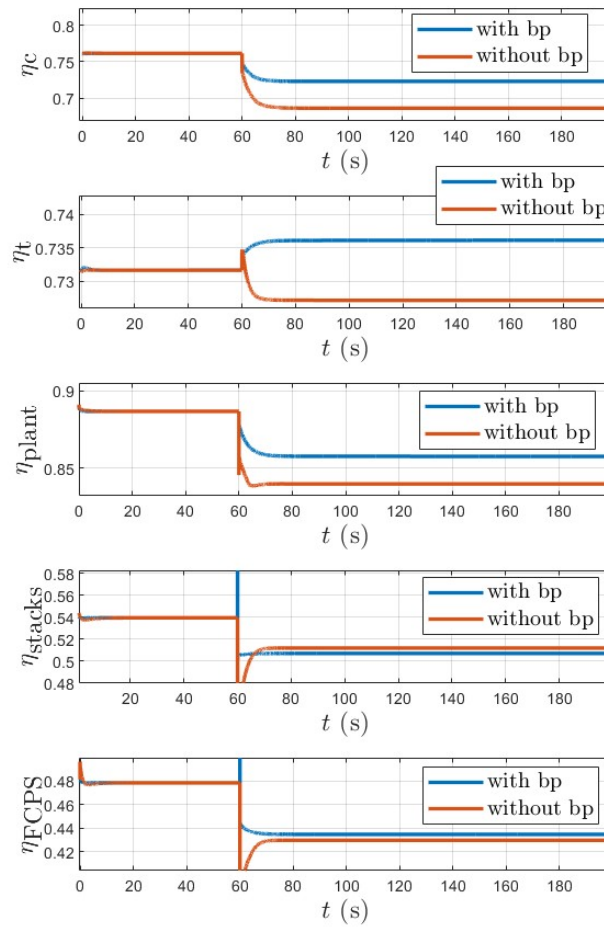


Figure 6.52: Effect of a positive step disturbance on efficiencies for the system without bypass valve

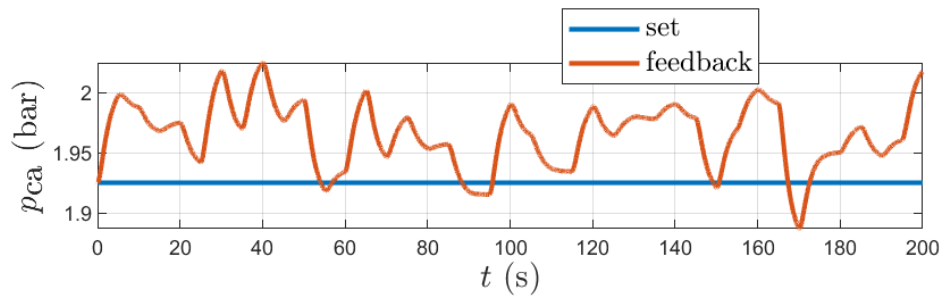


Figure 6.53: Effect of a Gaussian disturbance on cathode pressure for the system without bypass valve

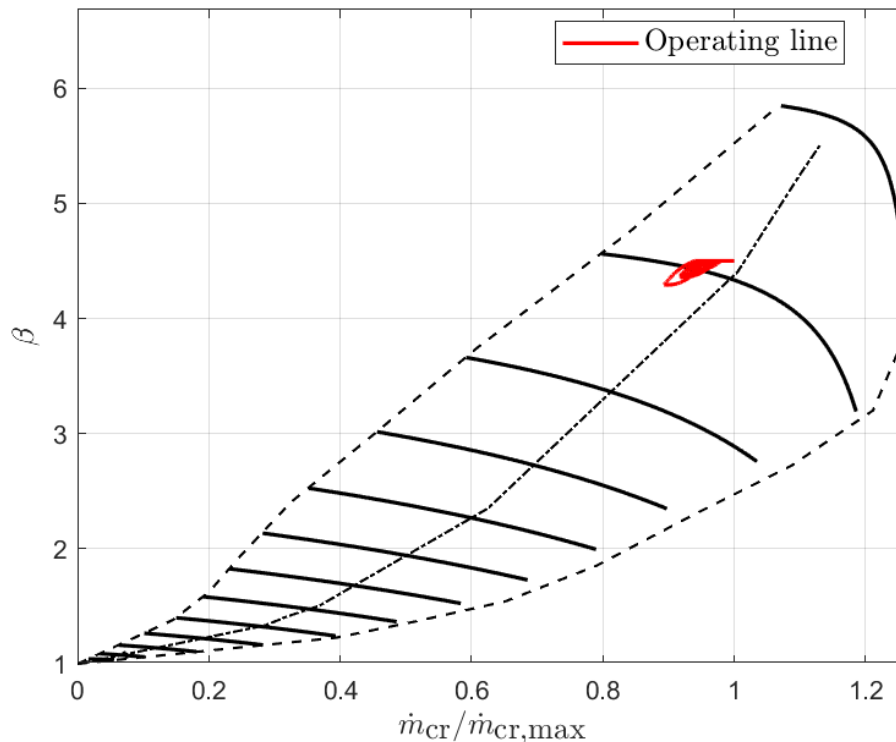


Figure 6.54: effect of a Gaussian disturbance on cathode pressure for the system without bypass valve

7 Conclusions

This thesis work is based on the study and modelling of an air supply system for a fuel cell power system (FCPS) for the propulsion of a regional hybrid aircraft of the more electric type. In particular, the impact of an energy recovery system by means of a turbo-compressor, in which the gases exiting the fuel cell stack are exploited, on the performance, size and power density of the entire FCPS was evaluated; The architecture of the energy recovery system was compared with the results of the sizing of an electric compressor type architecture, where the compressor is powered by an electric motor, modelled in a previous thesis work carried out at the Politecnico di Torino.

After an initial research activity on the state of the art of the various aspects and architectures used for energy recovery of the gases exiting the stack of an FCPS, two architectures most commonly used in the automotive field were considered:

- the electric turbocharger type architecture, where there is only one compression stage and where the engine and turbocharger are splined to the same shaft with the compressor being fed by both the engine and the turbine.
- The serial booster type architecture, where there is a first compression ratio carried out by a turbocharger and the compressor is entirely fed by the turbine, and a second compression ratio where the compressor is fed by the electric motor; this second architecture presents greater complexity in layout but allows higher compression ratios to be achieved.

Using Matlab software, an automated process was implemented for the sizing of the turbocharger through a turbo matching and scaling process, using formulas derived from partial fluid-dynamic

similarity, of compressor and turbine performance maps taken from suppliers and entered into a special database; the sizing process was implemented for both architectures analysed.

The two architectures and the electric compressor architecture were sized for the same net power generated in the cruise phase.

The results of the static air supply system sizing of the two architectures were compared with each other and with the electric compressor architecture, which does not have the energy recovery system.

From the comparisons, it was found that by recovering the energy of the gases exiting the fuel cell, it is possible to reduce the size of the stack, the motor, and the compressor. This is possible because by exploiting the energy of the gases exiting the stack through the turbine, the power required by the electric motor is reduced, and the gross power that the FC must generate for the same net power is also reduced, thus decreasing the consumption of the reagents during the oxidation-reduction reaction.

The size-decreasing effects of these three components are at the expense of the additional weight of the turbine.

In more detail, comparisons with the electric compressor type architecture show an increase in power density of approximately 7.4 % for the electric turbocharger type architecture, and a decrease in power density of 2% for the serial booster type architecture.

These results are at the expense of an increase in overall FCPS efficiency of only 0.5 % for the serial booster-type architecture compared to the electric turbocharger-type architecture.

From these analyses, it was found that it is more convenient to use the electric turbocharger type architecture for the case study considered.

For aircraft that have to reach higher altitudes and therefore higher compression ratios, it may be more convenient to use the serial booster architecture.

Once the architecture was chosen, it was implemented in the dynamic model on the Simulink software.

Modelling is based on equations describing the physical behaviour of the systems.

The turbine and compressor are modelled through performance maps dimensioned in static sizing. A control system was implemented in order to keep the excess oxygen ratio and the working pressure of the stack constant in order to optimise performance and always work within the safety region of the compressor.

The system's response to the dynamic effects of changing environmental conditions during the flight mission and the application of current disturbances was simulated.

The results of the simulations were satisfactory, obtaining a good response of the control system on the controlled variables and in particular the compressor always works under safe conditions, that is, at stability points of its performance map, the excess oxygen value does not fall below the critical value of 1.2 which may lead to the phenomenon of reagent starvation and pressure fluctuations at the cathode do not exceed the indicative safety values of 100-200mbar.

The results of the simulations were compared with those of the system without a turbine, and these show an increase of about 3.2 % in the overall cruising efficiency of the FCPS for the electric turbocharger type architecture compared to the electric compressor type architecture, both designed to work in their optimum conditions.

Bibliography

- [1] Fuel Cells and Hydrogen 2 Joint Undertaking., "Hydrogen-powered aviation : a fact-based study of hydrogen technology, economics, and climate impact by 2050.," 2020, doi: 10.2843/766989.
- [2] Iberdrola, "Green hydrogen: an alternative that reduces emissions and cares for our planet." [Online]. Available: <https://www.iberdrola.com/sustainability/green-hydrogen>
- [3] J. T. Pukrushpan, A. G. Stefanopoulou, and H. Peng, "Control of Fuel Cell Power Systems," London, 2004. doi: 10.1007/978-1-4471-3792-4.
- [4] A. Kerviel, A. Pesyridis, and D. Chalet, "An Evaluation of Turbocharging and Supercharging Options for High-Efficiency Fuel Cell Electric Vehicles," 2018.
- [5] Dr.-I. Lukas Barchewitz, "In-flight Air Supply System for PEM Fuel Cells," University of Hannover, 2008.
- [6] James. Larminie and Andrew. Dicks, "Fuel cell systems explained," p. 406, 2003.
- [7] D. Juschus, "Preliminary Propulsion System Sizing Methods for PEM Fuel Cell Aircraft," 2021, [Online]. Available: <http://repository.tudelft.nl/>.
- [8] H. Cruz-Martínez *et al.*, "Mexican contributions for the improvement of electrocatalytic properties for the oxygen reduction reaction in PEM fuel cells," *Int J Hydrogen Energy*, pp. 12477–12491, May 2019, doi: 10.1016/j.ijhydene.2018.05.168.
- [9] S. Campanari, G. Manzolini, A. Beretti, and U. Wollrab, "Performance assessment of turbocharged pem fuel cell systems for civil aircraft onboard power production," *J Eng Gas Turbine Power*, vol. 130, no. 2, Mar. 2008, doi: 10.1115/1.2772636.
- [10] P. Kahroba, I. Mirzaee, H. Shirvani, P. Kahroba, I. Mirzaee, and H. Shirvani, "The Inlet Humidification Effect on PEM Fuel Cell Performance," 2009. [Online]. Available: <https://www.researchgate.net/publication/310832359>
- [11] Davide Comincini, "Modular approach to hydrogen hybrid-electric aircraft design," Master degree thesis, Politecnico di Milano, 2018.
- [12] B. Blunier and A. Miraoui, "Air Management in PEM Fuel Cells: State-of-the-Art and Perspectives," 2022.
- [13] Federico Fasiello, "Preliminary study of an air supply system for an aviation fuel cell power plant," Master degree thesis, Politecnico di Torino, 2022.
- [14] "ATR 72-600 website." [Online]. Available: <https://www.atr-aircraft.com/our-aircraft/atr-72-600/>.
- [15] "ATR web page." [Online]. Available: <https://www.atr-aircraft.com/>.
- [16] F. Uhrig, M. Schinnerl, P. Haluska, P. Kurzweil, and T. von Unwerth, "Comparative Study of Different Air Supply Systems for Automotive Fuel Cell Applications," 2019.
- [17] C. Bao, M. Ouyang, and B. Yi, "Modeling and optimization of the air system in polymer exchange membrane fuel cell systems," *J Power Sources*, vol. 156, no. 2, pp. 232–243, Jun. 2006, doi: 10.1016/j.jpowsour.2005.06.008.

- [18] W. Jiuxuan, Q. Mingxu, Z. Hong, and L. Xue, "Investigation on exhaust energy recovery system using radial turbine in high-power proton exchange membrane fuel cells," 2022. [Online]. Available: <http://asmedigitalcollection.asme.org/GT/proceedings-pdf/GT2022/86052/V007T18A018/6936067/v007t18a018-gt2022-82822.pdf>
- [19] J. T. Pukrushpan, "Modeling and control of fuel cell systems and fuel processors," 2003.
- [20] P. Moraal and I. Kolmanovsky, "Turbocharger Modeling for Automotive Control Applications," 1999.
- [21] J. Hoeflinger and P. Hofmann, "Air mass flow and pressure optimisation of a PEM fuel cell range extender system," *Int J Hydrogen Energy*, vol. 45, no. 53, pp. 29246–29258, Oct. 2020, doi: 10.1016/j.ijhydene.2020.07.176.
- [22] Y. Li, P. Pei, Z. Wu, H. Xu, D. Chen, and S. Huang, "Novel approach to determine cathode two-phase-flow pressure drop of proton exchange membrane fuel cell and its application on water management," *Appl Energy*, vol. 190, pp. 713–724, 2017, doi: 10.1016/j.apenergy.2017.01.010.
- [23] H. Chen, H. Guo, F. Ye, and C. F. Ma, "An experimental study of cell performance and pressure drop of proton exchange membrane fuel cells with baffled flow channels," *J Power Sources*, vol. 472, Oct. 2020, doi: 10.1016/j.jpowsour.2020.228456.
- [24] M. Mortazavi and K. Tajiri, "Two-phase flow pressure drop in flow channels of proton exchange membrane fuel cells: Review of experimental approaches," *Renewable and Sustainable Energy Reviews*, vol. 45. Elsevier Ltd, pp. 296–317, 2015. doi: 10.1016/j.rser.2015.01.044.
- [25] M. Gambini and M. Vellini, "Turbomachinery Fundamentals, Selection and Preliminary Design," 2021. [Online]. Available: https://doi.org/10.1007/978-3-030-51299-6_2.
- [26] A. A. Sonin, "The Physical Basis of dimensional analysis," 2001.
- [27] Alessandro Ferrari, *Fondamenti di termofluidodinamica per le macchine.*, Ed. by Città Studi., vol. 1. 2019.
- [28] C. Dongiovanni, "Appunti del corso di Macchine," 2017.
- [29] G. Dufour, X. Carbonneau, J.-B. Cazalbou, and P. Chassaing, "Practical use of similarity and scaling laws for centrifugal compressor design," *Power for Land*, 2006. [Online]. Available: <https://proceedings.asmedigitalcollection.asme.org>
- [30] B. Lakshminarayana, "Fluid Dynamics and Heat Transfer of Turbomachinery. John Wiley & Sons, Inc., NYC.," 1996.
- [31] Y. Liu, W. Zhuge, Y. Zhang, S. Zhang, J. Zhang, and X. Huo, "A Matching Method for Two-Stage Turbocharging System," 2014. [Online]. Available: <http://www.asme.org/about-asme/terms-of-use>
- [32] M. Tancrez, J. Galindo, C. Guardiola, P. Fajardo, and O. Varnier, "Turbine adapted maps for turbocharger engine matching," *Exp Therm Fluid Sci*, vol. 35, no. 1, pp. 146–153, Jan. 2011, doi: 10.1016/j.expthermflusci.2010.07.018.
- [33] B. Lee, "Dual-Stage Boosting Systems: Modeling of Configurations, Matching and Boost Control Options," 2009.
- [34] E. Spessa, "Turbocharging & Supercharging," in *Appunti del corso di "Design of Engine and Control System"*, Politecnico di Torin, 2020.

- [35] Y. Zhang, S. Xu, and C. Lin, "Performance improvement of fuel cell systems based on turbine design and supercharging system matching," *Appl Therm Eng*, vol. 180, Nov. 2020, doi: 10.1016/j.applthermaleng.2020.115806.
- [36] D. Filsinger, G. Kuwata, and N. Ikeya, "Tailored Centrifugal Turbomachinery for Electric Fuel Cell Turbocharger," *International Journal of Rotating Machinery*, vol. 2021, 2021, doi: 10.1155/2021/3972387.
- [37] G. Dufour, X. Carbonneau, J.-B. Cazalbou, and P. Chassaing, "Practical use of similarity and scaling laws for centrifugal compressor design," *Power for Land*, 2006. [Online]. Available: <https://proceedings.asmedigitalcollection.asme.org>
- [38] "GARRETT G25-550." [Online]. Available: <https://www.garrettmotion.com/it/racing-and-performance/performance-catalog/turbo/g-series-g25-550/>.
- [39] M. V Casey, D. Krähenbühl Celeroton Ltd, and S. Christof Zwysig, "The Design of Ultra-High-Speed Miniature Centrifugal Compressors," 2013.
- [40] Y. Zhang, S. Xu, and C. Lin, "Performance improvement of fuel cell systems based on turbine design and supercharging system matching," *Appl Therm Eng*, vol. 180, Nov. 2020, doi: 10.1016/j.applthermaleng.2020.115806.
- [41] J.-P. Jensen, A. F. Kristensen, S. C. Sorenson, N. Houbak, and E. Hendricks, "Mean Value Modeling of a Small Turbocharged Diesel Engine," 1991.
- [42] P. Andersson, *Air charge estimation in turbocharged spark ignition engines*. Dept. of Electrical Engineering, Linköping University, 2005.
- [43] A. Vondrák, "Fitting & Extrapolation of Turbine Performance Maps of Automotive Turbochargers," *MATEC Web of Conferences*, vol. 328, p. 03010, 2020, doi: 10.1051/mateconf/202032803010.
- [44] J. Heimersson and A. Johannesson, "Online modelling and control of charging system."
- [45] "BorgWarner." [Online]. Available: <https://www.borgwarner.com/home>
- [46] Sa charging solution, "<https://www.turbomap.ch/Home/>."
- [47] X. Fang and Y. Xu, "Development of an empirical model of turbine efficiency using the Taylor expansion and regression analysis," *Energy*, vol. 36, no. 5, pp. 2937–2942, 2011, doi: 10.1016/j.energy.2011.02.036.
- [48] "GARRETT G55-2100." [Online]. Available: <https://www.garrettmotion.com/it/racing-and-performance/performance-catalog/turbo/g-series-g55-2100-91mm/>.
- [49] Adam Vondrák, "Fitting and extrapolation of turbocharger turbine maps," 2021.
- [50] "GARRETT GBC14-200." [Online]. Available: <https://www.garrettmotion.com/it/racing-and-performance/performance-catalog/turbo/garrett-boost-club-line-gbc14-200/>
- [51] L. Eriksson, "Modeling and control of turbocharged SI and DI engines," in *Oil and Gas Science and Technology*, Jul. 2007, pp. 523–538. doi: 10.2516/ogst:2007042.
- [52] K. Rong, "Modeling of turbocharged spark ignited engine and model predictive control of hybrid turbocharger," 2014.
- [53] "Feedforward.(control)."[Online].Available: <https://www.basicknowledge101.com/pdf/control/Feed%20forward%20%28control%29.pdf>